THE ANALYSIS OF DIGITAL MAMMOGRAMS: SPICULATED TUMOR DETECTION AND NORMAL MAMMOGRAM CHARACTERIZATION

A Thesis
Submitted to the Faculty

of

Purdue University

by

Sheng Liu

In Partial Fulfillment of the
Requirements for the Degree

of

Doctor of Philosophy

May 1999

To my parents

ACKNOWLEDGMENTS

I wish to express my sincere gratitude to my major Professor Edward J. Delp for his guidance and support. I greatly appreciate his care and dedication in constructively criticizing my work. I have truly benefited and enjoyed from working with him.

I would like to thank Dr. Charles F. Babbs and Prof. Zygmunt Pizlo for many insightful and detailed suggestions they provided on my research. I would also like to thank the other members of my committee, Prof. Charles A. Bouman and Prof. Peter C. Doerschuk, for their support.

I wish to thank the National Institutes of Health and the Purdue Cancer Center for funding my research.

Finally, I would like to thank my husband for his love and understanding during many hours I am away from him, and my parents for their constant support and encouragement.

DISCARD THIS PAGE

TABLE OF CONTENTS

Page

LIST OF TABLES vi

LIST OF FIGURES vii

ABSTRACT xvii

1. INTRODUCTION 1

2. COMPUTER AIDED DIAGNOSIS IN DIGITAL MAMMOGRAPHY . . . 5

2.1 Features of Breast Lesions in Mammograms 5
2.2 Current Status of CAD research in Digital Mammography 6

3. MULTIRESOLUTION REPRESENTATIONS OF IMAGES 17

3.1 Introduction 17
3.2 Notation 17
3.3 Multiresolution Analysis of One Dimensional Signals 18
3.3.1 Orthogonal Wavelet Representation 18
3.3.2 Biorthogonal Wavelet Representation 22
3.3.3 M Voices Per Octave 23
3.3.4 Undecimated Wavelet Representation 24
3.4 Extension to Two Dimensional Signals 25
3.4.1 Separable Wavelet Representation 25
3.4.2 Non-Separable Wavelet Representation 25
3.5 Wavelet Transform of Digital Images 26

4. MULTIRESOLUTION DETECTION OF SPICULATED LESIONS 37

4.1 Introduction 37
4.2 Multiresolution Decomposition 38
4.3 Multiresolution Feature Analysis 39
4.4 Classification Algorithm 43
4.5 Results and Conclusions 44

Page

5. CHARACTERIZATION OF NORMAL MAMMOGRAMS 61

5.1 Introduction 61
5.2 Normal Mammograms 63
5.3 Linear Structure Identification 64
5.3.1 Introduction 64
5.3.2 Model For Lines 67
5.3.3 Detection Algorithm 68
5.3.4 Experimental Results and Discussions 71
5.4 Residual Images Generation 72
5.5 Experimental Results 73

6. CONCLUSION 137

LIST OF REFERENCES 141

VITA 150

DISCARD THIS PAGE

LIST OF TABLES

Table Page

3.1 Filter coefficients for implementing a biorthogonal wavelet representation. 27

3.2 Analysis Lowpass Filter Coefficients. 27

3.3 Analysis Highpass Filter Coefficients. 28

3.4 Synthesis Lowpass Filter Coefficients. 28

3.5 Synthesis Highpass Filter Coefficients. 28

5.1 Compass line detection operators. 77

DISCARD THIS PAGE

LIST OF FIGURES

Figure		Page
2.1	A normal mammogram.	10
2.2	Two basic types of malignant microcalcifications. (a) Granular: tiny with dot-like or elongated shape, innumerable. (b) Casting: fragments with irregular contour, differ in length.	11
2.3	Benign microcalcifications. (a) Homogeneous, solid, sharply outlined, spherical, pearl-like, very fine and dense. (b) Ring-shaped, oval, center radiolucent. (c) Coarse, irregular but sharply outlined and very dense.	11
2.4	Mammographic characteristics of calcifications.	12
2.5	Malignant masses. (a) High density radiopaque. (b) Solid tumor with random orientation.	13
2.6	Benign masses. (a) Halo: a narrow radiolucent ring or a segment of a ring around the periphery of a tumor, (b) Capsule: a thin, curved, radiopaque line that is seen only when it surrounds tumors containing fat. (c) A cyst with smooth borders and orient in the direction of the nipple following the trabecular structure of the breast.	13
2.7	Mammographic characteristics of circumscribed lesions.	14
2.8	Malignant spiculated lesions. (a) Distinct central tumor mass with dense spicules radiating in all directions. The spicule length usually increases with tumor size. (b) Very small, hardly perceptible tumor center and a lace-like, fine reticular radiating structure which causes parenchymal distortion and/or asymmetry.	15
2.9	Benign spiculated lesions. (a) Center is translucent, oval or circular. (b) Translucent areas are within a loose structure, spicules are fine and of low density.	15
2.10	Mammographic characteristics of spiculated lesions.	16

Figure		Page
3.1	Orthogonal wavelet decomposition of α_n^0.	29
3.2	Reconstruction of α_n^0 from its orthogonal wavelet representation.	29
3.3	Scaling functions $\phi(x)$, $\tilde{\phi}(x)$, and wavelet basis functions $\psi(x)$, $\tilde{\psi}(x)$ for the biorthogonal example.	30
3.4	Phase space grids (a) octave-by-octave. (b) 2-voices per octave.	30
3.5	(a) Scaling functions for scale $a = 2^j$ (top) and $a = 2^{j+1/2}$ (bottom). (b) Wavelet basis functions for scale $a = 2^j$ (top) and $a = 2^{j+1/2}$ (bottom). .	31
3.6	(a) Lowpass filters for scale $a = 2^j$ (top) and $a = 2^{j+1/2}$ (bottom). (b) Corresponding magnitude responses.	31
3.7	(a) Highpass filters for scale $a = 2^j$ (top) and $a = 2^{j+1/2}$ (bottom). (b) Corresponding magnitude responses.	32
3.8	Separable 2D wavelet transform: (a) Decomposition. (b)Reconstruction.	32
3.9	Two dimensional quincunx sublattice.	33
3.10	Non-separable perfect reconstruction 2D filter (magnitude response). . .	33
3.11	Original image Barbara. Its pixel values can be viewed as the approximation coefficients of a continuous function $\tilde{f}(x, y)$ at resolution $j = 0$. . . .	34
3.12	First level wavelet decomposition of the Barbara image. (a) approximation coefficients α_n^{-1}. (b) horizontal detail signal $\beta_{1,n}^{-1}$. (c) vertical detail signal $\beta_{2,n}^{-1}$. (d) diagonal detail signal $\beta_{3,n}^{-1}$.	35
3.13	Second level wavelet decomposition of the Barbara image obtained by decomposing the approximation coefficients α_n^{-1} at the first level $j = -1$. (a) approximation coefficients α_n^{-2}. (b) horizontal detail signal $\beta_{1,n}^{-2}$. (c) vertical detail signal $\beta_{2,n}^{-2}$. (d) diagonal detail signal $\beta_{3,n}^{-2}$.	36
4.1	Diagram of system for multiresolution spiculated lesion detection, illustrated here for only two resolutions — fine (left) and coarse (right). . . .	48
4.2	Multiresolution representation of a spiculated lesion (a) spiculated lesion in the original mammogram of resolution $N \times N$. (b) in the coarser resolution $N/2 \times N/2$. (c) in the coarser resolution $N/4 \times N/4$. (d) in the coarsest resolution $N/8 \times N/8$	49

Appendix
Figure Page

4.3 Folding edge orientation makes the feature $\sigma_{\theta'}$ insensitive to the nominal value of θ, but sensitive to the actual edge orientation variances. 50

4.4 (a) Directions of spicules of a spiculated lesion differ from the directions of normal linear markings in a mammogram; (b) standard deviation of gradient orientation histogram differentiates the area near a spiculated lesion from normal. 50

4.5 (a) A spiculated lesion region. (b) A normal region. (c) Gradient orientation histograms of (a) and (b) 51

4.6 Multiresolution representation of a test pattern consisting of an idealized spiculated lesion and normal structures embedded in uncorrelated Gaussian distributed noise. The lesion has a radius of 128 pixels in the original image: (a) original $N \times N$ image. (b) coarser resolution $N/2 \times N/2$. (c) coarsest resolution $N/4 \times N/4$. 52

4.7 Feature $\sigma_{\theta'}$ obtained in circular neighborhoods of radius 30 pixels at all resolutions for the test pattern shown in Figure 4.6. Here large values (bright pixels) indicate spiculated regions as explained in Figure 4.4. (a) original $N \times N$ image. (b) coarser resolution $N/2 \times N/2$. (c) coarsest resolution $N/4 \times N/4$. (d) a circular neighborhood of size 30 pixels in radius. 53

4.8 Feature σ_{hist} obtained in circular neighborhoods of radius 30 pixels at all resolutions for the test pattern shown in Figure 4.6. Here small values (dark pixels) indicate spiculated regions as explained in Figure 4.4. (a) original $N \times N$ image. (b) coarser resolution $N/2 \times N/2$. (c) coarsest resolution $N/4 \times N/4$. (d) a circular neighborhood of size 30 pixels in radius. 54

4.9 Feature $\bar{f}$ obtained in circular neighborhoods of radius 20 pixels at all resolutions for the test pattern shown in Figure 4.6: (a) original $N \times N$ image. (b) coarser resolution $N/2 \times N/2$. (c) coarsest resolution $N/4 \times N/4$. (d) a circular neighborhood of size 20 pixels in radius. 55

Appendix
Figure Page

4.10 Feature σ_f obtained in circular neighborhoods of radius 20 pixels at all resolutions for the test pattern shown in Figure 4.6. Note that feature values are smaller (darker) in the background area at coarser resolutions because of the smoothing effect of the lowpass filtering step in obtaining coarser resolution images. (a) original $N \times N$ image. (b) coarser resolution $N/2 \times N/2$. (c) coarsest resolution $N/4 \times N/4$. (d) a circular neighborhood of size 20 pixels in radius. 56

4.11 A spiculated lesion of size 6.6 mm detected at the finest resolution (a) mammogram with automatic detection. (b) mammogram with tumor as determined by expert radiologists. 57

4.12 A spiculated lesion of size 12.4 mm detected at the second coarsest resolution (a) mammogram with automatic detection. (b) mammogram with tumor as determined by expert radiologists. 58

4.13 A spiculated lesion of size 35.0 mm detected at the coarsest resolution (a) mammogram with automatic detection. (b) mammogram with tumor as determined by expert radiologists. 59

4.14 FROC curve for detection of spiculated lesions in the MIAS database . . 60

4.15 The first missed spiculated lesion when the detection sensitivity is decreased. It lacks visible spicules at all directions. 60

5.1 Entirely normal mammograms may have very different appearance. These normal mammograms have ACR breast tissue density ratings of: (a) 1. (b) 2. (c) 3. (d) 4. 78

5.2 (a) A normal region of a mammogram. (b) A spiculated lesion region of a mammogram. (c) Normal structures appear as quasi-parallel linear markings. (d) A spiculated lesion has linear markings that radiate in all directions. 79

5.3 (a) A straight line at a distance s and orientation θ. (b) Hough transform maps all the pixels on this line into one point in the (s, θ) parameter space, or Hough space. 80

5.4 Filter impulse response of correlation line detectors 80

Appendix
Figure Page

5.5 (a) Test pattern with lines and solid areas. (b) Line angle image including "lines" without solid features, in which brightness corresponding to line orientation. (c) Individual line detector output at 0^o. (d) 45^o. (e) 90^o. (f) 135^o. 81

5.6 A linear marking may not be extracted accurately if its width does not match well with the width of the correlation filters. (a) Original mammogram containing circumscribed mass. (b) Highpass filtered enhanced image. (c) Linear structures detected from the enhanced image using correlation filters with width 0.85 mm. (d) Removed detected linear structures from the enhanced image. 82

5.7 Pixels belonging to a line are not necessarily edge pixels. (a) An image with a 1 pixel wide "thin" line at the top and a 10 pixel wide "thick" line at the bottom. (b) The shaded pixel in the middle of the "thick" line looks unlike an edge pixel within a 9×9 neighborhood, which is larger than the spatial support of most edge operators. 83

5.8 The E-W compass gradient operator detects only edges of the lines in the image shown in Figure 5.7 (a). 83

5.9 If a pixel belongs to a line, then there exists a string of pixels with similar graylevels along the direction of the line that contains this pixel. 84

5.10 Lines are perceived at orientations (a) 0^o. (b) 11.25^o. (c) 22.5^o. and (d) 33.75^o. 85

5.11 Necessary conditions for a line to be perceived in an image. (a) Its surrounding region has different graylevels from those of the pixels on the line. (b) Its length is larger than its width. 86

5.12 Two strings of the same length contain different number of pixels. 86

5.13 Relationship between $\sigma_{i,j}(\theta, l)$ and θ. (a) Repeat the image shown in Figure 5.7 (a). (b) For a pixel on the thin line. (c) For a pixel in the uniform region. (d) For a pixel on the thick line. 87

5.14 Block diagram of our line detector. 88

5.15 There are $N_{L(\theta,l)}$ number of strings passing through each pixel for given θ and l. 88

Appendix
Figure Page

5.16 The proposed line detector detects both the "thin" line and the "thick line" in the image shown in Figure 5.7 (a). 89

5.17 (a) White Gaussian noise with mean the same as that of the lines is introduced to the background of the image in Figure 5.7 (a). (b) The E-W compass gradient operator failed to detect the lines. (c) Our proposed line detector correctly identified both lines. 90

5.18 Lines with width narrower than the l applied are detected, While those wider lines are considered as uniform regions. (a) Input image with the top line 1 pixel wide and each subsequent line is 2 pixel wider than the one directly above it. (b) Direction result using $l = 5$. (c) Direction result using $l = 10$. and (d) Direction result using $l = 20$. 91

5.19 (a) Original normal mammogram. (b) Highpass filtered enhanced image. (c) Linear structures detected from the enhanced image. (d) Removed detected linear structures from the enhanced image. 92

5.20 (a) Original mammogram containing circumscribed mass. (b) Highpass filtered enhanced image. (c) Linear structures detected from the enhanced image. (d) Removed detected linear structures from the enhanced image and the mass becomes more conspicuous. 93

5.21 Block diagram of normal tissue identification and removal algorithm, where W_s = weighting factor; K = constant offset factor; G = gain. . . . 94

5.22 Smoothing and background subtraction. 95

5.23 Normal structure removal. 96

5.24 (a) Original mammogram with the circumscribed masses outlined. (b) Background subtracted image I_1. (c) Normal linear structure map I_m. (d) Residual image consisting of only the tumor on featureless background. 97

5.25 Results in Figure 5.24 repeated for the region centered at the masses. (a) Original mammogram containing circumscribed masses. (b) Background subtracted image I_1. (c) Normal linear structure map I_m. (d) Residual image consisting of only the tumor on featureless background. 98

5.26 (a) Original mammogram with the spiculated lesion outlined. (b) Background subtracted image I_1. (c) Normal linear structure map I_m contains the spiculations. (d) Residual image does not preserve the spiculations. . 99

Appendix
Figure Page

5.27 Results in Figure 5.26 repeated for the region centered at the spiculated lesion. (a) Original mammogram containing spiculated lesion. (b) Background subtracted image I_1. (c) Normal linear structure map I_m contains the spiculations. (d) Residual image does not preserve the spiculations. . 100

5.28 (a) Original mammogram with the microcalcifications outlined. (b) Background subtracted image I_1. (c) Normal linear structure map I_m. (d) Residual image with more conspicuous microcalcifications. 101

5.29 Results in Figure 5.28 repeated for the region centered at the microcalcifications. (a) Original mammogram containing microcalcifications. (b) Background subtracted image I_1. (c) Normal linear structure map I_m. (d) Residual image with more conspicuous microcalcifications. 102

5.30 Original mammograms containing microcalcifications. 103

5.31 Enhanced image using technique by Strickland and Hahn. 103

5.32 Residual image with more conspicuous microcalcifications. 104

5.33 (a) Original normal mammogram. (b) Background subtracted image I_1. (c) Normal linear structure map I_m. (d) Residual image. 105

5.34 (a) Original normal mammogram. (b) Background subtracted image I_1. (c) Normal linear structure map I_m. (d) Residual image. 106

5.35 (a) Original normal mammogram. (b) Background subtracted image I_1. (c) Normal linear structure map I_m. (d) Residual image. 107

5.36 (a) Original normal mammogram. (b) Background subtracted image I_1. (c) Normal linear structure map I_m. (d) Residual image. 108

5.37 (a) Original normal mammogram. (b) Background subtracted image I_1. (c) Normal linear structure map I_m. (d) Residual image. 109

5.38 (a) Original normal mammogram. (b) Background subtracted image I_1. (c) Normal linear structure map I_m. (d) Residual image. 110

5.39 (a) Original normal mammogram. (b) Background subtracted image I_1. (c) Normal linear structure map I_m. (d) Residual image. 111

5.40 (a) Original normal mammogram. (b) Background subtracted image I_1. (c) Normal linear structure map I_m. (d) Residual image. 112

Appendix
Figure Page

5.41 (a) Original mammogram with the circumscribed masses outlined. (b) Background subtracted image I_1. (c) Normal linear structure map I_m. (d) Residual image consisting of only the tumor on featureless background. 113

5.42 Results in Figure 5.41 repeated for the region centered at the masses. (a) Original mammogram containing circumscribed masses. (b) Background subtracted image I_1. (c) Normal linear structure map I_m. (d) Residual image consisting of only the tumor on featureless background. 114

5.43 (a) Original mammogram with the circumscribed masses outlined. (b) Background subtracted image I_1. (c) Normal linear structure map I_m. (d) Residual image consisting of only the tumor on featureless background. 115

5.44 Results in Figure 5.43 repeated for the region centered at the masses. (a) Original mammogram containing circumscribed masses. (b) Background subtracted image I_1. (c) Normal linear structure map I_m. (d) Residual image consisting of only the tumor on featureless background. 116

5.45 (a) Original mammogram with the circumscribed masses outlined. (b) Background subtracted image I_1. (c) Normal linear structure map I_m. (d) Residual image consisting of only the tumor on featureless background. 117

5.46 Results in Figure 5.45 repeated for the region centered at the masses. (a) Original mammogram containing circumscribed masses. (b) Background subtracted image I_1. (c) Normal linear structure map I_m. (d) Residual image consisting of only the tumor on featureless background. 118

5.47 (a) Original mammogram with the circumscribed masses outlined. (b) Background subtracted image I_1. (c) Normal linear structure map I_m. (d) Residual image consisting of only the tumor on featureless background. 119

5.48 Results in Figure 5.47 repeated for the region centered at the masses. (a) Original mammogram containing circumscribed masses. (b) Background subtracted image I_1. (c) Normal linear structure map I_m. (d) Residual image consisting of only the tumor on featureless background. 120

5.49 (a) Original mammogram with the spiculated lesion outlined. (b) Background subtracted image I_1. (c) Normal linear structure map I_m contains the spiculations. (d) Residual image does not preserve the spiculations. . 121

Appendix
Figure Page

5.50 Results in Figure 5.49 repeated for the region centered at the spiculated lesion. (a) Original mammogram containing spiculated lesion. (b) Background subtracted image I_1. (c) Normal linear structure map I_m contains the spiculations. (d) Residual image does not preserve the spiculations. . 122

5.51 (a) Original mammogram with the spiculated lesion outlined. (b) Background subtracted image I_1. (c) Normal linear structure map I_m contains the spiculations. (d) Residual image does not preserve the spiculations. . 123

5.52 Results in Figure 5.51 repeated for the region centered at the spiculated lesion. (a) Original mammogram containing spiculated lesion. (b) Background subtracted image I_1. (c) Normal linear structure map I_m contains the spiculations. (d) Residual image does not preserve the spiculations. . 124

5.53 (a) Original mammogram with the spiculated lesion outlined. (b) Background subtracted image I_1. (c) Normal linear structure map I_m contains the spiculations. (d) Residual image does not preserve the spiculations. . 125

5.54 Results in Figure 5.53 repeated for the region centered at the spiculated lesion. (a) Original mammogram containing spiculated lesion. (b) Background subtracted image I_1. (c) Normal linear structure map I_m contains the spiculations. (d) Residual image does not preserve the spiculations. . 126

5.55 (a) Original mammogram with the spiculated lesion outlined. (b) Background subtracted image I_1. (c) Normal linear structure map I_m contains the spiculations. (d) Residual image does not preserve the spiculations. . 127

5.56 Results in Figure 5.55 repeated for the region centered at the spiculated lesion. (a) Original mammogram containing spiculated lesion. (b) Background subtracted image I_1. (c) Normal linear structure map I_m contains the spiculations. (d) Residual image does not preserve the spiculations. . 128

5.57 (a) Original mammogram with the microcalcifications outlined. (b) Background subtracted image I_1. (c) Normal linear structure map I_m. (d) Residual image with more conspicuous microcalcifications. 129

5.58 Results in Figure 5.57 repeated for the region centered at the microcalcifications. (a) Original mammogram containing microcalcifications. (b) Background subtracted image I_1. (c) Normal linear structure map I_m. (d) Residual image with more conspicuous microcalcifications. 130

Appendix
Figure Page

5.59 (a) Original mammogram with the microcalcifications outlined. (b) Background subtracted image I_1. (c) Normal linear structure map I_m. (d) Residual image with more conspicuous microcalcifications. 131

5.60 Results in Figure 5.59 repeated for the region centered at the microcalcifications. (a) Original mammogram containing microcalcifications. (b) Background subtracted image I_1. (c) Normal linear structure map I_m. (d) Residual image with more conspicuous microcalcifications. 132

5.61 (a) Original mammogram with the microcalcifications outlined. (b) Background subtracted image I_1. (c) Normal linear structure map I_m. (d) Residual image with more conspicuous microcalcifications. 133

5.62 Results in Figure 5.61 repeated for the region centered at the microcalcifications. (a) Original mammogram containing microcalcifications. (b) Background subtracted image I_1. (c) Normal linear structure map I_m. (d) Residual image with more conspicuous microcalcifications. 134

5.63 (a) Original mammogram with the microcalcifications outlined. (b) Background subtracted image I_1. (c) Normal linear structure map I_m. (d) Residual image with more conspicuous microcalcifications. 135

5.64 Results in Figure 5.63 repeated for the region centered at the microcalcifications. (a) Original mammogram containing microcalcifications. (b) Background subtracted image I_1. (c) Normal linear structure map I_m. (d) Residual image with more conspicuous microcalcifications. 136

ABSTRACT

Liu, Sheng, Ph.D., Purdue University, May 1999. The Analysis Of Digital Mammograms: Spiculated Tumor Detection And Normal Mammogram Characterization. Major Professor: Edward J. Delp.

Mammography is currently the best technique for reliable detection of early, non-palpable, potentially curable breast cancer. In the past decade there has been tremendous interest in computer aided diagnosis (CAD) in digital mammograms. The goal has been to increase diagnostic accuracy as well as the reproducibility of mammographic interpretation.

Among breast abnormalities, spiculated masses having a stellate appearance are the most difficult type of tumor to detect. We propose a multiresolution feature analysis and classification approach for the detection of spiculated lesions. In general, it is difficult to determine the size of the neighborhood that should be used to extract local features of spiculated lesions. There is a fundamental difference in our method compared to other approaches, in that we extract and classify features at multiple resolutions, hence overcoming the difficulty of choosing a neighborhood size a priori to capture tumors of varying sizes. Furthermore, the top-down classification requires less computation by starting with the coarsest resolution image and propagating detection results to finer resolutions. On the MIAS database, we achieved 84.2% true positive detection at less than 1 false positive per image and 100% true positive detection at 2.2 false positive per image.

The effectiveness of algorithms for detecting cancers can be greatly increased if these algorithms work synergistically with algorithms for recognizing normal mammograms. However, little work has been done on understanding normal mammograms.

We propose a novel technique to specifically characterize normal mammograms based on normal tissue identification and removal, which is independent of the types of abnormalities that may exist in the mammogram. Experimental results have shown that this approach also facilitates the classification of abnormalities, since suppressing normal background structures enhances the contrast and obviousness of abnormal structures.

1. INTRODUCTION

Breast cancer is the second major cause of death from cancer among American women and continues to be the leading cause of nonpreventable cancer death [1]. It is a serious health problem in the United States, the incidence of which continues to rise [2]. The American Cancer Society (ACS) estimates that, on average, every 15 minutes five women are diagnosed with breast cancer, and one woman dies of this disease. It is also estimated that one in eight women will be diagnosed with breast cancer in her lifetime, and 1 in 30 will die from it [2]. Mammography is currently the best technique for reliable detection of early, non-palpable, potentially curable breast cancer [3]. The mortality rate from this disease decreased for the first time in 1995, due in part to the increasing utilization of screening mammography [2]. However, radiologists vary in their interpretation of mammograms. In addition, the interpretation is a repetitive task that requires much attention to minute detail. Therefore, in the past decade there has been tremendous interest in the use of image processing and analysis techniques [4, 5, 6, 7, 8, 9] for Computer Aided Diagnosis (CAD) in digital mammograms, which will replace conventional mammograms in the near future. The goal has been to increase diagnostic accuracy as well as the reproducibility of mammographic interpretation.

Among breast abnormalities, spiculated masses having a stellate appearance in mammograms are the worst and most difficult type of tumor to detect [1]. Their central masses are usually irregular with ill-defined borders. Their sizes vary from a few millimeters to several centimeters in diameter. Computer aided tumor detection in digital mammograms usually consists of feature extraction followed by classification [4]. In general, it is difficult to determine the size of the neighborhood that

should be used to extract local features of spiculated lesions. If the neighborhood is too large, small lesions may be missed; while if the neighborhood is too small, parts of large lesions may be missed. In this thesis we propose a new multiresolution image analysis algorithm for the detection of spiculated lesions in mammograms [10, 11] that specifically addresses this difficulty of predetermining the neighborhood size for feature extraction. We first obtain a multiresolution representation of the original mammogram using a linear phase nonseparable 2-D wavelet transform. Features that are designed to differentiate spiculated lesions from normal structures are then extracted for every pixel at each resolution. Detection is performed from the coarsest resolution to the finest resolution using a binary tree classifier. There is a fundamental difference in our method than other approaches, in that we extract and classify features at multiple resolutions, hence overcoming the difficulty of choosing a neighborhood size *a priori* to capture tumors of varying sizes. Furthermore, the top-down classification we use requires less computation by starting with the coarsest resolution image (least amount of data) and propagating detection results to finer resolutions.

Cancer treatment is most effective when the cancer is detected early, it follows that the progress in treatment will be closely related to the ability to reduce the proportion of "misses" in the cancer detection task. This, in turn, requires better methods for analyzing hard abnormal mammograms, which are hard because they are very similar to normal mammograms. The effectiveness of algorithms for detecting cancers can be greatly increased if these algorithms work synergistically with algorithms for characterizing normal mammograms. However, little work has been done on understanding normal mammograms [12]. In this thesis we propose a novel algorithm to specifically characterize normal mammograms. This algorithm is based on normal tissue identification and removal, which is independent of the types of abnormalities that may exist in the mammogram. This approach also facilitates the classification of abnormalities, since suppressing normal background structures enhances the contrast and obviousness of abnormal structures. In addition, the normal tissue characterization problem is fundamentally simpler and easier for computers to solve than is the

tumor detection problem, because the properties of images of normal tissue are much simpler than the properties of images of abnormalities of various types, sizes, and stages of development.

In Chapter 2, we first summarize the features of three types of breast lesions in digital mammograms: microcalcifications, circumscribed lesions, and spiculated or stellate lesions. We then present a survey of the current status of CAD research in digital mammography.

In Chapter 3, we provide an overview of multiresolution representations of signals using wavelets. In Section 3.3, one dimensional multiresolution analysis is discussed, including the orthogonal and biorthogonal wavelet representations. Then in Section 3.4, multiresolution analysis is extended to two dimensions. Both separable and non-separable wavelet transforms are discussed.

We present the new multiresolution analysis algorithm for automatic detection of spiculated lesions in Chapter 4. In Section 4.2, we describe the multiresolution decomposition method. In Section 4.3, we discuss the mammographic features used to characterize spiculated lesions of different sizes at various resolutions. The top-down classification approach is discussed in Section 4.4. Experimental results and discussion are presented in Section 4.5.

The normal mammogram characterization technique is then presented in Chapter 5. First we describe features of normal mammograms in Section 5.2. Then in Section 5.3, we present a new line detector that is capable of extracting linear mammographic features. The characterization algorithm is discussed in Section 5.4. Finally we present experimental results and discussion in Section 5.5.

2. COMPUTER AIDED DIAGNOSIS IN DIGITAL MAMMOGRAPHY

2.1 Features of Breast Lesions in Mammograms

Mammograms are X-ray breast images whose usefulness in the study of breast cancer was first reported in 1913 and has been proved over time [2]. Figure 2.1 shows the appearance of a normal mammogram. Mammographic abnormalities in breast cancer can be characterized into three classes [13]: microcalcifications, circumscribed masses, and spiculated or stellate lesions. These mammographic features are summarized as follows (example mammograms are taken from [13] except noted otherwise).

1. Microcalcifications

   Malignant microcalcifications vary extremely in form, size, density, and number. They are usually clustered within one area of the breast, often within one lobe. Figure 2.2 shows two basic types of malignant microcalcifications. The granular type in (a) is tiny with dot-like or elongated shape and innumerable. The casting type in (b) consists of fragments with irregular contour and varying length. Benign microcalcifications are characterized by homogeneous shape, uniform density, sharp outline, or radiolucent density. Some examples are given in Figure 2.3. The microcalcifications in (a) are very fine and dense with homogeneous spherical, pearl-like shape, and are sharply outlined. The microcalcifications in (b) are oval, ring-shaped with radiolucent centers. The microcalcifications in (c) are coarse, irregular but sharply outlined and uniformly dense. A more detailed summary of mammographic characteristics of microcalcifications is shown in Figure 2.4.

2. Circumscribed Masses

   Malignant masses are high density radiopaque and random oriented. Two examples are shown in Figure 2.5. On the other hand, halo and capsule are characteristics of benign masses with rare exceptions. A halo is a narrow radiolucent ring or a segment of a ring around the periphery of a tumor, as shown in Figure 2.6 (a). A capsule is a thin, curved, radiopaque line that is seen only when it surrounds tumors containing fat, as shown in Figure 2.6 (b). A cyst with smooth borders and orient in the direction of the nipple following the trabecular structure of the breast also indicates a benign lesion, as shown in Figure 2.6 (c). A more detailed summary of mammographic characteristics of circumscribed masses is shown in Figure 2.7.

3. Spiculated Lesions

   Spiculated lesions are almost all malignant. Figure 2.8 shows two examples. The lesion in (a) has a distinct central tumor mass with dense spicules radiating in all directions. The spicule length usually increases with tumor size. The lesion in (b) has a very small, hardly perceptible tumor center and a lace-like, fine reticular radiating structure which causes parenchymal distortion and/or asymmetry. Occasionally benign spiculated lesions are characterized by translucent, oval or circular center, as shown in Figure 2.9 (a), or translucent areas within a loose structure and low density spicules, as shown in Figure 2.9 (b). A more detailed summary of mammographic characteristics of spiculated lesions is shown in Figure 2.10.

2.2 Current Status of CAD research in Digital Mammography

Studies have shown that mammography can be used to detect breast cancer two years before it is palpable and, when properly administered, can reduce the overall mortality from breast cancer by up to 30% [14]. However, radiologists' interpretation of the same mammogram may differ substantially [15] since mammograms are

generally low in contrast and high in noise, while breast structures are small and complex. The false negative rate in current clinical mammography is reported to vary from 4% to 20% [2, 16, 17, 18, 19, 20]. On the other hand, of women who have positive mammograms and are sent for a biopsy, only $15 - 34\%$ actually have cancer [21, 22]. Therefore, in the past decade tremendous research has been done on Computer Aided Diagnosis (CAD) techniques in mammography. The goal has been to increase diagnostic accuracy as well as the reproducibility of mammographic interpretation.

For detecting microcalcifications, Strickland and Hahn [23] designed multiscale matched filters using wavelet transforms for enhancing and detecting calcifications. Nishikawa *et al* [24] used a difference image technique to enhance microcalcifications first, then extracted potential microcalcifications with a series of three different techniques: a global thresholding, an erosion operator, and a local adaptive thresholding. Finally, some false positives are eliminated by a texture analysis technique and remaining detections are grouped by a non-linear clustering algorithm. Cheng *et al* [25] proposed a five-step approach based on fuzzy logic technique, which includes image fuzzification, enhancement, irrelevant structure removal, segmentation, and reconstruction. Chan *et al* [26] investigated a convolution neural network (CNN) based approach and showed its effectiveness in reducing false positive detections. Nagel *et al* [27] examined three feature analysis methods, namely, rule based, an artificial neural network (ANN), and a combined method, and concluded that the combined method performs best because each of the two methods eliminates different types of false positives. Gürcan *et al* [28] described a statistical method using skewness and kurtosis to detect microcalcifications. Shen *et al* [29] developed a set of shape factors, including measures of compactness, moments, and Fourier descriptors, to measure the roughness of contours of calcifications and for use in their classification as malignant or benign. Dhawan *et al* [30] presented a feature analysis approach. Their combined set of image structure features include first and second order gray-level histogram statistics and wavelet decomposition-based features.

For circumscribed masses, Lai *et al* [31] relied on a combination of criteria including the shape, brightness contrast, and uniform density of tumor areas for detecting circumscribed masses. Petrick *et al* [32] used an adaptive density-weighted contrast enhancement filter in conjunction with Laplacian-Gaussian edge detection to detect suspicious mass regions in mammograms. Yin *et al* [33] and Méndez *et al* [34] investigated bilateral subtraction technique based on the alignment of corresponding right and left mammograms. Wei *et al* [35] proposed the use of local texture features in combination with global multiresolution texture features for the detection of masses from normal breast tissue. Kupinski and Giger [36] developed two lesion segmentation techniques — one based on a single feature called the radial gradient index (RGI) and the other based on simple probabilistic models. Brzakovic *et al* [37] used thresholding and fuzzy pyramid linking for mass localization and classification. Comer *et al* [9] and Li *et al* [38] used Markov random fields to classify a mammogram into different texture regions.

For spiculated lesions, Kegelmeyer *et al* [8, 39] extracted a five-dimensional feature vector for each pixel which included the standard deviation of the edge orientation histogram (ALOE) and the output of four spatial filters. Each feature vector was then classified using a binary decision tree. Karssemeijer and Brake [40] investigated a method based on statistical analysis of a map of edge orientations. Two features were derived from the edge orientation map that were used to classify suspicious regions. Huo *et al* [41] developed a technique that involves lesion extraction using region growing and feature extraction using radial edge-gradient analysis. Two measures are obtained from four different neighborhoods about the extracted lesion to evaluate the degree of spiculation. Kobatake and Yoshinaga [42] proposed the use of line skeletons and a modified Hough transform to characterize spiculated patterns.

Others have explored classifying breast lesions as benign or malignant. Sahiner *et al* [43] introduced a rubber band straightening transform (RBST) for characterization of mammographic masses. Features extracted from the RBST images were found to be significantly more effective for tumor classification than those extracted from the

original images. Rangayyan *et al* [44] investigated the potential of acutance in quantifying the sharpness of the boundaries of tumors, and distinguishing between benign and malignant mammographic tumors in combined usage of other shape factors, such as compactness, Fourier descriptors, moments, and chord-length statistics. Kilday *et al* [45] studied the use of tumor boundary roughness, circularity, and other shape factors for classification of mammographic lesions as fibroadenomas, cysts, and cancers. Pohlman *et al* [46] developed a technique based on shape morphology for classifying breast lesions as benign or malignant.

However, little work has been done on understanding normal mammograms. Heine, *et al* [47] used a statistical method based on wavelet expansion to separate normal regions from potentially abnormal regions containing isolated calcifications. Kalman, *et al* [48] studied the feasibility of combining the wavelet transform and artificial neural networks to screen normal mammograms from mammograms containing masses.

Significant progress in computer aided diagnosis in mammography has been made. It has even spawned the development of a company called R2 Technology, Inc, where the name "R2" symbolizes second reader. According to the second reader concept, the computer is used to double check the initial reading of a radiologist, much as would a second human reader. The job of the second reader is to detect subtle abnormalities that the first reader might have missed. This approach has been proven successful at increasing the sensitivity for breast cancer detection by up to 15% [49].

With the advent of digital mammography systems, the implementation of CAD systems in everyday clinical applications looks promising [7]. When this occurs, it will change the practice of radiology.

Fig. 2.1. A normal mammogram.

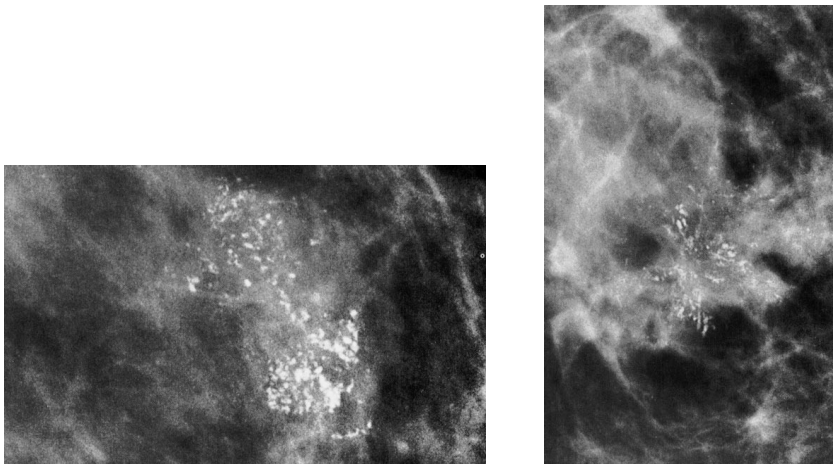

(a) (b)

Fig. 2.2. Two basic types of malignant microcalcifications. (a) Granular: tiny with dot-like or elongated shape, innumerable. (b) Casting: fragments with irregular contour, differ in length.

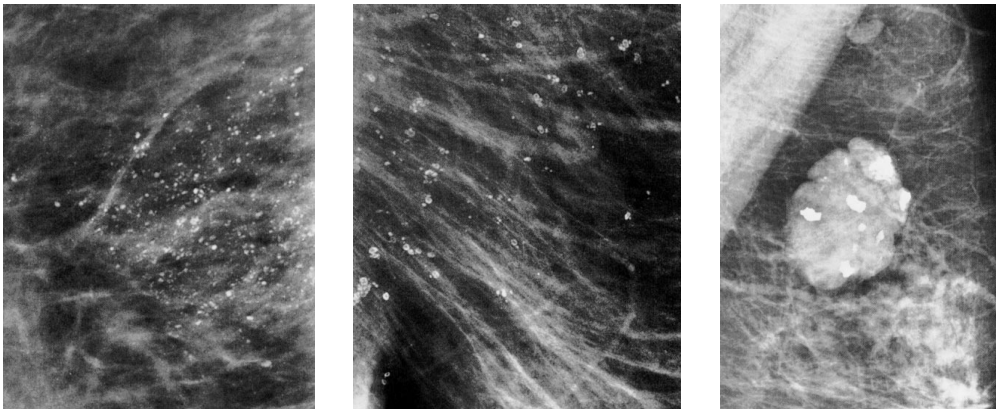

(a) (b) (c)

Fig. 2.3. Benign microcalcifications. (a) Homogeneous, solid, sharply outlined, spherical, pearl-like, very fine and dense. (b) Ring-shaped, oval, center radiolucent. (c) Coarse, irregular but sharply outlined and very dense.

Characteristics of Calcifications

anatomical origin	*form*	*size*	*density*	*number*	*distribution*	*note*
terminal ducts and ductules	dot-like or elongated	tiny	great variations within an individual particle and among adjacent particles	innumerable	usually clustered within an area of the breast, often within one lobe	malignant-type calcifications, extremely variable in form, size, density and
	fragments with irregular contour	differ in length				
cyst-like dilated lobules	homogeneous, solid, sharply outlined, spherical, pearl-like	very fine, powder-like	dense	numerous	scattered throughout much of the breast parenchyma	almost certain cystic hyperplasia, very rare lobular carcinoma in situ
	crescent-shaped or elongate on lateral view and circular, faint, opaque smudges on cranio-caudal view	variable saccular dilation of the lobules causes different sizes	differ according to size			
miscellaneous	ring surrounds dilated duct, oval or elongated when extends around and along duct		varying lucency center, very dense periphery	multiple	often bilateral, scattered, oriented towards the nipple, following the course of the ducts	benign intraductal calcifications have high and uniform density, generally wide caliber, and tend to follow the course of normal ducts
	linear, often needle like, occasionally branching	uniform, varying length and width	high, uniform density			
	ring-shaped, oval	same as skin pore	center is always radiolucent	very numerous	occur only within the skin	sebaceous gland calcifications
	small eggshell	up to a few mm in diameter	high, uniform periphery and lucent, often irregular center	range from solitary to numerous	may occur anywhere in the breast	usually subcutaneous, calcified micro-hematomas
	larger eggshell	variable, up to several cm	center radiolucent or of parenchymal density			almost invariably benign
	similar to raspberry	up to the size of a dilated duct	high, uniform but often contain small, oval-shaped lucent areas	solitary	tend to be central or retro-areolar	papilloma, papillomatosis
	coarse, irregular bizarre appearance		very dense	sharply outlined		fibroadenomas

Fig. 2.4. Mammographic characteristics of calcifications.

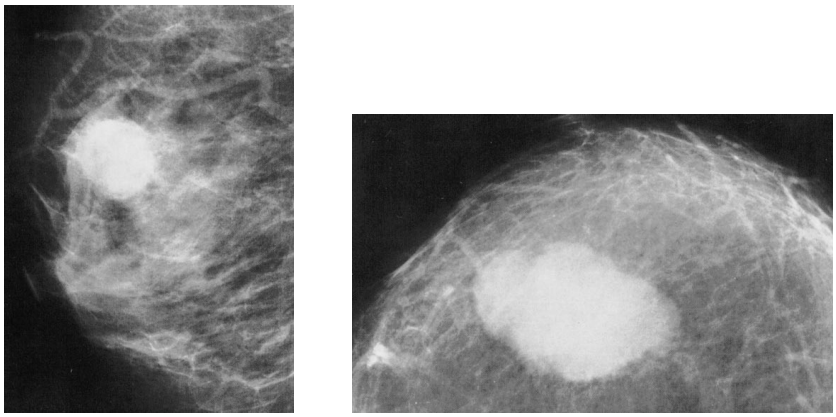

(a) (b)

Fig. 2.5. Malignant masses. (a) High density radiopaque. (b) Solid tumor with random orientation.

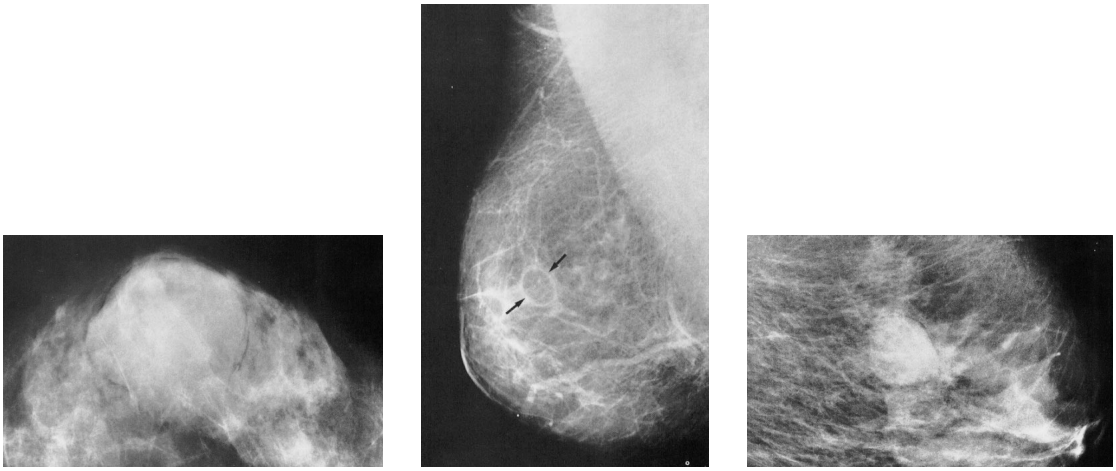

(a) (b) (c)

Fig. 2.6. Benign masses. (a) Halo: a narrow radiolucent ring or a segment of a ring around the periphery of a tumor, (b) Capsule: a thin, curved, radiopaque line that is seen only when it surrounds tumors containing fat. (c) A cyst with smooth borders and orient in the direction of the nipple following the trabecular structure of the breast.

Characteristics of Circumscribed Lesions

importance	*sign*	*description*	*category*	*note*
primary	halo	a narrow radiolucent ring or a segment of a ring around the periphery of a lesion	present	both the halo sign and the capsule are characteristic of benign tumors, with rare exceptions
			absent	
	capsule	a thin, curved, radiopaque line that is seen only when it surrounds lesions containing fat	present	
			absent	
	density	evaluated in relation to the surrounding parenchyma, or, in the case of fatty involution, to the nipple	radiolucent	all radiolucent, all radiolucent and radiopaque combined, and most low density radiopaque lesions are benign
			radiolucent and radiopaque combined	
			low density radiopaque	
			high density radiopaque	
secondary	form and orientation	spherical or ovoid with smooth borders, orientation is in the direction of the nipple following the trabecular structure of the breast	cyst	These serve as confirmation of diagnoses which should have already been made on the basis of primary signs
		may be smooth or lobulated, random orientation	solid tumor	
	size		very large (> 5 cm)	
			intermediate (3-5 cm)	
			smaller (< 3 cm)	

Fig. 2.7. Mammographic characteristics of circumscribed lesions.

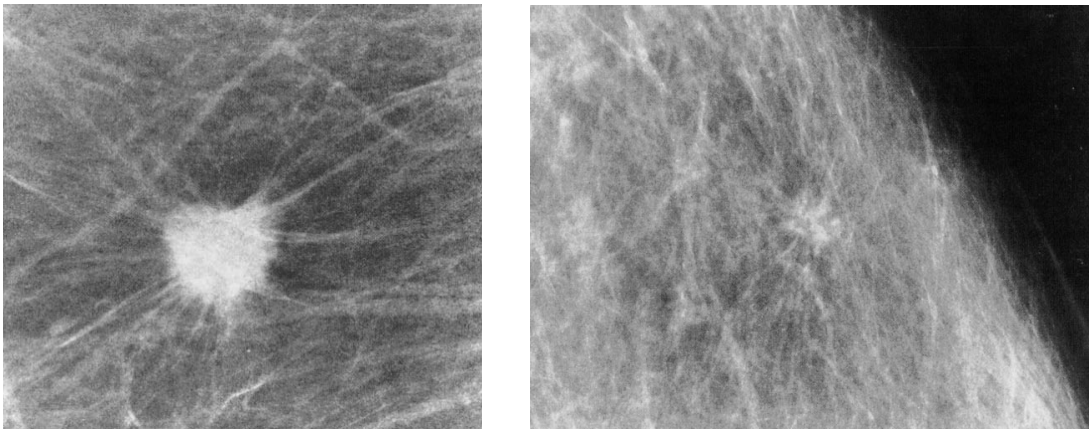

(a) (b)

Fig. 2.8. Malignant spiculated lesions. (a) Distinct central tumor mass with dense spicules radiating in all directions. The spicule length usually increases with tumor size. (b) Very small, hardly perceptible tumor center and a lace-like, fine reticular radiating structure which causes parenchymal distortion and/or asymmetry.

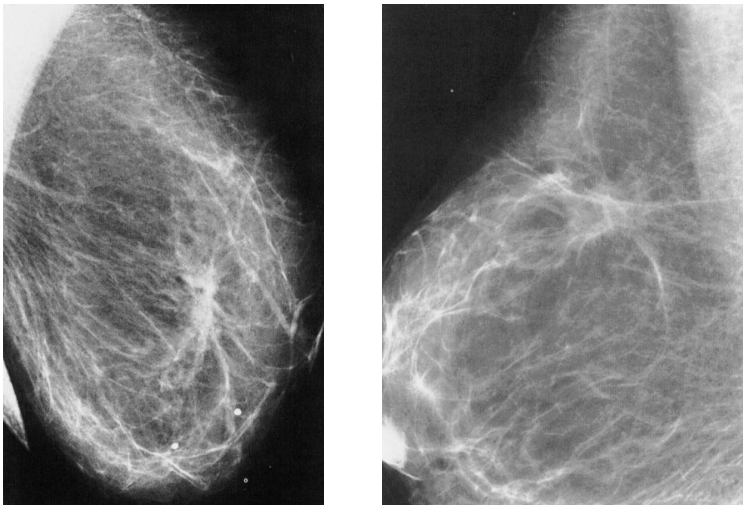

(a) (b)

Fig. 2.9. Benign spiculated lesions. (a) Center is translucent, oval or circular. (b) Translucent areas are within a loose structure, spicules are fine and of low density.

Characteristics of Stellate Lesions

diagnose	*tumor center*	*radiating structure*	*skin*	*note*
scirrhous carcinoma	distinct central tumor mass	dense spicules radiate in all directions; spicule length increases with tumor size	may cause retraction and localized skin thickening	associated malignant-type calcifications are common
small scirrhous carcinoma, early stage	small, may be imperceptible	form only a lace-like, fine reticular structure which causes parenchymal distortion and/or asymmetry		histopathologically not a separate entity
sclerosing duct hyperplasia	translucent, oval or circular center of the radiating structure	The longest spicules are very thin and very long; closer to the lesion center, spicules become much more numerous and are clumped together in thick aggregates; there frequently appear to be radiolucent linear structures parallel to some spicules	never skin thickening nor retraction over the lesion	benign, rarely palpable; the same lesion varies in appearance from one projection to the other
traumatic fat necrosis	translucent areas are within a loose, reticular structure	spicules are fine and of low density	localized skin thickening and retraction may be present	
hyalinized fibroadenoma				myxoid degeneration of a fibroadenoma results in retraction of the surrounding tissue which simulates a lesion with radiating structure

Fig. 2.10. Mammographic characteristics of spiculated lesions.

3. MULTIRESOLUTION REPRESENTATIONS OF IMAGES

3.1 Introduction

In computer vision and image processing, the objects one is interested in generally have very different sizes. Hence, it is impossible to define *a priori* an optimal resolution for analyzing images. A multiresolution representation reorganizes image information into a set of details appearing at different resolutions, and thus provides a hierarchical framework for image analysis [50]. Recently the wavelet transform has become the most popular technique of obtaining multiresolution representations of signals. It has the advantage of localizing information in both the time (or space) and frequency domains. In particular, it is capable of trading one type of resolution for the other, which makes it especially suitable for the analysis of nonstationary signals [51]. In this chapter, we give an overview of wavelet transform based multiresolution representations of signals.

3.2 Notation

The notation used throughout this chapter is similar to that in [50]. Let $\mathbf{Z}$ and $\mathbf{R}$ denote the set of integers and real numbers respectively. $\mathbf{L}^2(\mathbf{R})$ and $\mathbf{L}^2(\mathbf{R}^2)$ denote the vector space of measurable, square-integrable one-dimensional functions $f(x)$ and two dimensional functions $f(x, y)$, respectively. The inner product of $f(x) \in \mathbf{L}^2(\mathbf{R})$ and $g(x) \in \mathbf{L}^2(\mathbf{R})$ is written as

$$\langle f(x), g(x) \rangle = \int_{-\infty}^{+\infty} f(x)g(x)dx$$

Similarly, the inner product of $f(x,y) \in \mathbf{L}^2(\mathbf{R}^2)$ and $g(x,y) \in \mathbf{L}^2(\mathbf{R}^2)$ is written as

$$\langle f(x,y), g(x,y) \rangle = \int_{-\infty}^{+\infty} \int_{-\infty}^{+\infty} f(x,y) g(x,y) dxdy$$

The Fourier transform of $f(x) \in \mathbf{L}^2(\mathbf{R})$ is defined by

$$\hat{f}(\omega) = \int_{-\infty}^{+\infty} f(x) e^{-i\omega x} dx$$

and the Fourier transform of $f(x,y) \in \mathbf{L}^2(\mathbf{R}^2)$ is defined by

$$\hat{f}(\omega_x, \omega_y) = \int_{-\infty}^{+\infty} \int_{-\infty}^{+\infty} f(x,y) e^{-i(\omega_x x + \omega_y y)} dxdy$$

$\mathbf{I}^2(\mathbf{Z})$ is the vector space of square-summable sequences

$$\mathbf{I}^2(\mathbf{Z}) = \left\{ (\alpha(i))_{i \in \mathbf{Z}} : \sum_{i=-\infty}^{+\infty} |\alpha(i)|^2 < \infty, \alpha(i) \in \mathbf{R} \right\}$$

The discrete time Fourier transform of $h(n) \in \mathbf{I}^2(\mathbf{Z})$ is defined by

$$H(\omega) = \sum_{n=-\infty}^{+\infty} h(n) e^{-i\omega n}$$

3.3 Multiresolution Analysis of One Dimensional Signals

3.3.1 Orthogonal Wavelet Representation

The resolution r of a signal $f(x)$ can be described and indexed by the number of samples per length or time unit needed to fully describe $f(x)$. For example, if the highest frequency contained in $f(x)$ is 1kHz , then by the sampling theorem [52], 2000 samples/sec is needed to fully represent the signal. We can say the resolution of $f(x)$ is $r = 2$. If we lowpass filter $f(x)$ such that it is bandlimited to 500Hz, therefore 1000 samples/sec is sufficient to represent the new signal, we then say the resolution is decreased to $r = 1$. Resolution is really a relative term. If we let the resolution of the original signal $f(x)$ be described by the index $r = 1$, then the resolution of its lowpass filtered version is $r = 0.5$. We usually are interested in representing a signal at various resolutions $(r_j)_{j \in \mathbf{Z}}$ that varies exponentially, such as $r_j = 2^j$. In such cases, j can be used to index the resolutions, instead of r_j. For a non-bandlimited signal, infinitely

many samples per unit are needed to fully represent it, thus it has resolution $j = +\infty$. In practice, a physical measuring device can only measure a signal at finite resolution, i.e., the signal is bandlimited. Usually we index the resolution of the original signal as $j = 0$. Then in the above example, the lowpass filtered signal has a resolution $j = -1$.

Let the original signal $f(x) \in \mathbf{L}^2(\mathbf{R})$ and let A_{2^j} be an operator that approximates $f(x)$ at resolution 2^j, hence $g_j(x) = A_{2^j} f(x) \in \mathbf{L}^2(\mathbf{R})$ is an approximation of $f(x)$ and has resolution 2^j. For example, the operator A_{2^j} could be a lowpass filter that has cutoff frequency $2^j F_{ref}$, where F_{ref} is some reference frequency. Obviously, $g_j(x)$ remains the same if we approximate it again at the same resolution 2^j. Therefore, A_{2^j} is a projection operator on a particular vector space $\mathbf{V}_{2^j} \subset \mathbf{L}^2(\mathbf{R})$, where $\mathbf{V}_{2^j}$ is the set of all possible approximations at the resolution 2^j of all functions in $\mathbf{L}^2(\mathbf{R})$. For example, all possible signals that are bandlimited to $2^j F_{ref}$. The set of vector spaces $(\mathbf{V}_{2^j})_{j \in \mathbf{Z}}$ is said to be a multiresolution approximation of $\mathbf{L}^2(\mathbf{R})$ if it satisfies the following properties [50]:

1. The approximation of a signal at resolution 2^{j+1} contains all the necessary information to obtain its approximation at a coarser resolution 2^j:

$$\mathbf{V}_{2^j} \subset \mathbf{V}_{2^{j+1}}, \forall j \in \mathbf{Z} \tag{3.1}$$

2. The spaces of approximated functions can be derived from one another by scaling each approximated function by the ratio of their resolutions:

$$f(x) \in \mathbf{V}_{2^j} \Longleftrightarrow f(2x) \in \mathbf{V}_{2^{j+1}}, \forall j \in \mathbf{Z} \tag{3.2}$$

3. The approximation $A_{2^j} f(x)$ of a signal $f(x)$ can be characterized by 2^j samples per length unit, or equivalently, there exists a mapping $\mathbf{M} : \mathbf{V}_1 \longrightarrow \mathbf{I}^2(\mathbf{Z})$ such that signals in $\mathbf{V}_1$ can be represented at 1 sample per length unit. This is essentially the sampling theorem:

$$\mathbf{M}(\mathbf{V}_1) = (\alpha_i)_{i \in \mathbf{Z}} \tag{3.3}$$

4. When $f(x)$ is translated by a length proportional to 2^{-j}, $A_{2^j}f(x)$ is translated by the same amount and is characterized by the same samples that have been translated. As a consequence of Property 2, it is sufficient to express this for resolution $j = 0$:

$$A_1 f_k(x) = A_1 f(x-k), \text{ where } f_k(x) = f(x-k), \forall k \in \mathbf{Z} \tag{3.4}$$

$$\mathbf{M}(A_1 f(x)) = (\alpha_i)_{i\in\mathbf{Z}} \Longleftrightarrow \mathbf{M}(A_1 f_k(x)) = (\alpha_{i-k})_{i\in\mathbf{Z}}, \forall k \in \mathbf{Z} \tag{3.5}$$

5. As the resolution increases to $+\infty$ the approximated signal converges to the original signal. On the other hand, as the resolution decreases to zero, the approximated signal converges to zero:

$$\lim_{j\to+\infty} \mathbf{V}_{2^j} = \bigcup_{j=-\infty}^{+\infty} \mathbf{V}_{2^j} \text{ is dense in } \mathbf{L}^2(\mathbf{R}) \tag{3.6}$$

$$\lim_{j\to-\infty} \mathbf{V}_{2^j} = \bigcap_{j=-\infty}^{+\infty} \mathbf{V}_{2^j} = \{0\} \tag{3.7}$$

Let $\mathbf{O}_{2^j}$ be the vector space that satisfies: (1) $\mathbf{O}_{2^j}$ is orthogonal to $\mathbf{V}_{2^j}$ and (2) $\mathbf{O}_{2^j} \bigoplus \mathbf{V}_{2^j} = \mathbf{V}_{2^{j+1}}$, i.e. it is the orthogonal complement of $\mathbf{V}_{2^j}$ in $\mathbf{V}_{2^{j+1}}$.

It can be shown [50] that there exists a unique *scaling function* $\phi(x) \in \mathbf{L}^2(\mathbf{R})$, such that if we let $\phi_{2^j}(x) = 2^j\phi(2^j x)$ for $j \in \mathbf{Z}$, then $(2^{-j/2}\phi_{2^j}(x - 2^{-j}n))_{n\in\mathbf{Z}}$ is an orthonormal basis of $\mathbf{V}_{2^j}$. Accordingly, an *orthogonal wavelet function* $\psi(x)$ can be defined as a function with Fourier transform $\hat{\psi}(\omega) = G(\frac{\omega}{2})\hat{\phi}(\frac{\omega}{2})$, where

$$G(\omega) = e^{-j\omega}\overline{H(\omega+\pi)} \tag{3.8}$$

and $H(\omega)$ is the transfer function of a discrete time (or space) filter with impulse response

$$h(n) = \langle \phi_{2^{-1}}(x), \phi(x-n)\rangle, \forall n \in \mathbf{Z} \tag{3.9}$$

Similarly if we let $\psi_{2^j}(x) = 2^j\psi(2^j x)$ for $j \in \mathbf{Z}$, then $(2^{-j/2}\psi_{2^j}(x - 2^{-j}n))_{n\in\mathbf{Z}}$ is an orthonormal basis of $\mathbf{O}_{2^j}$ and $(2^{-j/2}\psi_{2^j}(x - 2^{-j}n))_{(n,j)\in\mathbf{Z}^2}$ is an orthonormal basis of $\mathbf{L}^2(\mathbf{R})$.

The approximation of any signal $f(x) \in \mathbf{L}^2(\mathbf{R})$ at resolution 2^j can then be obtained by projecting $f(x)$ onto the vector space $\mathbf{V}_{2^j}$

$$g_j(x) = A_{2^j}f(x) = 2^{-j}\sum_{n=-\infty}^{+\infty}\langle f(x), \phi_{2^j}(x - 2^{-j}n)\rangle\phi_{2^j}(x - 2^{-j}n)$$

The detail signal at resolution 2^j, defined as the "difference" between the approximation of function $f(x)$ at resolutions 2^{j+1} and 2^j, is given by a similar decomposition in the vector space $\mathbf{O}_{2^j}$

$$D_{2^j}f(x) = 2^{-j}\sum_{n=-\infty}^{+\infty}\langle f(x), \psi_{2^j}(x - 2^{-j}n)\rangle\psi_{2^j}(x - 2^{-j}n)$$

Let $\alpha_n^j = \langle f(x), \phi_{2^j}(x-2^{-j}n)\rangle$ and let $\beta_n^j = \langle f(x), \psi_{2^j}(x-2^{-j}n)\rangle$, we can then rewrite the above equations as

$$g_j(x) = A_{2^j}f(x) = 2^{-j}\sum_{n=-\infty}^{+\infty}\alpha_n^j\phi_{2^j}(x - 2^{-j}n)$$

$$D_{2^j}f(x) = 2^{-j}\sum_{n=-\infty}^{+\infty}\beta_n^j\psi_{2^j}(x - 2^{-j}n)$$

For any $J \in \mathbf{Z}$, the set of coefficients

$$(\alpha_n^J, (\beta_n^j)_{J\le j<+\infty})_{n\in\mathbf{Z}}$$

known as the wavelet coefficients, are called an *orthogonal wavelet representation* of $f(x)$ [53], where J is arbitrary and denotes the depth of the decomposition.

Define $\tilde{h}(n) = h(-n)$ and $\tilde{g}(n) = g(-n)$, where $h(n)$ is defined as in Equation 3.9 and $g(n)$ is the impulse response of the transfer function defined in Equation 3.8. It can be further shown that both $(\alpha_n^j)_{n\in\mathbf{Z}}$ and $(\beta_n^j)_{n\in\mathbf{Z}}$ can be obtained from the finer approximation $(\alpha_n^{j+1})_{n\in\mathbf{Z}}$ as follows: treat $(\alpha_n^{j+1})_{n\in\mathbf{Z}}$ as a discrete time signal indexed by n and convolve it with the discrete time filters $\tilde{h}(n)$ and $\tilde{g}(n)$, respectively, then retain every other sample of the output. $\tilde{h}(n)$ is known as the analysis lowpass filter

and $\tilde{g}(n)$ is known as the analysis highpass filter. This is a decimation process that consists of filtering followed by downsampling:

$$\alpha_n^j = \sum_{k=-\infty}^{+\infty} \tilde{h}(2n-k)\alpha_k^{j+1}$$

$$\beta_n^j = \sum_{k=-\infty}^{+\infty} \tilde{g}(2n-k)\alpha_k^{j+1}$$

The approximation coefficients of $f(x)$ at resolution $r = 1$ or $j = 0$, $(\alpha_n^0)_{n\in\mathbf{Z}}$, can therefore be used as a starting point to obtain wavelet coefficients at coarser resolutions by successively decomposing $(\alpha_n^{j+1})_{n\in\mathbf{Z}}$ into $(\alpha_n^j)_{n\in\mathbf{Z}}$ and $(\beta_n^j)_{n\in\mathbf{Z}}$ for $-J \leq j \leq -1$, $J > 0$. This is illustrated in Figure 3.1.

On the other hand, $(\alpha_n^{j+1})_{n\in\mathbf{Z}}$ can be reconstructed from $(\alpha_n^j)_{n\in\mathbf{Z}}$ and $(\beta_n^j)_{n\in\mathbf{Z}}$ by treating them as discrete time signals indexed by n and putting zeros between each sample, followed by convolving the resulting signals with the discrete time filters $h(n)$ and $g(n)$, respectively. $h(n)$ is known as the synthesis lowpass filter and $g(n)$ is known as the synthesis highpass filter. This is an interpolation process consists of upsampling followed by filtering:

$$\alpha_n^{j+1} = 2\sum_{k=-\infty}^{+\infty} \{h(n-2k)\alpha_k^j + g(n-2k)\beta_k^j\}$$

$(\alpha_n^0)_{n\in\mathbf{Z}}$ can then be reconstructed from lower resolution wavelet coefficients by repeating this procedure for $-J \leq j \leq -1$, $J > 0$, as shown in Figure 3.2.

3.3.2 Biorthogonal Wavelet Representation

The multiresolution analysis for a biorthogonal wavelet representation [54] consists of two hierarchies of approximation spaces

$$\ldots \subset \mathbf{V}_{-2} \subset \mathbf{V}_{-1} \subset \mathbf{V}_0 \subset \mathbf{V}_1 \subset \mathbf{V}_2 \ldots$$

$$\ldots \subset \tilde{\mathbf{V}}_{-2} \subset \tilde{\mathbf{V}}_{-1} \subset \tilde{\mathbf{V}}_0 \subset \tilde{\mathbf{V}}_1 \subset \tilde{\mathbf{V}}_2 \ldots$$

$\mathbf{W}_j$ and $\tilde{\mathbf{W}}_j$ will be the complements of $\mathbf{V}_j$ in $\mathbf{V}_{j+1}$ and of $\tilde{\mathbf{V}}_j$ in $\tilde{\mathbf{V}}_{j+1}$, respectively. They are not the orthogonal complements described above, instead $\mathbf{W}_j \perp \tilde{\mathbf{V}}_j$ and

$\tilde{\mathbf{W}}_j \perp \mathbf{V}_j$. Accordingly, there are two scaling functions $\phi(x)$ and $\tilde{\phi}(x)$, and two wavelet basis functions $\psi(x)$ and $\tilde{\psi}(x)$. Biorthogonal wavelet representation can be implemented in a similar filter bank structure as shown in Figure 3.1 and Figure 3.2. However, the synthesis filters will be different from the analysis filters, in contrast to the implementation of orthogonal wavelet representation, where the same filters $h(n)$ and $g(n)$, (or their mirror images $h(-n)$ and $g(-n)$) are used for both reconstruction and decomposition. Such filter banks have more flexibility in terms of designing. Moreover, symmetric filters can be used, which is impossible in the orthonormal case.

As an example, [23] used a biorthogonal wavelet bases for detecting microcalcifications in mammograms. The filter coefficients are shown in Table 3.1.

The two scaling functions and wavelet basis functions are shown in Figure 3.3.

3.3.3 M Voices Per Octave

Generally speaking, wavelets constitute a family of functions derived from one single function $\psi(x)$ by scaling and shifting [55]

$$\psi^{(a,b)}(x) = a^{-1/2}\psi(\frac{x-b}{a})$$

where $a, b \in \mathbf{R}, a > 0$. The shifting parameter b gives the position of the wavelet, while the scaling parameter a governs its frequency. If sampling the phase space (b, a) [55] at $a = 2^j, b = 2^j n$, we obtain a so-called "dyadic" grid, as shown in Figure 3.4(a). Sometimes finer sampling in scale may be desired for signal analysis, which results in a denser grid in the phase space, as shown in Figure 3.4(b). In other words, $a = 2^j$ is replaced by $a = 2^{j+m/M}$, $m = 0, \ldots, M-1$, where m is known as "voice" [56]. The standard "octave-by-octave" algorithm, shown in Figure 3.1 and Figure 3.2, can be used to obtain the wavelet coefficients on M voices per octave as follows [56]:

1. Given the lowpass filter $h(n)$ and the highpass filter $g(n)$, solve for the corresponding scaling function $\phi(x)$ and wavelet basis function $\psi(x)$

$$\phi(x) = \sum_n h(n)\phi(2x-n) \tag{3.10}$$

$$\psi(x) = \sum_n g(n)\phi(2x - n) \tag{3.11}$$

2. For each $m = 0, \ldots, M-1$, let

$$\phi_m(x) = 2^{-m/2M}\phi(2^{-m/M}x)$$

$$\psi_m(x) = 2^{-m/2M}\psi(2^{-m/M}x)$$

3. Solve Equation 3.10 and Equation 3.11 for new lowpass filter $h_m(n)$ and highpass filter $g_m(n)$

4. Apply the standard "octave-by-octave" algorithm

As an example, given the analysis lowpass filter $h(n)$ and highpass filter $g(n)$ of the biorthogonal wavelet discussed in Section 3.3.2, we are to derive another set of filters $h_1(n)$ and $g_1(n)$ that can generate wavelet coefficients at scale $a = 2^{j+1/2}$. First we solve the two-scale difference Equations 3.10 and 3.11 [57] to obtain the corresponding scaling function $\phi(x)$ and wavelet basis function $\psi(x)$. This is shown in Figure 3.3 and also repeated in Figure 3.5.

Stretching $\phi(x)$ and $\psi(x)$ by a factor of $\sqrt{2}$, we then find $h_1(n)$ and $g_1(n)$ by using the stretched functions in Equations 3.10 and 3.11. Both filters are no longer FIR. The truncated $h_1(n)$ and $g_1(n)$, along with the original $h(n)$ and $g(n)$, as well as their magnitude responses, are shown in Figure 3.6 and Figure 3.7, respectively.

3.3.4 Undecimated Wavelet Representation

Notice that the wavelet decomposition and reconstruction structure described in Figure 3.1 and Figure 3.2 employ down-sampling and up-sampling operations, which results in a shift-variant system [58]. For signal analysis, feature extraction, and object detection, a shift-invariable representation is usually preferable [51, 23]. This can be achieved by up-sampling (or down-sampling) the filter coefficients at further decompositions (or reconstructions), instead of down-sampling (or up-sampling) the resulting filter outputs after each level of decomposition (or reconstruction).

3.4 Extension to Two Dimensional Signals

For image processing applications, the signal is a two dimension finite energy function $f(x, y) \in \mathbf{L^2}(\mathbf{R^2})$. A multiresolution approximation of $\mathbf{L^2}(\mathbf{R^2})$ is a sequence of subspaces of $\mathbf{L^2}(\mathbf{R^2})$ which satisfies a straightforward two-dimensional extension of the properties of $(\mathbf{V}_{2^j})_{j\in\mathbf{Z}}$ [50].

3.4.1 Separable Wavelet Representation

A separable two dimensional multiresolution representation can be obtained by extending the one-dimensional algorithm described in Section 3.3 to the horizontal and vertical directions. Hence, extra importance is given to the horizontal and vertical directions in the image. A one level decomposition and reconstruction structures are shown in Figure 3.8 (a) and (b), respectively.

3.4.2 Non-Separable Wavelet Representation

In general, 2D filters and/or subsampling are not separable. From a discrete space filtering point of view, subsampling is defined by a sublattice of the original lattice [59]. The down sampling operation is characterized by a dilation matrix $\mathbf{D}$. The indices of points belonging to the sublattice are given as weighted integer combinations of the columns of $\mathbf{D}$. For example,

$$D = \begin{bmatrix} 1 & 1 \\ 1 & -1 \end{bmatrix}$$

is a possible representation of the so-called two dimensional quincunx sublattice, as shown in Figure 3.9.

Coefficients of four nonseparable 2D filters, which form a perfect reconstruction filter bank with down sampling matrix $\mathbf{D}$, are shown in Table 3.2, Table 3.3, Table 3.4, and Table 3.5. Their magnitude responses are shown in Figure 3.10.

The corresponding linear phase nonseparable 2-D wavelet transform will be used to obtain multiresolution representations of images in the breast tumor detection algorithm discussed in Chapter 4. This transform does not introduce phase distortions

in the decomposed images, and no bias is introduced in the horizontal and vertical directions as a separable transform would.

3.5 Wavelet Transform of Digital Images

In practice, we usually deal with discrete time (or space) signals. For example, a digital image is a two dimensional discrete space signal $f(m,n) \in \mathbf{I}^2(\mathbf{Z}^2)$. Its pixel values can be viewed as the approximation coefficients at resolution $j = 0$ of a continuous function $\tilde{f}(x,y)$ [60] given by

$$\tilde{f}(x,y) = \sum_{m=-\infty}^{+\infty} \sum_{n=-\infty}^{+\infty} f(m,n)\phi(x-m, y-n)$$

The wavelet transform of $\tilde{f}(x,y)$ is then considered as the wavelet transform of the digital image $f(m,n)$. As an example, we demonstrate how to obtain a separable biorthogonal wavelet transform of the Barbara image using the procedure illustrated in Figure 3.8 [60, 53, 50], where the filters $\tilde{H}$, $\tilde{G}$, H, and G are the analysis LPF, the analysis HPF, the synthesis LPF, and the synthesis HPF, respectively, as shown in Table 3.1. The input α_n^j to the filter bank in Figure 3.8 (a), when $j = 0$, are the pixel values of the original Barbara image, shown in Figure 3.11. After filtering and downsampling, the outputs α_n^{-1}, $\beta_{1,n}^{-1}$, $\beta_{2,n}^{-1}$, and $\beta_{3,n}^{-1}$, are as shown in Figure 3.12 (a), (b), (c), and (d), respectively. The approximation coefficients α_n^{-1} at the coarser resolution $j = -1$ can again be input to the filter bank to obtain the wavelet transform at an even coarser resolution $j = -2$. The outputs α_n^{-2}, $\beta_{1,n}^{-2}$, $\beta_{2,n}^{-2}$, and $\beta_{3,n}^{-2}$, are as shown in Figure 3.13 (a), (b), (c), and (d), respectively. Higher level of wavelet decomposition can be obtained by repeating this process.

Table 3.1 Filter coefficients for implementing a biorthogonal wavelet representation.

n	analysis LPF	analysis HPF	synthesis LPF	synthesis HPF
-5	0	0	0	0.026749
-4	0.026749	0	0	0.016864
-3	-0.016864	0	-0.045636	-0.078223
-2	-0.078223	0.045626	-0.028772	-0.266864
-1	0.266864	-0.028772	0.295636	0.602949
0	0.602949	-0.295636	0.557543	-0.266864
1	0.266864	0.557543	0.295636	-0.078223
2	-0.078223	-0.295636	-0.028772	0.016864
3	-0.016864	-0.028772	-0.045636	0.026749
4	0.026749	0.045626	0	0

Table 3.2 Analysis Lowpass Filter Coefficients.

	-1	0	1
-1	0.0000	0.0625	0.0000
0	0.0625	0.2500	0.0625
1	0.0000	0.0625	0.0000

Table 3.3 Analysis Highpass Filter Coefficients.

	-2	-1	0	1	2
-3	0.0000	0.0000	-0.0625	0.0000	0.0000
-2	0.0000	-0.1250	-0.2500	-0.1250	0.0000
-1	-0.0625	-0.2500	1.7500	-0.2500	-0.0625
0	0.0000	-0.1250	-0.2500	-0.1250	0.0000
1	0.0000	0.0000	-0.0625	0.0000	0.0000

Table 3.4 Synthesis Lowpass Filter Coefficients.

	-2	-1	0	1	2
-2	0.0000	0.0000	-0.0625	0.0000	0.0000
-1	0.0000	-0.1250	0.2500	-0.1250	0.0000
0	-0.0625	0.2500	1.7500	0.2500	-0.0625
1	0.0000	-0.1250	0.2500	-0.1250	0.0000
2	0.0000	0.0000	-0.0625	0.0000	0.0000

Table 3.5 Synthesis Highpass Filter Coefficients.

	-1	0	1
0	0.0000	-0.0625	0.0000
1	-0.0625	0.2500	-0.0625
2	0.0000	-0.0625	0.0000

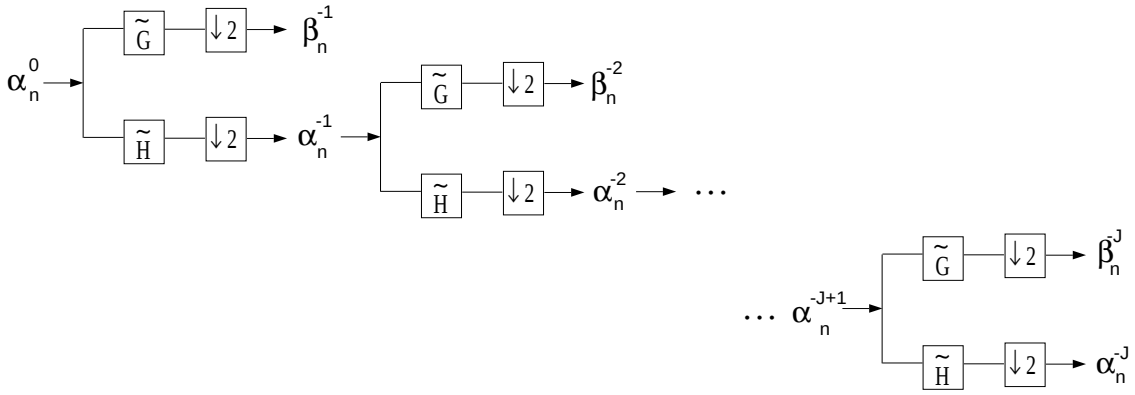

Fig. 3.1. Orthogonal wavelet decomposition of α_n^0.

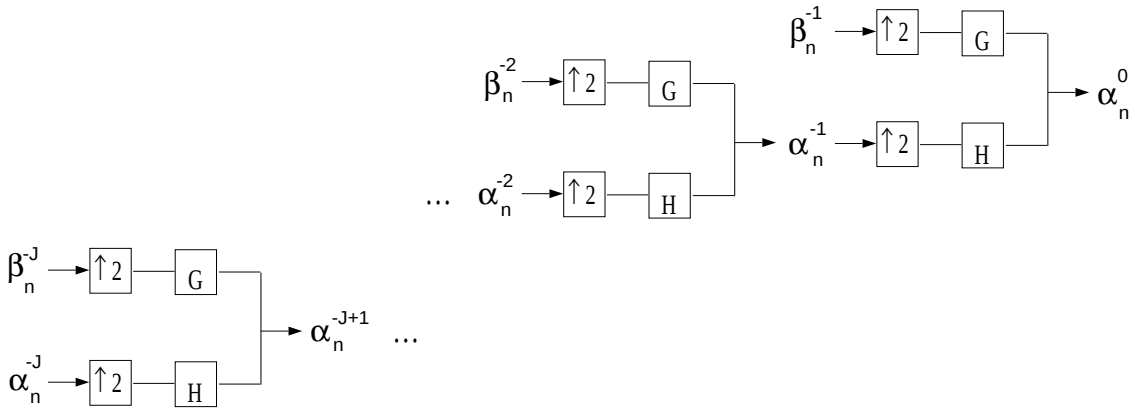

Fig. 3.2. Reconstruction of α_n^0 from its orthogonal wavelet representation.

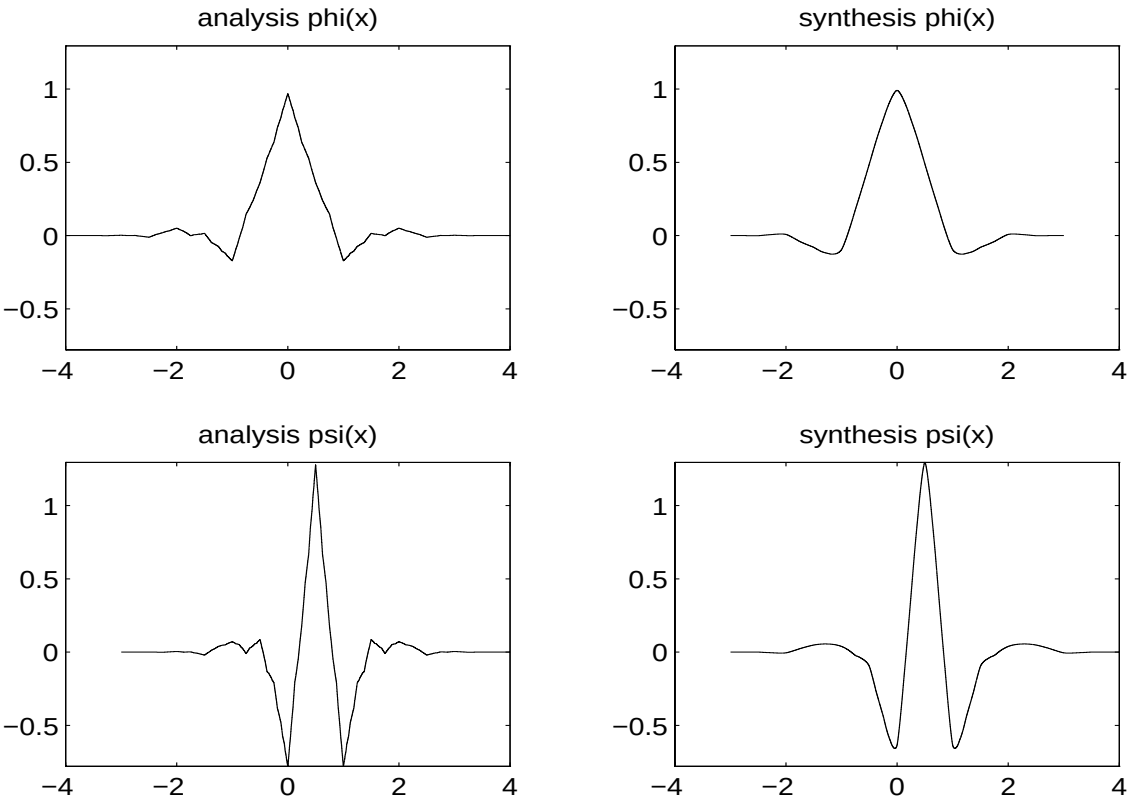

Fig. 3.3. Scaling functions $\phi(x)$, $\tilde{\phi}(x)$, and wavelet basis functions $\psi(x)$, $\tilde{\psi}(x)$ for the biorthogonal example.

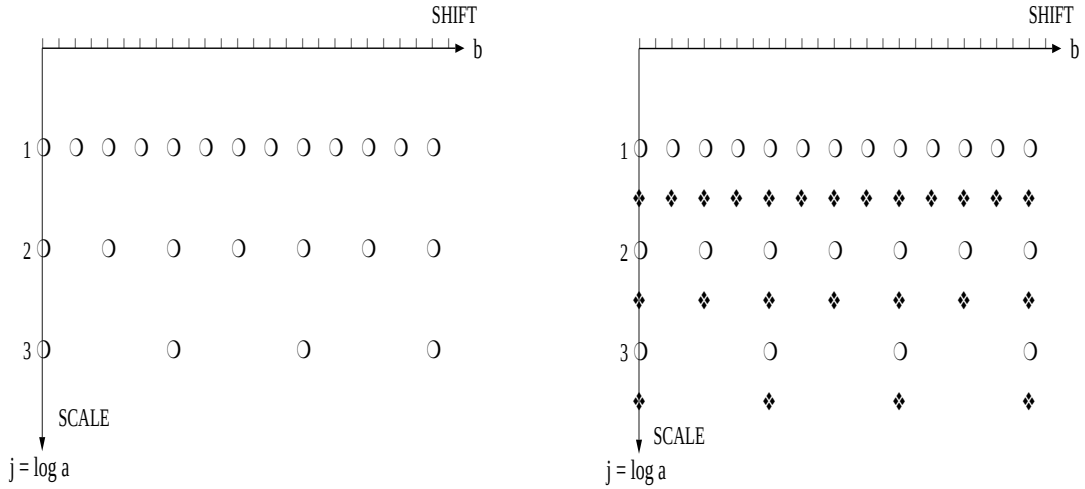

(a) (b)

Fig. 3.4. Phase space grids (a) octave-by-octave. (b) 2-voices per octave.

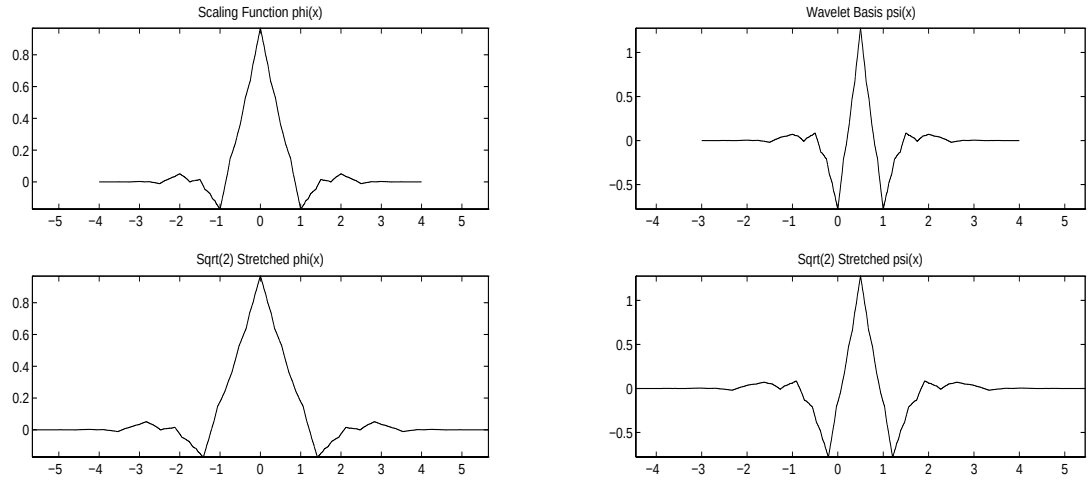

(a) (b)

Fig. 3.5. (a) Scaling functions for scale $a = 2^j$ (top) and $a = 2^{j+1/2}$ (bottom). (b) Wavelet basis functions for scale $a = 2^j$ (top) and $a = 2^{j+1/2}$ (bottom).

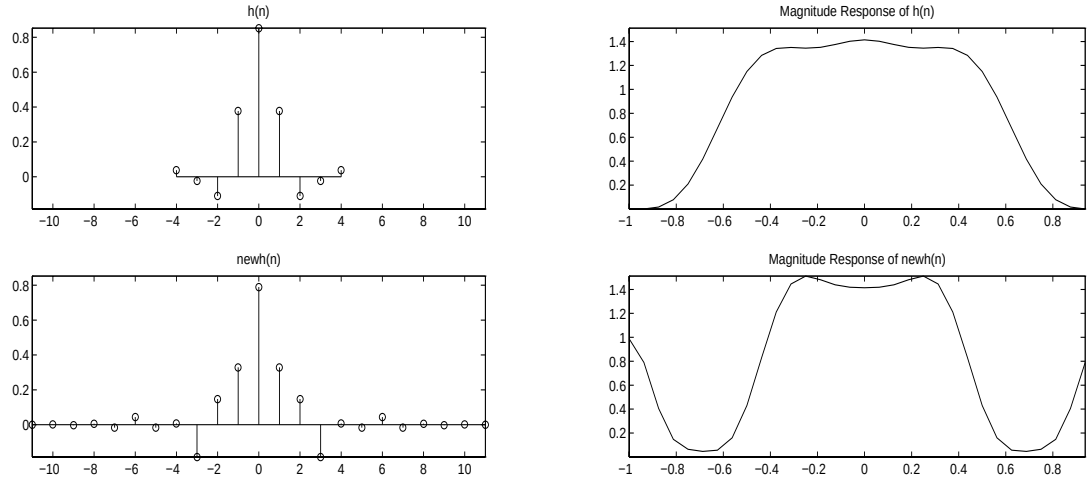

(a) (b)

Fig. 3.6. (a) Lowpass filters for scale $a = 2^j$ (top) and $a = 2^{j+1/2}$ (bottom). (b) Corresponding magnitude responses.

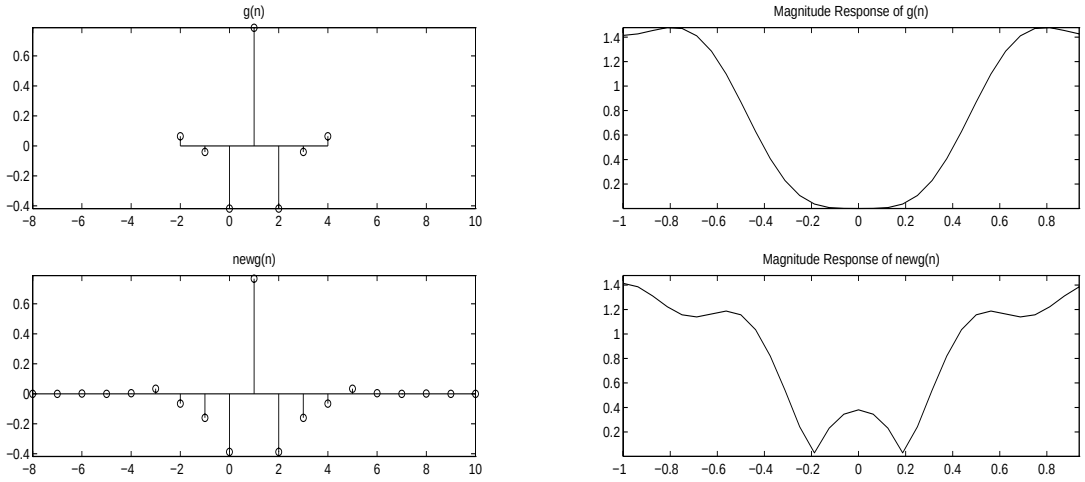

Fig. 3.7. (a) Highpass filters for scale $a = 2^j$ (top) and $a = 2^{j+1/2}$ (bottom). (b) Corresponding magnitude responses.

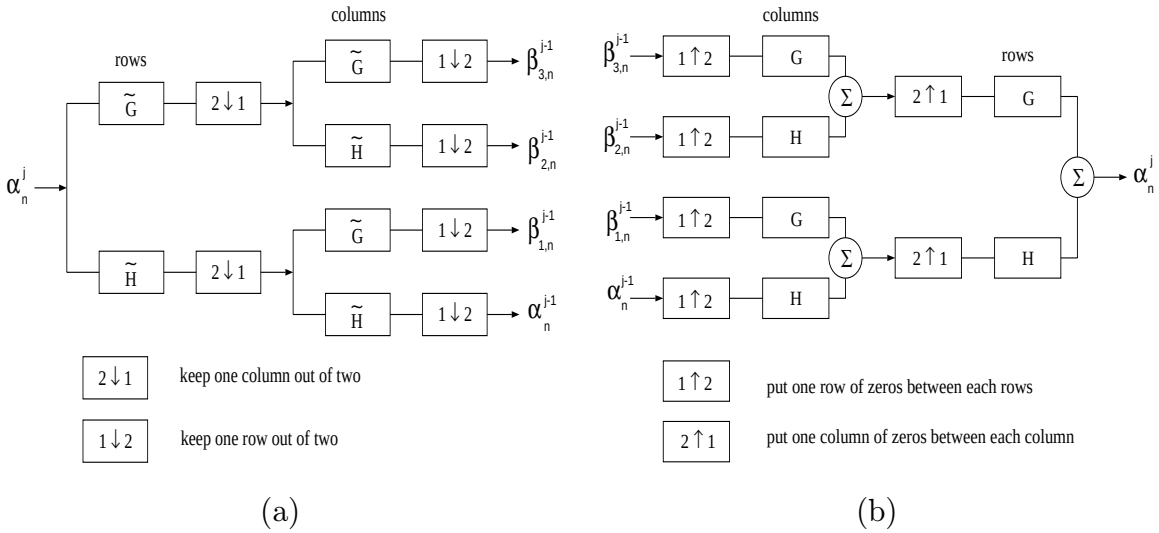

Fig. 3.8. Separable 2D wavelet transform: (a) Decomposition. (b)Reconstruction.

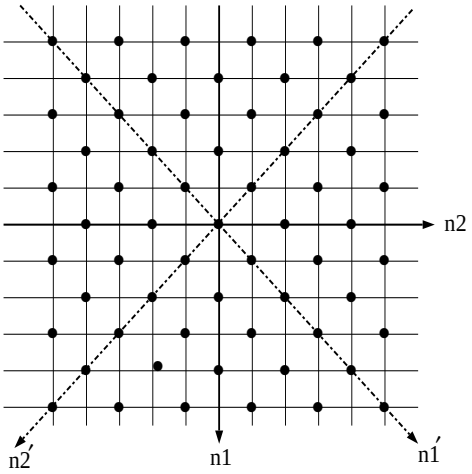

Fig. 3.9. Two dimensional quincunx sublattice.

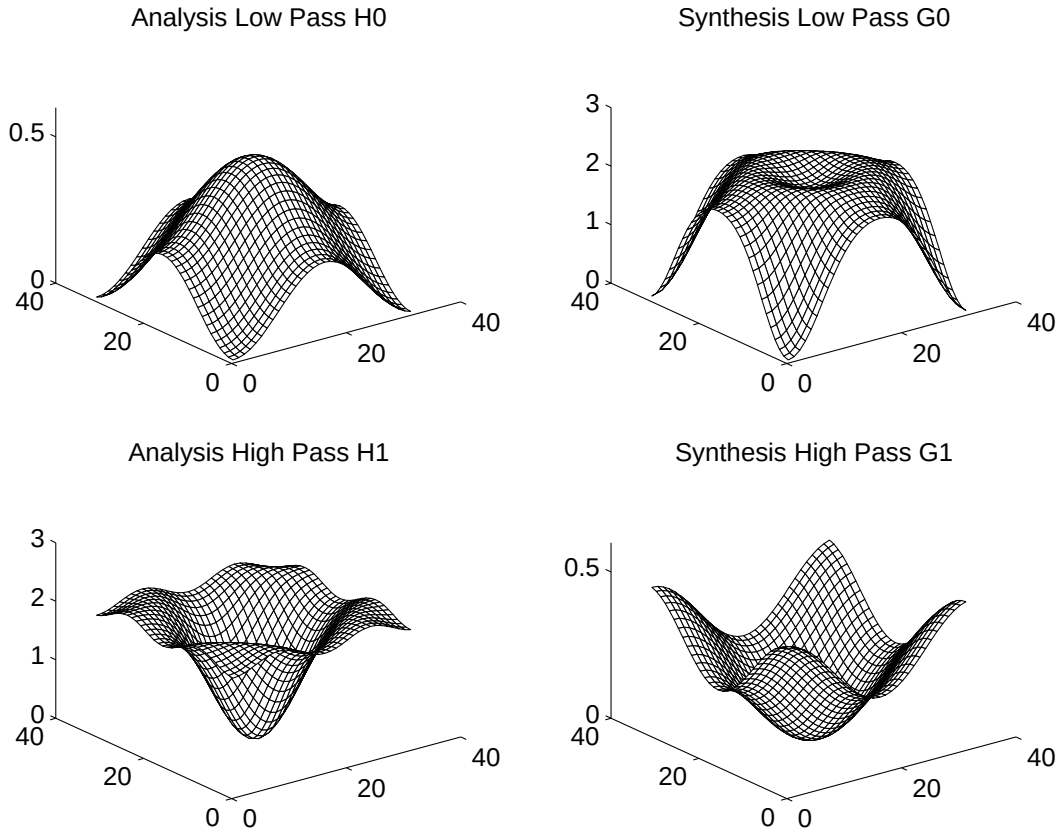

Fig. 3.10. Non-separable perfect reconstruction 2D filter (magnitude response).

Fig. 3.11. Original image Barbara. Its pixel values can be viewed as the approximation coefficients of a continuous function $\tilde{f}(x, y)$ at resolution $j = 0$.

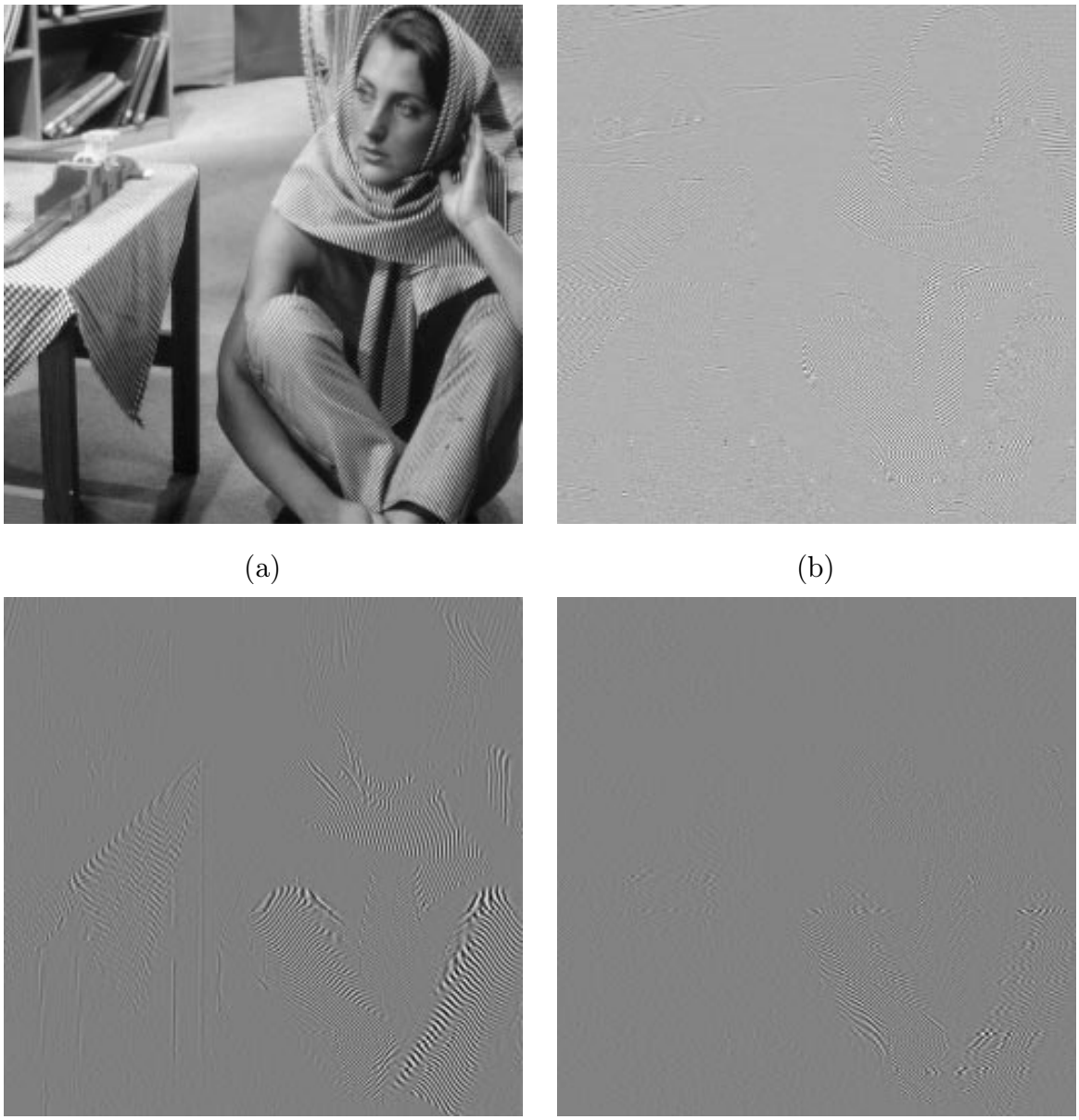

(a) (b)

(c) (d)

Fig. 3.12. First level wavelet decomposition of the Barbara image. (a) approximation coefficients α_n^{-1}. (b) horizontal detail signal $\beta_{1,n}^{-1}$. (c) vertical detail signal $\beta_{2,n}^{-1}$. (d) diagonal detail signal $\beta_{3,n}^{-1}$.

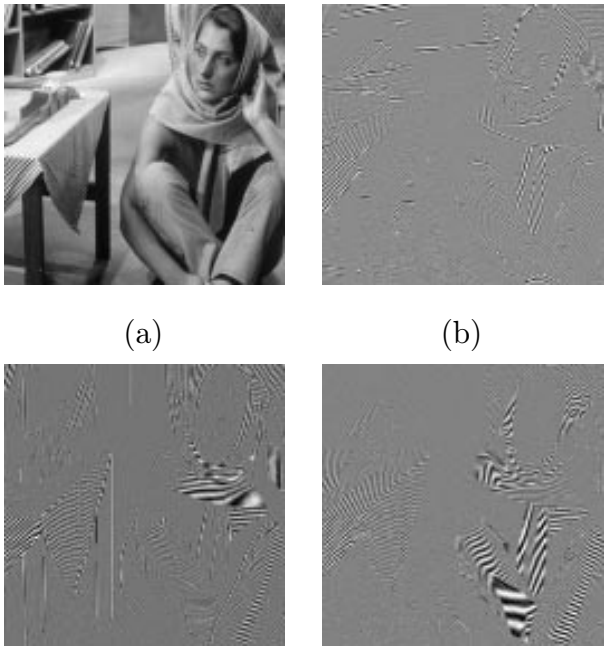

(a) (b)

(c) (d)

Fig. 3.13. Second level wavelet decomposition of the Barbara image obtained by decomposing the approximation coefficients α_n^{-1} at the first level $j = -1$. (a) approximation coefficients α_n^{-2}. (b) horizontal detail signal $\beta_{1,n}^{-2}$. (c) vertical detail signal $\beta_{2,n}^{-2}$. (d) diagonal detail signal $\beta_{3,n}^{-2}$.

4. MULTIRESOLUTION DETECTION OF SPICULATED LESIONS

4.1 Introduction

Among breast abnormalities, spiculated masses having a stellate appearance in mammograms are strong indicators of breast cancer [1]. Their central masses are usually irregular with ill-defined borders. Their sizes vary from a few millimeters to several centimeters in diameter. Computer aided diagnosis of digital mammograms generally consists of feature extraction followed by classification [4]. For spiculated lesions, Kegelmeyer, *et al* [8, 39] extracted a five-dimensional feature vector for each pixel which included the standard deviation of the edge orientation histogram (they called this the ALOE feature) and the output of four spatial filters. Each feature vector was then classified using a binary decision tree. They chose the window size for obtaining the ALOE feature to be 4 cm so that it was large enough to encompass all of the spiculated lesions in their data. Karssemeijer and Brake [40] investigated a method based on statistical analysis of a map of edge orientations. Two features were derived from the edge orientation map that were used to classify suspicious regions. To cover the range of sizes of the spicules in their data set, edge orientations were derived at 3 spatial scales and the one with the maximum absolute value was used. In general, it has proved difficult to determine the size of the neighborhood that should be used to extract local features of spiculated lesions. If the neighborhood is too large, small lesions may be missed; while if the neighborhood is too small, parts of large lesions may be missed.

In this chapter, we present a multiresolution scheme for the detection of spiculated lesions in mammograms that specifically addresses this difficulty of predetermining

the neighborhood size for feature extraction. The system diagram is shown in Figure 4.1. We first obtain a multiresolution representation of the original mammogram using a linear phase nonseparable 2-D wavelet transform. Features that are designed to differentiate spiculated lesions from normal structures are then extracted for every pixel at each resolution. Detection is performed from the coarsest resolution to the finest resolution using a binary tree classifier. There is a fundamental difference in our method than other approaches, which is also the novelty of our algorithm, in that we extract and classify features at multiple resolutions, hence overcoming the difficulty of choosing a neighborhood size *a priori* to capture tumors of varying sizes. Furthermore, the top-down classification we use requires less computation by starting with the coarsest resolution image (least amount of data) and propagating detection results to finer resolutions.

In Section 4.2, we describe the multiresolution decomposition method. In Section 4.3, we discuss the mammographic features used to characterize spiculated lesions of different sizes at various resolutions. The top-down classification approach is discussed in Section 4.4. Finally we present experimental results and discussion in Section 4.5.

4.2 Multiresolution Decomposition

As indicated above, the spiculated lesions we are interested in can occur in very different sizes. Hence, it is impossible to define *a priori* an optimal resolution for analyzing a mammogram. In Chapter 3, we have shown that a multiresolution representation reorganizes image information into a set of details appearing at different spatial resolutions, and thus provides a hierarchical framework for image analysis [50]. Recently the wavelet transform has become a popular technique for multiresolution representation and analysis in a wide variety of image processing applications, including computer aided diagnosis of mammograms [51, 10, 23, 61, 62].

The linear phase nonseparable 2-D perfect reconstruction wavelet transform described in [59] is used to obtain a multiresolution representation of the original mammogram. This transform does not introduce phase distortions in the decomposed images. In addition, no bias is introduced in the horizontal and vertical directions as would occur with a separable transform. However, it may not be able to conclude that this transform significantly improves the algorithm performance over other multiresolution decomposition methods. The impulse response of the analysis low pass filter is

$$h(n_1, n_2) = \begin{pmatrix} 0 & 0.125 & 0 \\ 0.125 & 0.5 & 0.125 \\ 0 & 0.125 & 0 \end{pmatrix}$$

The dilation matrix used to represent the subsampling lattice is

$$D = \begin{bmatrix} 1 & 1 \\ 1 & -1 \end{bmatrix}$$

which corresponds to the 2-D quincunx sublattice [59], as shown in Figure 3.9.

Let the original mammogram have the finest resolution $N \times N$ pixels. Since D expands the sampling lattice by $\sqrt{2}$ in each direction, image resolution decreases by a factor of $1/\sqrt{2}$ after each decomposition. For example, the image at the second finest resolution has $N/\sqrt{2} \times N/\sqrt{2}$ pixels. We will use only images of spatial resolutions $(N \times N)$, $(N/2 \times N/2), \ldots$ for feature extraction and classification.

4.3 Multiresolution Feature Analysis

Spiculated lesions range in size from a few millimeters to several centimeters. Usually the larger the tumor center, the longer is its spicules or "arms" [13]. Hence a large lesion preserves a stellate appearance at several more coarse resolutions. This can be seen in Figure 4.2, in which a spiculated lesion of 1 cm in radius is shown at multiple resolutions.

Also note that an $M \times M$ region at a coarser spatial resolution $N/n \times N/n$ corresponds to an $nM \times nM$ region in the original mammogram with spatial resolution

$N \times N$. Therefore, if a set of features extracted within an $M \times M$ window in the original mammogram differentiates spiculated lesions of size $\approx S$ from normal tissue, then the same set of features extracted at another resolution $N/n \times N/n$, using the same sized $M \times M$ window, should be able to detect spiculated lesions of size $\approx nS$. For example, if a set of features extracted within an 8×8 window in the original mammogram with spatial resolution $N \times N$ differentiates spiculated lesions of size ≈ 1 mm from normal tissue, then the same set of features extracted at the coarser resolution $N/4 \times N/4$, using the same sized 8×8 window, should be able to detect similar spiculated lesions of size ≈ 4 mm. This enables us to choose a fairly small neighborhood for feature extraction at the finest resolution and detect the smallest possible spiculated lesions. Larger lesions will be detected using the same set of features extracted at a coarser resolution. This strategy circumvents the difficulty of choosing a neighborhood size *a priori* to capture features of objects of varying sizes.

We extract four features from the low frequency wavelet coefficients for every pixel at each resolution. Let (i, j) be the spatial location in the mammogram at row i and column j; $f(i, j)$ be the pixel brightness at (i, j); ∂S_{ij} be some neighborhood of (i, j), and K be the number of pixels within ∂S_{ij}. The first two features are then defined as the following:

- mean pixel brightness in ∂S_{ij}:

$$\bar{f}(i,j) = \frac{1}{K} \sum_{(m,n) \in \partial S_{ij}} f(m,n)$$

- standard deviation of pixel brightnesses in ∂S_{ij}:

$$\sigma_f(i,j) = \sqrt{\frac{1}{K-1} \sum_{(m,n) \in \partial S_{ij}} (f(m,n) - \bar{f}(i,j))^2}$$

Let $D_y(i, j)$ and $D_x(i, j)$ be an estimate of the vertical and horizontal spatial derivatives of f at (i, j), respectively. Let $\theta(i, j) = \tan^{-1}\{D_y(i, j)/D_x(i, j)\}$ be an estimate of the gradient orientation at (i, j) with value $\in (-\pi/2, \pi/2]$. Also let $hist_{ij}$ be the histogram of θ within ∂S_{ij} using 256 bins, hence $hist_{ij}(n) = \#$ of pixels in

∂S_{ij} that have gradient orientations $\in (-\pi/2 + n\pi/256, -\pi/2 + (n+1)\pi/256]$, where $n = 0, 1, \ldots, 255$. Let $\overline{hist}(i,j) = \frac{1}{256}\sum_{n=0}^{255} hist_{ij}(n)$ be the average bin height of $hist_{ij}$.

The third feature is defined as:

- standard deviation of gradient orientation histogram in ∂S_{ij}:

$$\sigma_{hist}(i,j) = \sqrt{\frac{1}{255}\sum_{n=0}^{255}(hist_{ij}(n) - \overline{hist}(i,j))^2}$$

Note that this feature is the same as the ALOE feature described in [8].

Let $K_{\theta_+}(i,j)$ and $K_{\theta_-}(i,j)$ be the number of positive and negative gradient orientations within ∂S_{ij}, respectively; $\overline{\theta}_+(i,j) = \frac{1}{K_{\theta_+}(i,j)}\sum_{\theta(m,n)\geq 0,(m,n)\in\partial S_{ij}}\theta(m,n)$ and $\overline{\theta}_-(i,j) = \frac{1}{K_{\theta_-}(i,j)}\sum_{\theta(m,n)<0,(m,n)\in\partial S_{ij}}\theta(m,n)$ be the average positive and negative gradient orientations within ∂S_{ij}, respectively.

The folded gradient orientation $\theta'(i,j)$ at (i,j) is defined as:

$$\theta'(i,j) = \begin{cases} \theta(i,j) + \pi & \text{if } \overline{\theta}_+(i,j) - \theta(i,j) > \frac{\pi}{2} \text{ and } K_{\theta_+}(i,j) \geq K_{\theta_-}(i,j) \\ \theta(i,j) - \pi & \text{if } \theta(i,j) - \overline{\theta}_-(i,j) > \frac{\pi}{2} \text{ and } K_{\theta_+}(i,j) < K_{\theta_-}(i,j) \\ \theta(i,j) & \text{otherwise} \end{cases}$$

And the fourth feature is then defined as:

- standard deviation of the folded gradient orientations in ∂S_{ij}:

$$\sigma_{\theta'}(i,j) = \sqrt{\frac{1}{K-1}\sum_{(m,n)\in\partial S_{ij}}(\theta'(m,n) - \bar{\theta}'(i,j))^2}$$

This modification of θ to θ' in generating $\sigma_{\theta'}$ is necessary for this feature not to be sensitive to the nominal value of θ, but to the actual gradient orientation variances. As one can see from Figure 4.3, the gradient orientation distance between $\theta_1 = \pi/2$ and $\theta_2 = -\pi/4$ is the same as that between $\theta_1 = \pi/2$ and $\theta_3 = \pi/4$. For our purpose of detecting spicules, we would like to obtain similar feature values for these two cases. However, if the θs are used directly, the variance of the pair (θ_1, θ_2) would be 2.8 and

much larger than the variance of the pair (θ_1, θ_3), which is 0.3; while using the folded gradient orientations θ's, θ_2 will be folded to $\theta_2' = 3\pi/4$ and so we obtain the same $\sigma_{\theta'}$ for both cases. Even when all θ's are rotated by some angle α, the feature $\sigma_{\theta'}$ will remain the same value although the foldings may be different. For example, let $\alpha = \pi/8$, then $\tilde{\theta}_1 = -3\pi/8$, $\tilde{\theta}_2 = -\pi/8$, and $\tilde{\theta}_3 = 3\pi/8$. To obtain the folded gradient orientations for the pair $(\tilde{\theta}_1, \tilde{\theta}_2)$, no folding is needed and the feature value remains to be 0.3 as that of the pair (θ_1, θ_2). While for the pair $(\tilde{\theta}_1, \tilde{\theta}_3)$, $\tilde{\theta}_1$ will be folded to $5\pi/8$ and so the feature $\sigma_{\theta'}$ has the value 0.3 as the same as that of the pair (θ_1, θ_3) before rotating. This feature is different than a similar one we presented in [10] and has proved to better characterize spiculated lesions.

The features σ_{hist} and $\sigma_{\theta'}$ are chosen to be especially responsive to spiculated lesions. As illustrated in Figure 4.4, a spiculated lesion differs from the normal ducts and connective tissue septae of the breast that tend to radiate from the nipple to the chest wall. It appears as an irregular tumor center surrounded by spicules that radiate in all directions. Accordingly, pixels in normal areas have rather similar gradient orientations, while pixels near spiculated lesions tend to have gradient orientations in many directions. Therefore, the standard deviation of gradient orientations in the neighborhood of a lesion pixel will be larger than that in the neighborhood of a normal pixel. For the same reason, the gradient orientation histogram will be flat near a lesion pixel, but will have a peak corresponding to normal structure orientations near a normal pixel [8]. This result is shown in Figure 4.5 which compares the gradient orientation histograms within a spiculated lesion region and within a normal region, respectively. The mean $\bar{f}$ and standard deviation σ_f of the pixel brightnesses help further to differentiate lesions from normal tissue regions, because lesions usually have higher density, or appear brighter, in mammograms.

Figure 4.6 shows a test pattern at multiple resolutions, which consists of an idealized spiculated lesion and parallel linear markings, embedded in uncorrelated Gaussian distributed noise with PSNR (Peak Signal to Noise Ratio) of 7db. The lesion has a radius of 128 pixels in the original image. Figure 4.7, Figure 4.8, Figure 4.9, and

Figure 4.10 show the features $\sigma_{\theta'}$, σ_{hist}, $\bar{f}$, and σ_f, respectively, for this test pattern. Each feature at different resolutions is extracted within same sized circular neighborhoods. For this test pattern, the neighborhood radius is 30 pixels for features $\sigma_{\theta'}$ and σ_{hist}, and 20 pixels for features $\bar{f}$ and σ_f. A larger neighborhood size is used for features $\sigma_{\theta'}$ and σ_{hist} because they respond stronger to a spiculated lesion if the entire halo of spicules is included in the feature extraction window, while features $\bar{f}$ and σ_f respond better to the central mass of the lesion. These features are able to differentiate a spiculated lesion from a complex background. From Figure 4.7 and Figure 4.8, we can see that the features best discriminate the lesion from its background at resolution ($N/4 \times N/4$) when the size of the feature extraction neighborhood matches that of the lesion. In this case, the brightest spot in the feature image in Figure 4.7 (c) and the darkest spot in the feature image in Figure 4.8 (c) directly overlay both the central mass and the spicules of the lesion.

4.4 Classification Algorithm

A sequential hierarchical decision scheme has been shown to achieve better performance than employing a single "best" set of features in a one-step decision [63, 64]. A Binary Classification Tree (BCT) is simple, fast, and efficient type of hierarchical classifier. This tree structured classification approach has several advantages over more traditional nonparametric methods such as the nearest neighbor method [63]:

- BCT does automatic stepwise feature selection and complexity reduction
- BCT is robust with respect to outliers and misclassified points in the training set
- The final classifier can be compactly stored
- BCT efficiently classifies new data
- BCT provides easily understood and interpreted information regarding the predictive structure of the data

We choose the iterative growing and pruning algorithm proposed in [64] for our classification tree design because it not only produces trees with higher classification accuracy, but also requires less computation than other widely used tree design algorithms, such as CART [63].

Considering that there is redundancy in mapping the feature space by spatially adjacent samples, only a subsampling of the training set is used to grow BCT. After the BCT is generated, we associate with each terminal node a suspicious probability which is the percentage of lesion pixels in the training images that falls in this terminal node. The suspicious probability is then recomputed using the entire set of training samples. This partly compensates for the lost classification accuracy due to the fact that not all the training samples are used to design the tree [8].

At each resolution, five features are used for classification: the four features extracted at that resolution plus the feature $\sigma_{hist_{ij}}$ extracted at the next coarser resolution. Our experiments have shown that using features across resolutions simultaneously helps capture spiculated lesions of varying sizes. Detection starts from the second coarsest resolution and then goes to the next finer resolution until the original mammogram is reached. A positive detection at a coarser resolution propagates to finer resolutions, which effectively reduces the number of pixels to be classified. A negative result at a coarser resolution will be combined with those at finer resolutions via a weighted sum.

We obtain a probability image from the BCT for each test mammogram, in which the pixel values represent the probability that a pixel belongs to a spiculated lesion. A median filter is then used to eliminate isolated positive responses, followed by a smoothing filter to reach a consensus within neighboring pixels. Final results are obtained by thresholding the filtered probability image.

4.5 Results and Conclusions

We tested the proposed multiresolution detection algorithm on the MIAS database [65] provided by the Mammographic Image Analysis Society (MIAS) in the

UK. Images in the MIAS database have 50 micron resolution. There is a total of 19 mammograms containing spiculated lesions. The smallest lesion extends 3.6 mm in radius, while the biggest one is nearly 10 times larger and extends to 35.0 mm. These 19 together with another 19 normal mammograms, also taken from the MIAS database, were randomly split into two sets with approximately an equal number of lesions and normal mammograms in each set. Each set was then used separately as a training set to generate two BCTs, according to a split-half training paradigm similar to Kegelmeyer *et al* [8]. A BCT trained by one set was used to classify mammograms in the other set, and vice versa. Therefore, no mammogram was used both for training and testing.

The wavelet transform described in Section 4.2 was used to generate the multiresolution representations of each mammogram. Features described in Section 4.3 were extracted from images of spatial resolutions $(N \times N)$, $(N/2 \times N/2)$, $(N/4 \times N/4)$, and $(N/8 \times N/8)$. Circular regions were used for all feature extractions so that features behave equally in all directions. In this experiment, the neighborhood radius for extracting features $\sigma_{\theta'}$ and σ_{hist} was 60 at all resolutions, which corresponds to a radius of 3 mm, 6 mm, 12 mm, and 24 mm in the original resolution $(N \times N)$, and coarser resolutions $(N/2 \times N/2)$, $(N/4 \times N/4)$, and $(N/8 \times N/8)$, respectively. The neighborhood radius for extracting features $\bar{f}$ and σ_f was 20 at all resolutions, which corresponds to a radius of 1 mm, 2 mm, 4 mm, and 8 mm in the original resolution $(N \times N)$, and coarser resolutions $(N/2 \times N/2)$, $(N/4 \times N/4)$, and $(N/8 \times N/8)$, respectively. Extracting features at coarser resolutions for relatively large regions significantly reduces the amount of computation.

Accordingly, three-level classifications were performed for each mammogram, starting from resolution $(N/4 \times N/4)$ and going to $(N \times N)$. At each resolution, the corresponding five dimensional feature vector, including the four features extracted at that resolution and σ_{hist} extracted at the next coarser resolution, was classified through the BCT trained by the other half test set. The output is a probability image, in which the pixel values represent the probability of belonging to spiculated

lesions. We then used a median filter of radius 5 to eliminate isolated positive responses, followed by a smoothing filter to reach a consensus within neighboring pixels. Because we are looking for larger lesions at coarser resolutions and smaller ones at finer resolutions, the radii used for smoothing filters were chosen to be 18 mm, 6 mm, and 2 mm at resolutions $(N/4 \times N/4)$, $(N/2 \times N/2)$, and $(N \times N)$, respectively. The detection result was obtained by thresholding the smoothed probability image. Using a small threshold is more likely to detect true lesions, but also to generate more false positive responses. Using a large threshold gives fewer false positive responses, but may miss more true lesions. Hence variation of thresholds gives different diagnostic accuracy which can be quantified using FROC ("Free response Receiver Operating Characteristic") analysis [66], where the true positive fraction (TPF) is plotted as a function of the average number of false positives (FP) per image. FROC analysis [66] is well suited for the assessment of computer aided diagnosis of mammograms because it is applicable to situations that involve any number of reported locations and any number of actual lesions in each image.

If there is a positive detection at a coarser resolution, no feature extraction and detection are needed at the corresponding pixel locations at all finer resolutions. This approach effectively reduces the number of pixels to be classified. Smaller probabilities that give negative responses are propagated to finer resolutions by weighted sum. Figure 4.11 shows a spiculated lesion of size 6.6 mm detected at the finest original resolution; Figure 4.12 shows a spiculated lesion of size 12.4 mm detected at the second coarsest resolution; and Figure 4.13 shows a spiculated lesion of size 35.0 mm detected at the coarsest resolution.

To evaluate the computer diagnosis results, we adopted the criteria in [8]: a computer finding is considered as a true positive detection if its area is overlapped by at least 50% of a true lesion as indicated by an expert radiologist; a computer finding that does not so overlap a true lesion is considered as false positive; and a true lesion that is not overlapped by any computer finding is considered as false negative. By these criteria, the diagnostic accuracy performance of our algorithm

on the MIAS database quantified using FROC curve is shown in Figure 4.14. We achieved 84.2% true positive detection at less than 1 false positive per image and 100% true positive detection at 2.2 false positive per image. The spiculated lesion that was missed first when the detection threshold was increased, or the sensitivity decreased, is shown in Figure 4.15. This lesion lacks visible spicules at all directions, hence it is hard to be captured by our features that are designed to respond to spiculations. Karssemeijer and Brake [40] reported their results on the MIAS database at around 90% true positive detection at 1 false positive per image and 100% true positive detection at more than 4 false positive per image. However they selected only malignant spiculated lesions and included architectural distortions as the abnormal test images, while we used all and only spiculated lesions as the abnormal test images. Since usually different dataset is used in testing, it is difficult to compare results with others.

In summary, our new multiresolution algorithm for the detection of spiculated lesions in digital mammograms has two advantages over other approaches. First we extract and classify features at multiple resolutions, hence overcoming the difficulty of choosing a neighborhood size *a priori* to capture tumors of varying sizes. Furthermore, the top-down classification we use requires less computation by starting with the coarsest resolution image (least amount of data) and propagating detection results to finer resolutions. Experimental results on the MIAS database showed that our algorithm is capable of detecting spiculated lesions of very different sizes at low false positive rates.

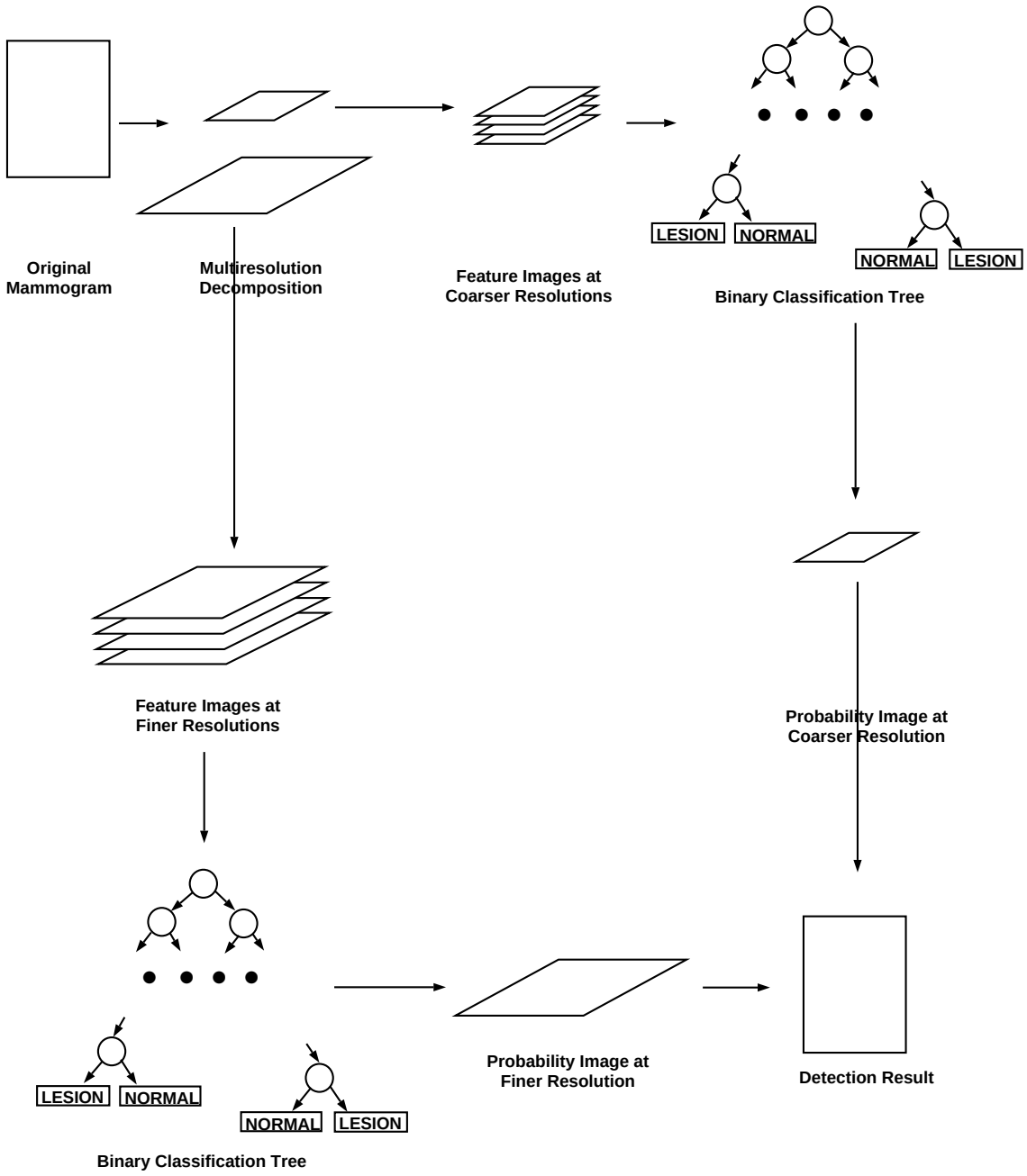

Fig. 4.1. Diagram of system for multiresolution spiculated lesion detection, illustrated here for only two resolutions — fine (left) and coarse (right).

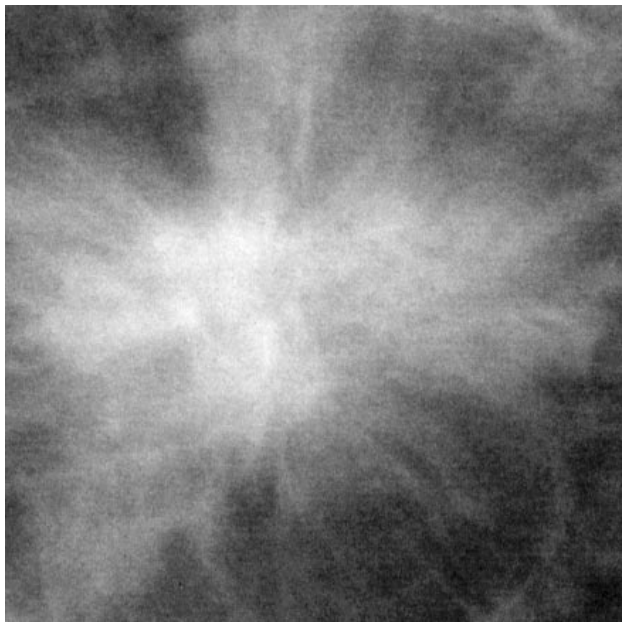

(a)

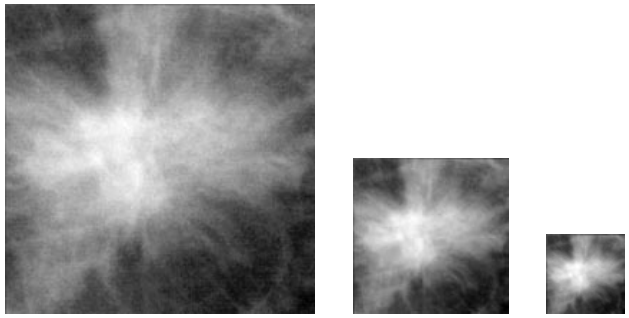

(b) (c) (d)

Fig. 4.2. Multiresolution representation of a spiculated lesion (a) spiculated lesion in the original mammogram of resolution $N \times N$. (b) in the coarser resolution $N/2 \times N/2$. (c) in the coarser resolution $N/4 \times N/4$. (d) in the coarsest resolution $N/8 \times N/8$

.

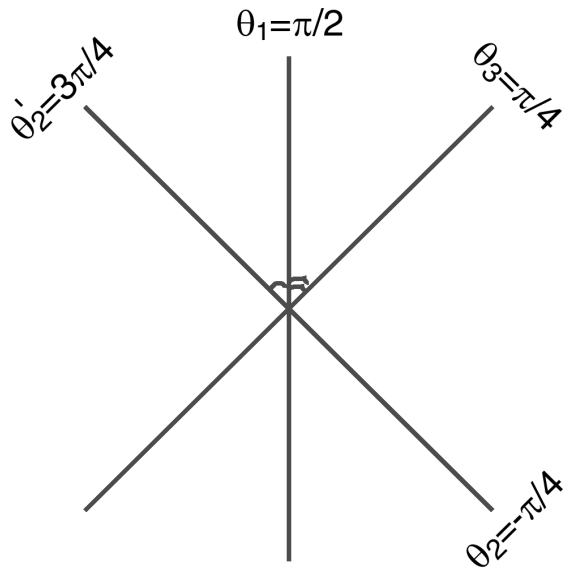

Fig. 4.3. Folding edge orientation makes the feature $\sigma_{\theta'}$ insensitive to the nominal value of θ, but sensitive to the actual edge orientation variances.

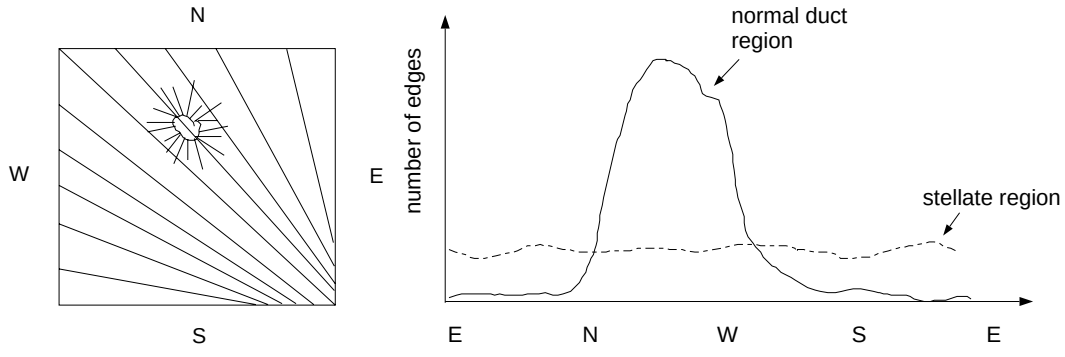

(a) (b)

Fig. 4.4. (a) Directions of spicules of a spiculated lesion differ from the directions of normal linear markings in a mammogram; (b) standard deviation of gradient orientation histogram differentiates the area near a spiculated lesion from normal.

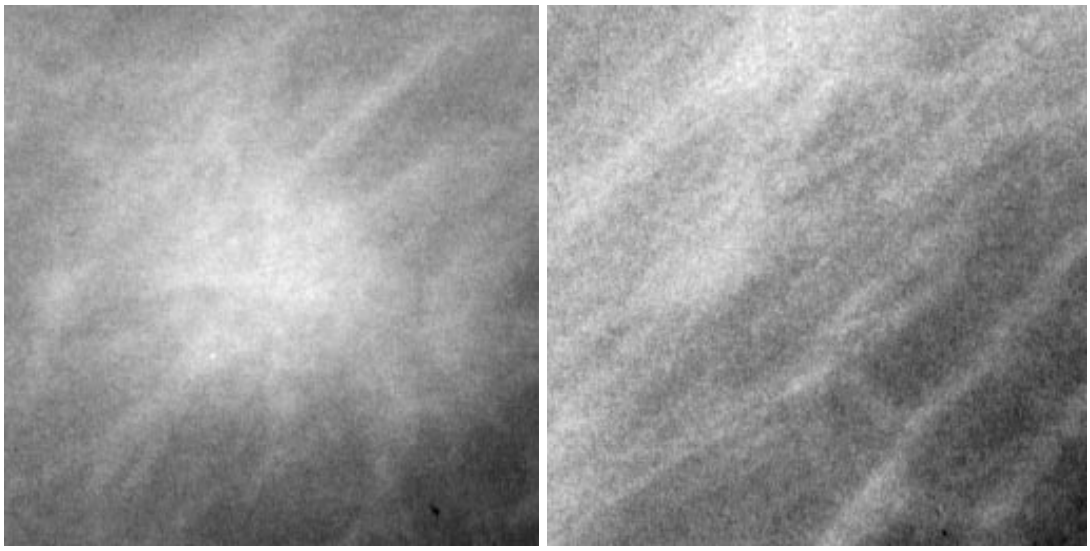

(a) (b)

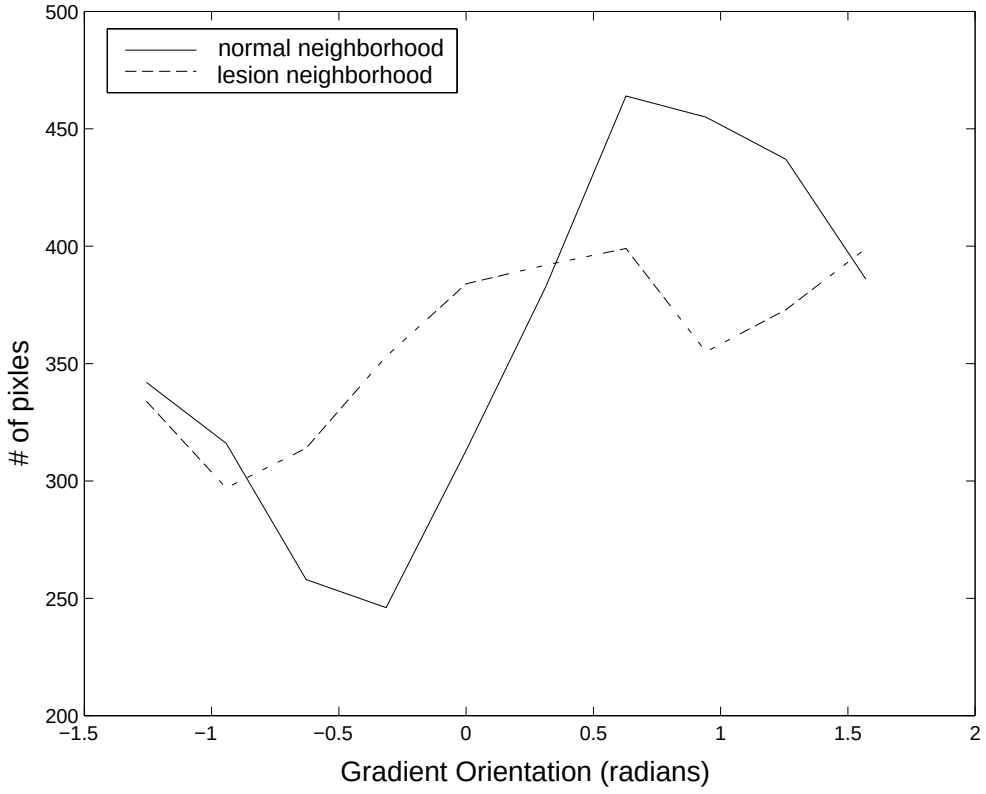

(c)

Fig. 4.5. (a) A spiculated lesion region. (b) A normal region. (c) Gradient orientation histograms of (a) and (b)

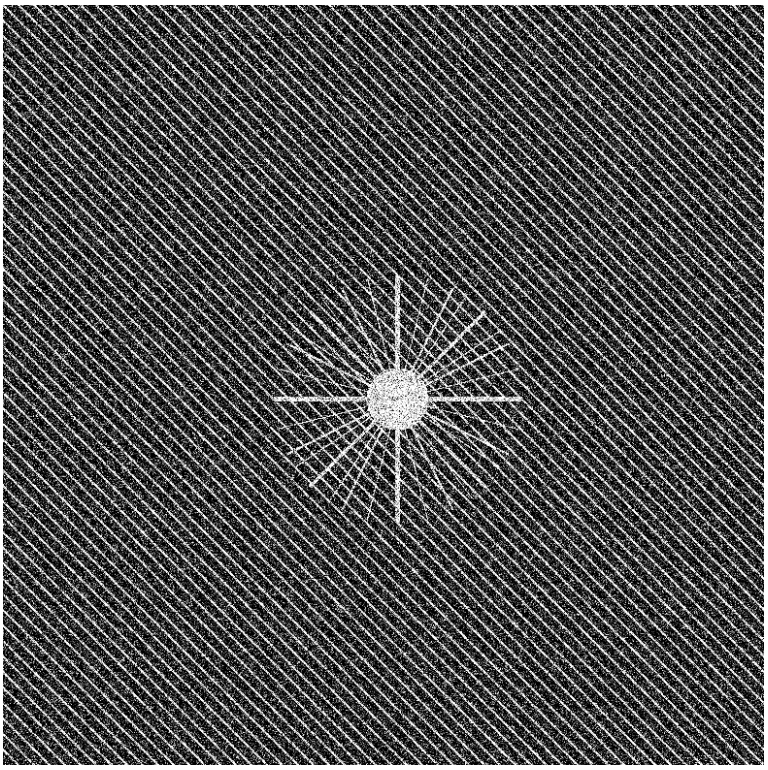

(a)

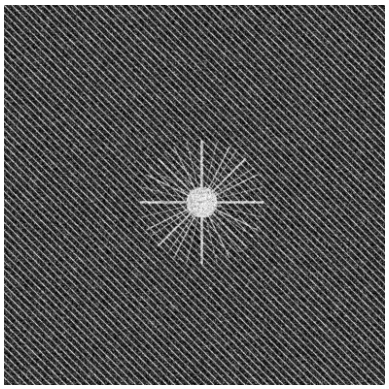

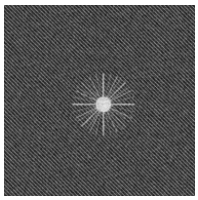

(b) (c)

Fig. 4.6. Multiresolution representation of a test pattern consisting of an idealized spiculated lesion and normal structures embedded in uncorrelated Gaussian distributed noise. The lesion has a radius of 128 pixels in the original image: (a) original $N \times N$ image. (b) coarser resolution $N/2 \times N/2$. (c) coarsest resolution $N/4 \times N/4$.

.

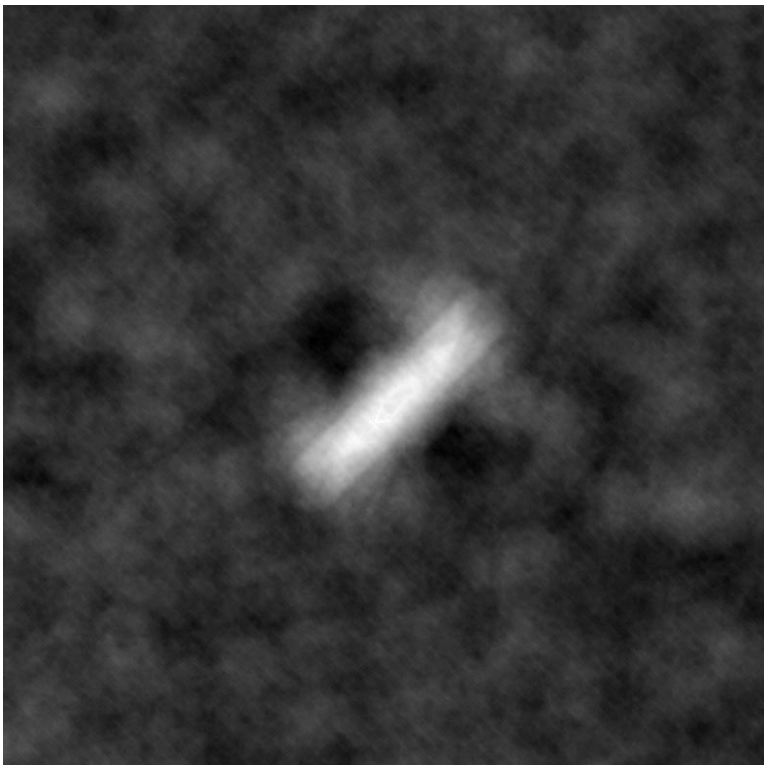

(a)

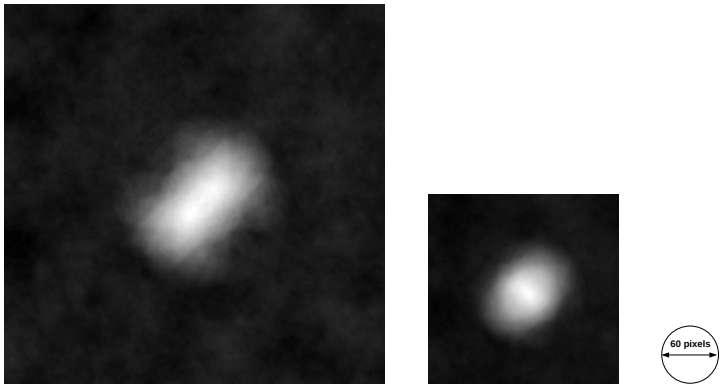

(b) (c) (d)

Fig. 4.7. Feature $\sigma_{\theta'}$ obtained in circular neighborhoods of radius 30 pixels at all resolutions for the test pattern shown in Figure 4.6. Here large values (bright pixels) indicate spiculated regions as explained in Figure 4.4. (a) original $N \times N$ image. (b) coarser resolution $N/2 \times N/2$. (c) coarsest resolution $N/4 \times N/4$. (d) a circular neighborhood of size 30 pixels in radius.

.

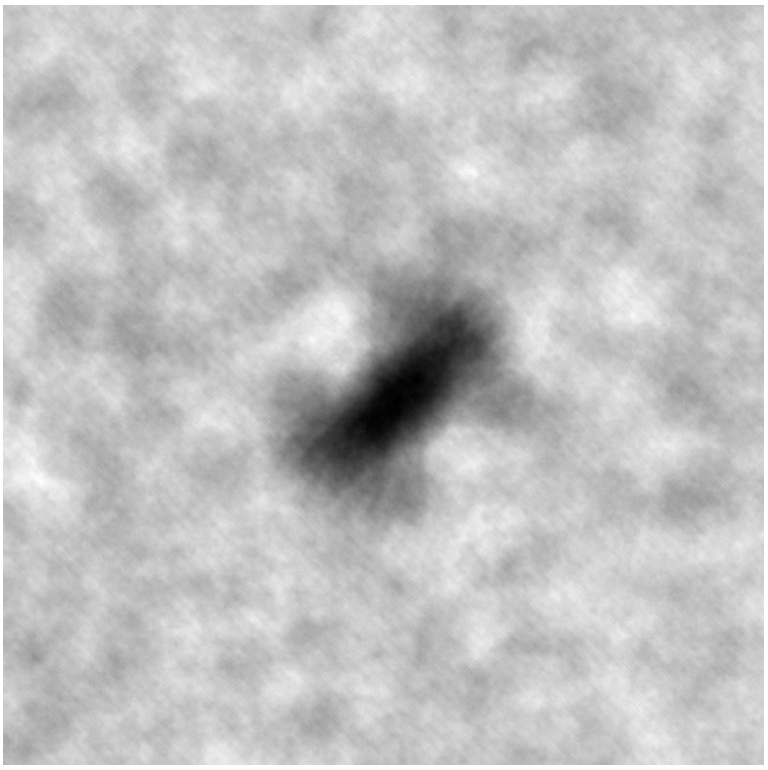

(a)

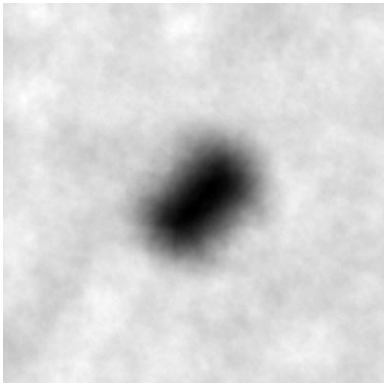

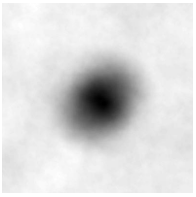

(b) (c) (d)

Fig. 4.8. Feature σ_{hist} obtained in circular neighborhoods of radius 30 pixels at all resolutions for the test pattern shown in Figure 4.6. Here small values (dark pixels) indicate spiculated regions as explained in Figure 4.4. (a) original $N \times N$ image. (b) coarser resolution $N/2 \times N/2$. (c) coarsest resolution $N/4 \times N/4$. (d) a circular neighborhood of size 30 pixels in radius.

.

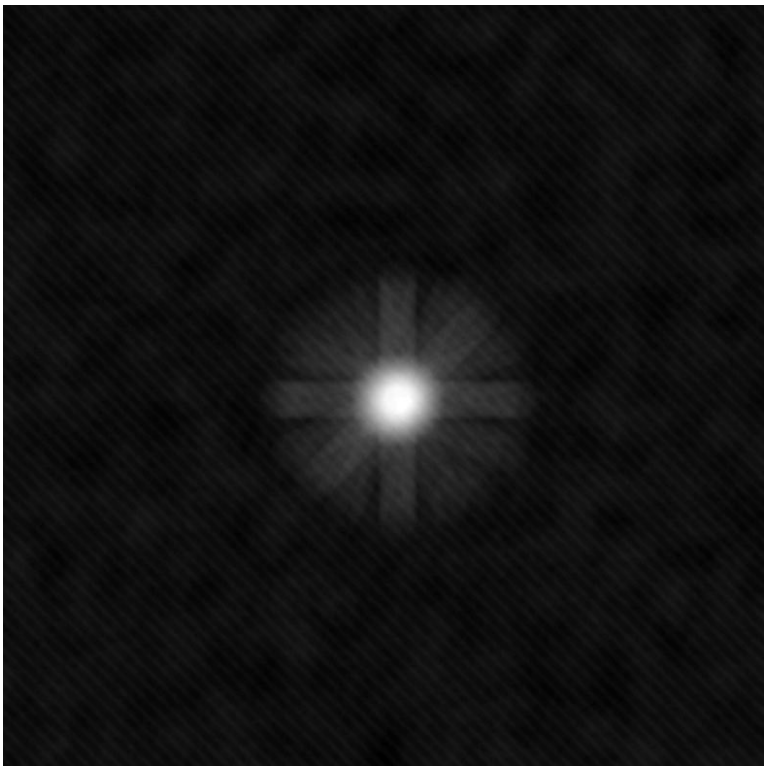

(a)

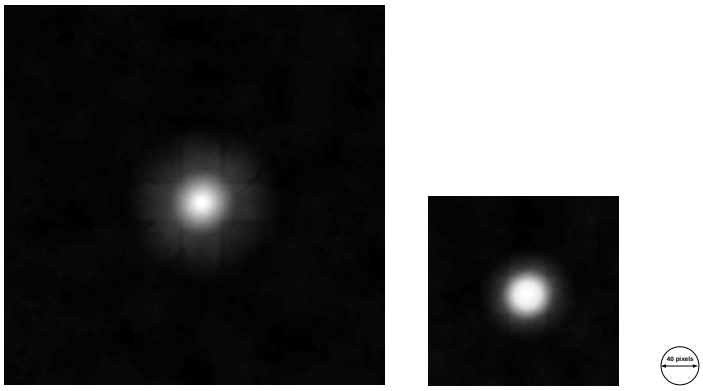

(b) (c) (d)

Fig. 4.9. Feature $\bar{f}$ obtained in circular neighborhoods of radius 20 pixels at all resolutions for the test pattern shown in Figure 4.6: (a) original $N \times N$ image. (b) coarser resolution $N/2 \times N/2$. (c) coarsest resolution $N/4 \times N/4$. (d) a circular neighborhood of size 20 pixels in radius.

.

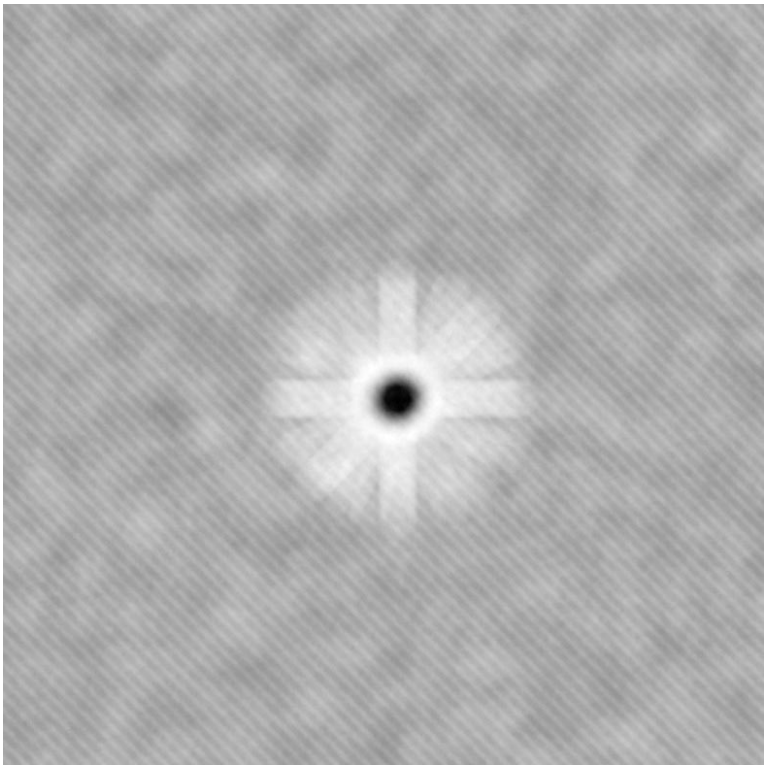

(a)

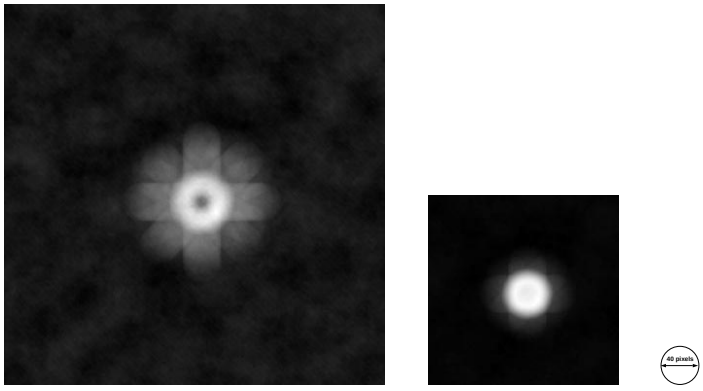

(b) (c) (d)

Fig. 4.10. Feature σ_f obtained in circular neighborhoods of radius 20 pixels at all resolutions for the test pattern shown in Figure 4.6. Note that feature values are smaller (darker) in the background area at coarser resolutions because of the smoothing effect of the lowpass filtering step in obtaining coarser resolution images. (a) original $N \times N$ image. (b) coarser resolution $N/2 \times N/2$. (c) coarsest resolution $N/4 \times N/4$. (d) a circular neighborhood of size 20 pixels in radius.

.

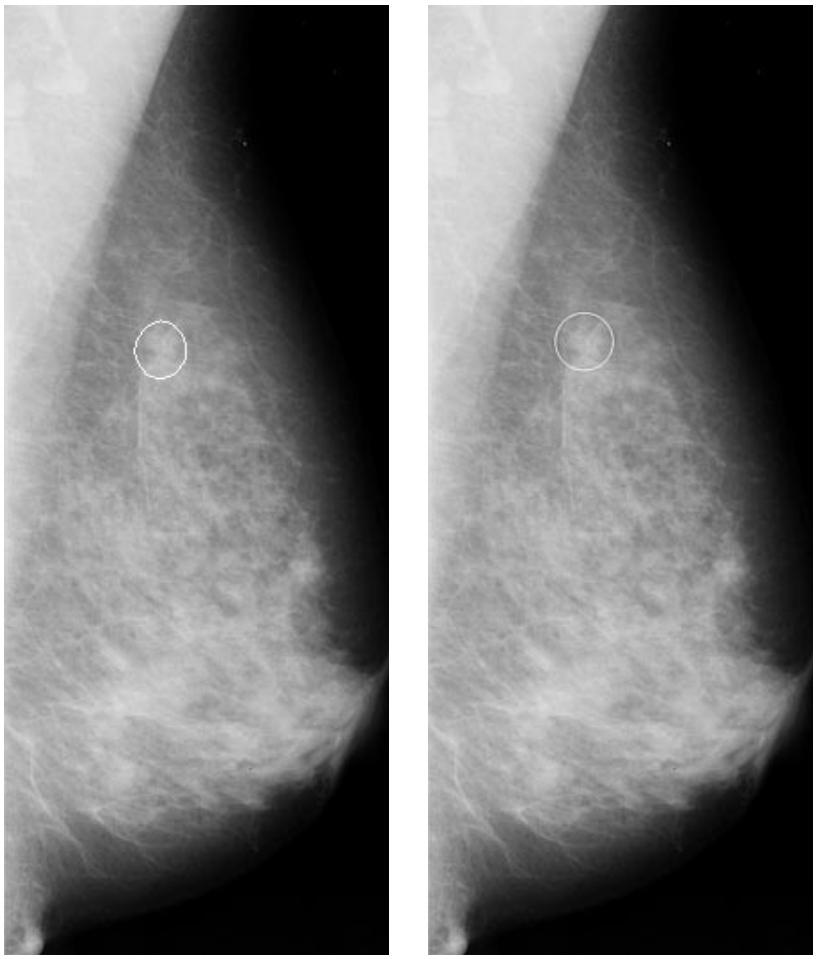

(a) (b)

Fig. 4.11. A spiculated lesion of size 6.6 mm detected at the finest resolution (a) mammogram with automatic detection. (b) mammogram with tumor as determined by expert radiologists.

.

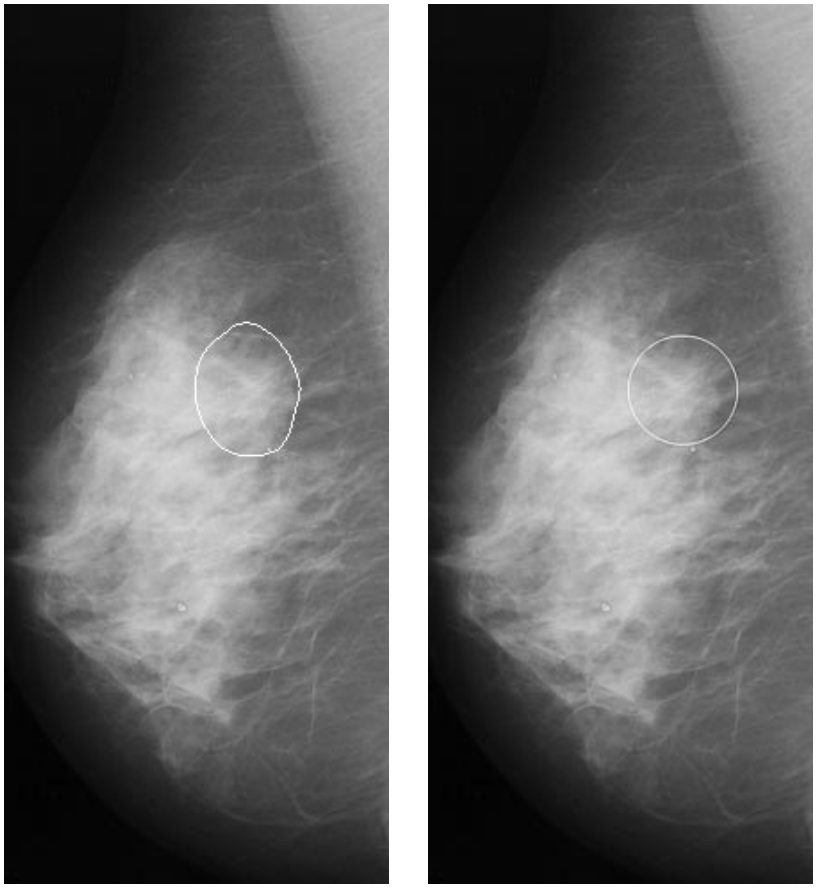

(a) (b)

Fig. 4.12. A spiculated lesion of size 12.4 mm detected at the second coarsest resolution (a) mammogram with automatic detection. (b) mammogram with tumor as determined by expert radiologists.

.

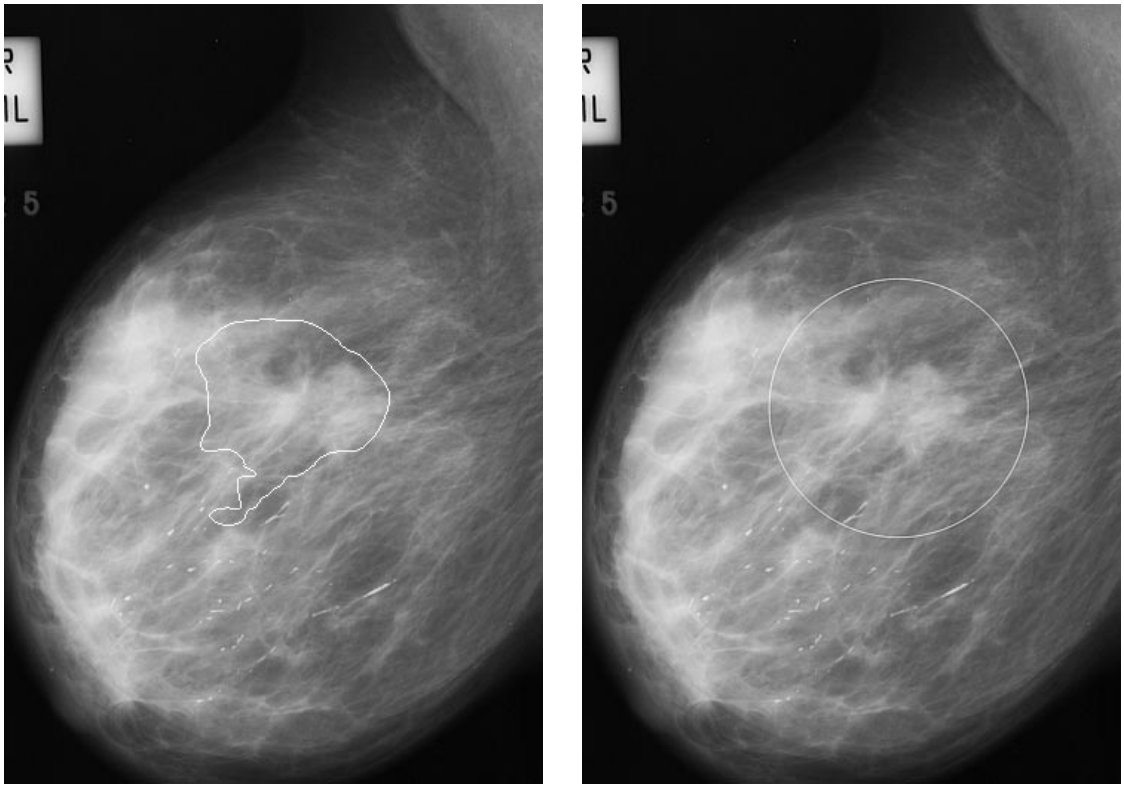

(a) (b)

Fig. 4.13. A spiculated lesion of size 35.0 mm detected at the coarsest resolution (a) mammogram with automatic detection. (b) mammogram with tumor as determined by expert radiologists.

.

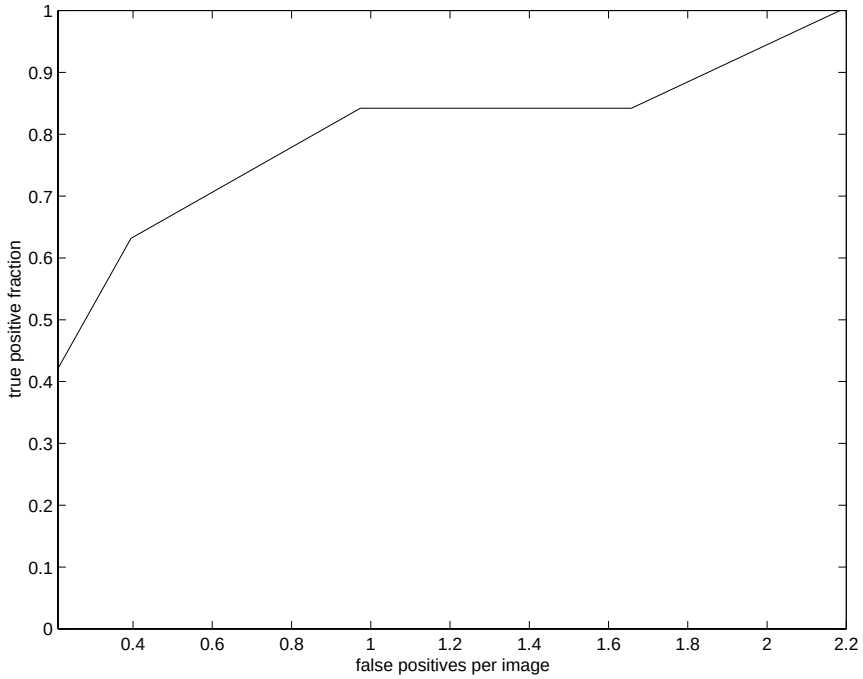

Fig. 4.14. FROC curve for detection of spiculated lesions in the MIAS database

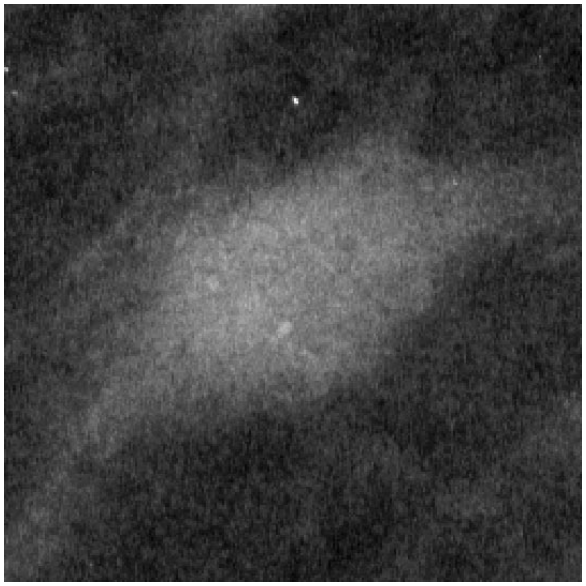

Fig. 4.15. The first missed spiculated lesion when the detection sensitivity is decreased. It lacks visible spicules at all directions.

5. CHARACTERIZATION OF NORMAL MAMMOGRAMS

5.1 Introduction

A great deal of effort has been devoted to Computer Aided Diagnosis (CAD) in digital mammography. The goal has been to increase diagnostic accuracy as well as the reproducibility of mammographic interpretation. Most work aims at detecting one or more of the three abnormal structures in mammograms [9]: microcalcifications (indicative of ductal carcinoma in situ and other lesions) [67, 24, 23], circumscribed masses [68, 5, 9, 32], and spiculated lesions [8, 40, 10, 11]. Others have explored classifying breast lesions as benign or malignant [37, 69]. There also has been work on distinguishing normal regions from regions containing calcifications [47, 70], or masses [48, 71]. However, little work has been done on specifically characterizing normal mammograms [12].

Since cancer treatment is most effective when the cancer is detected early, it follows that the progress in treatment will be closely related to the ability to reduce the proportion of "misses" in the cancer detection task. This, in turn, requires better methods for analyzing hard abnormal mammograms, which are hard because they are very similar to normal mammograms. We propose to develop algorithms to characterize normal mammograms, rather than mammograms with various possible abnormalities. The problem of detecting normal mammograms is different than the detection of lesions and is not simply "1 - the detection of abnormal mammograms." We shall examine this issue in the context of a decision model using Bayes's rule in probability theory. Let $P(cancer)$ be the probability of a cancer; $P(normal)$ be the probability of no cancer; $P(image)$ be the probability of obtaining a specific mammogram;

$P(cancer|image)$ be the probability of cancer detection given a specific mammogram; $P(image|cancer)$ be the probability of obtaining a specific mammogram given there is cancer; $P(image/normal)$ be the probability of obtaining a specific mammogram given there is no cancer. From Bayes's Rule we have

$$P(cancer|image) = \frac{P(image|cancer)P(cancer)}{P(image)} \tag{5.1}$$

where

$$P(image) = P(image|cancer)P(cancer) + P(image|normal)P(normal) \tag{5.2}$$

that is,

$$P(cancer|image) = \frac{P(image|cancer)P(cancer)}{P(image|cancer)P(cancer) + P(image|normal)P(normal)} \tag{5.3}$$

Decision about treatment (e.g. surgery) is based on the posterior probability $P(cancer|image)$. Note, however, that if $P(image|normal)$ is not known, the decision maybe highly suboptimal. For example, even if $P(image|cancer)$ is small, the posterior probability can be large if $P(image|normal)$ is close to zero. Note since $P(normal) \gg P(cancer)$, $P(image|normal)$ really dominates. Clearly, without knowing $P(image|normal)$ there is no way of obtaining the posterior probability accurately. In other words, this means that misses can be avoided more easily, if we know better how normal mammograms look. Even if there is little evidence that a malignant breast could have produced the given image, the medical decision can be positive (cancer present) if we know that it is very unlikely that the image could have been produced by a normal breast. Therefore, the effectiveness of algorithms for detecting cancers can be greatly increased if these algorithms work synergistically with algorithms for characterizing normal mammograms.

In this chapter, we propose to specifically characterize normal mammograms based on normal tissue identification and removal, which is independent of the types of abnormalities that may exist in the mammogram. This approach also facilitates the

classification of abnormalities, since suppressing normal background structures enhances the contrast and obviousness of abnormal structures. In addition, the normal tissue characterization problem is fundamentally simpler and easier for computers to solve than is the tumor detection problem, because the properties of images of normal tissue are much simpler than the properties of images of abnormalities of various types, sizes, and stages of development. First we describe features of normal mammograms in Section 5.2. Then in Section 5.3, we present a new line detector that is capable of extracting linear mammographic features. The residual image generation algorithm is discussed in Section 5.4. Finally we present experimental results in Section 5.5.

5.2 Normal Mammograms

There is a surprising lack of a clear definition of the "normal" breast [1, 2]. Entirely normal mammograms may have very different appearance. Figure 5.1 shows four normal mammograms taken from the Digital Database for Screening Mammography (DDSM). These mammograms, from (a) to (d), have ACR breast tissue density ratings of 1 (fatty) to 4 (dense) [72]. The shadows in the mammograms that appear as diffuse amorphous clouds of density with indistinct borders are caused by glandular tissue in the breast. These cloud-like densities raise the local average brightness of the image. Those "linear or gently curved" markings are formed by connective tissue septi between fat lobules.

In general, two observations can be made of normal mammograms:

- Unequivocally normal areas have lower overall density than abnormal ones. This means no spikes indicating microcalcifications, and no large bright areas indicating masses.

- Normal areas have "quasi-parallel" linear markings, as shown in Figure 5.2(a) and sketched in Figure 5.2(c). These markings are the shadows of ducts and connective tissue elements, which upon inspection are not randomly oriented,

but rather tend to radiate from the nipple toward the chest wall. These normal regions are distinct from spiculated or stellate lesions, in which linear markings radiate locally in all directions [10, 11], as shown in Figure 5.2(b) and sketched in Figure 5.2(d).

5.3 Linear Structure Identification

5.3.1 Introduction

Line or linear structure detection is a very basic, yet important problem in image processing and computer vision. It is also often the preprocessing step in other applications such as feature extraction, pattern recognition, and image enhancement.

Since 1960s, the Hough transform [73, 74, 75] has been widely used for detecting lines in binary images. Suppose there is a line at a distance s and orientation θ, as shown in Figure 5.3 (a). It can be represented as

$$s = x\cos\theta + y\sin\theta \tag{5.4}$$

for constants s and θ. The Hough transform maps all the pixels on this line into one point in the (s, θ) parameter space, or Hough space, as shown in Figure 5.3 (b). Thus, each point in the Hough space represents a line. Let $C_{s,\theta}(x, y) = 1$ if (x, y) satisfies Equation 5.4, and $C_{s,\theta}(x, y) = 0$, otherwise. Define accumulator $A(s, \theta) = \sum_{(x,y)\in image} C_{s,\theta}(x, y)$, then if a straight line as represented in Equation 5.4 exists in the image, $A(s, \theta)$ will show a local maximum in the Hough space. In other words, a local maximum of $A(s, \theta)$ indicates that there may be a line segment in the image. The value of $A(s, \theta)$ represents the length of the straight line assuming that the line has no gap. A line that is more than one pixel wide will map to a set of local maximum of $A(s, \theta)$ with identical orientation θ and successively varying distances s [76]. The Hough transform is fairly robust to noisy or missing data [75] because noisy points are unlikely to contribute coherently to a single accumulator in the Hough space, while a few missing points will not affect the count in an accumulator much. The same idea can be easily extended to detect shapes other than straight lines,

such as ellipse [77, 78] and circular objects [79]. However, this usually increases the dimension of the parameter space that needs to be considered [80], which, in turn, increases storage and computational complexity. Let the number of parameters be p and each parameter be quantized to n values, then the number of accumulators in the Hough space is n^p, which can be prohibitively large when either p or n is large. Since higher parameter accuracy requires a finer quantization, or larger n, there usually is a trade-off between accuracy and computation time [81] in the Hough transform. Storage and/or computation efficient algorithms [82, 83, 84, 85], as well as parallel processing [86, 87] of Hough transforms have been proposed to tackle this complexity problem. Another drawback of the Hough transform is that it is not suitable for direct use in grayscale images. It requires some preprocessing steps, such as edge detection and thresholding, to make an input grayscale image a binary pattern before applying. Lo and Tsai [76] proposed a "Gray-scale Hough transform" that added the graylevel G as another parameter to remove the preprocessing requirements in the conventional Hough transform. In addition, the Hough transform does not provide the actual position of the line in the (x, y) plane [88]. It can be seen from Figure 5.3 that the Hough transform gives us only the angle of the line (θ) and its distance from the origin (s). This is not sufficient for many applications.

Lines are commonly viewed as extended or contiguous edges. Consequently, many line detection algorithms extract local edges first, then group them into more globally defined lines based on certain criteria. For example, Nevatia and Babu [89] used edge positions and orientations to link edge detection results; Basak, *et al* [90] proposed two connectionist models; Lee and Kweon [91] developed a six-step algorithm that consists of, after edge extraction, edge scanning, edge normalization, line-blob extraction, line-feature computation, and line linking; Zucker, *et al* [92] used a relaxation process; Kanazawa and Kanatani [93] used an asymptotic approximation to fit a line to an edge segment; Nelson [94] combined explicit linear and end-stop terms with edge information to produce an energy landscape in which local minima correspond to linear features; and Mansouri, *et al* [95] used a hypothesis prediction/verification

paradigm to detect lines of predefined length. However, local edge operators usually enhance the noise and tend to generate dense edge maps due to their small spatial extent, which makes subsequent processing difficult [96].

Earlier in the research [12], we designed a set of correlation filters as normal line detectors to find normal linear markings at 16 radial orientations in mammograms. Their impulse responses are as shown in Figure 5.4. The length and width of their spatial extent were tuned to respond to linear shadows, such as those in Figure 5.2 (a), but not to the much smaller shadows of microcalcifications. An angle image could be obtained by taking maximum of the 16 line detectors' output at each pixel location and then assigning its pixel value related to the corresponding orientation. Figure 5.5 (a) shows a pattern with lines and solid areas used to test the set of line detectors. Figure 5.5 (b) shows the resultant angle image, in which brightness corresponds to line orientation. Sample detector outputs at 0^o, 45^o, 90^o, and 135^o are shown in Figure 5.5 (c), (d), (e), and (f), respectively. Note that curved sectors of the large circle are appropriately read as "lines" because they are locally linear within the tolerance of the line detectors. However, normal linear markings vary from 0.1 to 1.0 mm in width. If its width does not match well with the width of the correlation filters, then the linear marking may not be extracted accurately. This can be seen in Figure 5.6, where (a) shows part of a mammogram with a circumscribed mass in the center. This original image is then highpass filtered to facilitate line detection and the enhanced image is shown in Figure 5.6 (b). A set of correlation line detectors with width 0.85 mm is applied to the enhanced image. Figure 5.6 (c) shows the detected linear structures. To see how well they match the actual linear markings in the enhanced image, we subtract Figure 5.6 (c) from Figure 5.6 (b) and show the result in Figure 5.6 (d). We see in Figure 5.6 (d) that the correlation filters missed thinner lines while did not fully extract thicker lines in the enhanced image.

Then we proposed a novel line or linear structure detection algorithm based on a new model for lines, which solved the above "miss match" problem. It is capable of extracting lines with very different width, lines with irregular width, as well as

curves. This is especially telling when Figure 5.6 and Figure 5.20 are compared. In Section 5.3.2, we describe this new line model in detail. In Section 5.3.3, we present the detection algorithm as well as some implementation issues. Experimental results and discussions are presented in Section 5.3.4.

5.3.2 Model For Lines

Lines are commonly considered as extended or contiguous edges while edges are usually defined as local discontinuity in image graylevels. Therefore, many line detectors are based on gradients, such as the compass operator [73] shown in Table 5.1. However, pixels in the middle of a "thick" line do not possess the properties that characterize an edge pixel. (Here, "thick" line refers to a line that has more than 2 pixels in width.) Figure 5.7 (a) shows a "thin" line of 1 pixel in width at the top and a "thick" line of 10 pixels in width at the bottom. Part of the "thick" line is enlarged and shown in Figure 5.7 (b). It is obvious that no edge operator would indicate that the shaded pixel in Figure 5.7 (b) is an edge pixel, even when it operates in a neighborhood as large as the boxed 9×9 window, which is larger than the spatial support of most edge operators. This is simply because this 9×9 window is actually an uniform region. It is therefore not surprising that line detectors based on edge extraction results do not respond well to thick lines. As an example, we apply the E-W compass gradient operator, as shown in Table 5.1 (a), to the image in Figure 5.7 (a). The result is shown in Figure 5.8. As expected, we see that only the edges of those lines are detected.

We propose that the basic characteristic of a line, regardless of its thickness, is that pixels on it have similar graylevels. In other words, if a pixel belongs to a line, then there exists a string of pixels along the direction of the line that contains this pixel and has similar graylevels. String will be used to refer to a single pixel wide line throughout this chapter. This is illustrated in Figure 5.9, where a line at 45^o is described. The boxed string of pixels along 45^o has the same graylevels as that of the shaded pixel, which makes the shaded pixel seen as part of the line. The same idea

applies to why we see lines at 0^o, 11.25^o, 22.5^o, and 33.75^o, respectively, in Figure 5.10 (a), (b), (c), and (d). Another necessary condition for a line to be perceived is that its surrounding region has different graylevels from those of the pixels on the line. In the extreme case of an uniform region, as shown in Figure 5.11 (a), there are strings of pixels with the same graylevels along any direction, while no line will be seen. Finally, the length of a line is greater than its width. For example, we do not call the bright region in Figure 5.11 (b) a line.

In summary, our line model is as follows:

1. There is a string of pixels with similar graylevels along a certain direction.
2. The surrounding pixels have different graylevels.
3. The length of a line is greater than its width.

5.3.3 Detection Algorithm

As described in Section 5.3.2, the basic characteristic of a line is that pixels on it have similar graylevels. A good measure of graylevel similarity among pixels is the standard deviation. Let (i, j) be the spatial location in the image at row i and column j; $f(i, j)$ be the pixel graylevel at (i, j); $L(\theta, l)$ be a string of pixels in direction θ and of length l; and $N_{L(\theta,l)}$ be the number of pixels within $L(\theta, l)$. Note that $N_{L(\theta,l)}$ is different from the length l. For example, a string in the direction 45^o has about $1/\sqrt{2}$ the number of pixels as a string in the direction 0^o of the same length, as shown in Figure 5.12. Then the standard deviation of pixel graylevels in $L(\theta, l)$ is

$$\sigma(\theta, l) = \sqrt{\frac{1}{N_{L(\theta,l)} - 1} \sum_{(m,n)\in L(\theta,l)} (f(m, n) - \bar{f}_{L(\theta,l)})^2}$$

where $(m, n) \in L(\theta, l)$ means that the string $L(\theta, l)$ passes through the pixel (m, n) and $\bar{f}_{L(\theta,l)}$ is the average graylevel of $L(\theta, l)$

$$\bar{f}_{L(\theta,l)} = \frac{1}{N_{L(\theta,l)}} \sum_{(m,n)\in L(\theta,l)} f(m, n)$$

Let $L_{i,j}(\theta, l) = L(\theta, l)$ such that $\sigma_{i,j}(\theta, l) = \min_{(i,j)\in L(\theta,l)} \sigma(\theta, l)$. If pixel (i, j) belongs to a line in the direction θ^* and of length greater than l, then $\sigma_{i,j}(\theta^*, l)$ is small. In the case of an ideal line where all pixels on it have the same graylevels, $\sigma_{i,j}(\theta^*, l) = 0$. Also note that l is not the length of the line, but the *minimum* length. It can also be interpreted as the maximum width of the line, as we will explain later in this Section.

On the other hand, finding a small $\sigma_{i,j}(\theta^*, l)$ does not lead to the conclusion that (i, j) belongs to a line. As illustrated in Figure 5.11 (a), (i, j) may lies in an uniform region instead. However, if (i, j) is in an uniform region, then $\sigma_{i,j}(\theta, l)$ is small for all θ. Figure 5.13 (b), (c), and (d) compares the relationship between $\sigma_{i,j}(\theta, l)$ and θ for pixels on the thin line, in the background, and on the thick line, respectively, using the image shown in Figure 5.7 (a) and repeated here in Figure 5.13 (a). If we take the standard deviation of $\sigma_{i,j}(\theta, l)$ with regard to θ and denote

$$\sigma^2_{\sigma,(i,j)}(l) = \int_0^{2\pi} \{(\sigma_{i,j}(\theta, l) - \bar{\sigma}_{i,j}(l))^2 \frac{1}{2\pi}\} \partial\theta \tag{5.5}$$

where

$$\bar{\sigma}_{i,j}(l) = \int_0^{2\pi} \{\sigma_{i,j}(\theta, l) \frac{1}{2\pi}\} \partial\theta \tag{5.6}$$

Then $\sigma_{\sigma,(i,j)}(l)$ is small for the case that (i, j) lies in an uniform region. For the ideal uniform region, $\sigma_{\sigma,(i,j)}(l) = 0$ as shown in Figure 5.13 (c).

l is taken to be 15 in the above comparison. As mentioned earlier, l is actually the maximum width of the lines we want to detect. Note that the black uniform regions in Figure 5.13 (a) can also be seen as very thick lines. Because we set $l = 15$, which is smaller than the widths of the "black thick lines", $\sigma_{\sigma,(i,j)}(\theta, l) = 0$ for all θ and consequently $\sigma_{\sigma,(i,j)}(l) = 0$ for (i, j) in the black regions. Remember that the thick white line at the bottom is 10 pixel in width, so if we set $l < 10$, we would have $\sigma_{\sigma,(i,j)}(l) = 0$ for (i, j) on this line as well. Therefore, small $\sigma_{\sigma,(i,j)}(l)$ indicates an uniform region only when the lines we want to detect have widths smaller than l. This complies with the third characteristic in our line model that the length of a line is larger than its width.

Based on the above analysis, our line detector can be summarized in the block diagram shown in Figure 5.14. Since the only restriction is the maximum line width, this line detector is capable of detecting

- lines of very different width, from single pixel wide up to l
- lines of any length that is longer than l
- lines with varying width, provided that the changes are slower than l
- curves, provided that over short segment, they can be approximated as lines of length greater than l

Experimental results in Section 5.3.4 will demonstrate these capabilities.

In the actual implementation, it is not necessary to find at every pixel location (i, j) all $L(\theta, l)$ that passes through this pixel and its corresponding $\sigma(\theta, l)$ in order to obtain $\sigma_{i,j}(\theta, l)$. This would be computational intensive. As illustrated in Figure 5.15, for any given θ and l, there are $N_{L(\theta,l)}$ number of strings passing through each pixel. Instead, taking advantage of the fact that many $L(\theta, l)$ are the same for neighboring pixels, we only need to consider one of the $L(\theta, l)$s for each pixel (i, j), such as the one that starts at (i, j). The steps to obtain $\sigma_{i,j}(\theta, l)$ can be implemented as follows:

1. Initiate $\sigma_{i,j}(\theta, l)$ to a large value for every pixel (i, j) in the image.
2. For each pixel (i, j), obtain $\sigma(\theta, l)$ for the string $L(\theta, l)$ that starts at (i, j).
3. Compare this $\sigma(\theta, l)$ to every $\sigma_{m,n}(\theta, l)$, for $\forall(m, n) \in L(\theta, l)$.
4. Replace $\sigma_{m,n}(\theta, l)$ with $\sigma(\theta, l)$ if the latter is smaller.

It is not realistic to obtain $\sigma_{\sigma,(i,j)}(l)$ based on all $\theta \in [0, 2\pi)$ using Equation 5.5. Fortunately, due to the spatial redundancy in images, we can obtain a good estimation of $\sigma_{\sigma,(i,j)}(l)$ using a number of equally spaced θs. Denote this number to be N_θ and the set of θs as $\boldsymbol{\theta} = (\theta_1, \ldots, \theta_{N_\theta})$. Then Equation 5.5 becomes

$$\sigma^2_{\sigma,(i,j)}(l) = \frac{1}{N_\theta - 1} \sum_{\theta \in \boldsymbol{\theta}} (\sigma_{i,j}(\theta, l) - \bar{\sigma}_{i,j}(l))^2 \tag{5.7}$$

and Equation 5.6 becomes

$$\bar{\sigma}_{i,j}(l) = \frac{1}{N_\theta} \sum_{\theta \in \boldsymbol{\theta}} \sigma_{i,j}(\theta, l) \tag{5.8}$$

To make a binary decision as to whether or not a pixel (i, j) belongs to a line, we need to threshold $\sigma_{i,j}(l)$ and $\sigma_{\sigma,(i,j)}(l)$. First define

$$D(i,j) = \begin{cases} 1 & \text{if } (i,j) \text{ belongs to a line} \\ 0 & \text{otherwise} \end{cases}$$

Then given thresholds T_σ and T_{σ_σ},

$$D(i,j) = \begin{cases} 1 & \text{if } \sigma_{i,j}(l) < T_\sigma \text{ and } \sigma_{\sigma,(i,j)}(l) > T_{\sigma_\sigma} \\ 0 & \text{otherwise} \end{cases}$$

T_σ and T_{σ_σ} are related to the image noise level. In the ideal case, $T_\sigma = 0$ and $T_{\sigma_\sigma} = 0$. As the image gets noisier, both thresholds should be set larger.

5.3.4 Experimental Results and Discussions

We have shown in Figure 5.8 that gradient based line detector failed to extract thick lines. Our proposed line detector, on the other hand, gives a perfect detection in the same image, including both the "thin" line and the "thick" line. The result is shown in Figure 5.16.

Furthermore, uncorrelated Gaussian noise with mean the same as that of the lines is introduced in the background of the image in Figure 5.7 (a). This noisy image is shown in Figure 5.17 (a). Detection results of the gradient operator and the proposed line detector are shown in Figure 5.17 (b) and (c), respectively. We can see that the gradient based detector totally missed the lines, while the proposed line detector correctly identified both.

Figure 5.18 illustrates the idea that l is the maximum width of the lines we will detect. The input image is shown in (a), where the top line is 1 pixel wide, the second one is 3 pixel wide, and so on. Each line is 2 pixel wider than the one directly above it. Detection results using $l = 5$, $l = 10$, and $l = 20$ are shown in (b), (c), and (d),

respectively. In all cases, lines with width narrower than the l applied are detected. While those wider lines are considered as uniform regions.

There are many linear structures in digital mammograms, which are shadows of normal ducts and connective tissue elements. They usually appear slightly curved, but over short segments, are approximately linear and have varying thicknesses ranging from 0.1 to 1.0 mm in width. These linear structures may have low contrast in a very noisy background. This can be seen in Figure 5.19 (a), which shows part of a normal mammogram, and Figure 5.20 (a), which has a circumscribed mass in the center. To facilitate line detection, we first lowpass filter the original image, then subtract the result from the original. This is equivalent to a highpass filtering. The enhance images are shown in Figure 5.19 (b) and Figure 5.20 (b), respectively. Line detector with $l = 20$ is then used on the enhanced images. The detected linear structures are shown in Figure 5.19 (c) and Figure 5.20 (c), respectively. We then subtract the detected linear structures from the corresponding enhanced images to see how well our line detector has done. Figure 5.19 (d) and Figure 5.20 (d) demonstrate that the linear structures are accurately identified and removed from the enhanced mammograms. Also note that the circumscribed mass becomes more conspicuous after the linear structure removal.

In summary, the line detection technique we propose based on the new line model, as described in Section 5.3.2, is demonstrated using some test patterns and digital mammograms to be able to detect lines of very different width, lines of varying width, as well as curves.

5.4 Residual Images Generation

We propose to characterize normal mammograms by identifying and removing normal tissue structures shown in mammograms. We shall refer to the mammogram that results from the removal of normal structures as the *residual image*. Accordingly, the residual image of a normal mammogram would be uniformly dark and

featureless; whereas the residual image of an abnormal mammogram would show microcalcifications or masses against a featureless background. Following this rationale, we have implemented a normal tissue identification and removal algorithm as shown in Figure 5.21. The normal mammogram shown in Figure 5.1 (a) is used as a test image to demonstrate how this algorithm works. The major steps of normal tissue characterization are as follows:

1. Smooth the original mammogram I_0 and obtain a smoothed image I_s.

2. Subtract I_s from I_0 to remove background density and enhance contrast of normal structures. The result is denoted as I_1. This procedure is illustrated in Figure 5.22, where it can be seen that background densities are largely removed, and normal linear markings are enhanced in I_1.

3. Apply to I_1 the line detector described in Section 5.3 to identify normal linear structures in the mammogram. The resultant linear markings, or the normal line mask, is denoted as I_m.

4. Remove normal linear markings I_m from I_1 to create a "residual" or "background" image. As shown in Figure 5.23 for the test mammogram, we set to zeros (black) all pixels in the I_1 image that correspond to non-zero values in the normal line mask. Thus obtained residual image has its normal background structures removed and appears featureless.

For abnormal mammogram regions, residual images will consist of only pathology (masses and microcalcifications) on a featureless background. More experimental results are shown in Section 5.5.

5.5 Experimental Results

We tested the proposed normal mammogram characterization algorithm on the "Digital Database for Screening Mammography" (DDSM) [72]. The DDSM project is a collaborative effort involving Massachusetts General Hospital, the University

of South Florida, and Sandia National Laboratories. The primary purpose of the database is to facilitate sound research in the development of computer algorithms to aid in screening. At present time, this database contains more than 1600 cases with each case consisting of 4 images (left and right MLO and CC views) along with patient information and image parameters. Images containing suspicious areas have associated pixel-level "ground truth" information about the locations and types of suspicious regions. The images are digitized at resolutions of $42 - 100\mu$. It is expected that the DDSM project will add more cases to the database in the coming years.

In Section 5.4 we demonstrated our normal structure identification and removal algorithm using a normal mammogram as the test image. In obtaining the I_1 image, we used $W_s = 0.95$, $K = 0$, and $G = 10$. For extracting linear structures, we used $l = 20$, $T_\sigma = 30$, and $T_{\sigma_\sigma} = 4$. These parameters were determined experimentally using a variety of sample mammography images and are used for all the following studies as well.

Figure 5.24 shows results for a mammogram containing circumscribed masses, where (a) shows the original mammogram with the masses outlined, (b) shows the background subtracted I_1 image, (c) shows the normal linear markings I_m, and (d) shows the residual image I_R with its normal structures removed. To see details better, these results are repeated in Figure 5.25 for the region centered at the masses. Note that in Figure 5.24 (d) and Figure 5.25 (d) the masses can still be seen but the background structures have been removed.

Figure 5.26 shows results for a mammogram containing a spiculated lesion, where (a) shows the original mammogram with the lesion outlined, (b) shows the background subtracted I_1 image, (c) shows the normal linear markings I_m, and (d) shows the residual image I_R with its "normal" structures removed. In this case, however, the spiculations of the lesion are detected as linear markings and shown in I_m. Consequently, the residual image I_R loses the spiculations. This problem can be dealt

with by detecting stellate patterns in the "normal" mask before removal using features described in Chapter 4 so that spiculations remain in the residual image. To see details better, these results are repeated in Figure 5.27 for the region centered at the spiculated lesion.

Figure 5.28 shows results for a mammogram containing microcalcifications, where (a) shows the original mammogram with the microcalcifications outlined, (b) shows the background subtracted I_1 image, (c) shows the normal linear markings I_m, and (d) shows the residual image I_R with its normal structures removed. Again, results are repeated in Figure 5.29 for the region centered at the microcalcifications. Note that in Figure 5.28 (d) and Figure 5.29 (d) the microcalcifications can clearly be seen in the residual image and in fact have been enhanced.

We compared microcalcification enhancement results of the residual images with those using the technique developed by Strickland and Hahn [23]. Their method is based on wavelet transforms. First, an undecimated wavelet transform is applied to the original mammogram. Then candidate calcification pixels are detected by thresholding the detailed signals at several levels of decomposition and combining the results. Detected pixel sites are dilated and then weighted before computing the inverse wavelet transform. The output is a microcalcification enhanced image, where straightforward thresholding can be applied to segment the microcalcifications. Figure 5.30 shows two mammograms with microcalcifications. Figure 5.31 shows the corresponding enhanced images using the technique by Strickland and Hahn. Figure 5.32 shows the corresponding residual images. Since the residual images do not have the fairly complex linear markings produced by normal ducts and connective tissue elements, any potential abnormal structures remained in the mammograms are more conspicuous.

More experimental results for normal mammograms are shown from Figure 5.33 to Figure 5.40, results for mammograms containing circumscribed lesions are shown from Figure 5.41 to Figure 5.48, results for mammograms containing spiculated lesions

are shown from Figure 5.49 to Figure 5.56, and results for mammograms containing microcalcifications are shown from Figure 5.57 to Figure 5.64.

In summary, we proposed a normal mammogram characterization algorithm that specifically identifies and removes normal tissue structures shown in mammograms. This is fundamentally different than other approaches that identify normal mammograms by screening out a specific type of tumor. On the contrary, our technique is independent of the types of abnormalities that may exist in the mammogram. Experimental results have shown that suppressing normal background structures enhances the contrast and obviousness of abnormal structures. We feel that the "de-cluttered" residual images could help radiologists to make a better decision regarding the normality of the mammograms.

Table 5.1 Compass line detection operators.

$$\begin{bmatrix} -1 & -1 & -1 \\ 2 & 2 & 2 \\ -1 & -1 & -1 \end{bmatrix} \quad \begin{bmatrix} -1 & -1 & 2 \\ -1 & 2 & -1 \\ 2 & -1 & -1 \end{bmatrix} \quad \begin{bmatrix} -1 & 2 & -1 \\ -1 & 2 & -1 \\ -1 & 2 & -1 \end{bmatrix} \quad \begin{bmatrix} 2 & -1 & -1 \\ -1 & 2 & -1 \\ -1 & -1 & 2 \end{bmatrix}$$

(a) E-W (b) NE-SW (c) N-S (d) NW-SE

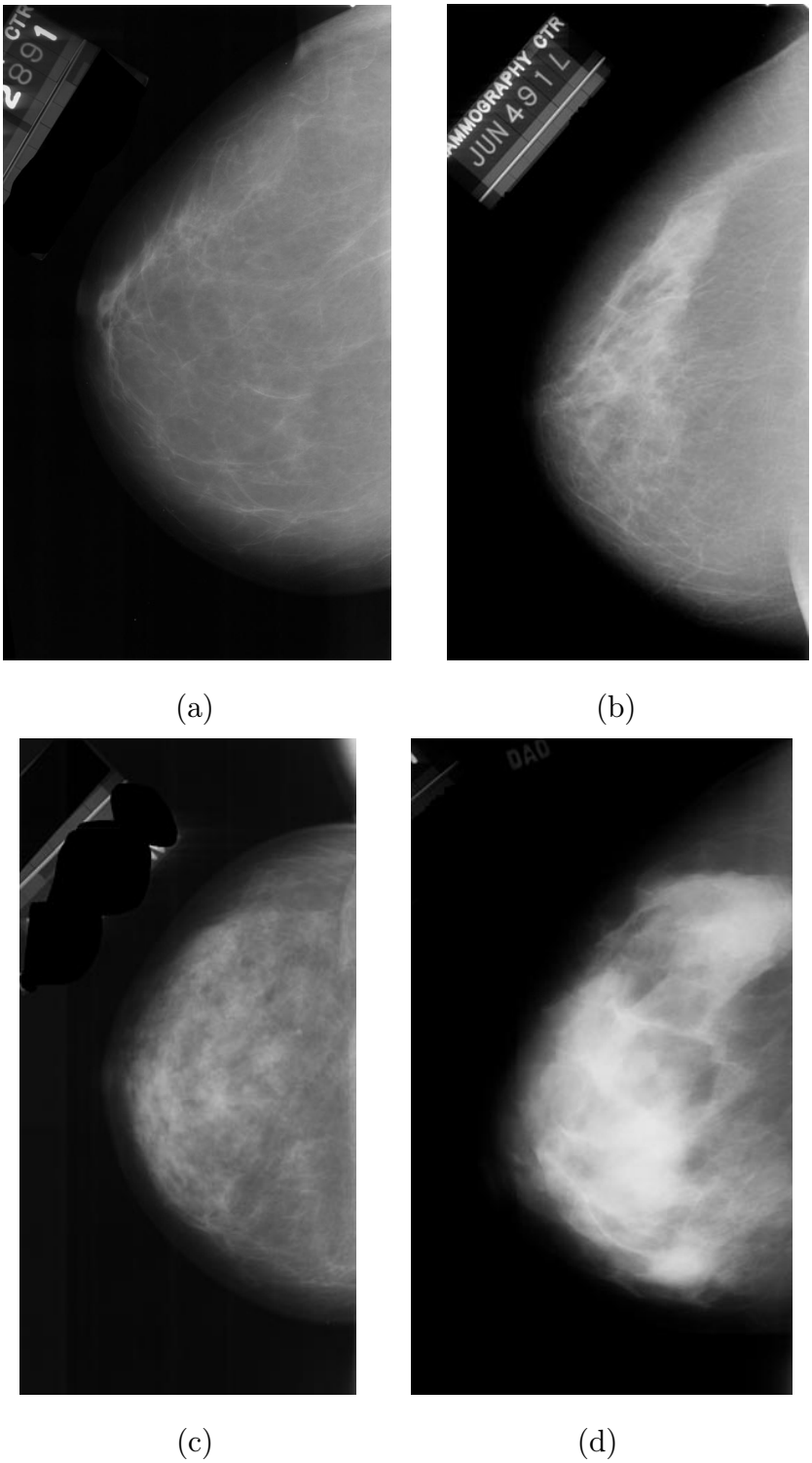

(a) (b)

(c) (d)

Fig. 5.1. Entirely normal mammograms may have very different appearance. These normal mammograms have ACR breast tissue density ratings of: (a) 1. (b) 2. (c) 3. (d) 4.

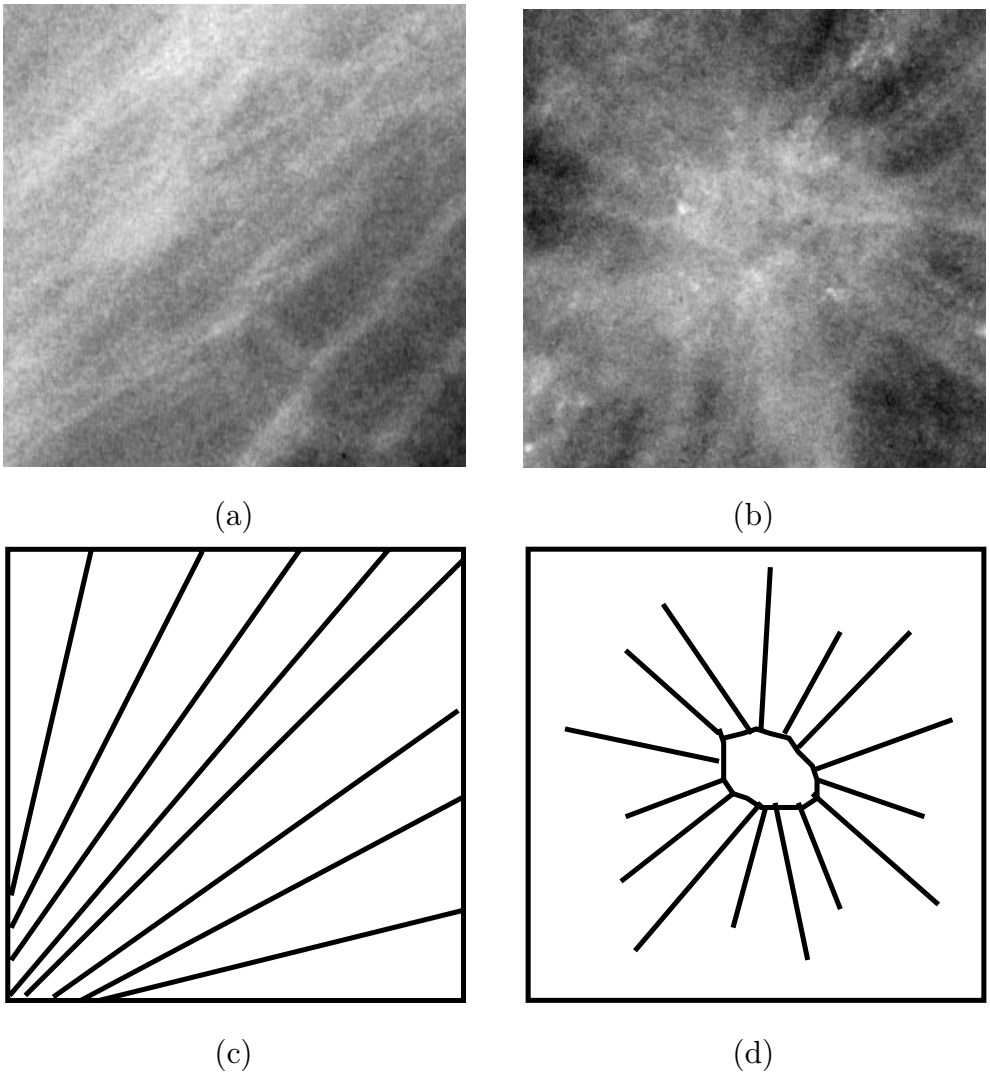

Fig. 5.2. (a) A normal region of a mammogram. (b) A spiculated lesion region of a mammogram. (c) Normal structures appear as quasi-parallel linear markings. (d) A spiculated lesion has linear markings that radiate in all directions.

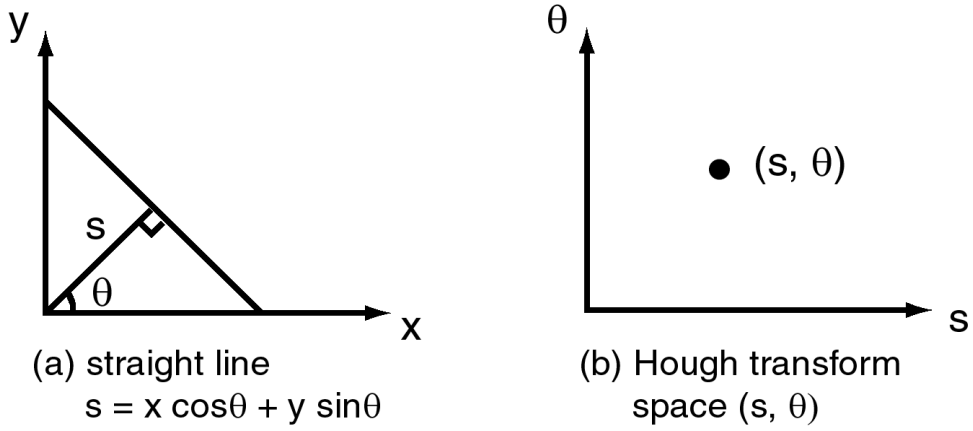

Fig. 5.3. (a) A straight line at a distance s and orientation θ. (b) Hough transform maps all the pixels on this line into one point in the (s, θ) parameter space, or Hough space.

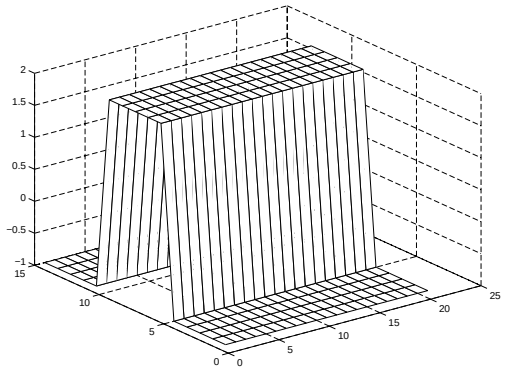

Fig. 5.4. Filter impulse response of correlation line detectors

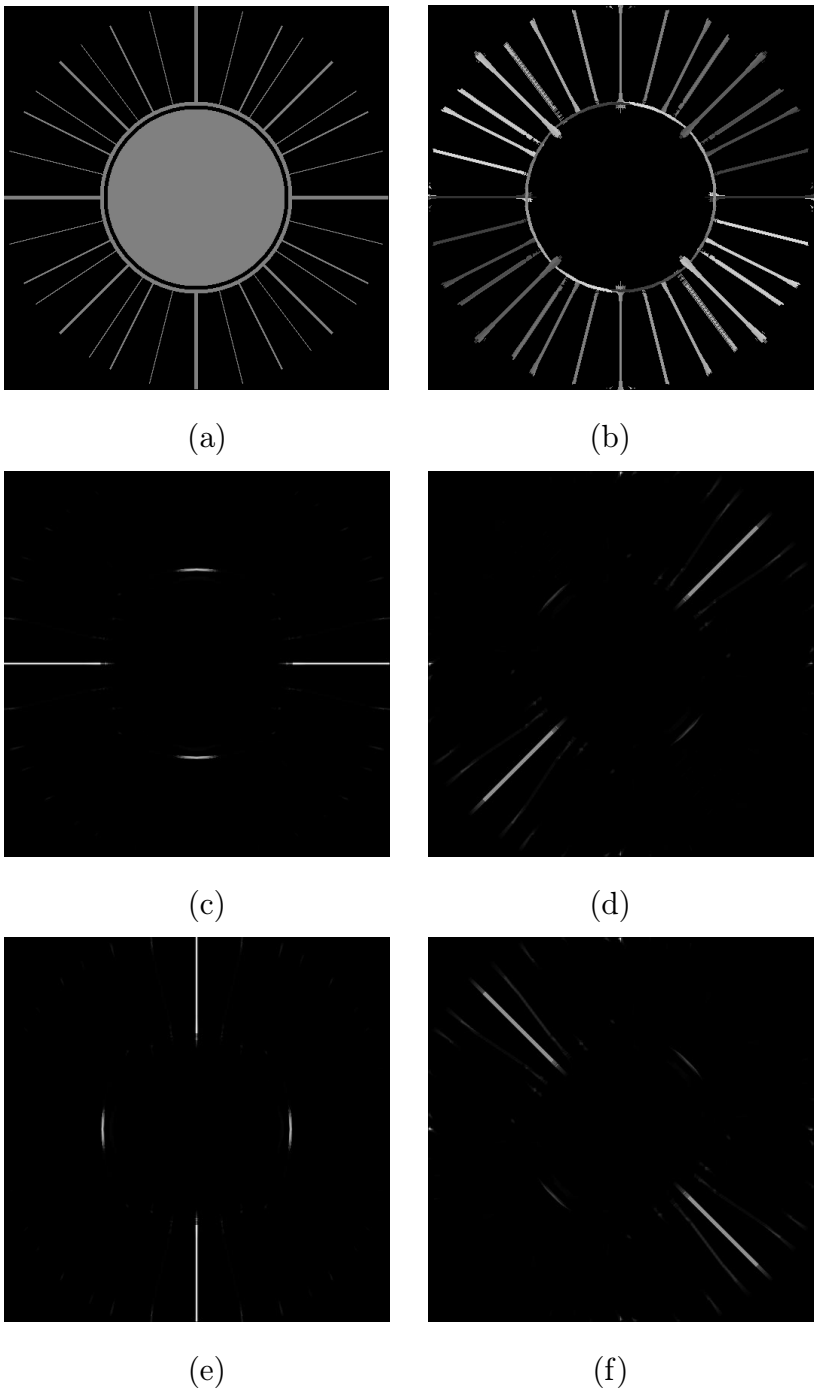

(a) (b)

(c) (d)

(e) (f)

Fig. 5.5. (a) Test pattern with lines and solid areas. (b) Line angle image including "lines" without solid features, in which brightness corresponding to line orientation. (c) Individual line detector output at 0^o. (d) 45^o. (e) 90^o. (f) 135^o.

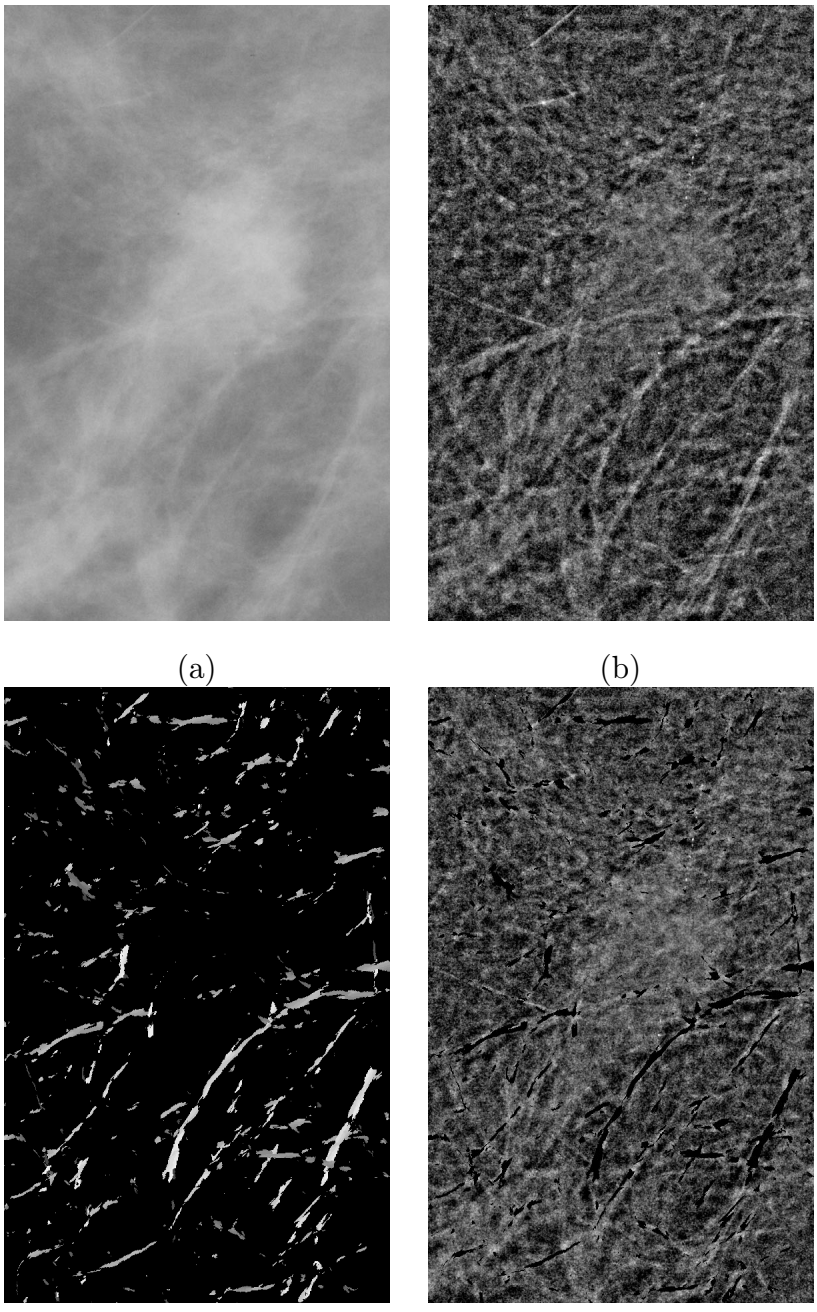

(a) (b)

(c) (d)

Fig. 5.6. A linear marking may not be extracted accurately if its width does not match well with the width of the correlation filters. (a) Original mammogram containing circumscribed mass. (b) Highpass filtered enhanced image. (c) Linear structures detected from the enhanced image using correlation filters with width 0.85 mm. (d) Removed detected linear structures from the enhanced image.

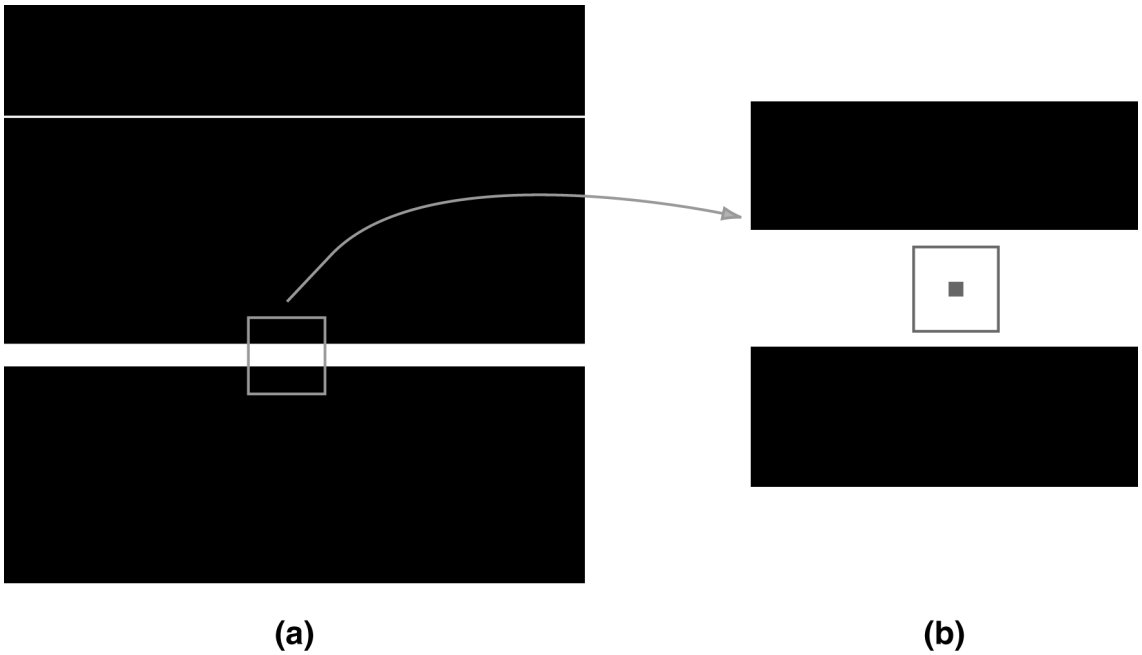

Fig. 5.7. Pixels belonging to a line are not necessarily edge pixels. (a) An image with a 1 pixel wide "thin" line at the top and a 10 pixel wide "thick" line at the bottom. (b) The shaded pixel in the middle of the "thick" line looks unlike an edge pixel within a 9×9 neighborhood, which is larger than the spatial support of most edge operators.

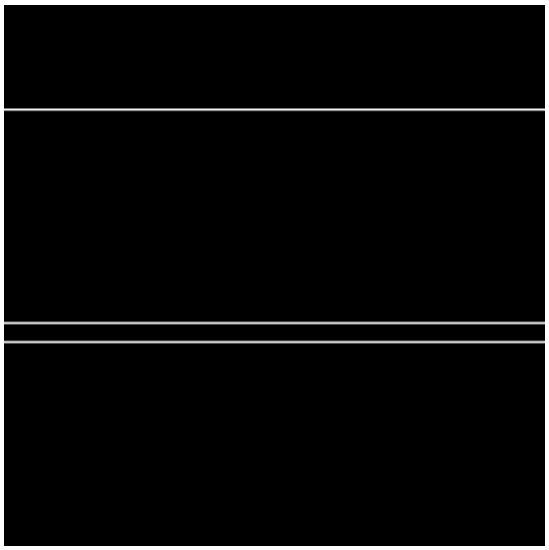

Fig. 5.8. The E-W compass gradient operator detects only edges of the lines in the image shown in Figure 5.7 (a).

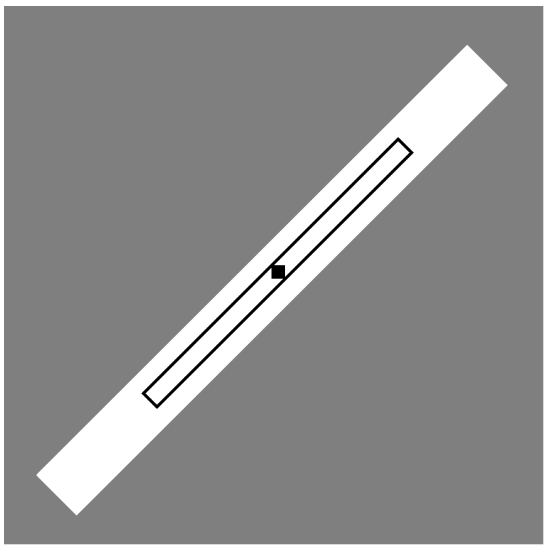

Fig. 5.9. If a pixel belongs to a line, then there exists a string of pixels with similar graylevels along the direction of the line that contains this pixel.

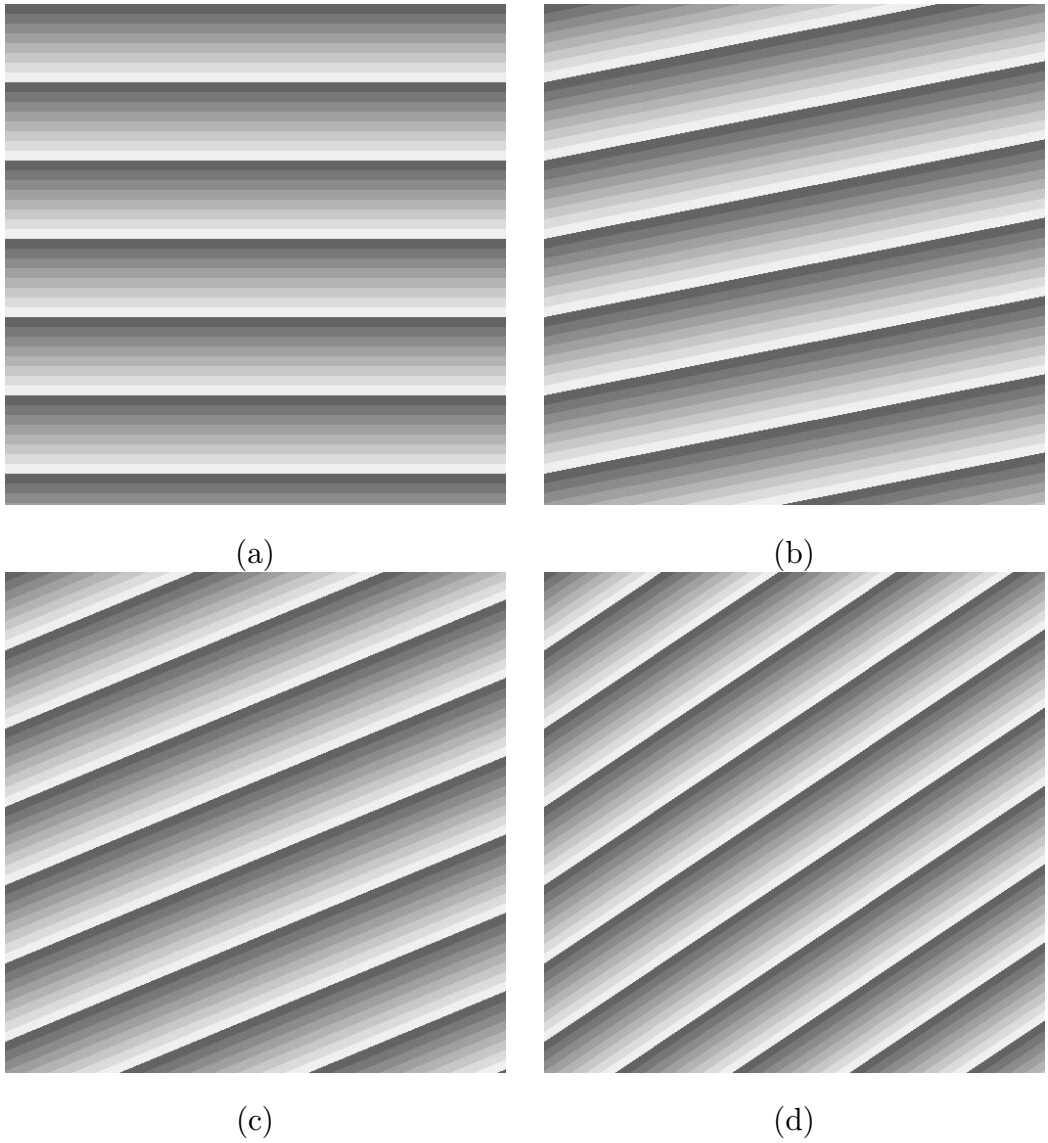

Fig. 5.10. Lines are perceived at orientations (a) 0^o. (b) 11.25^o. (c) 22.5^o. and (d) 33.75^o.

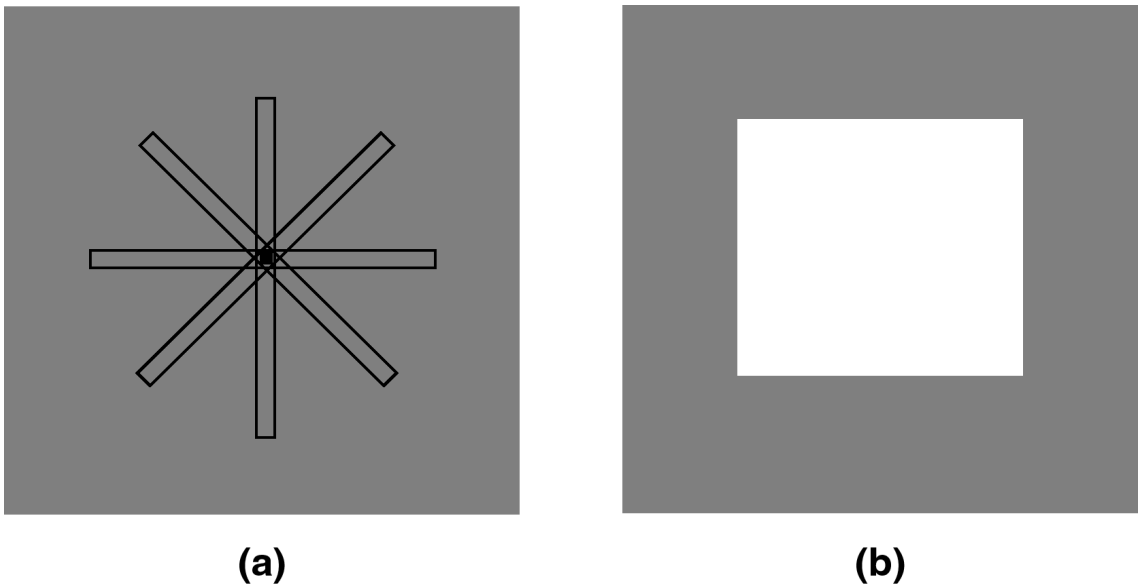

Fig. 5.11. Necessary conditions for a line to be perceived in an image. (a) Its surrounding region has different graylevels from those of the pixels on the line. (b) Its length is larger than its width.

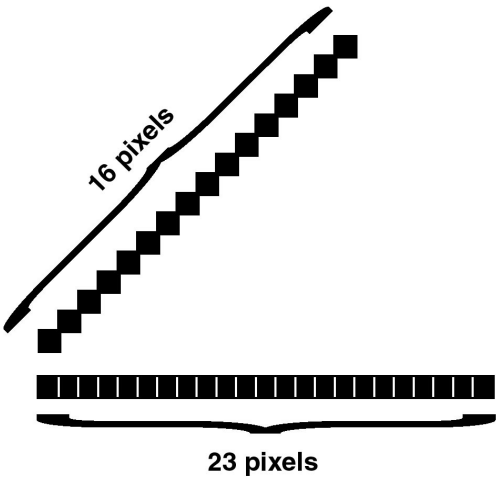

Fig. 5.12. Two strings of the same length contain different number of pixels.

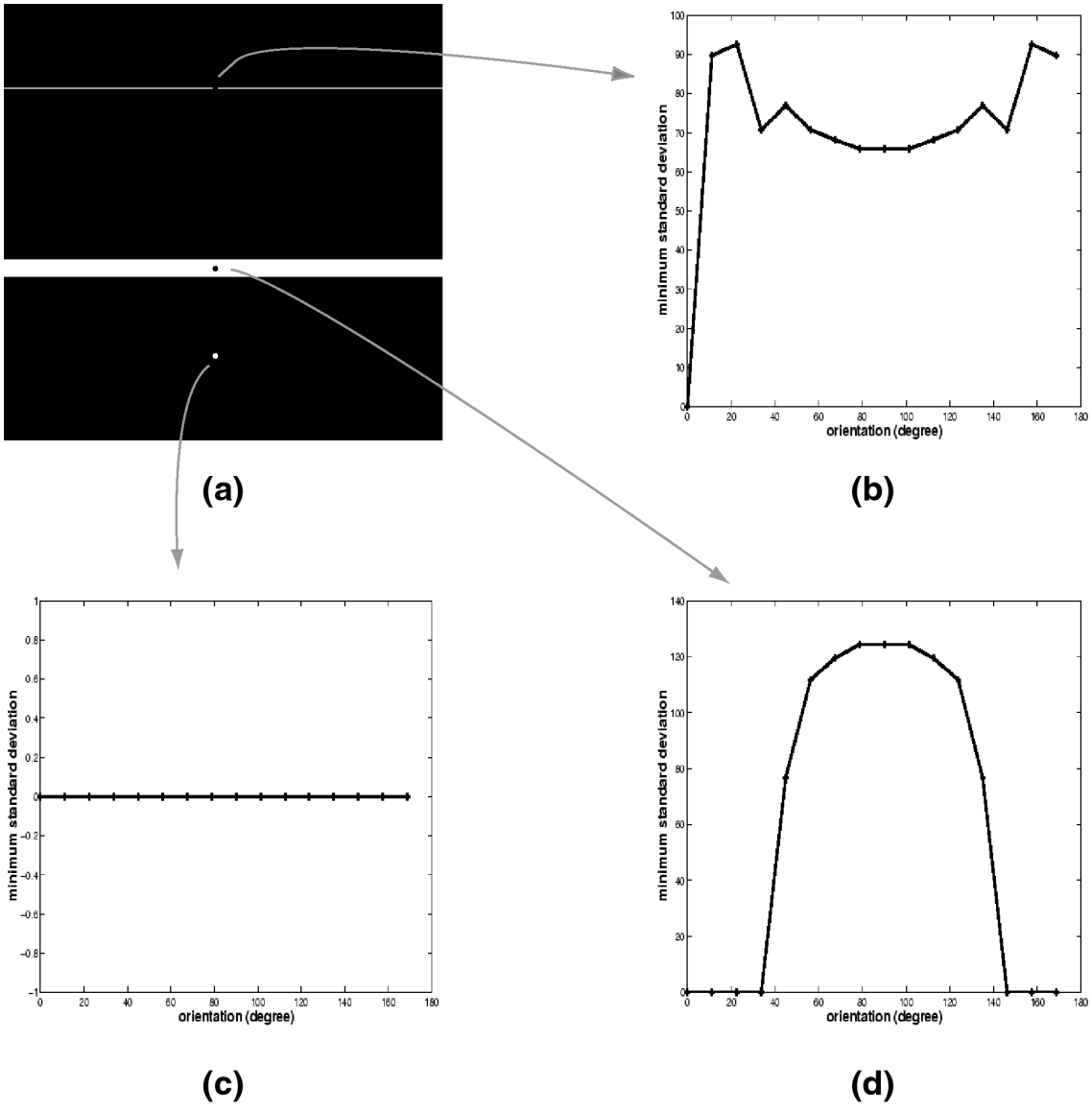

Fig. 5.13. Relationship between $\sigma_{i,j}(\theta, l)$ and θ. (a) Repeat the image shown in Figure 5.7 (a). (b) For a pixel on the thin line. (c) For a pixel in the uniform region. (d) For a pixel on the thick line.

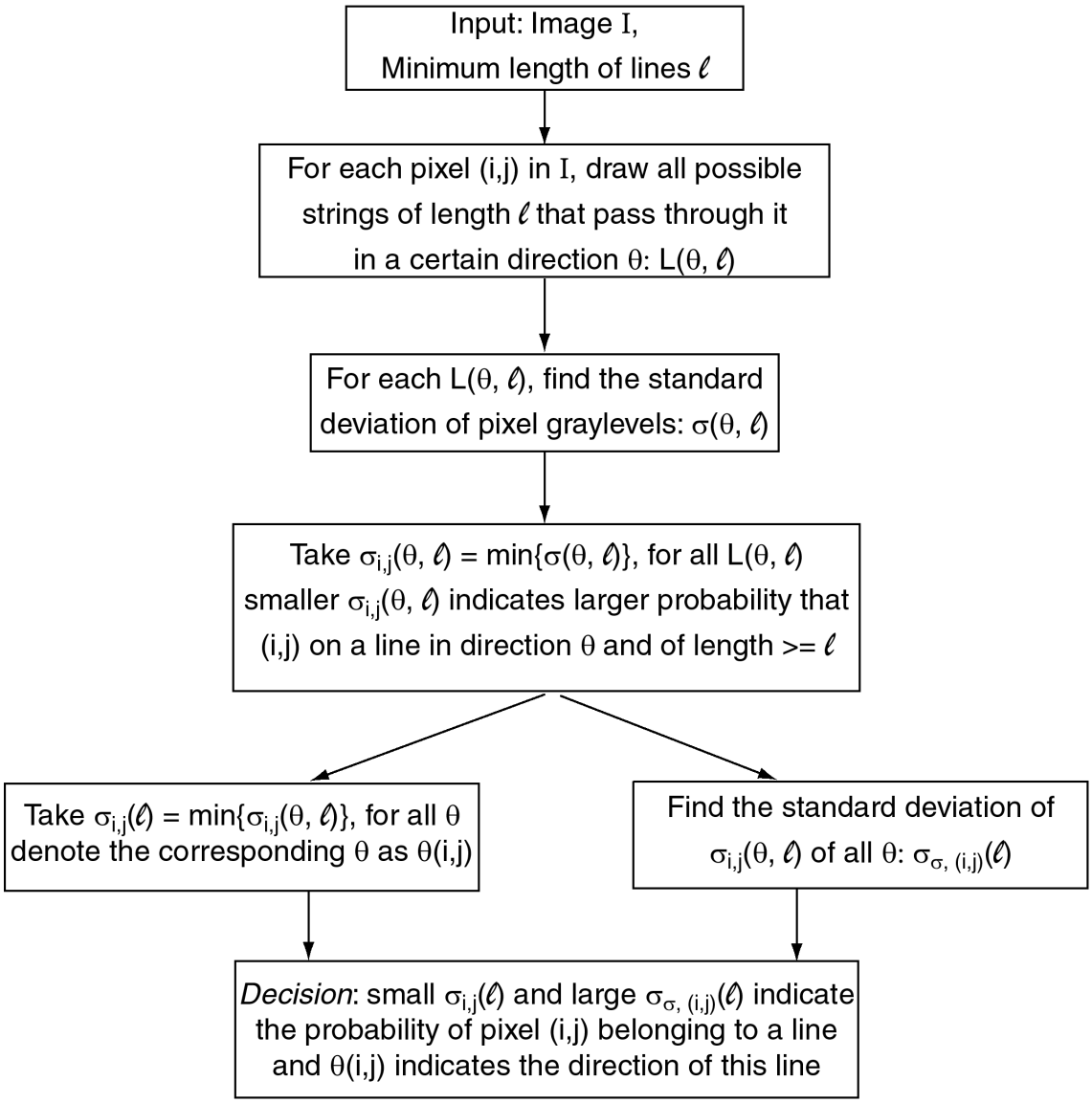

Fig. 5.14. Block diagram of our line detector.

Fig. 5.15. There are $N_{L(\theta,l)}$ number of strings passing through each pixel for given θ and l.

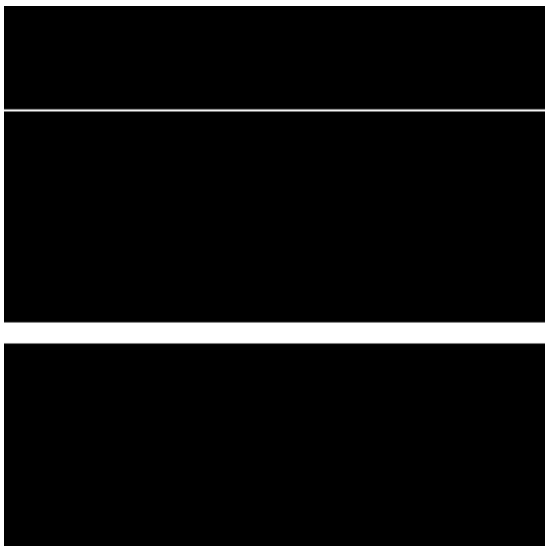

Fig. 5.16. The proposed line detector detects both the “thin” line and the “thick line” in the image shown in Figure 5.7 (a).

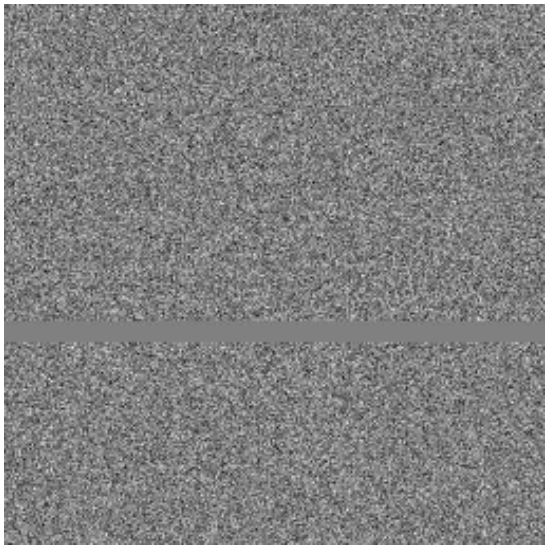

(a)

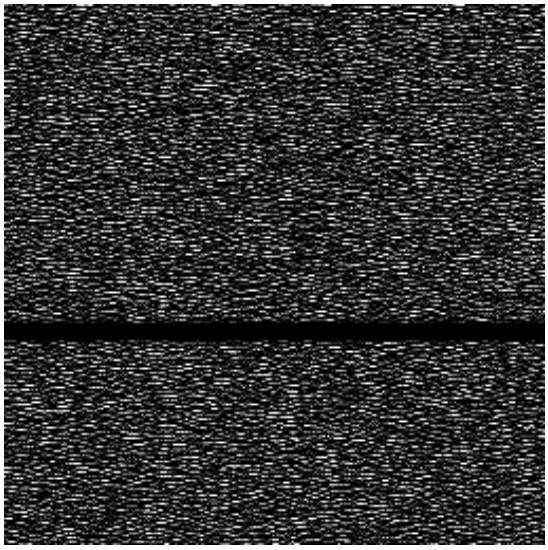

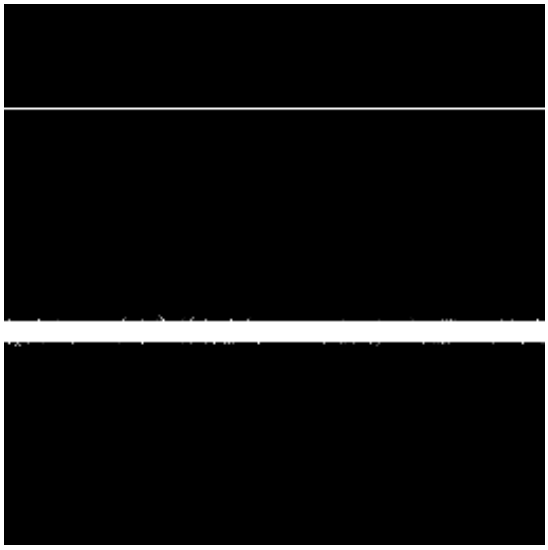

(b) (c)

Fig. 5.17. (a) White Gaussian noise with mean the same as that of the lines is introduced to the background of the image in Figure 5.7 (a). (b) The E-W compass gradient operator failed to detect the lines. (c) Our proposed line detector correctly identified both lines.

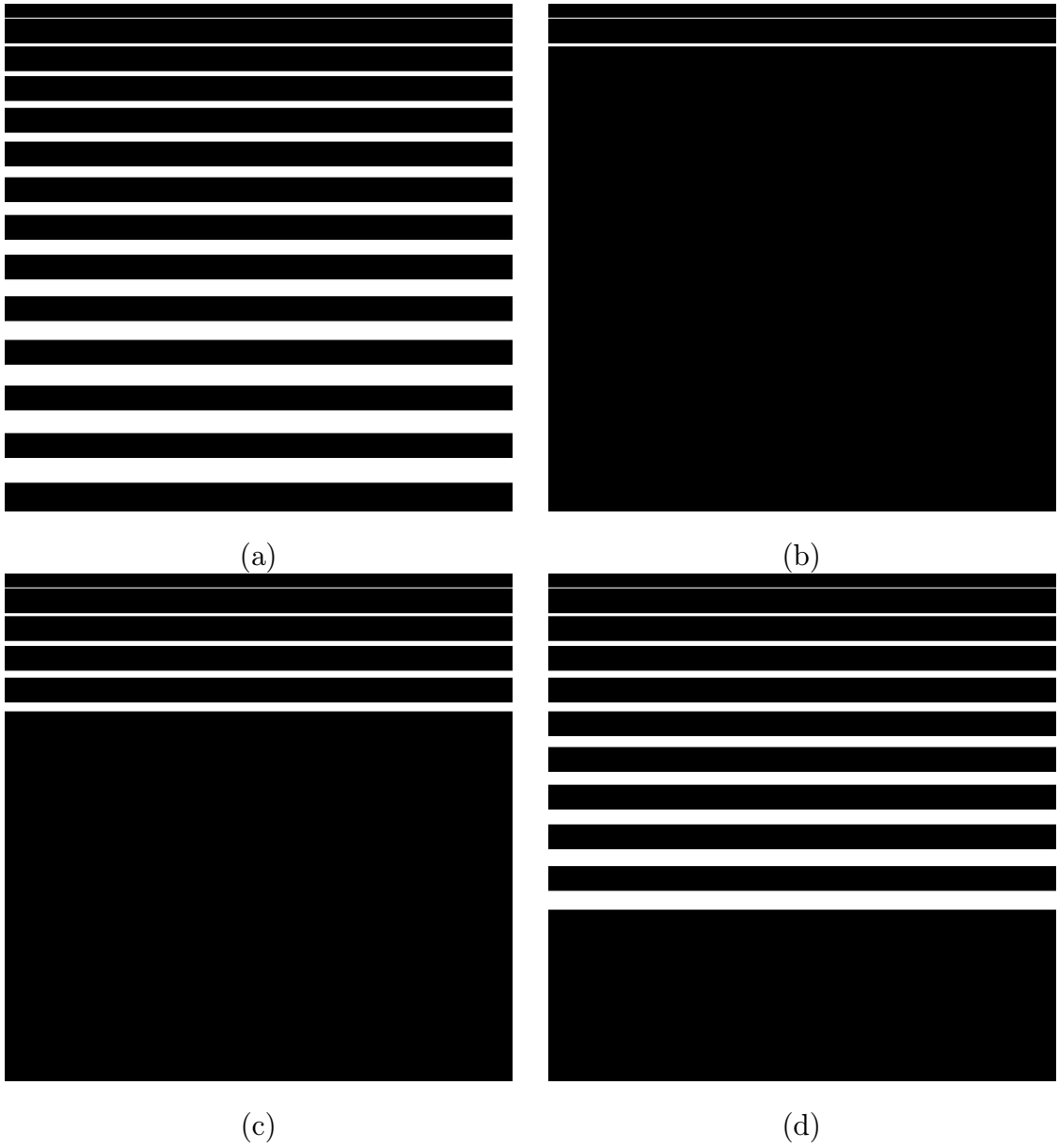

Fig. 5.18. Lines with width narrower than the l applied are detected, While those wider lines are considered as uniform regions. (a) Input image with the top line 1 pixel wide and each subsequent line is 2 pixel wider than the one directly above it. (b) Direction result using $l = 5$. (c) Direction result using $l = 10$. and (d) Direction result using $l = 20$.

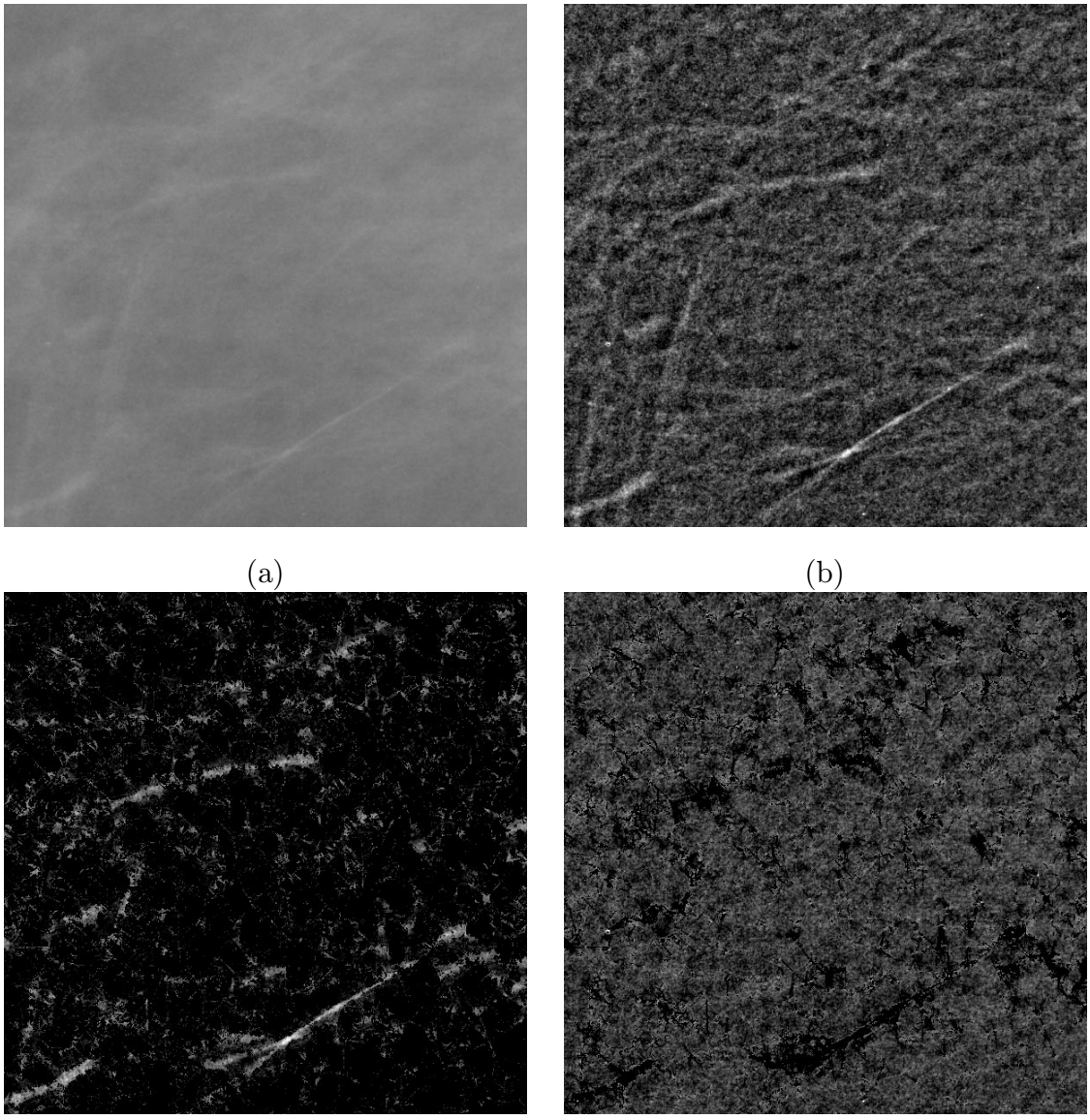

(a) (b)

(c) (d)

Fig. 5.19. (a) Original normal mammogram. (b) Highpass filtered enhanced image. (c) Linear structures detected from the enhanced image. (d) Removed detected linear structures from the enhanced image.

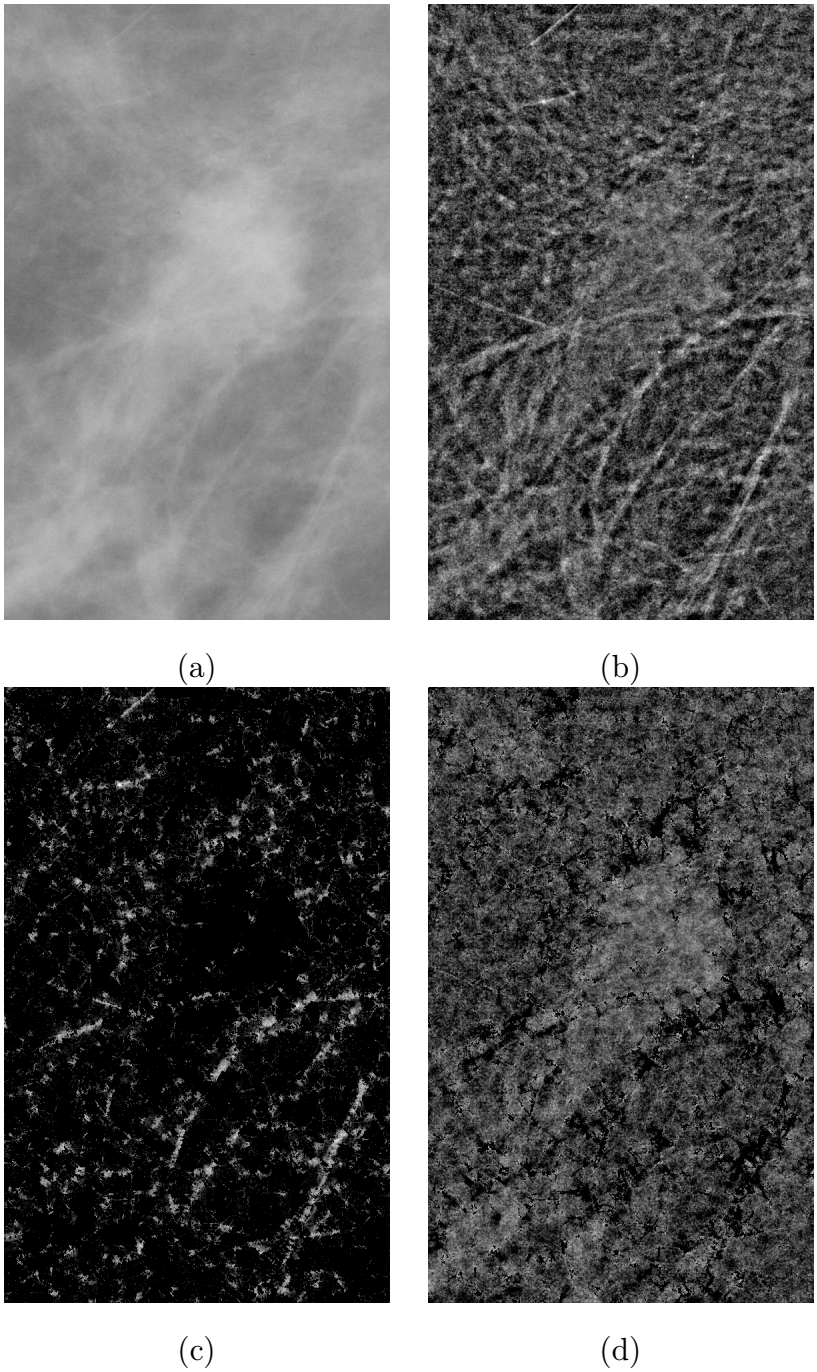

(a) (b)

(c) (d)

Fig. 5.20. (a) Original mammogram containing circumscribed mass. (b) Highpass filtered enhanced image. (c) Linear structures detected from the enhanced image. (d) Removed detected linear structures from the enhanced image and the mass becomes more conspicuous.

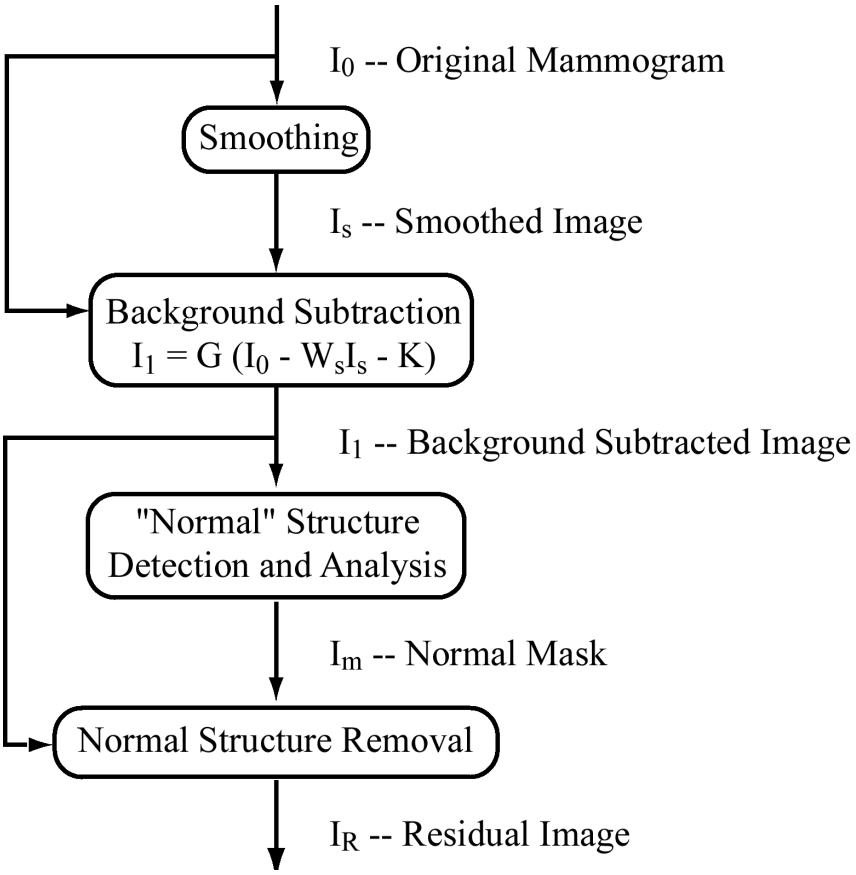

Fig. 5.21. Block diagram of normal tissue identification and removal algorithm, where W_s = weighting factor; K = constant offset factor; G = gain.

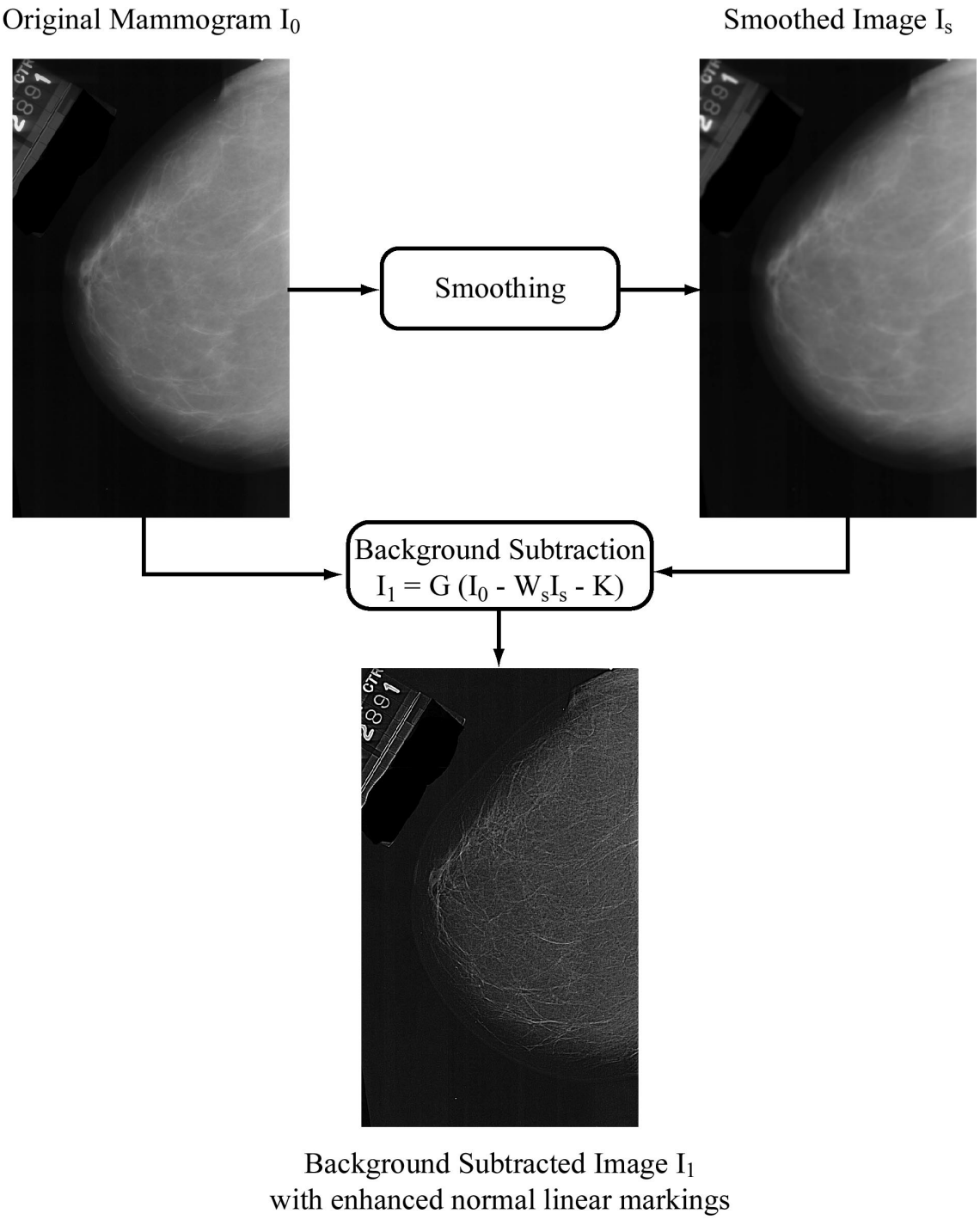

Fig. 5.22. Smoothing and background subtraction.

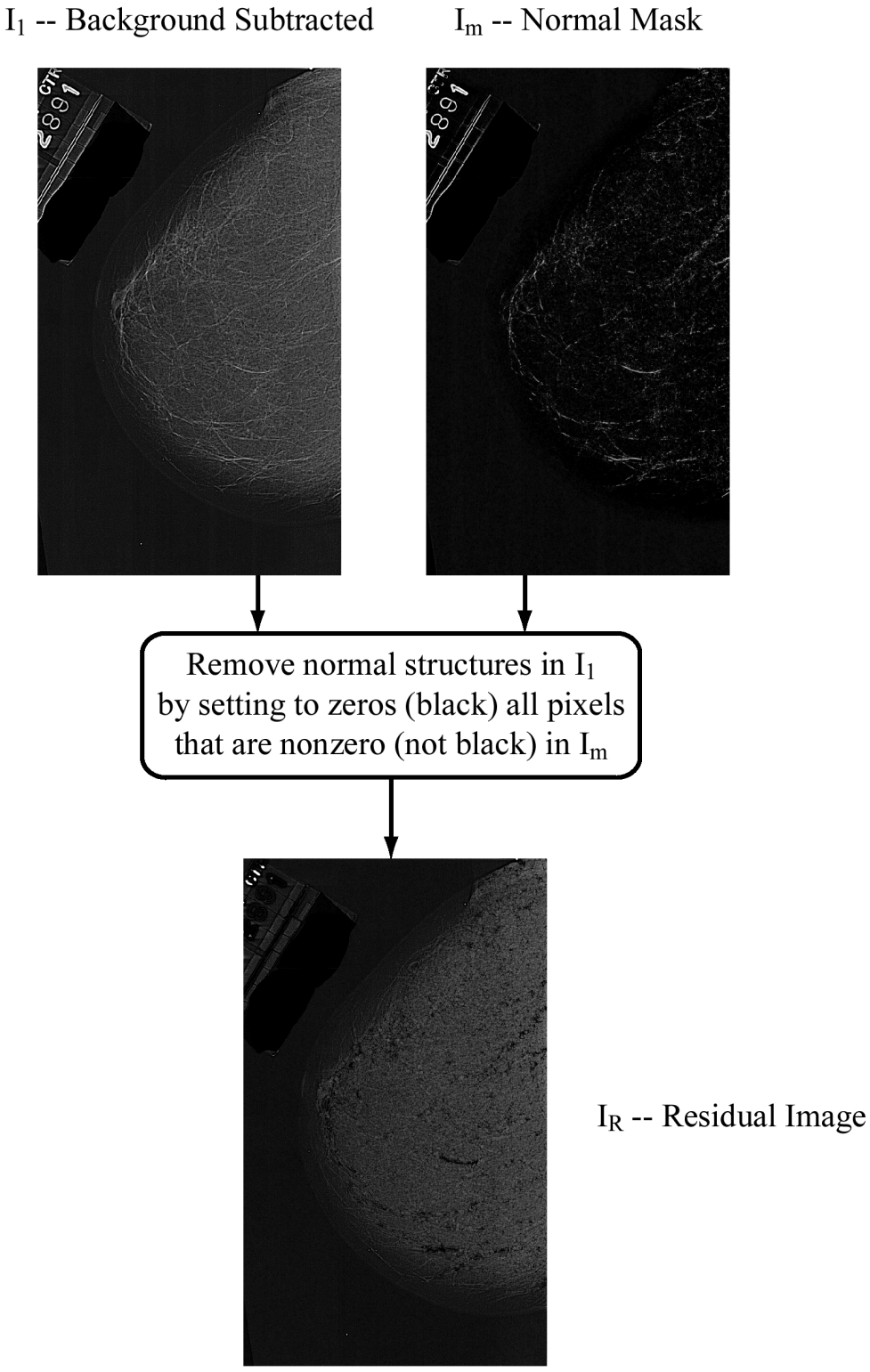

Fig. 5.23. Normal structure removal.

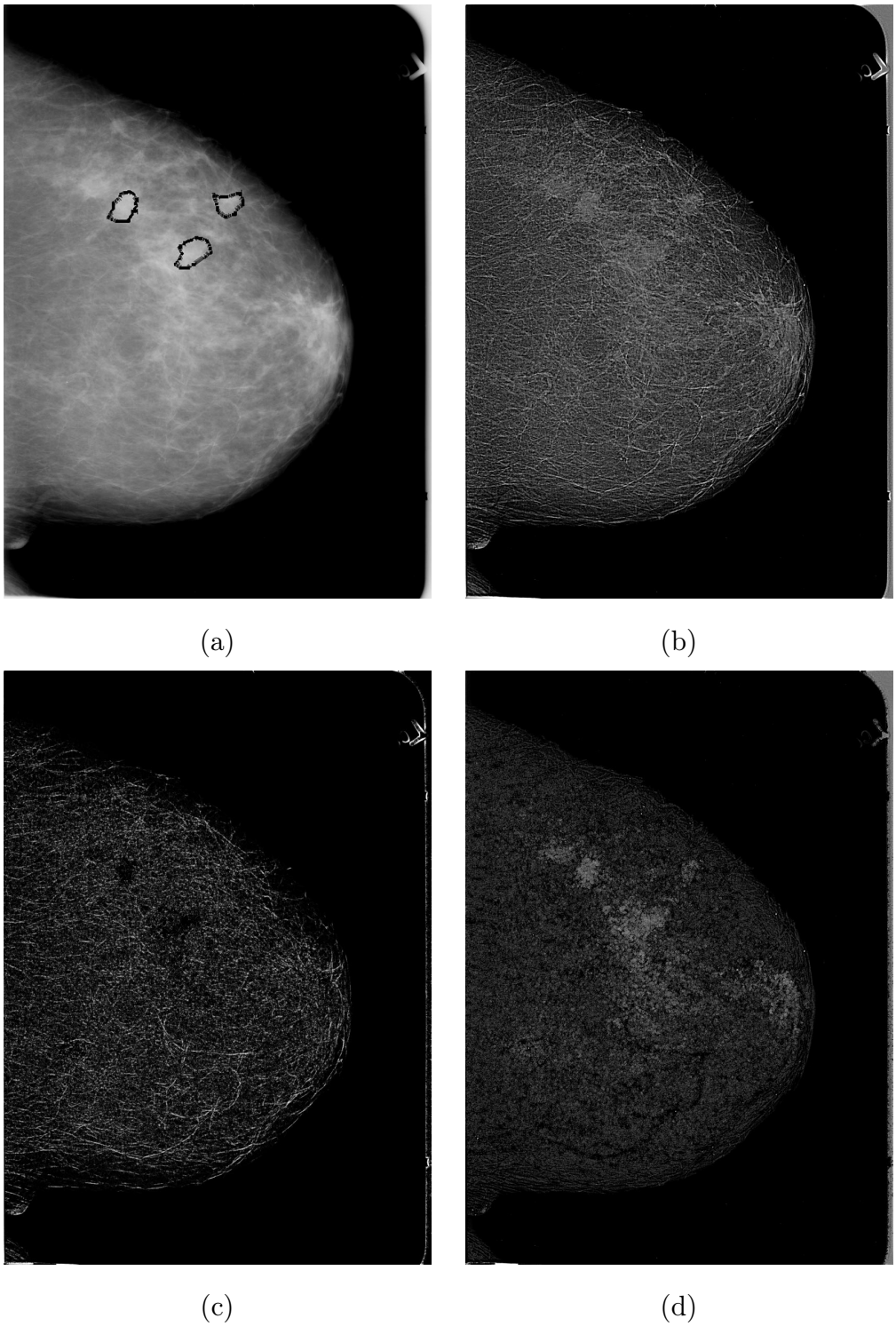

(a) (b)

(c) (d)

Fig. 5.24. (a) Original mammogram with the circumscribed masses outlined. (b) Background subtracted image I_1. (c) Normal linear structure map I_m. (d) Residual image consisting of only the tumor on featureless background.

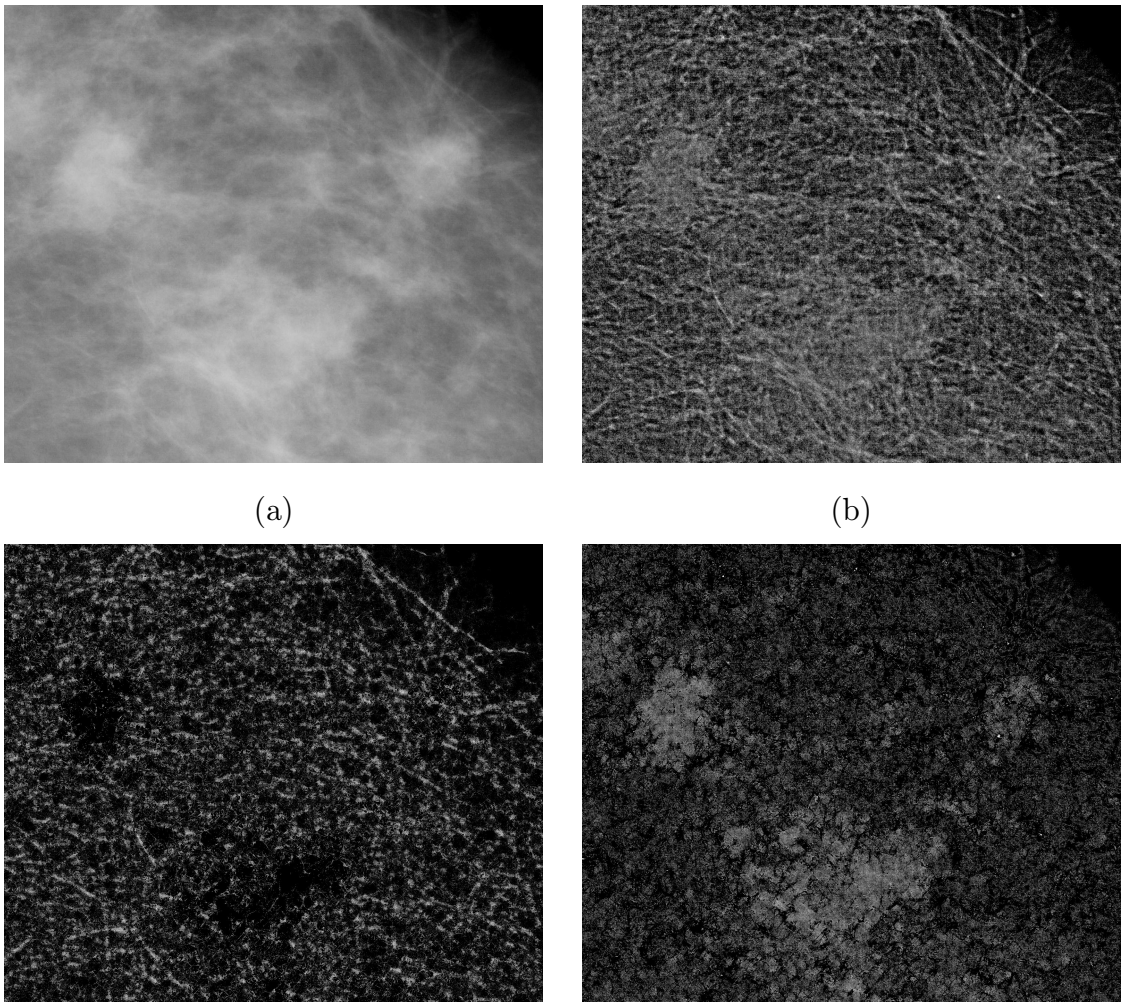

(a) (b)

(c) (d)

Fig. 5.25. Results in Figure 5.24 repeated for the region centered at the masses. (a) Original mammogram containing circumscribed masses. (b) Background subtracted image I_1. (c) Normal linear structure map I_m. (d) Residual image consisting of only the tumor on featureless background.

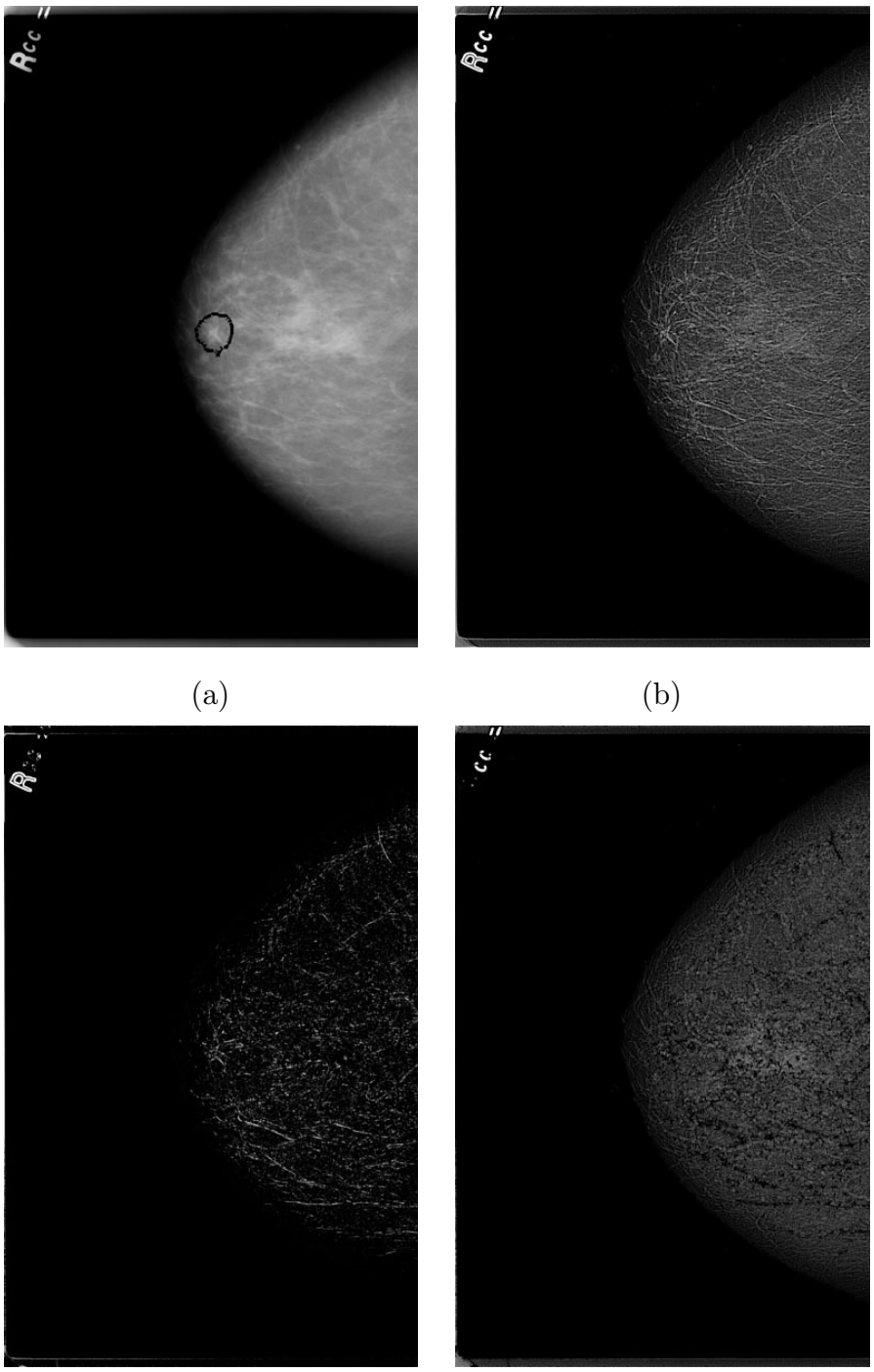

(a) (b)

(c) (d)

Fig. 5.26. (a) Original mammogram with the spiculated lesion outlined. (b) Background subtracted image I_1. (c) Normal linear structure map I_m contains the spiculations. (d) Residual image does not preserve the spiculations.

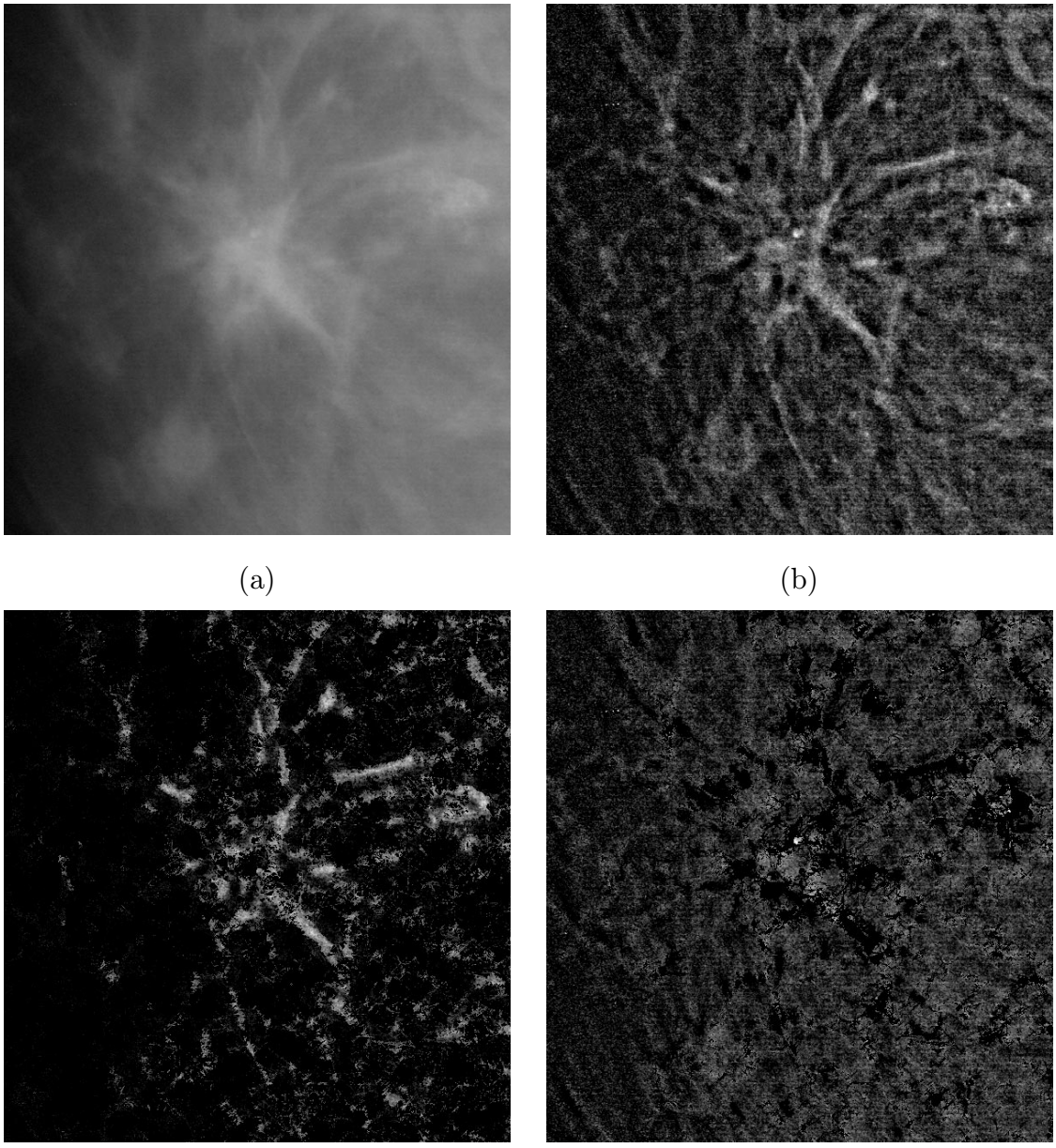

(a) (b)

(c) (d)

Fig. 5.27. Results in Figure 5.26 repeated for the region centered at the spiculated lesion. (a) Original mammogram containing spiculated lesion. (b) Background subtracted image I_1. (c) Normal linear structure map I_m contains the spiculations. (d) Residual image does not preserve the spiculations.

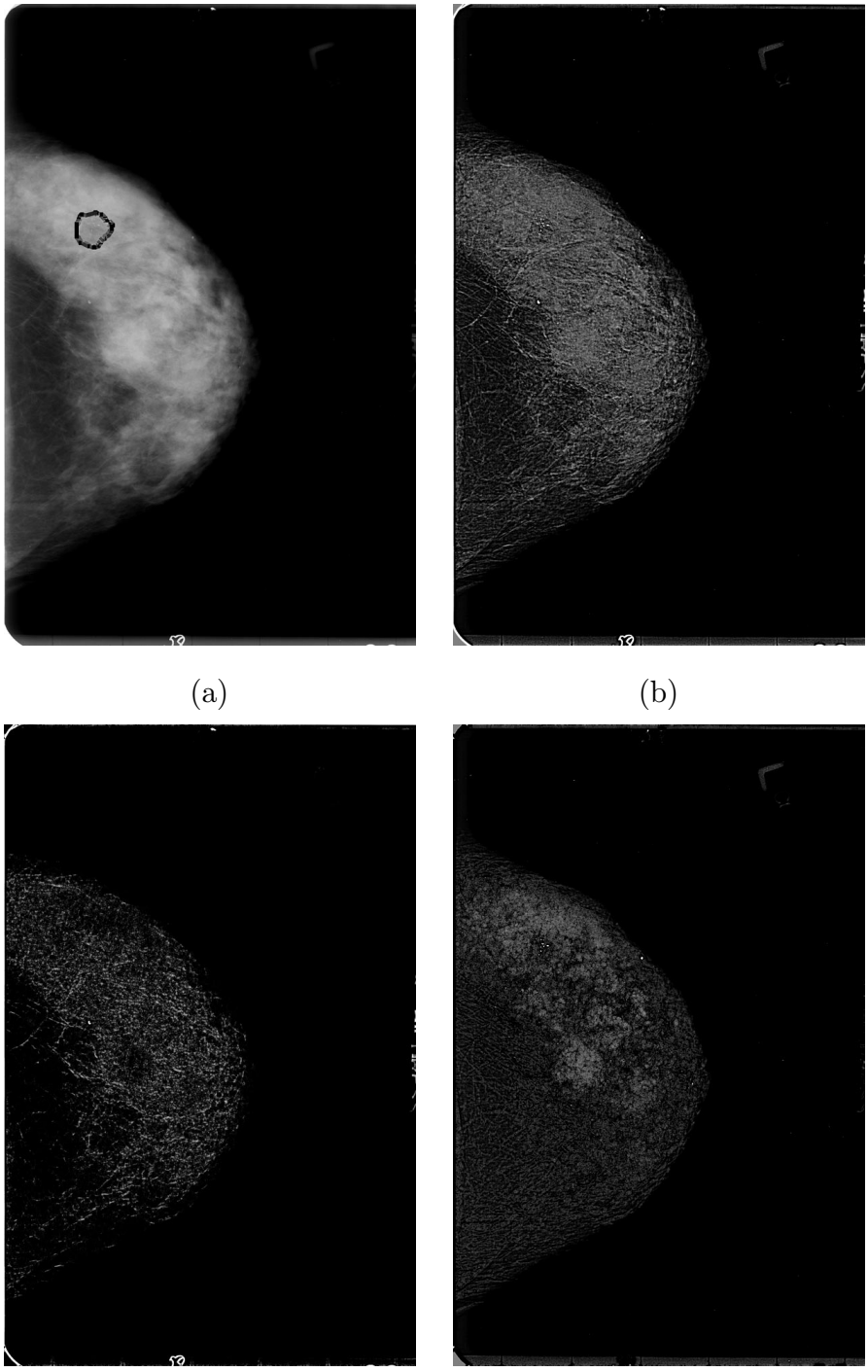

(a) (b)

(c) (d)

Fig. 5.28. (a) Original mammogram with the microcalcifications outlined. (b) Background subtracted image I_1. (c) Normal linear structure map I_m. (d) Residual image with more conspicuous microcalcifications.

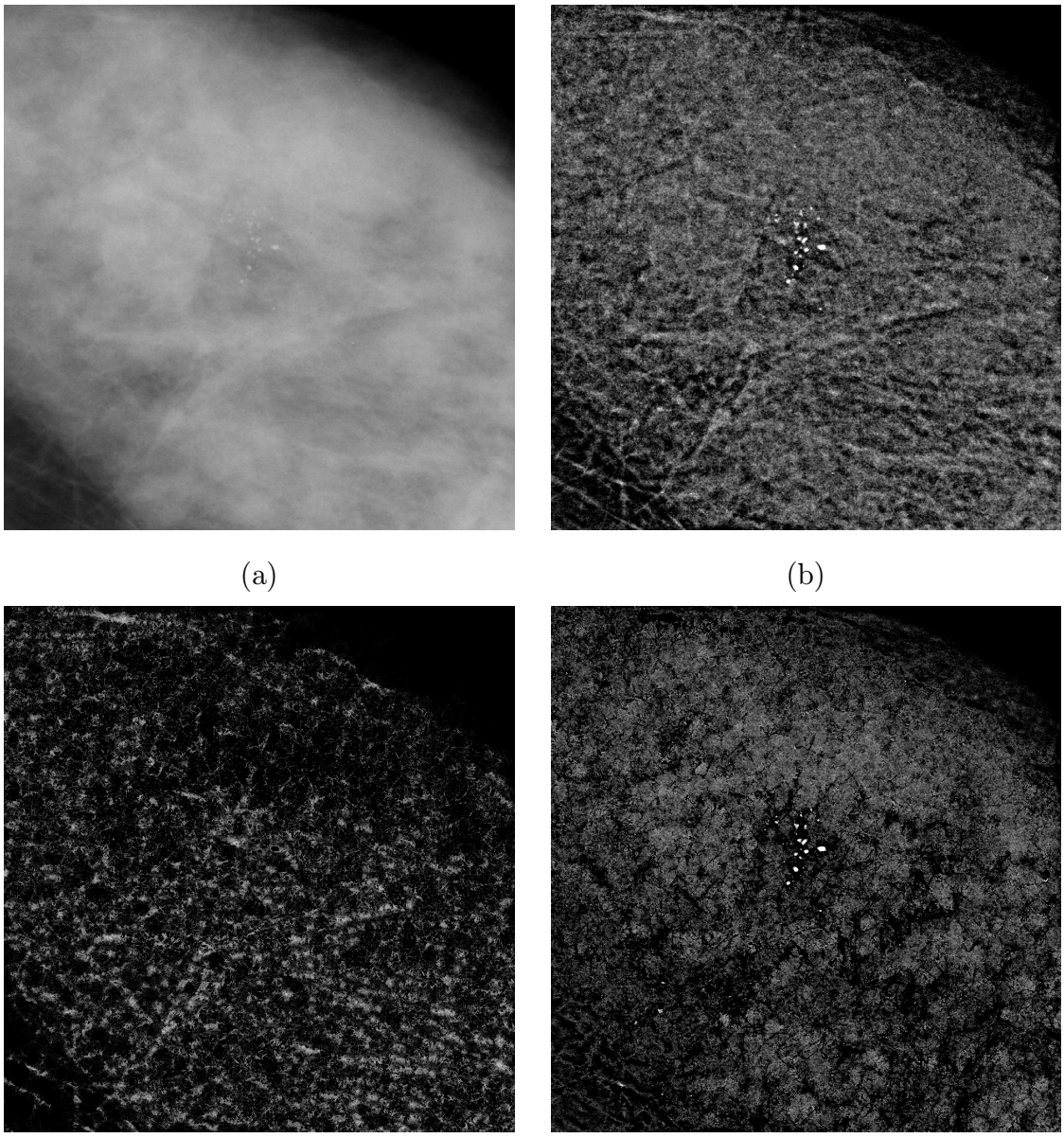

(a) (b)

(c) (d)

Fig. 5.29. Results in Figure 5.28 repeated for the region centered at the microcalcifications. (a) Original mammogram containing microcalcifications. (b) Background subtracted image I_1. (c) Normal linear structure map I_m. (d) Residual image with more conspicuous microcalcifications.

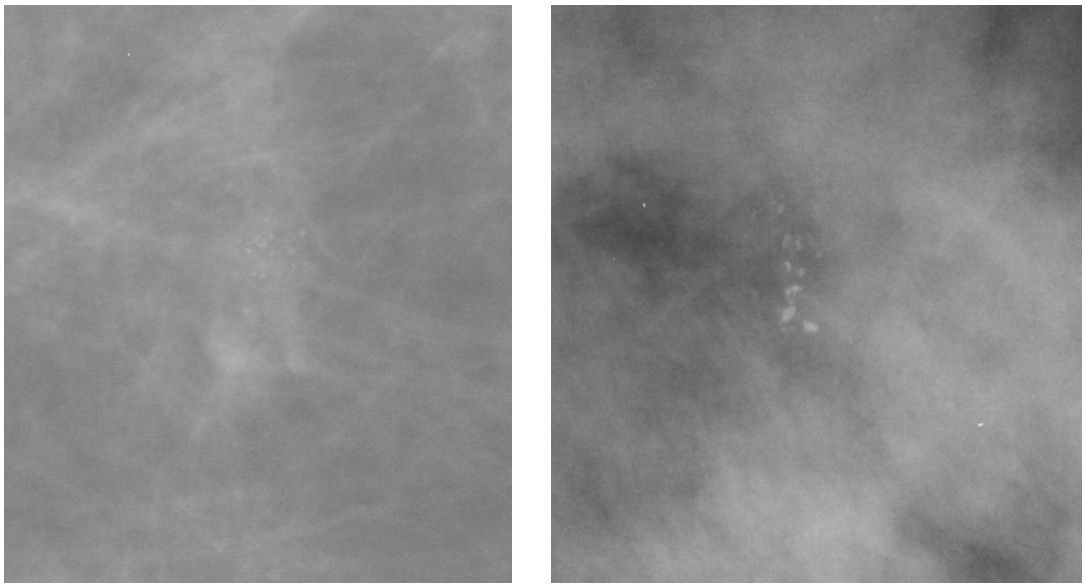

(a) (b)

Fig. 5.30. Original mammograms containing microcalcifications.

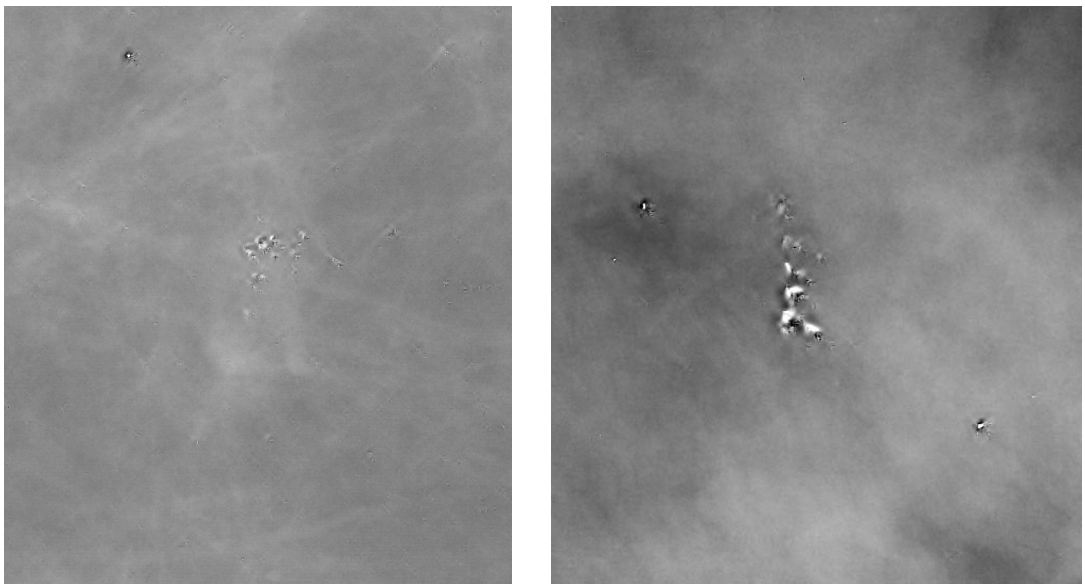

(a) (b)

Fig. 5.31. Enhanced image using technique by Strickland and Hahn.

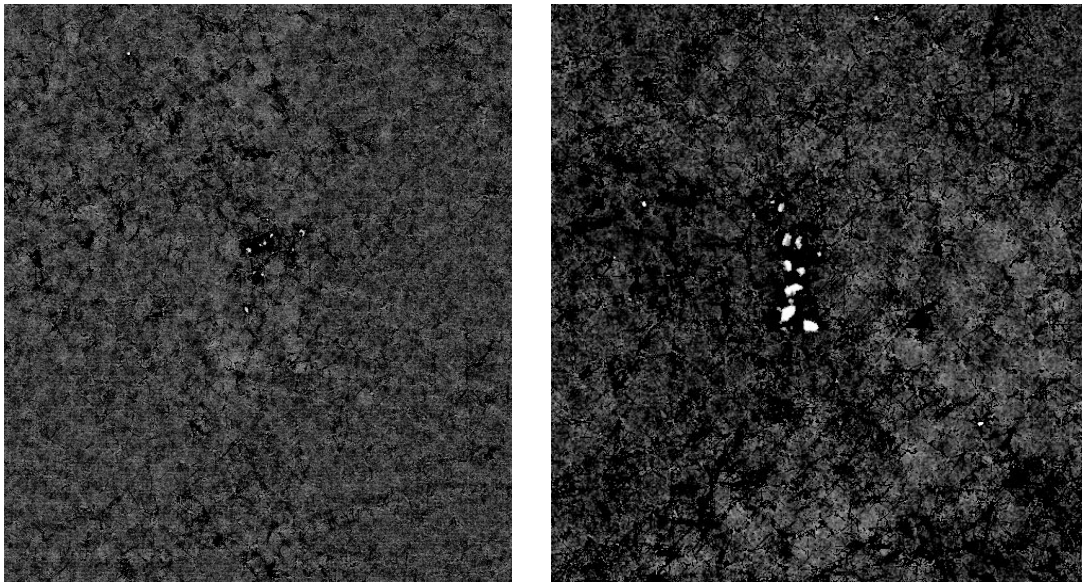

(a) (b)

Fig. 5.32. Residual image with more conspicuous microcalcifications.

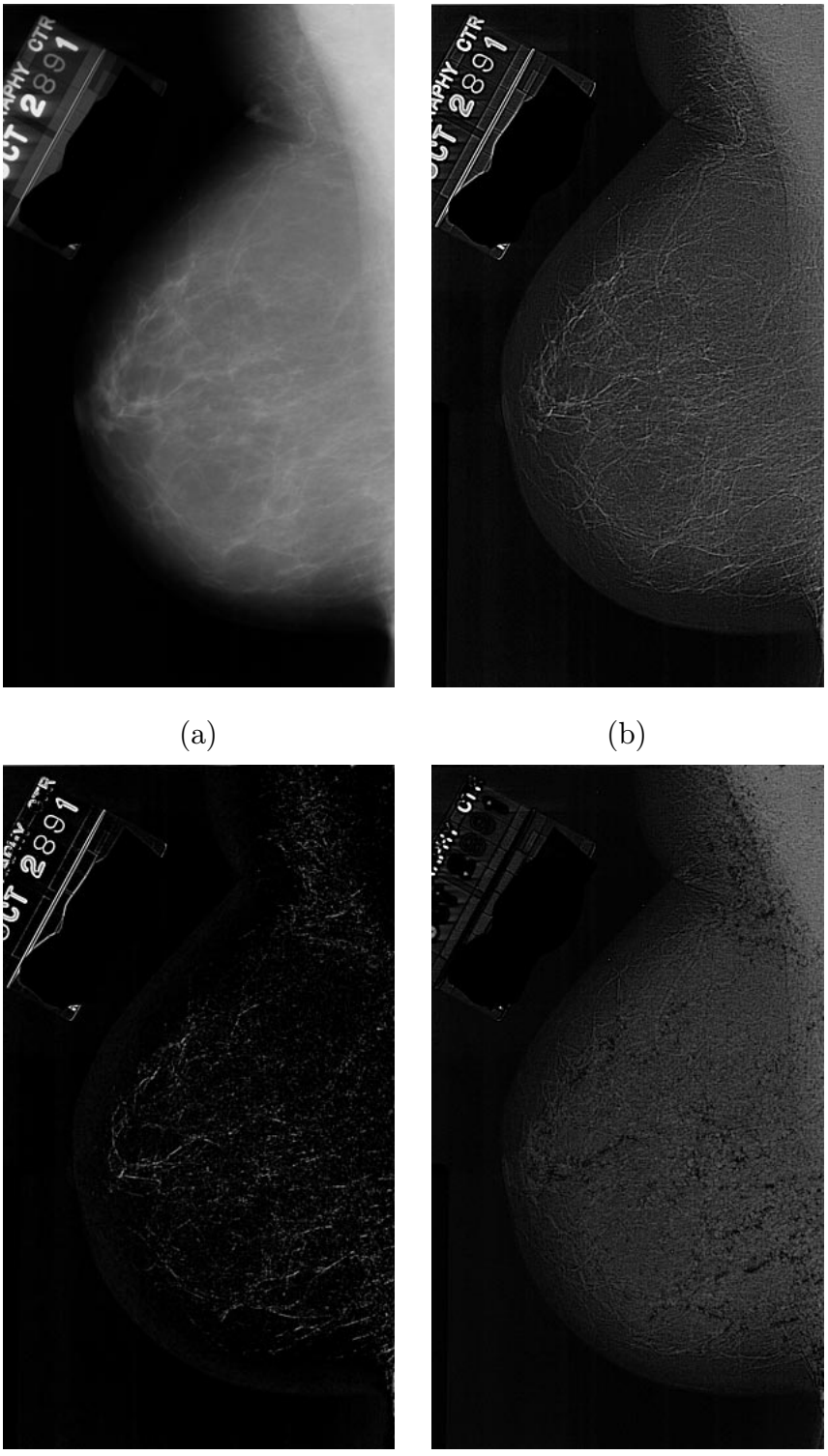

(a) (b)

(c) (d)

Fig. 5.33. (a) Original normal mammogram. (b) Background subtracted image I_1. (c) Normal linear structure map I_m. (d) Residual image.

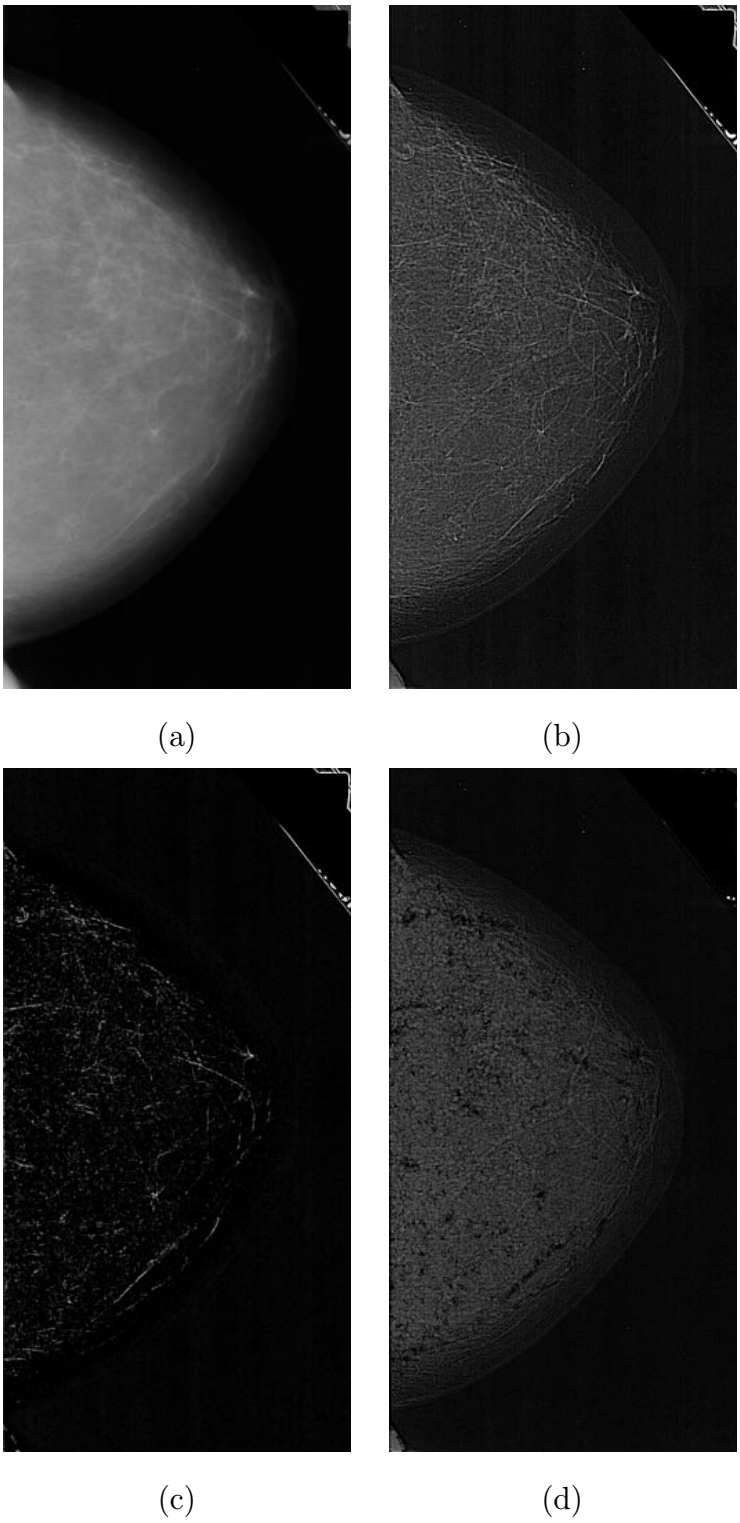

(a) (b)

(c) (d)

Fig. 5.34. (a) Original normal mammogram. (b) Background subtracted image I_1. (c) Normal linear structure map I_m. (d) Residual image.

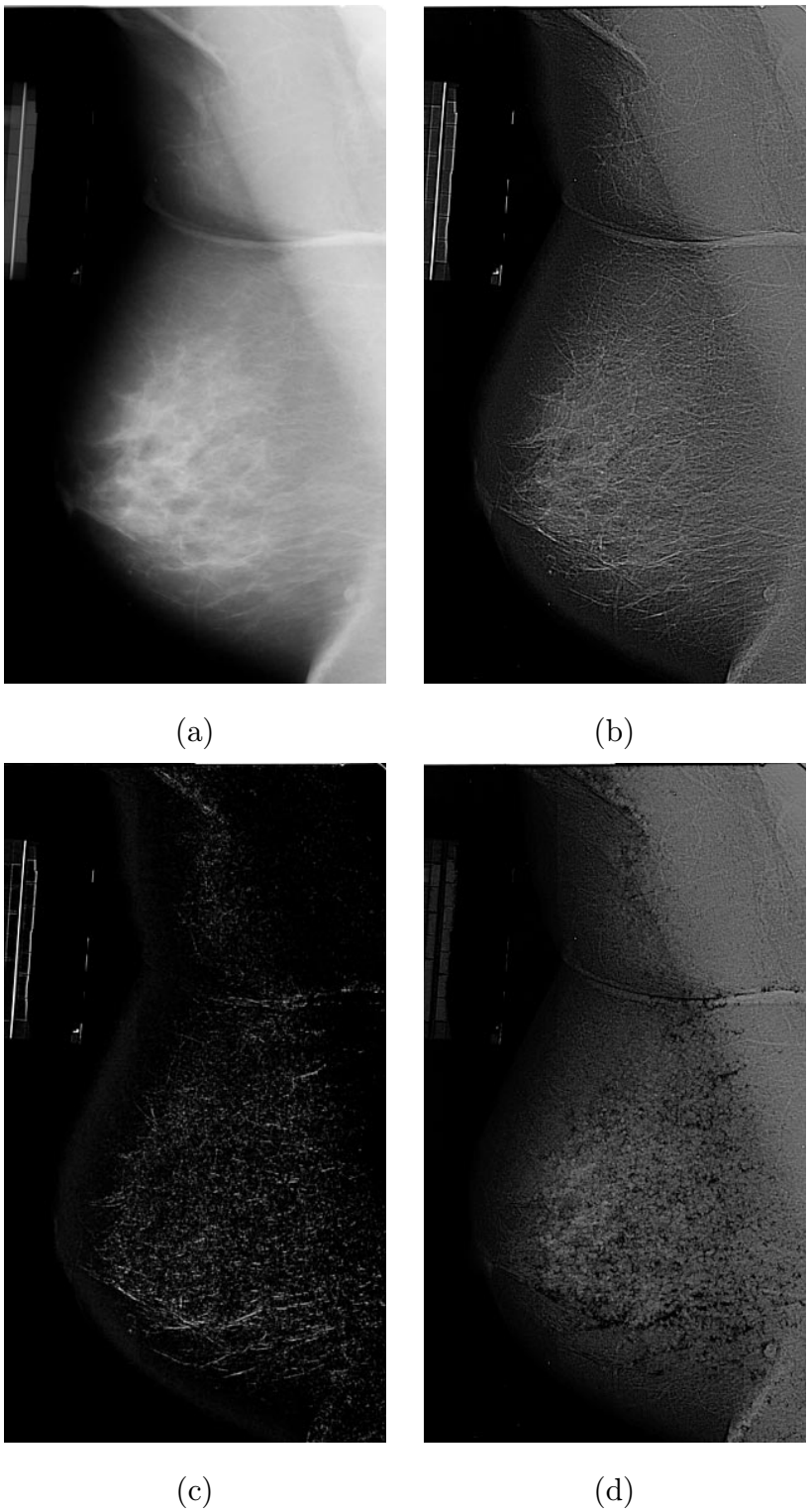

(a) (b)

(c) (d)

Fig. 5.35. (a) Original normal mammogram. (b) Background subtracted image I_1. (c) Normal linear structure map I_m. (d) Residual image.

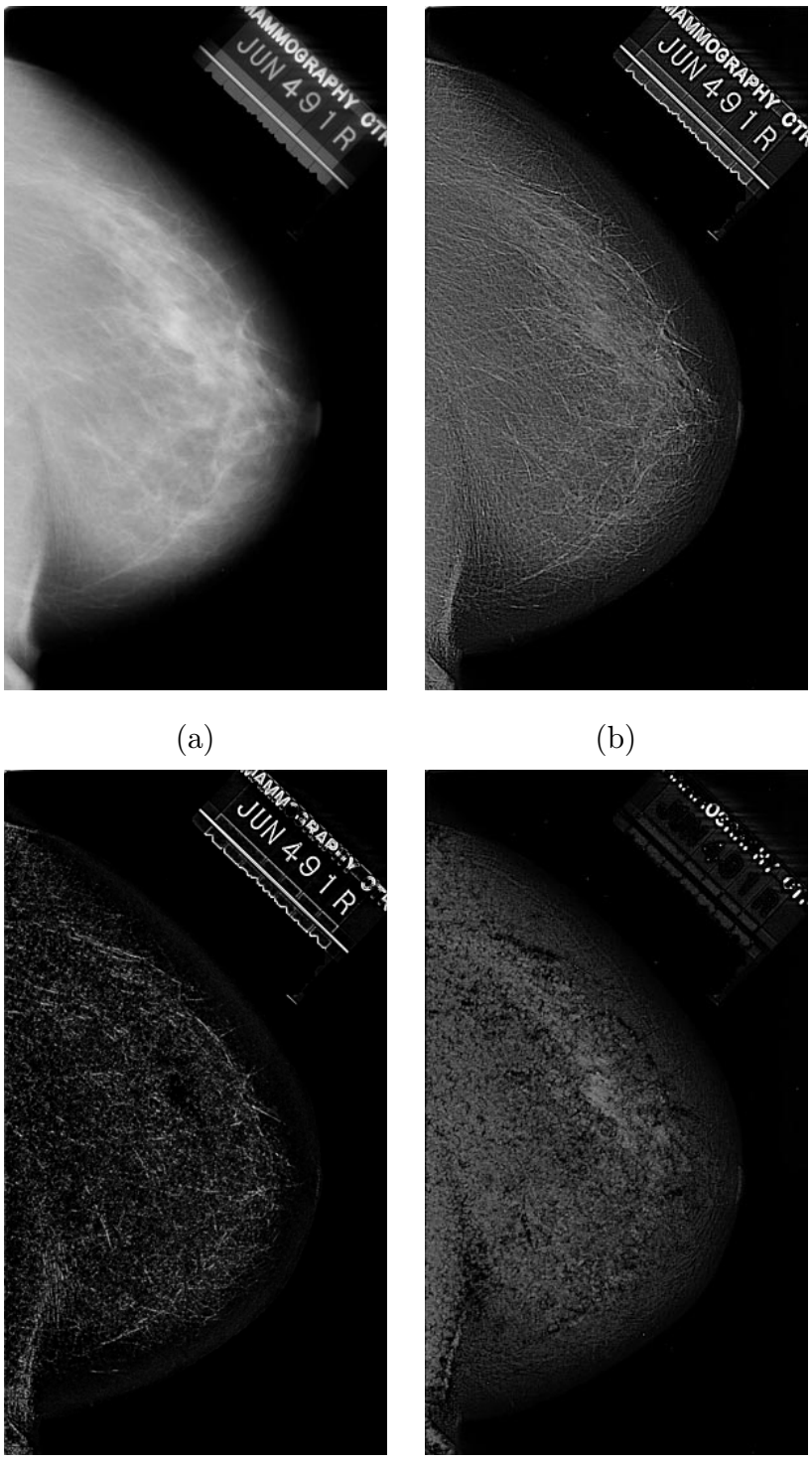

(a) (b)

(c) (d)

Fig. 5.36. (a) Original normal mammogram. (b) Background subtracted image I_1. (c) Normal linear structure map I_m. (d) Residual image.

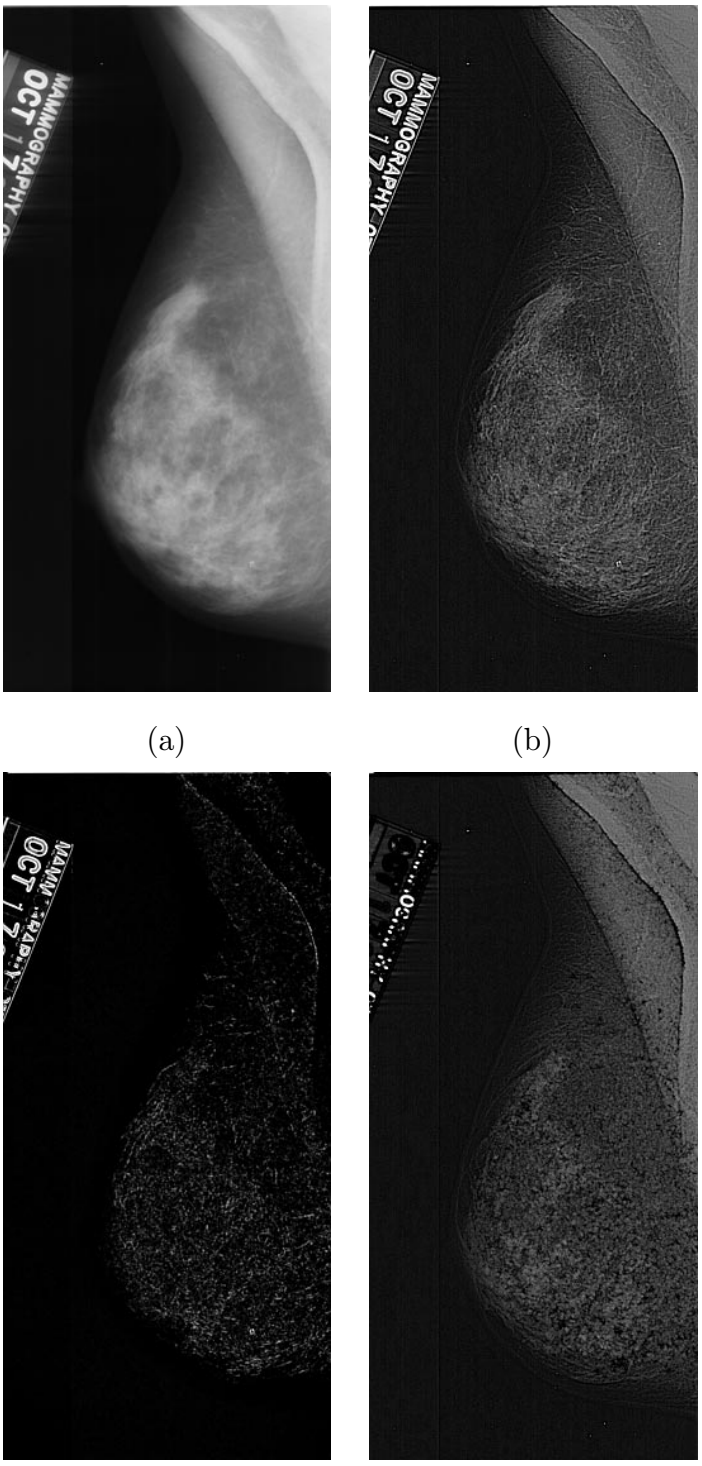

(a) (b)

(c) (d)

Fig. 5.37. (a) Original normal mammogram. (b) Background subtracted image I_1. (c) Normal linear structure map I_m. (d) Residual image.

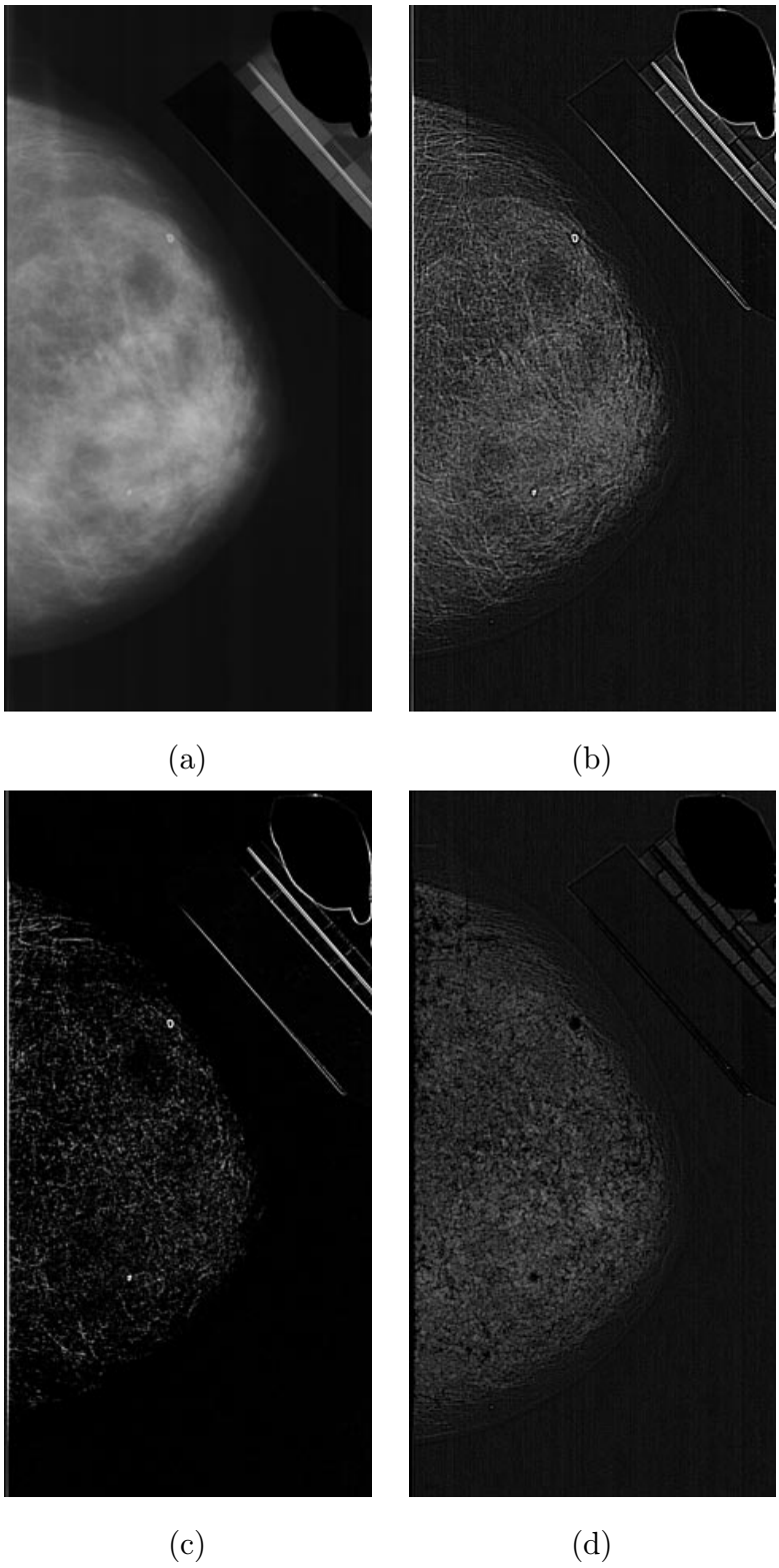

(a) (b)

(c) (d)

Fig. 5.38. (a) Original normal mammogram. (b) Background subtracted image I_1. (c) Normal linear structure map I_m. (d) Residual image.

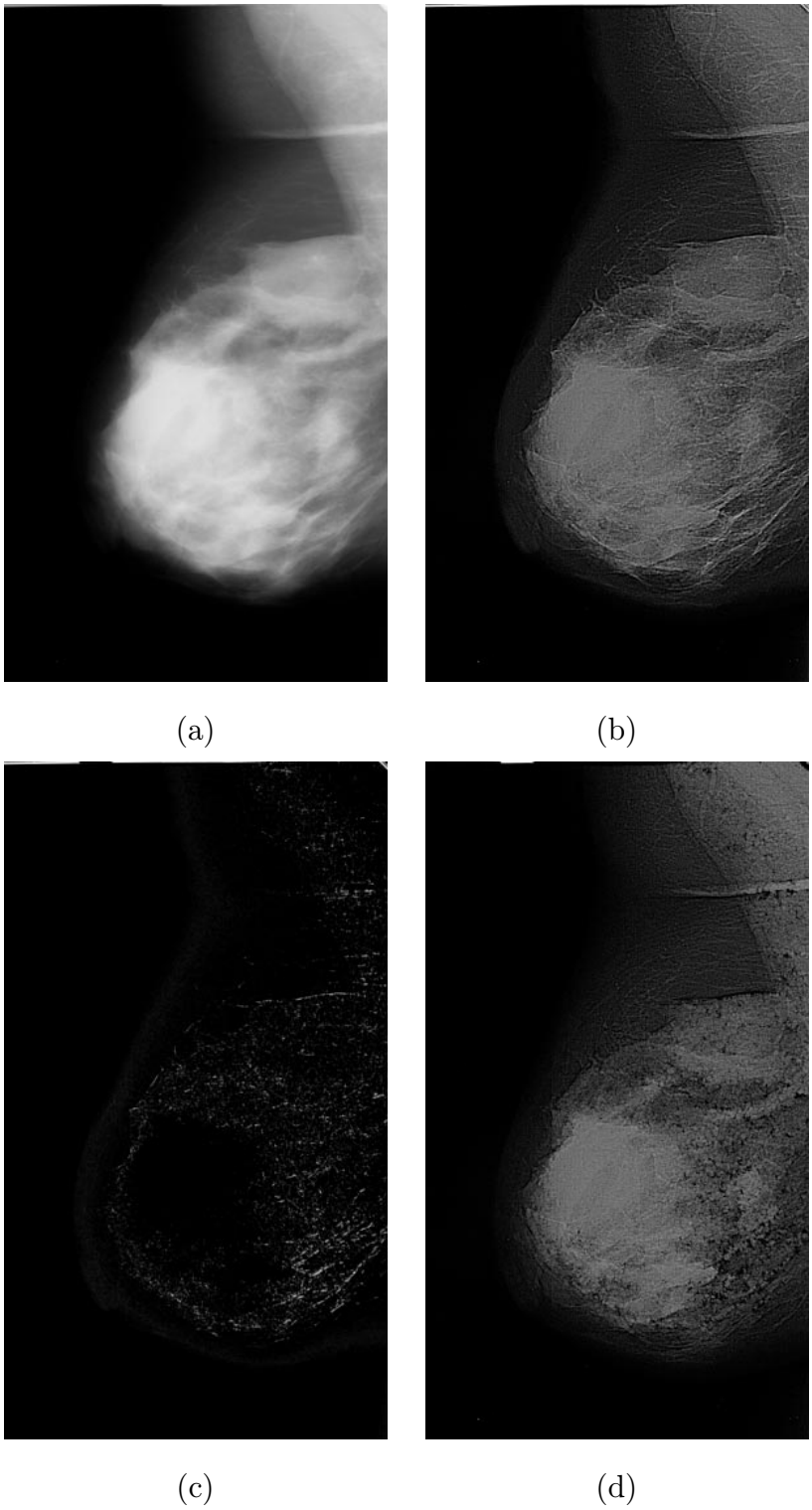

(a) (b)

(c) (d)

Fig. 5.39. (a) Original normal mammogram. (b) Background subtracted image I_1. (c) Normal linear structure map I_m. (d) Residual image.

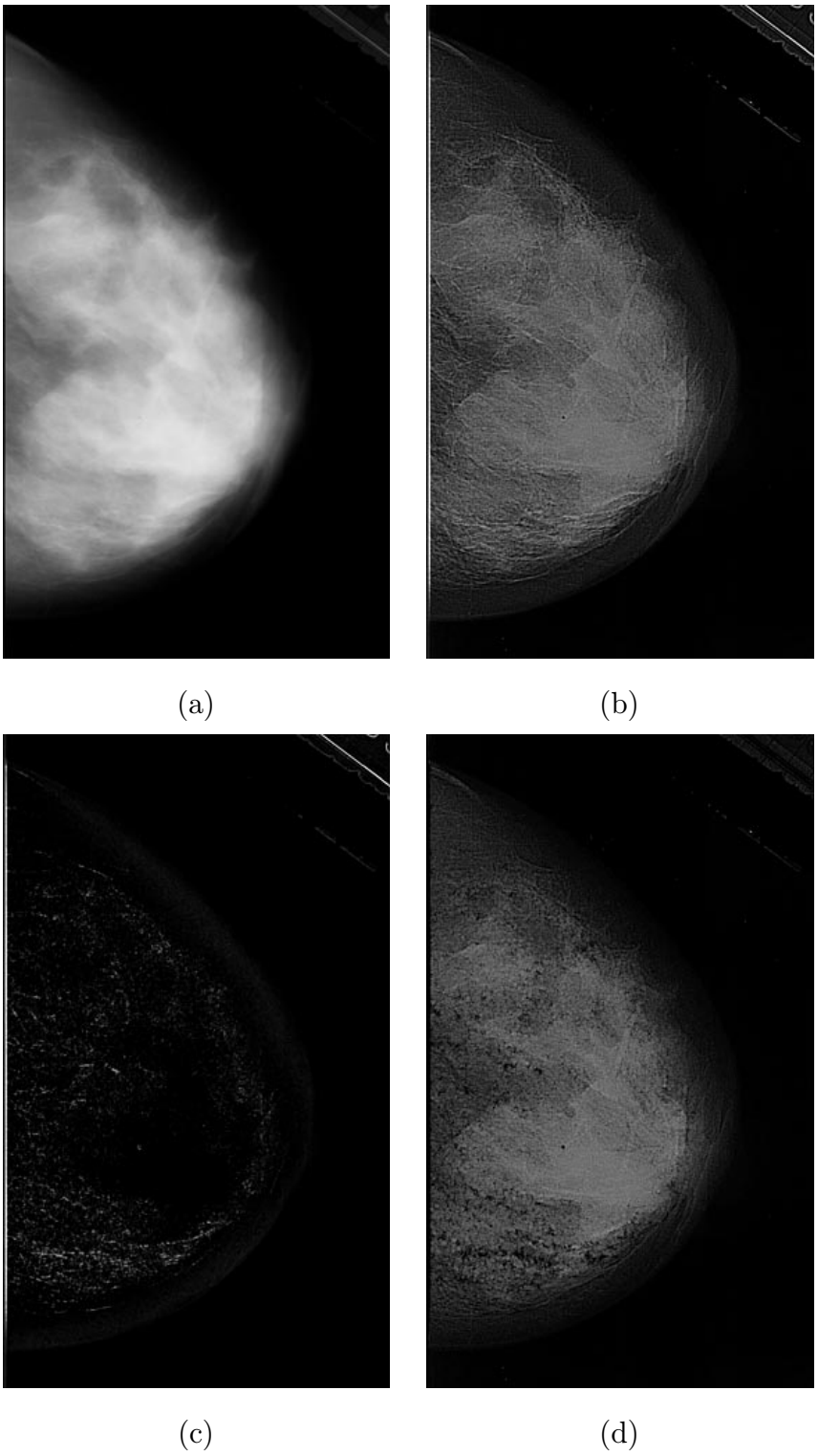

(a) (b)

(c) (d)

Fig. 5.40. (a) Original normal mammogram. (b) Background subtracted image I_1. (c) Normal linear structure map I_m. (d) Residual image.

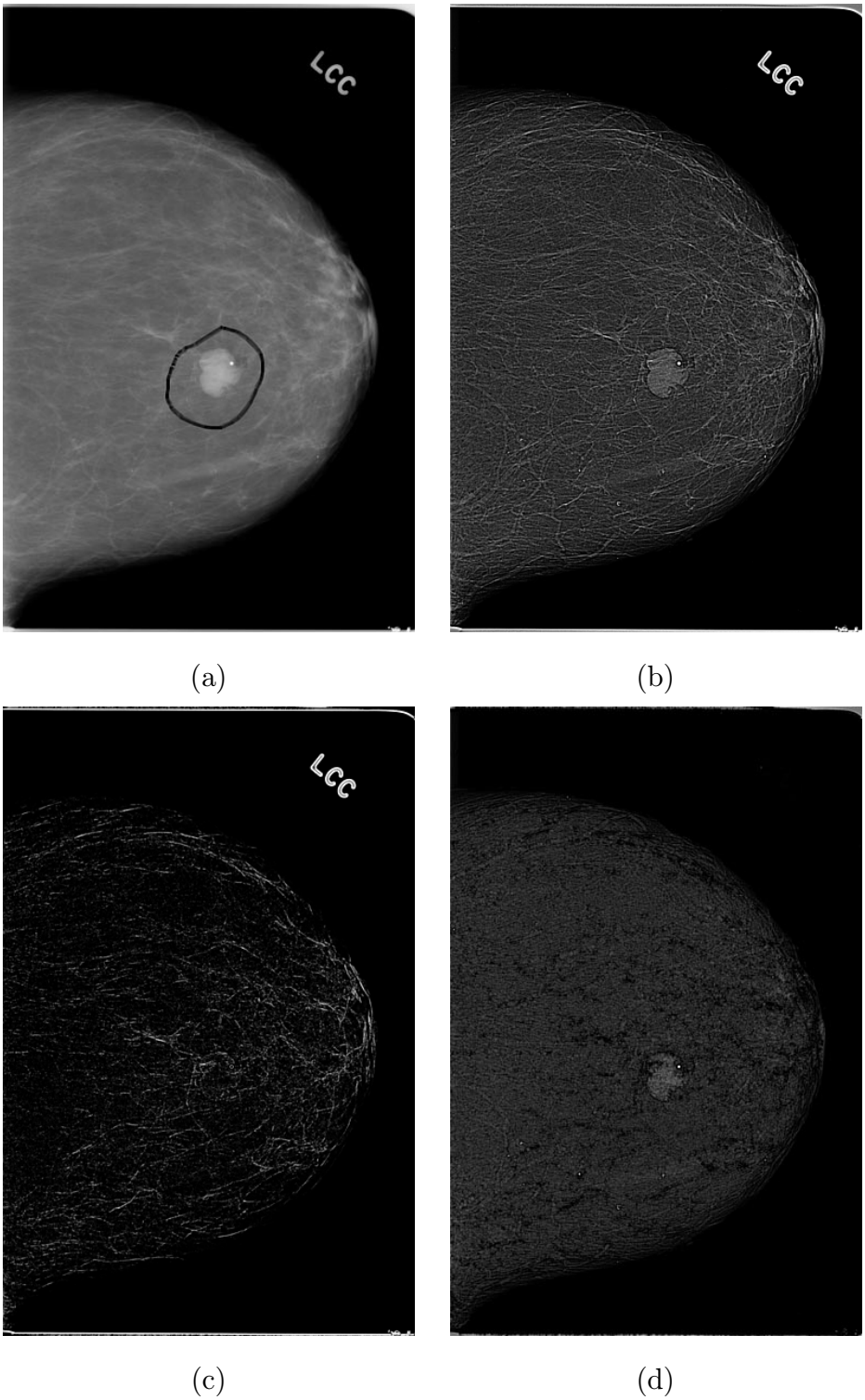

(a) (b)

(c) (d)

Fig. 5.41. (a) Original mammogram with the circumscribed masses outlined. (b) Background subtracted image I_1. (c) Normal linear structure map I_m. (d) Residual image consisting of only the tumor on featureless background.

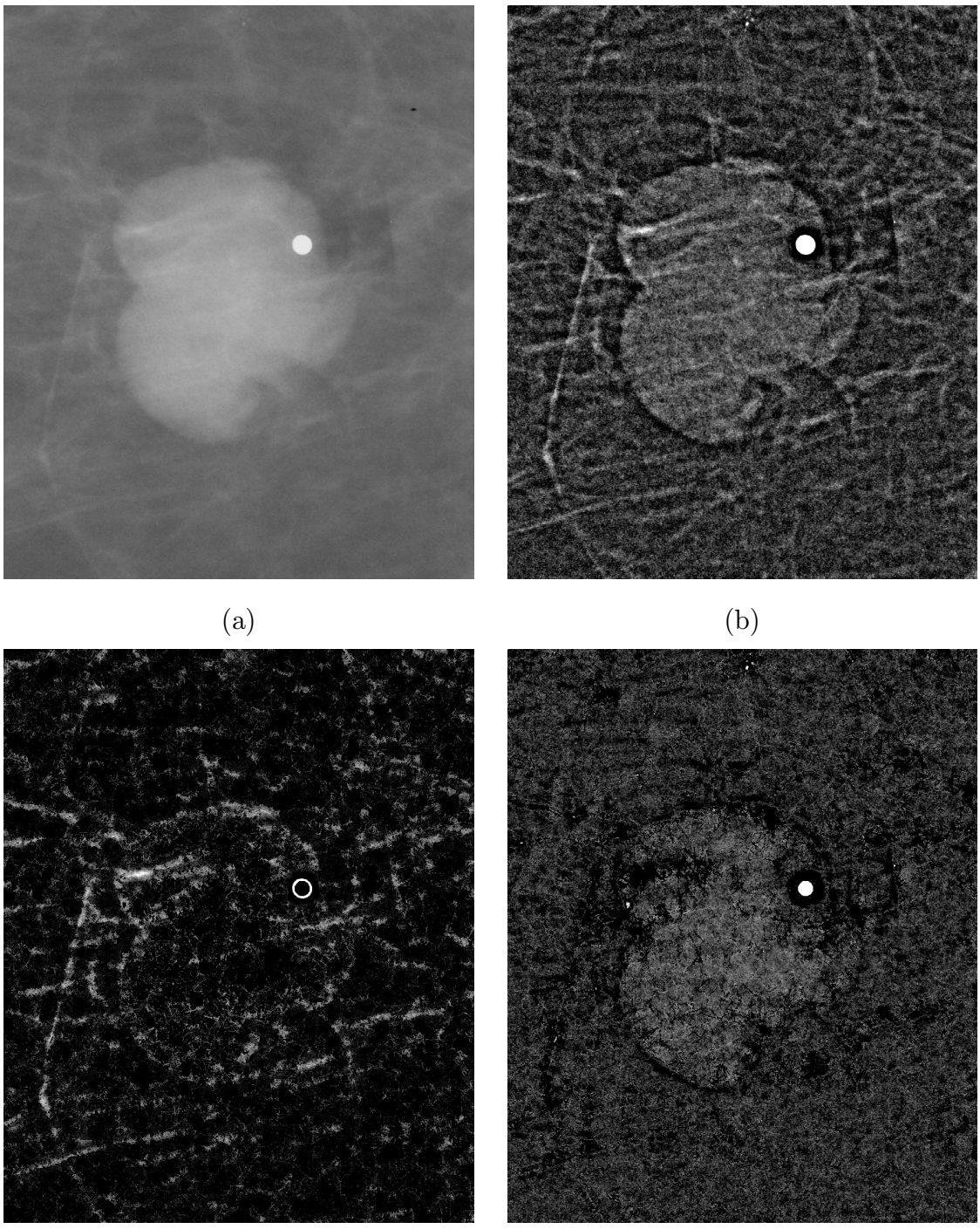

(a) (b)

(c) (d)

Fig. 5.42. Results in Figure 5.41 repeated for the region centered at the masses. (a) Original mammogram containing circumscribed masses. (b) Background subtracted image I_1. (c) Normal linear structure map I_m. (d) Residual image consisting of only the tumor on featureless background.

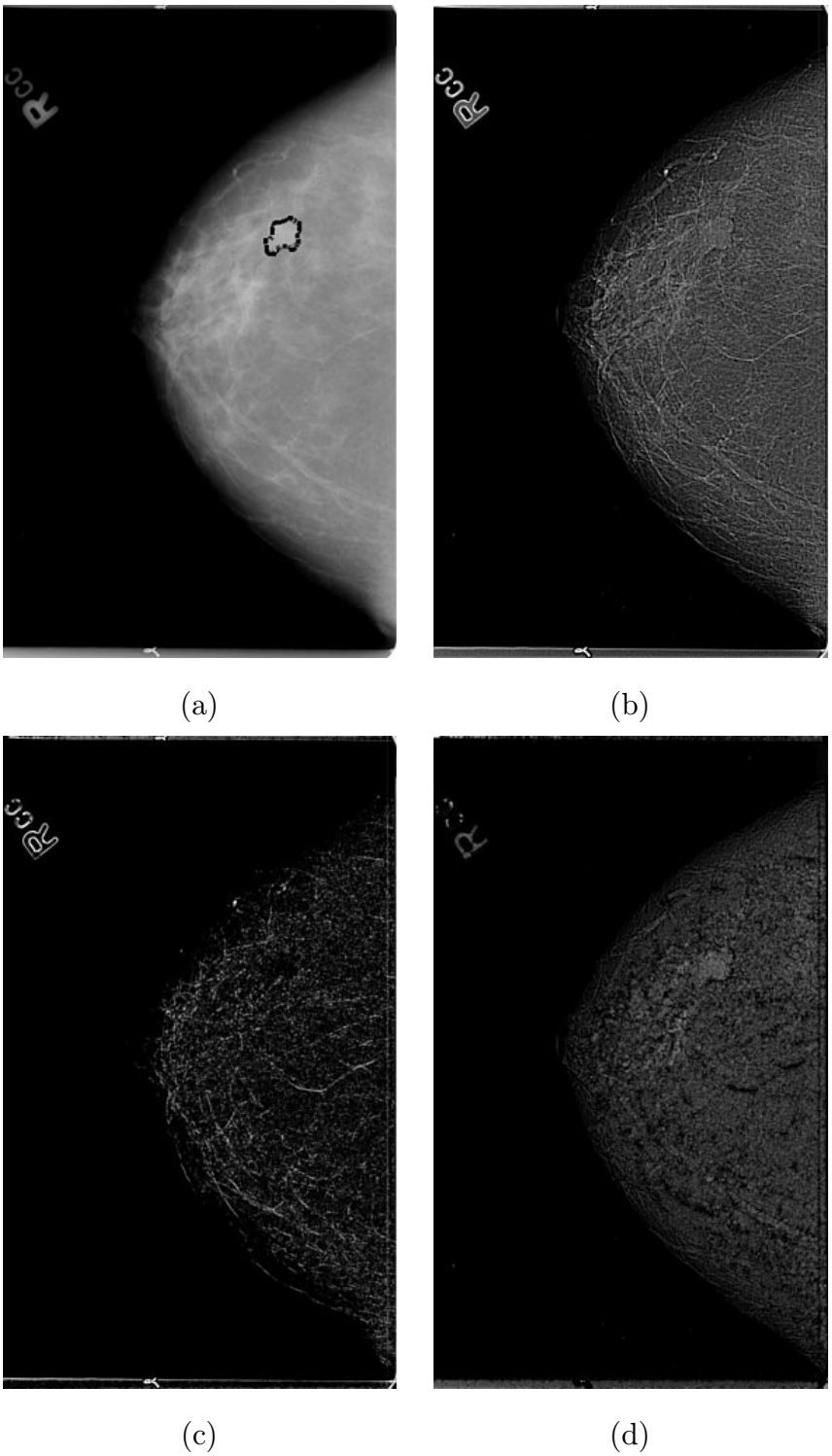

(a) (b)

(c) (d)

Fig. 5.43. (a) Original mammogram with the circumscribed masses outlined. (b) Background subtracted image I_1. (c) Normal linear structure map I_m. (d) Residual image consisting of only the tumor on featureless background.

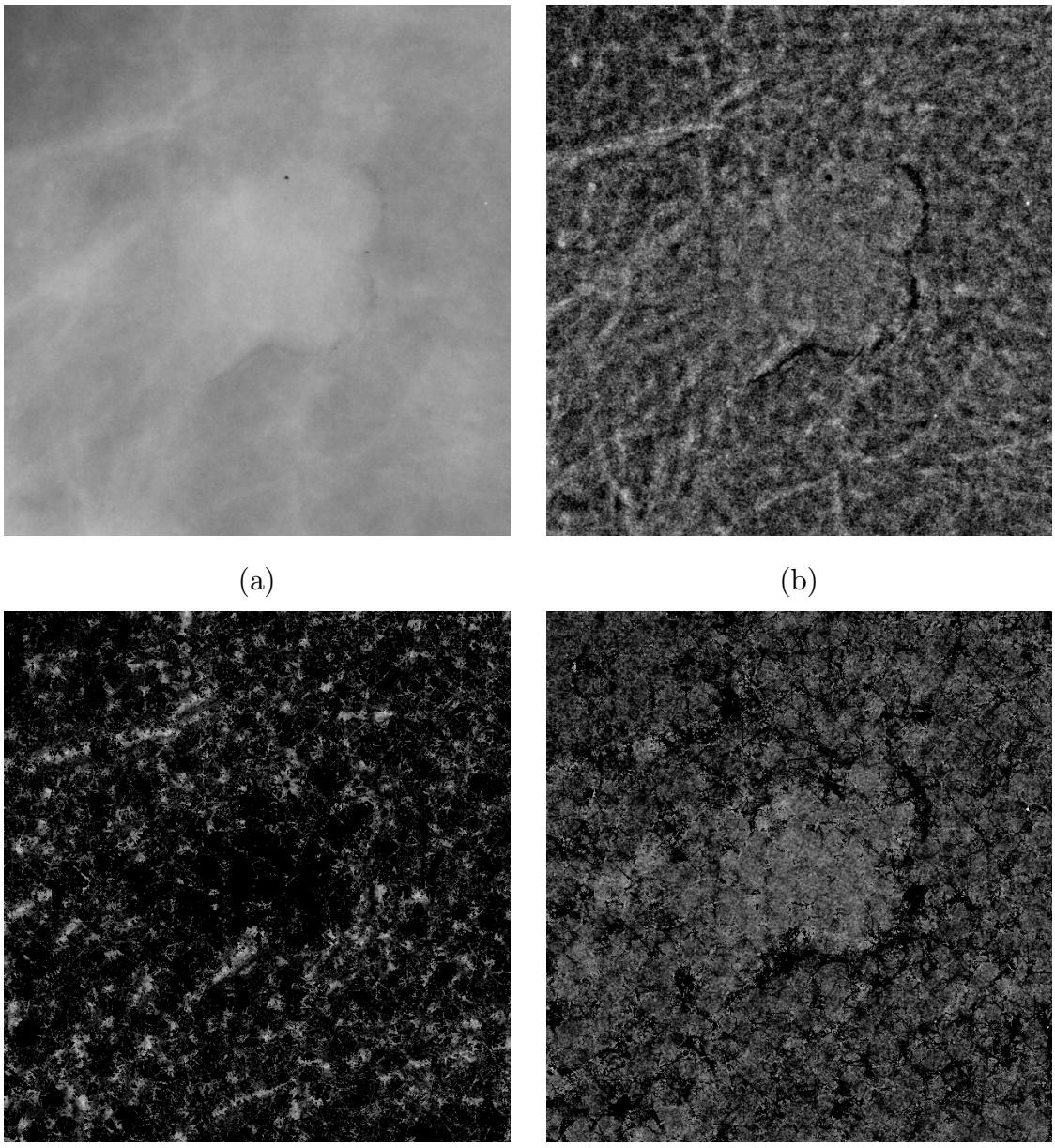

(a) (b)

(c) (d)

Fig. 5.44. Results in Figure 5.43 repeated for the region centered at the masses. (a) Original mammogram containing circumscribed masses. (b) Background subtracted image I_1. (c) Normal linear structure map I_m. (d) Residual image consisting of only the tumor on featureless background.

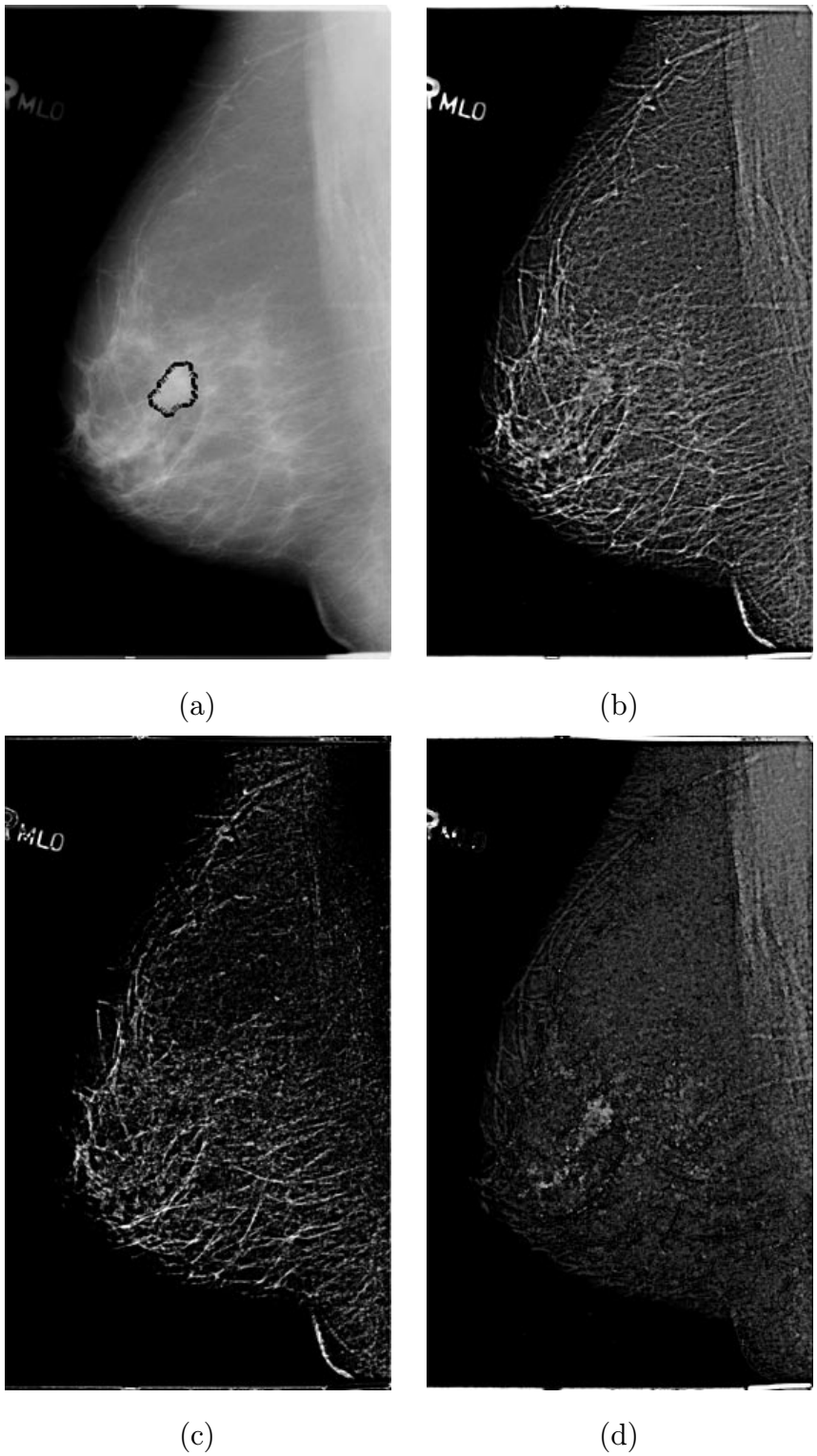

Fig. 5.45. (a) Original mammogram with the circumscribed masses outlined. (b) Background subtracted image I_1. (c) Normal linear structure map I_m. (d) Residual image consisting of only the tumor on featureless background.

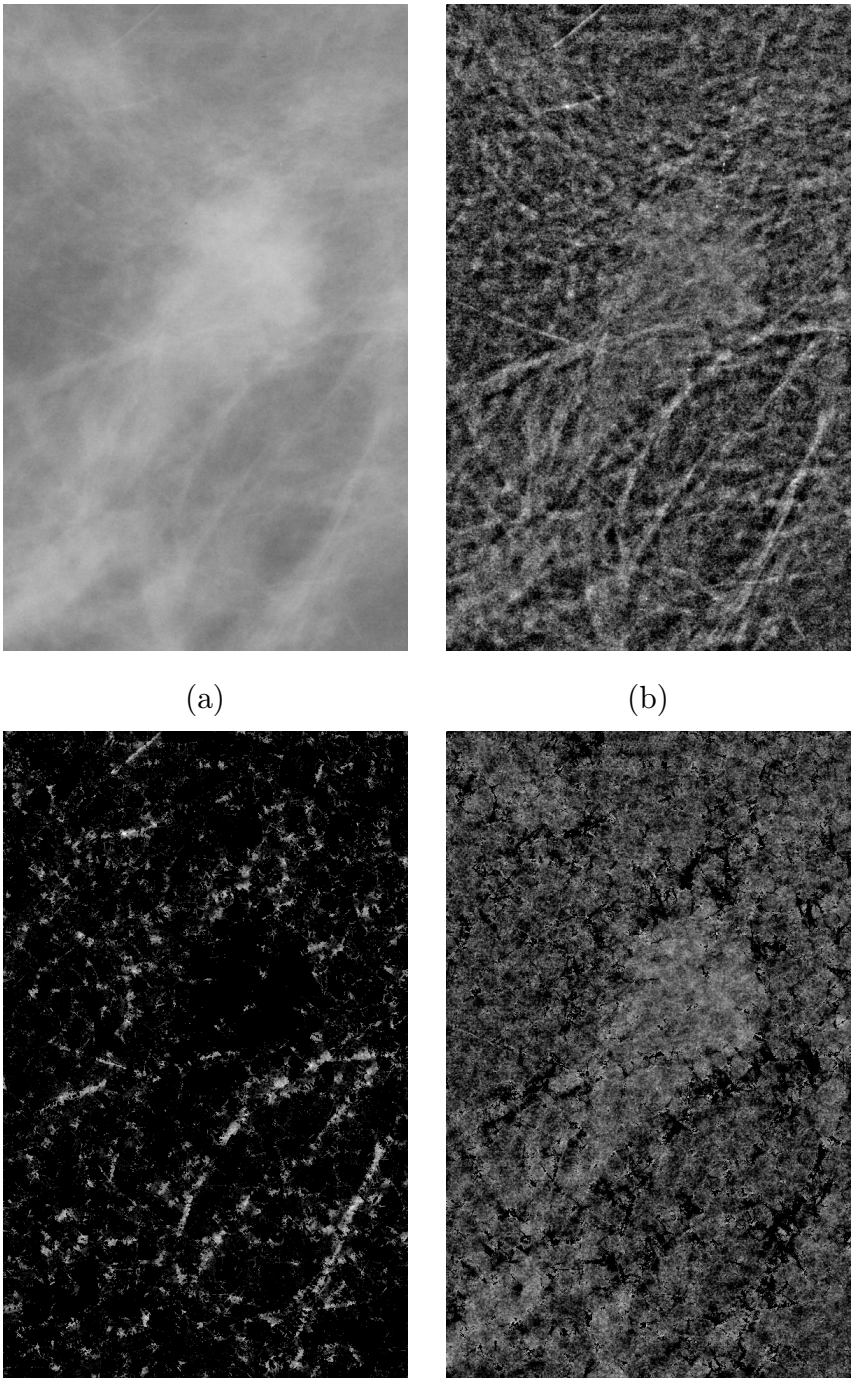

(a) (b)

(c) (d)

Fig. 5.46. Results in Figure 5.45 repeated for the region centered at the masses. (a) Original mammogram containing circumscribed masses. (b) Background subtracted image I_1. (c) Normal linear structure map I_m. (d) Residual image consisting of only the tumor on featureless background.

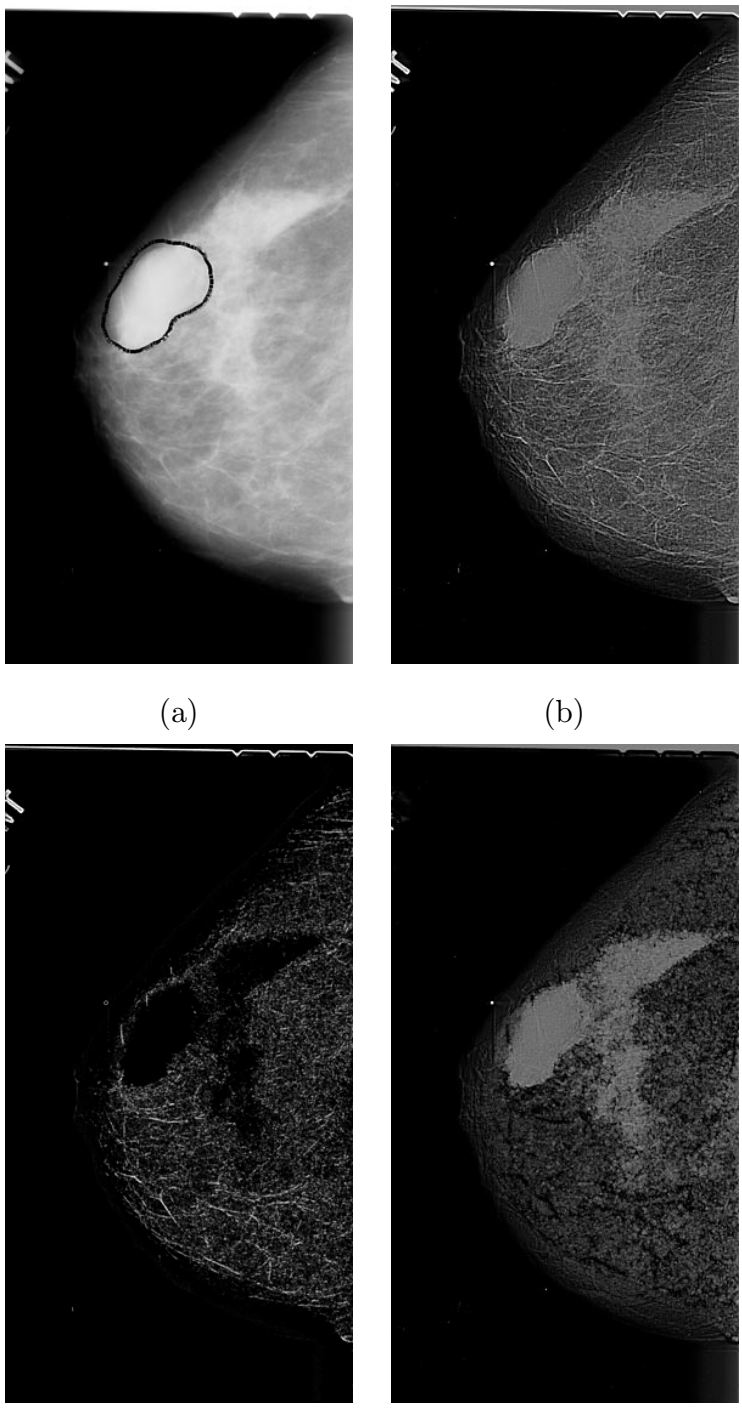

(a) (b)

(c) (d)

Fig. 5.47. (a) Original mammogram with the circumscribed masses outlined. (b) Background subtracted image I_1. (c) Normal linear structure map I_m. (d) Residual image consisting of only the tumor on featureless background.

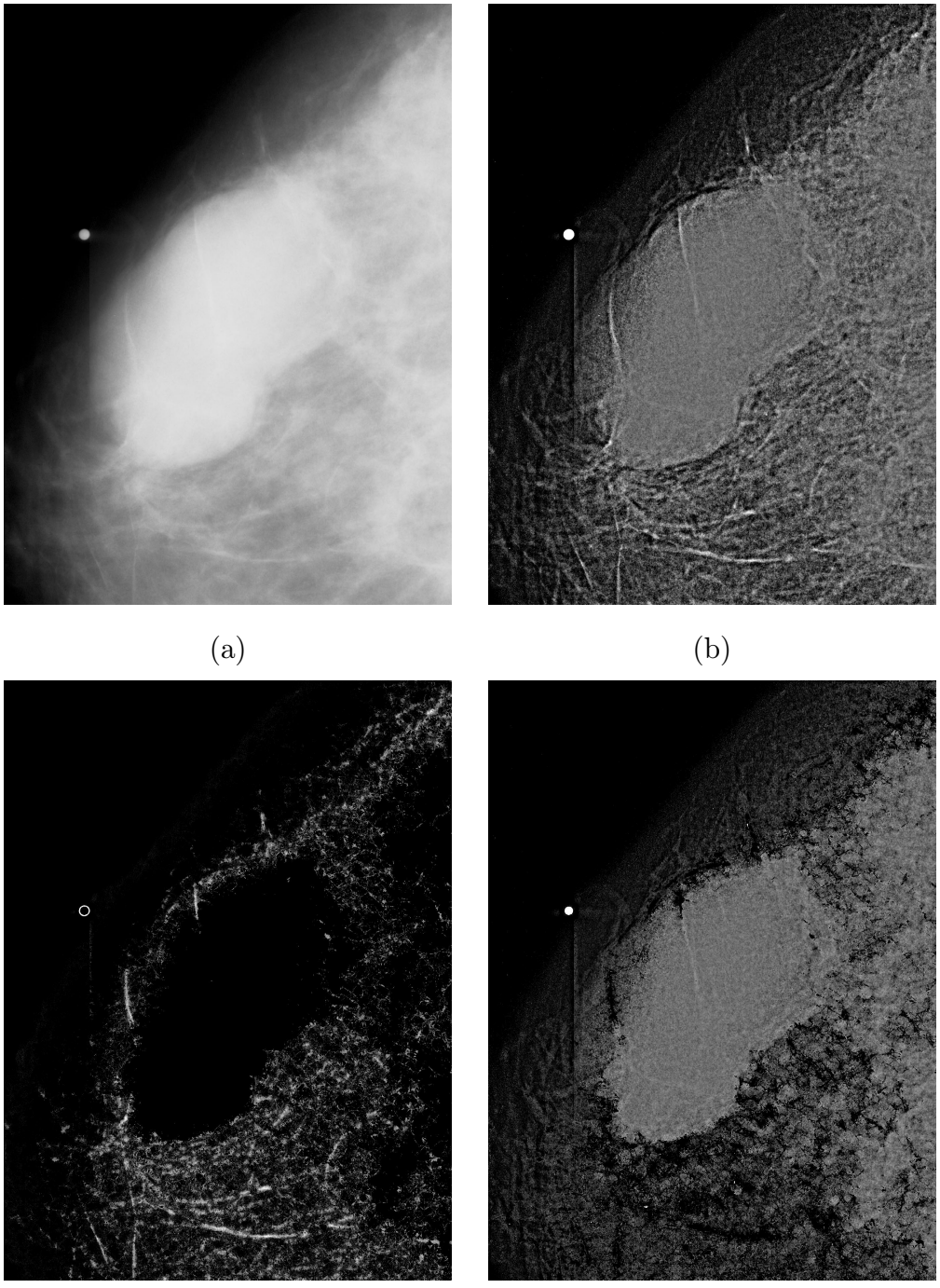

(a) (b)

(c) (d)

Fig. 5.48. Results in Figure 5.47 repeated for the region centered at the masses. (a) Original mammogram containing circumscribed masses. (b) Background subtracted image I_1. (c) Normal linear structure map I_m. (d) Residual image consisting of only the tumor on featureless background.

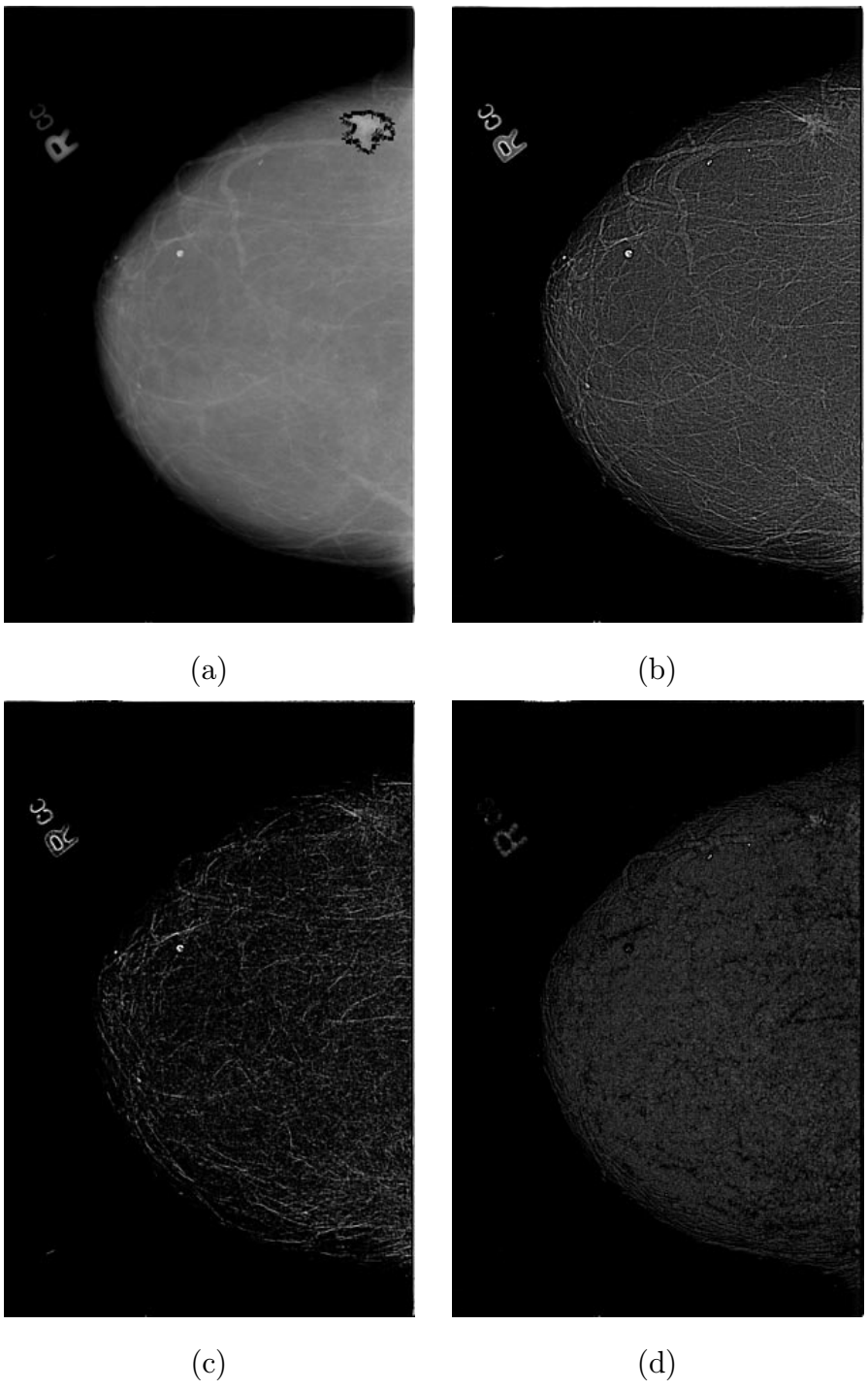

(a) (b)

(c) (d)

Fig. 5.49. (a) Original mammogram with the spiculated lesion outlined. (b) Background subtracted image I_1. (c) Normal linear structure map I_m contains the spiculations. (d) Residual image does not preserve the spiculations.

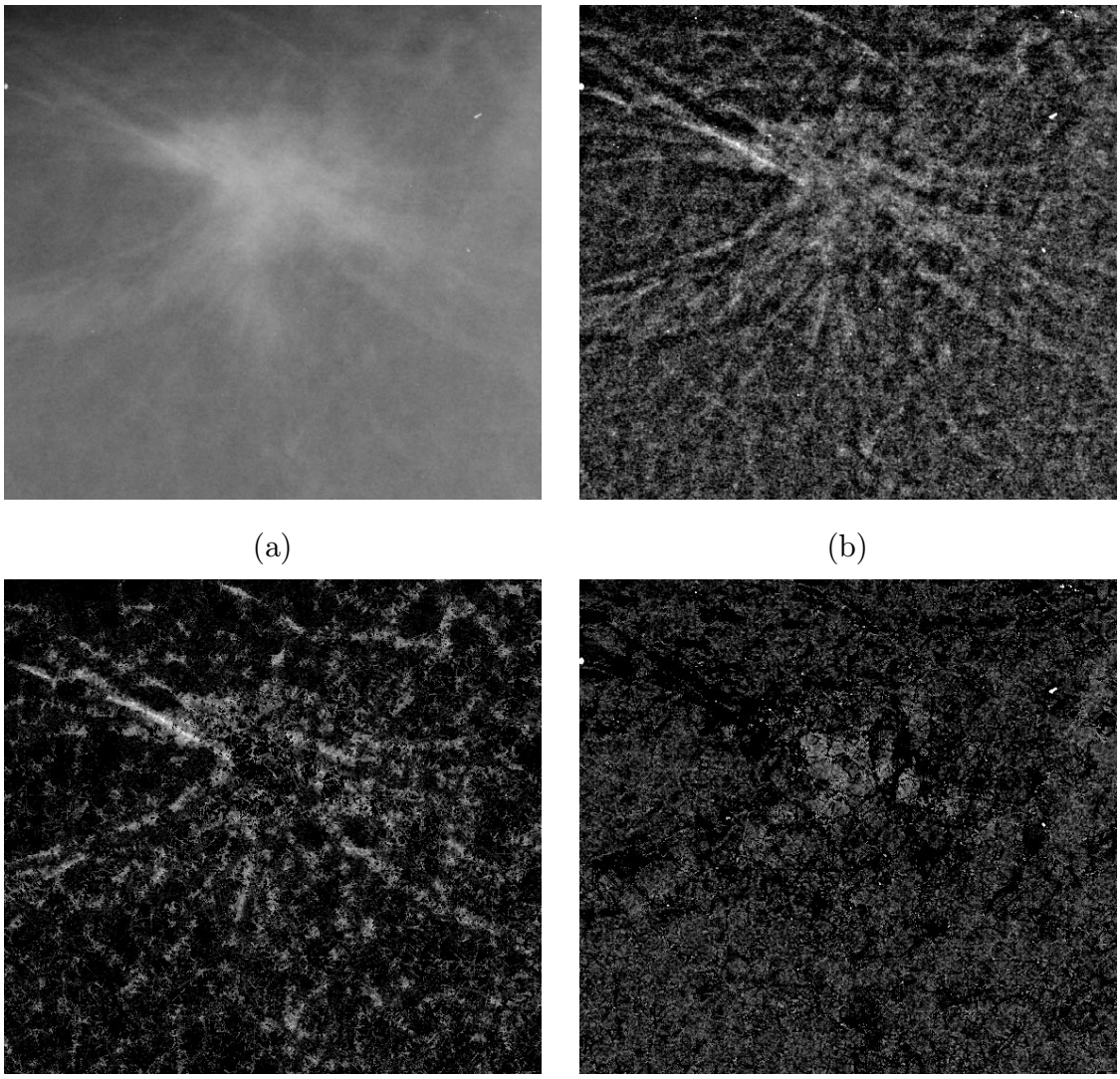

(a) (b)

(c) (d)

Fig. 5.50. Results in Figure 5.49 repeated for the region centered at the spiculated lesion. (a) Original mammogram containing spiculated lesion. (b) Background subtracted image I_1. (c) Normal linear structure map I_m contains the spiculations. (d) Residual image does not preserve the spiculations.

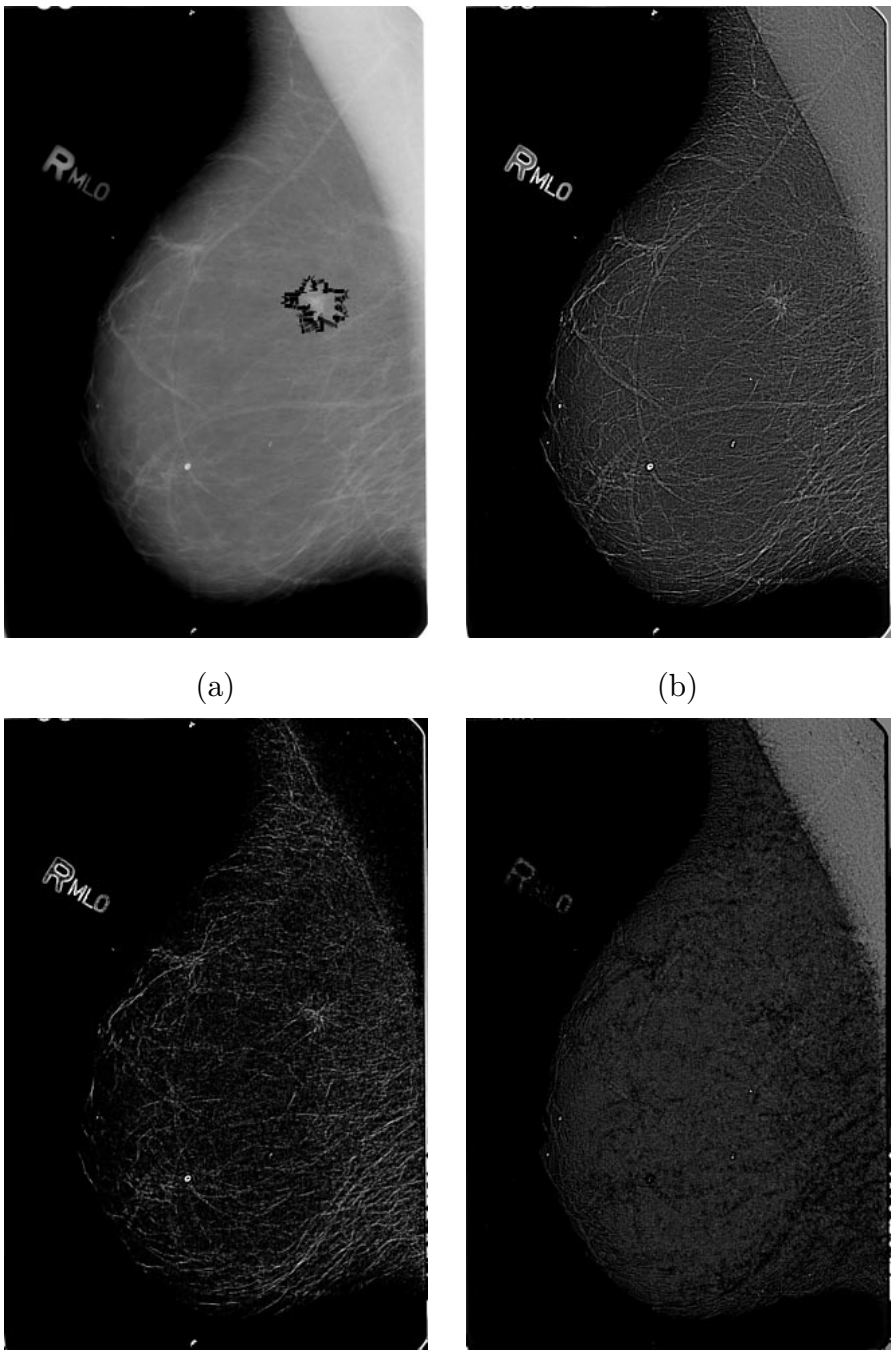

(a) (b)

(c) (d)

Fig. 5.51. (a) Original mammogram with the spiculated lesion outlined. (b) Background subtracted image I_1. (c) Normal linear structure map I_m contains the spiculations. (d) Residual image does not preserve the spiculations.

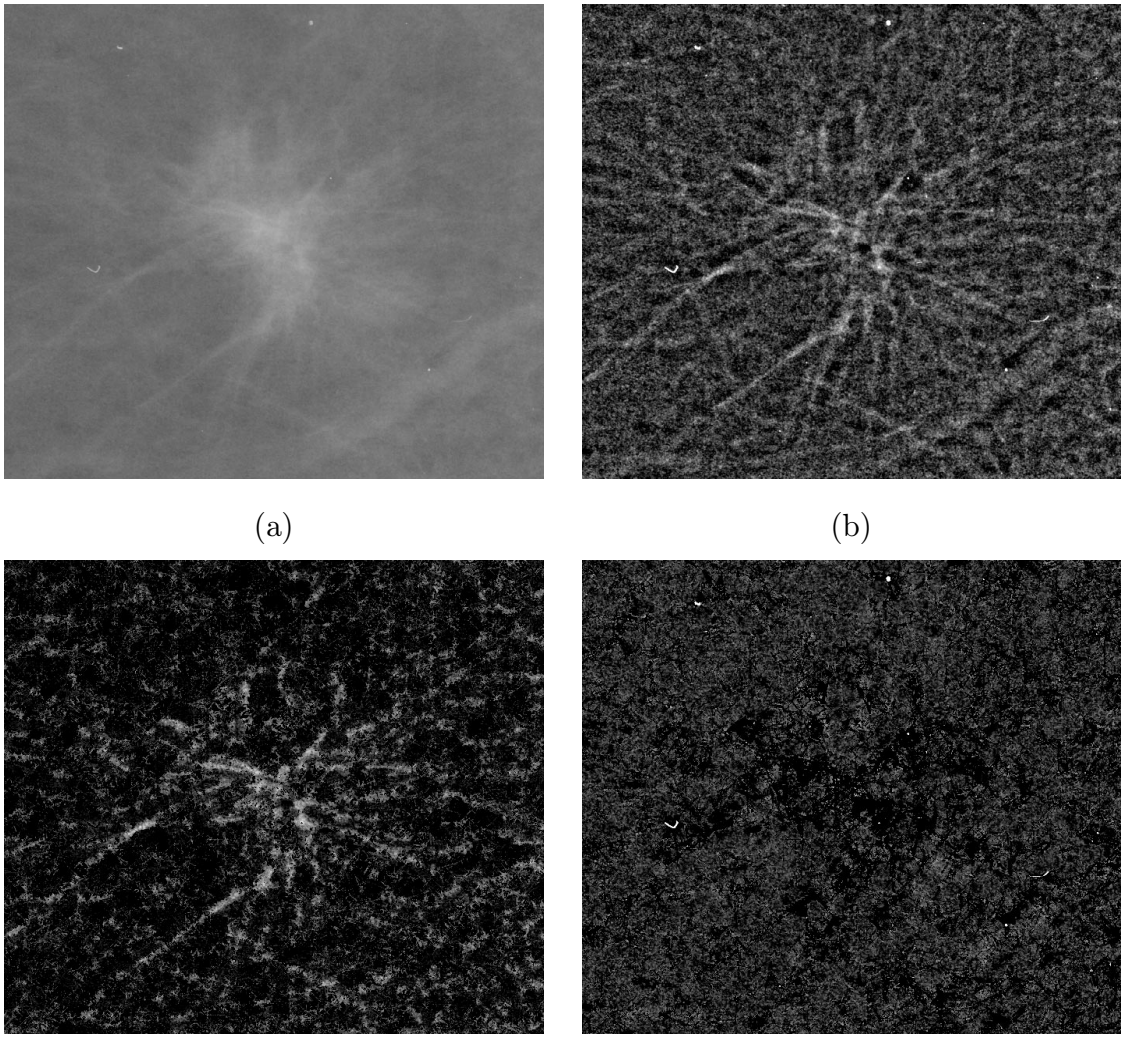

(a) (b)

(c) (d)

Fig. 5.52. Results in Figure 5.51 repeated for the region centered at the spiculated lesion. (a) Original mammogram containing spiculated lesion. (b) Background subtracted image I_1. (c) Normal linear structure map I_m contains the spiculations. (d) Residual image does not preserve the spiculations.

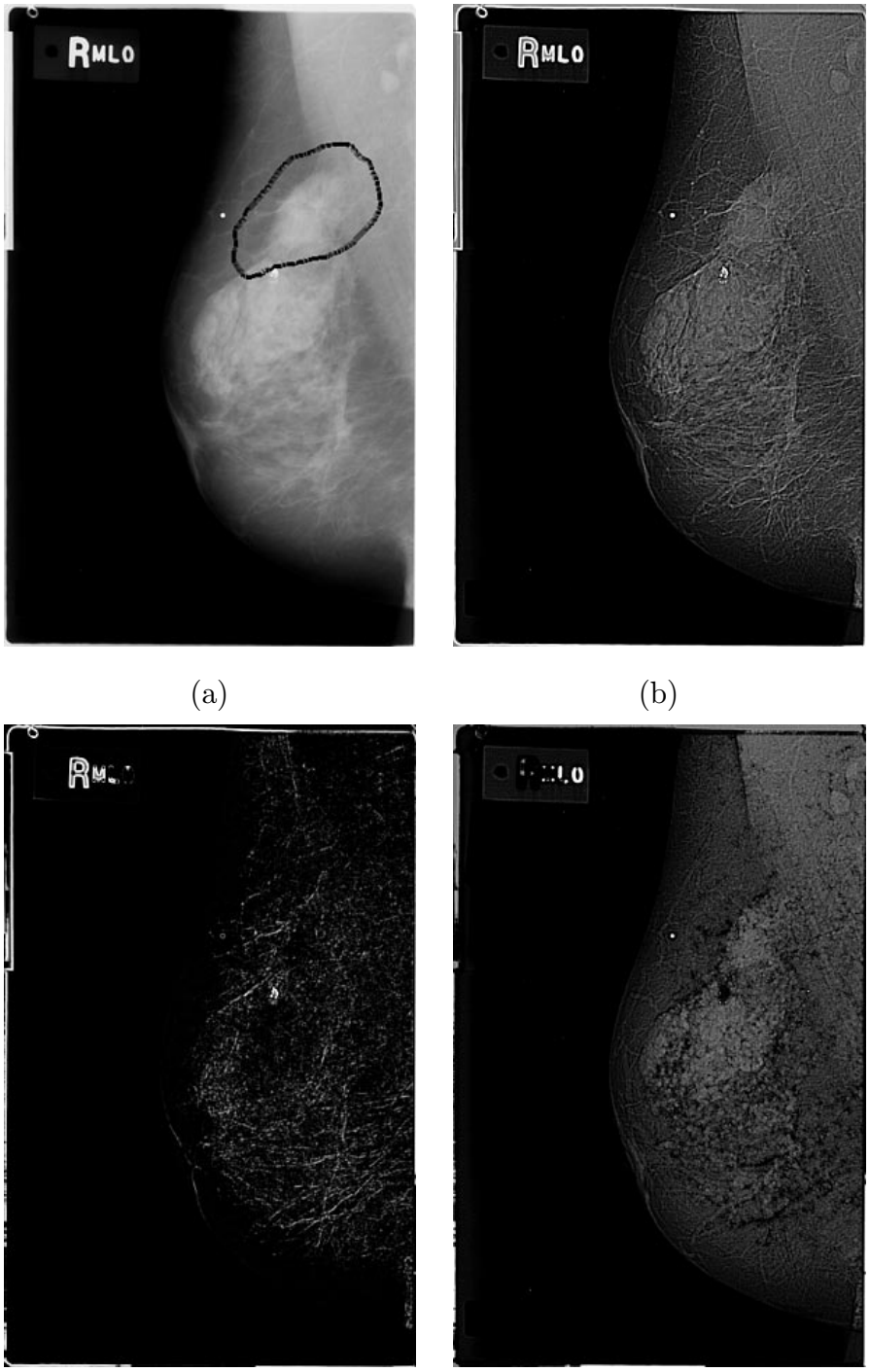

(a) (b)

(c) (d)

Fig. 5.53. (a) Original mammogram with the spiculated lesion outlined. (b) Background subtracted image I_1. (c) Normal linear structure map I_m contains the spiculations. (d) Residual image does not preserve the spiculations.

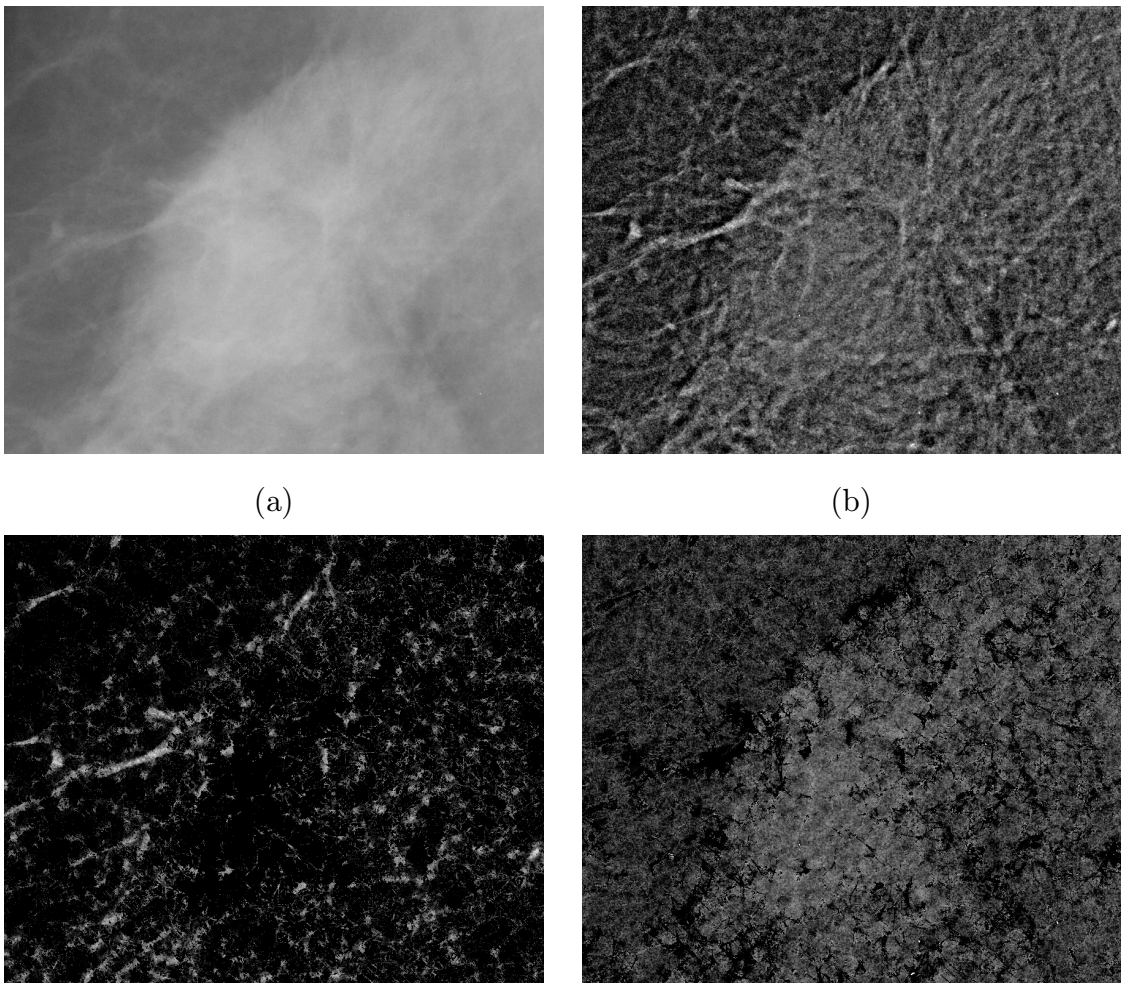

(a) (b)

(c) (d)

Fig. 5.54. Results in Figure 5.53 repeated for the region centered at the spiculated lesion. (a) Original mammogram containing spiculated lesion. (b) Background subtracted image I_1. (c) Normal linear structure map I_m contains the spiculations. (d) Residual image does not preserve the spiculations.

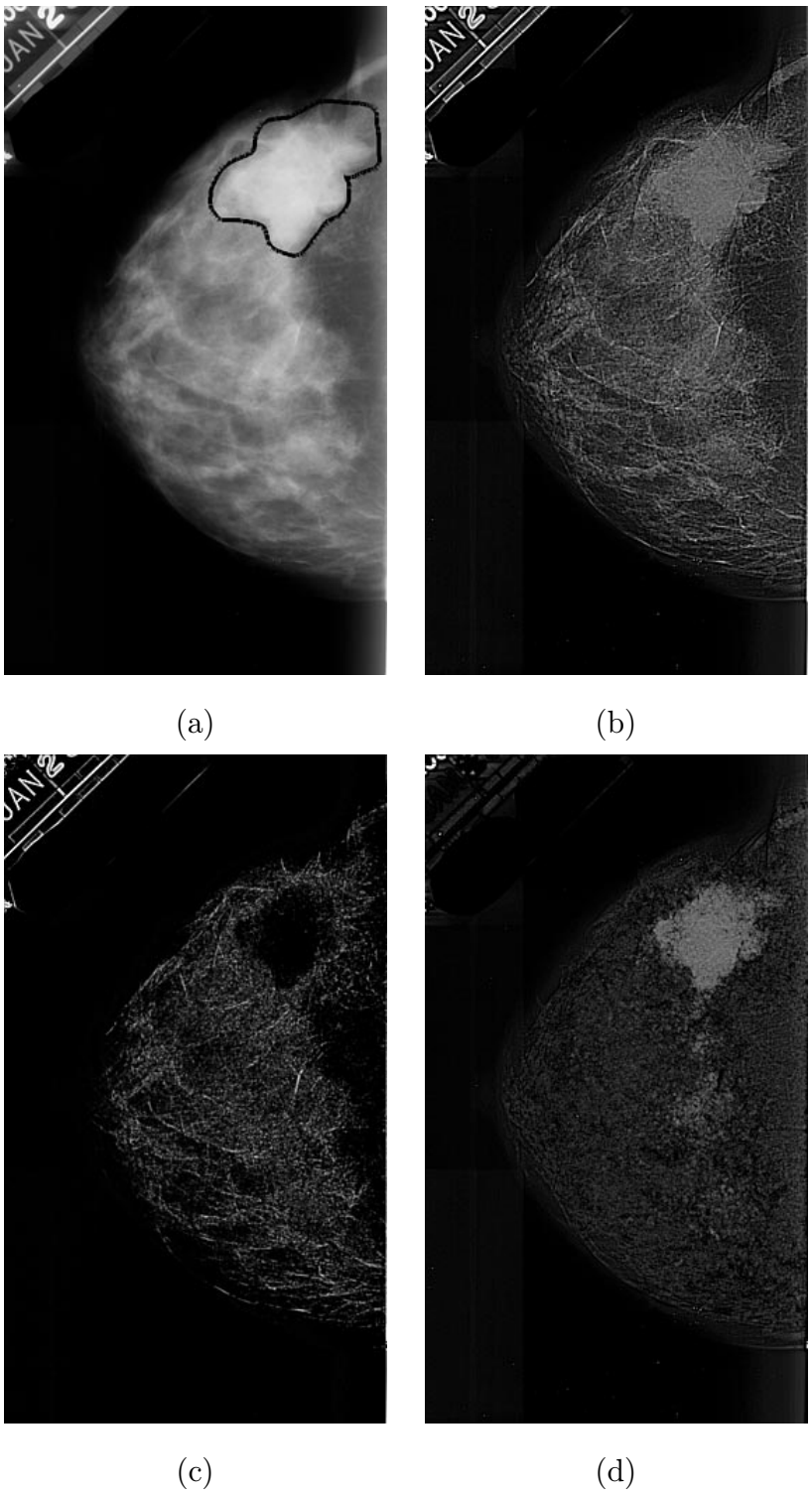

(a) (b)

(c) (d)

Fig. 5.55. (a) Original mammogram with the spiculated lesion outlined. (b) Background subtracted image I_1. (c) Normal linear structure map I_m contains the spiculations. (d) Residual image does not preserve the spiculations.

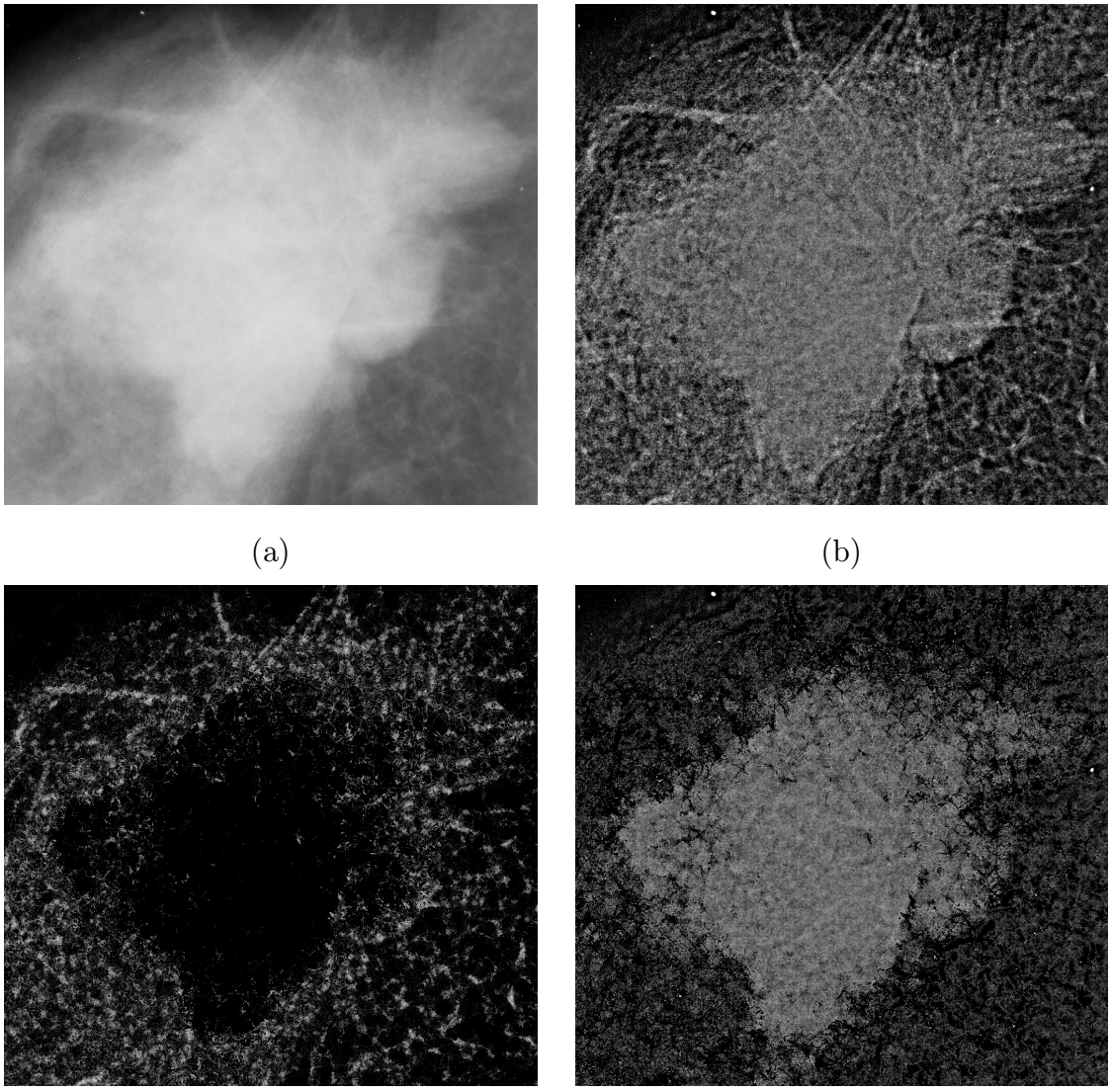

(a) (b)

(c) (d)

Fig. 5.56. Results in Figure 5.55 repeated for the region centered at the spiculated lesion. (a) Original mammogram containing spiculated lesion. (b) Background subtracted image I_1. (c) Normal linear structure map I_m contains the spiculations. (d) Residual image does not preserve the spiculations.

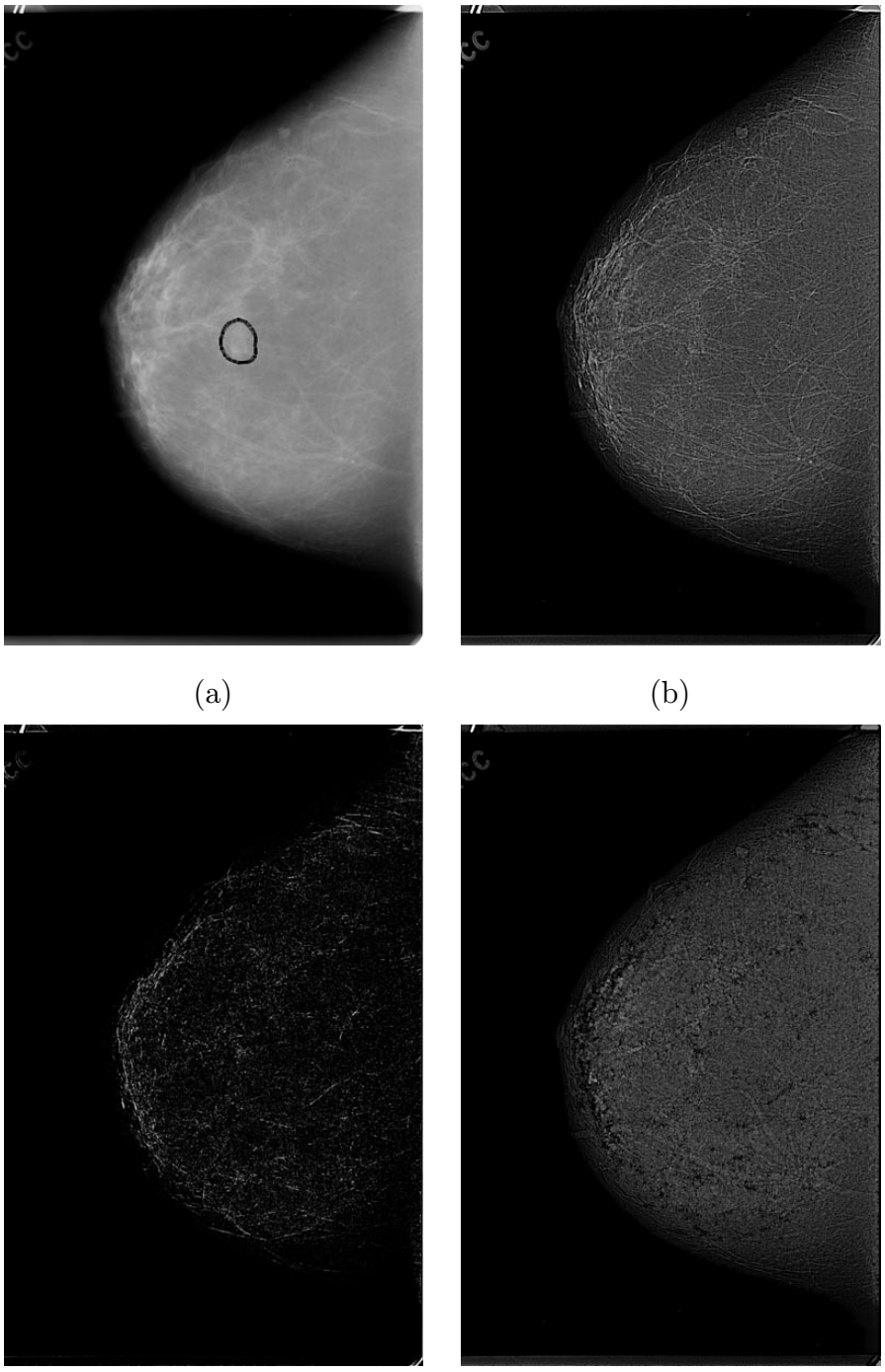

(a) (b)

(c) (d)

Fig. 5.57. (a) Original mammogram with the microcalcifications outlined. (b) Background subtracted image I_1. (c) Normal linear structure map I_m. (d) Residual image with more conspicuous microcalcifications.

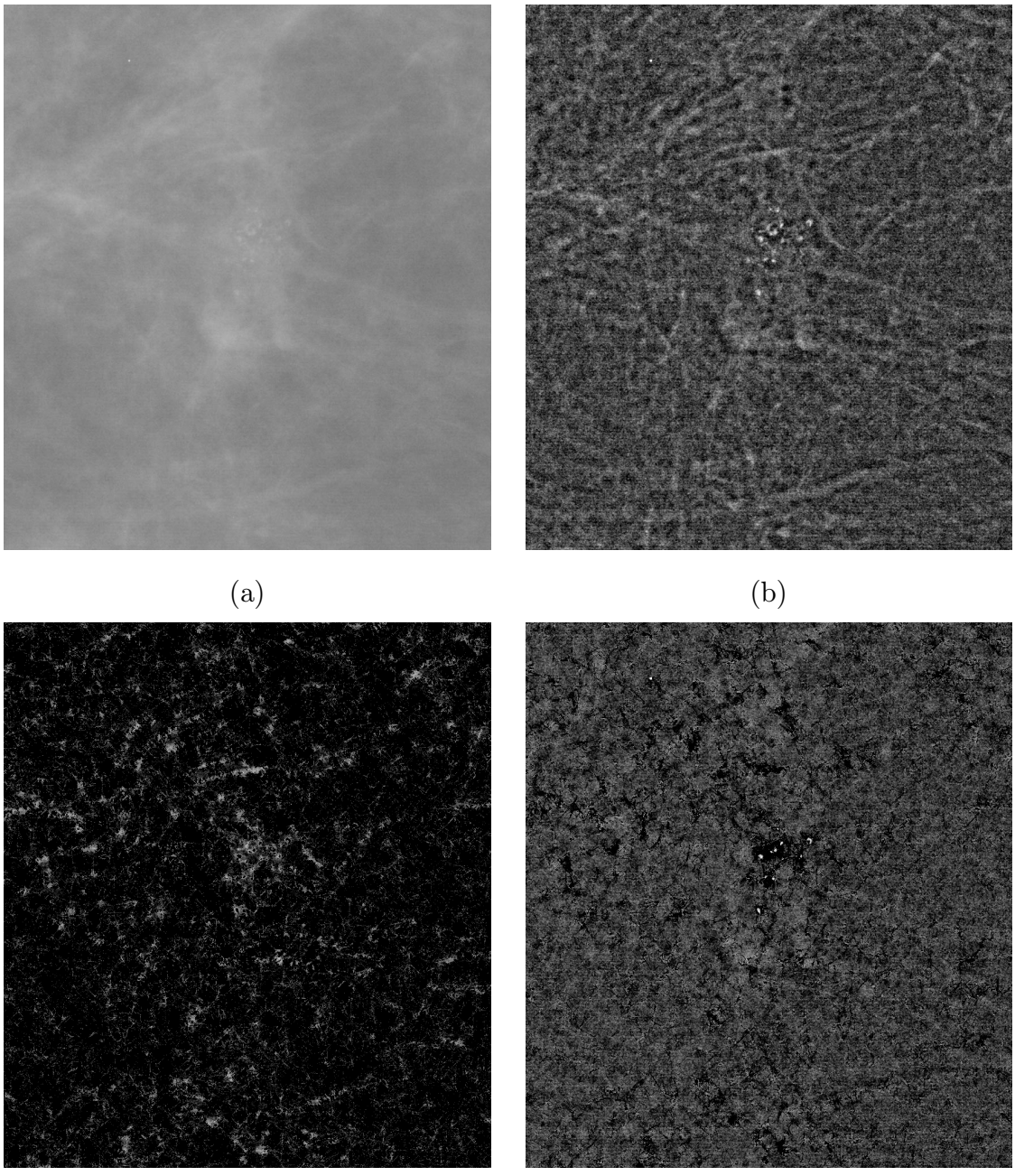

(a) (b)

(c) (d)

Fig. 5.58. Results in Figure 5.57 repeated for the region centered at the microcalcifications. (a) Original mammogram containing microcalcifications. (b) Background subtracted image I_1. (c) Normal linear structure map I_m. (d) Residual image with more conspicuous microcalcifications.

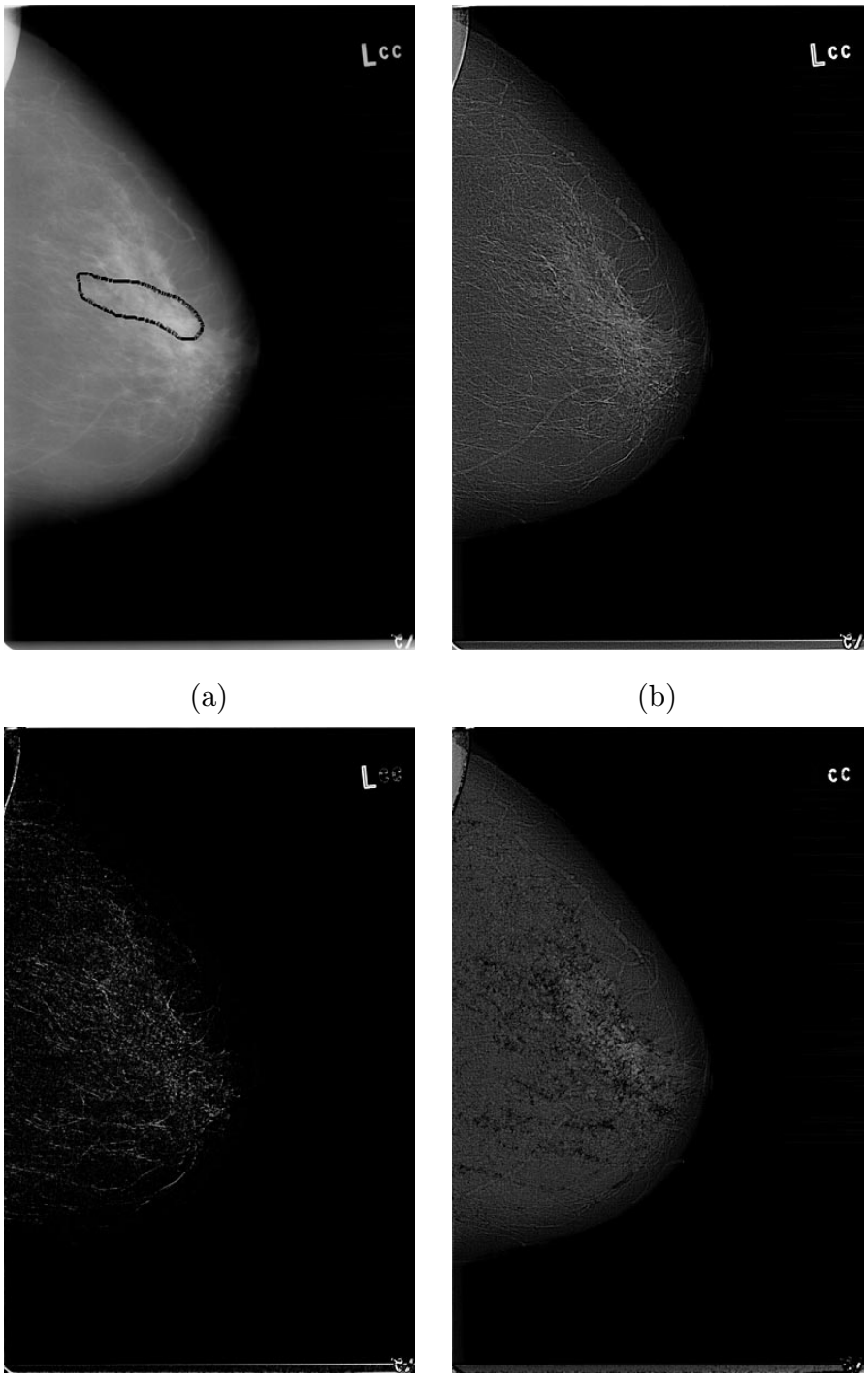

(a) (b)

(c) (d)

Fig. 5.59. (a) Original mammogram with the microcalcifications outlined. (b) Background subtracted image I_1. (c) Normal linear structure map I_m. (d) Residual image with more conspicuous microcalcifications.

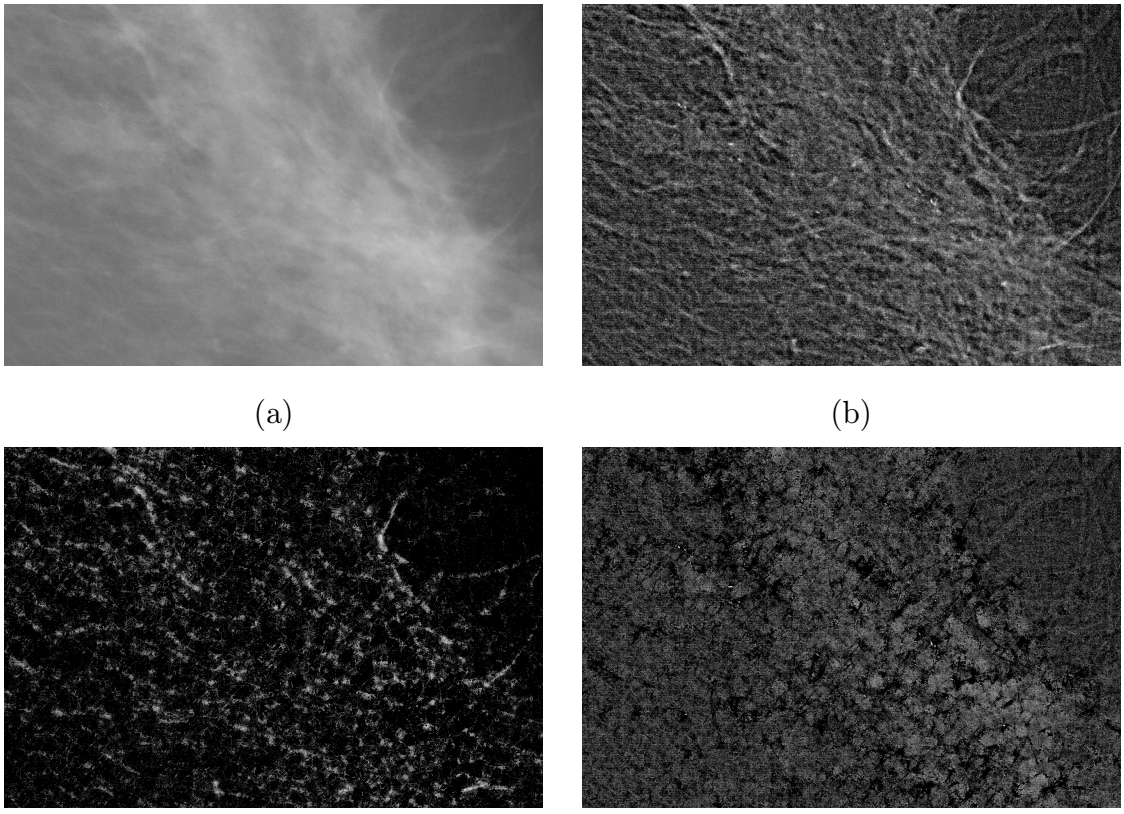

(a) (b)

(c) (d)

Fig. 5.60. Results in Figure 5.59 repeated for the region centered at the microcalcifications. (a) Original mammogram containing microcalcifications. (b) Background subtracted image I_1. (c) Normal linear structure map I_m. (d) Residual image with more conspicuous microcalcifications.

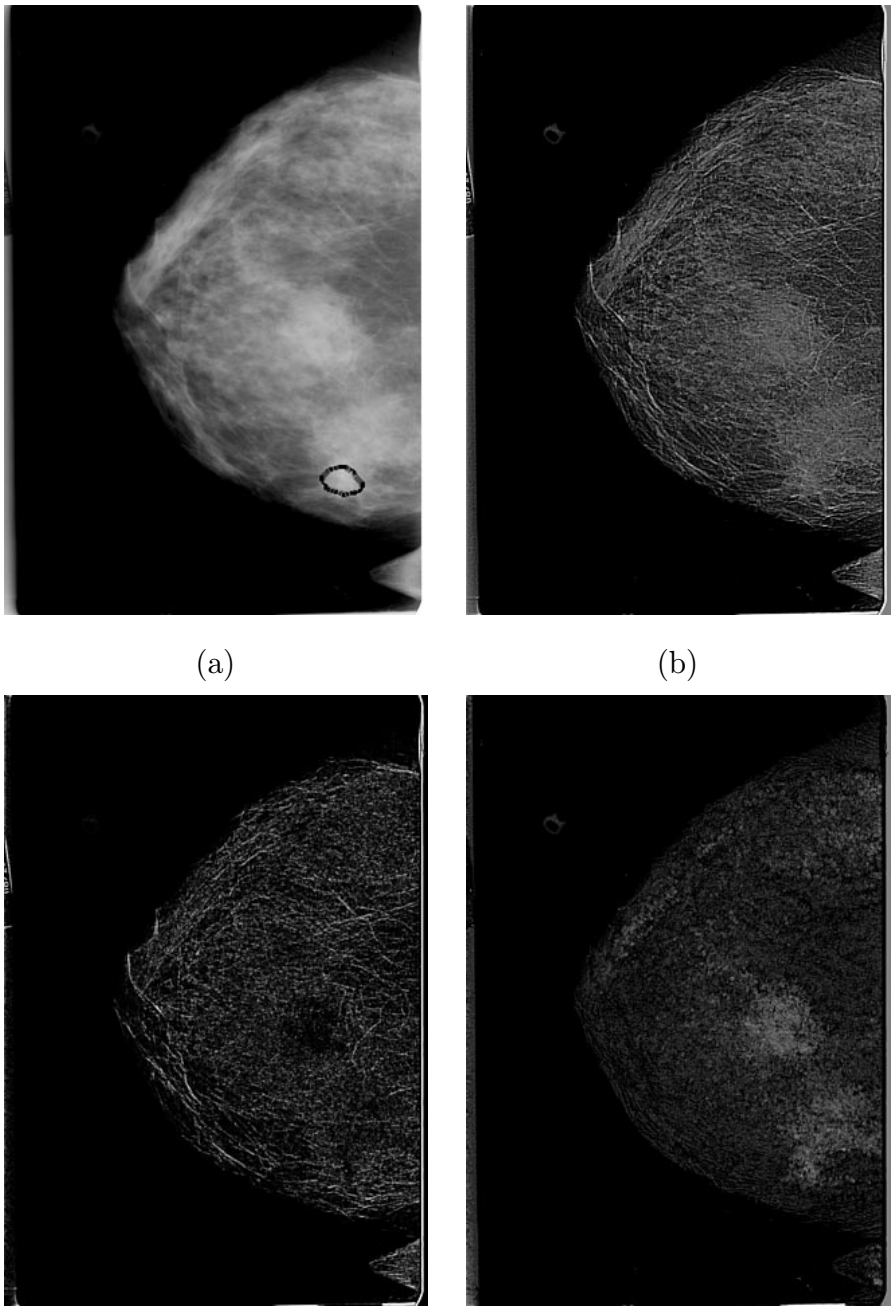

(a) (b)

(c) (d)

Fig. 5.61. (a) Original mammogram with the microcalcifications outlined. (b) Background subtracted image I_1. (c) Normal linear structure map I_m. (d) Residual image with more conspicuous microcalcifications.

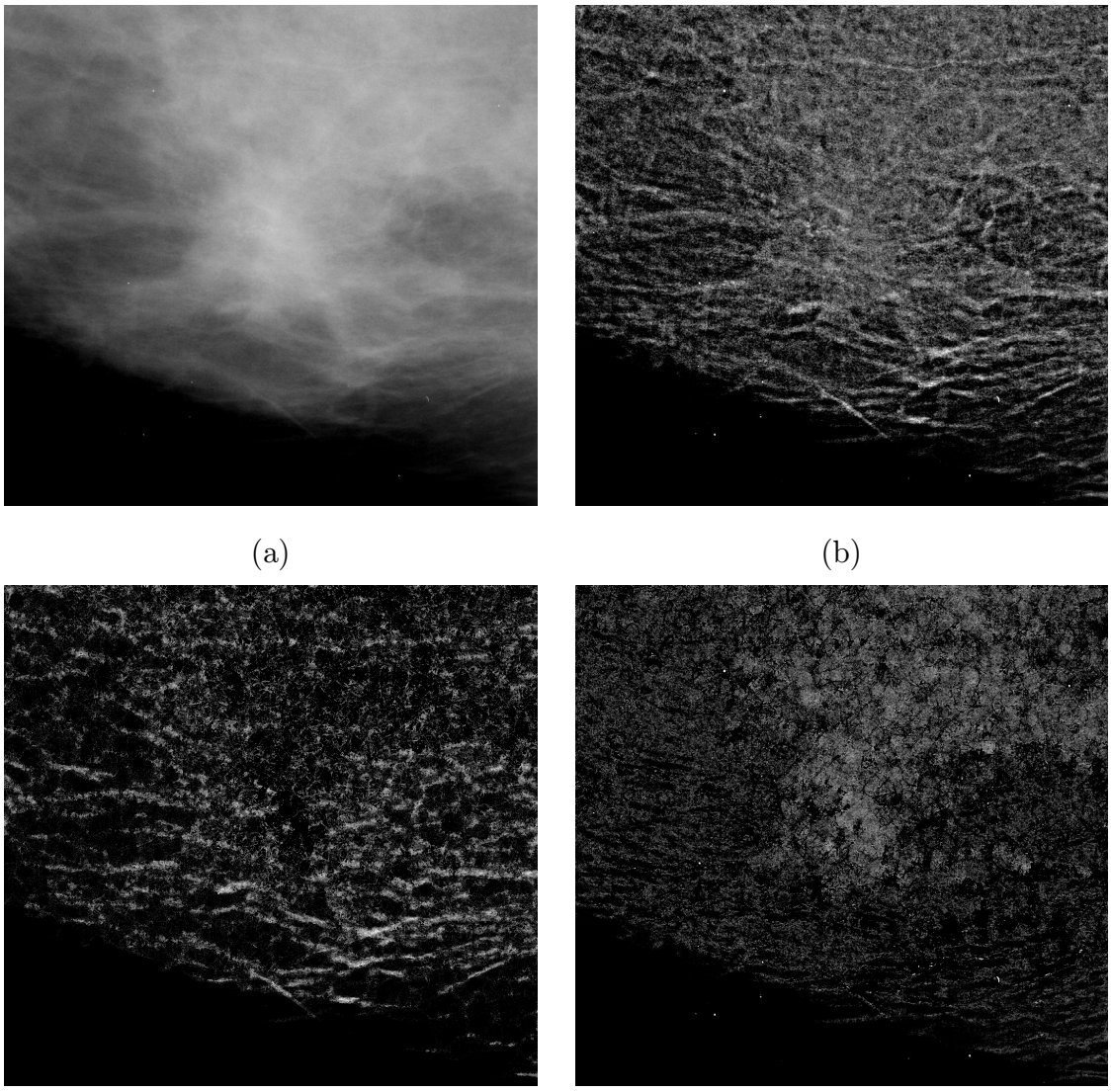

(a) (b)

(c) (d)

Fig. 5.62. Results in Figure 5.61 repeated for the region centered at the microcalcifications. (a) Original mammogram containing microcalcifications. (b) Background subtracted image I_1. (c) Normal linear structure map I_m. (d) Residual image with more conspicuous microcalcifications.

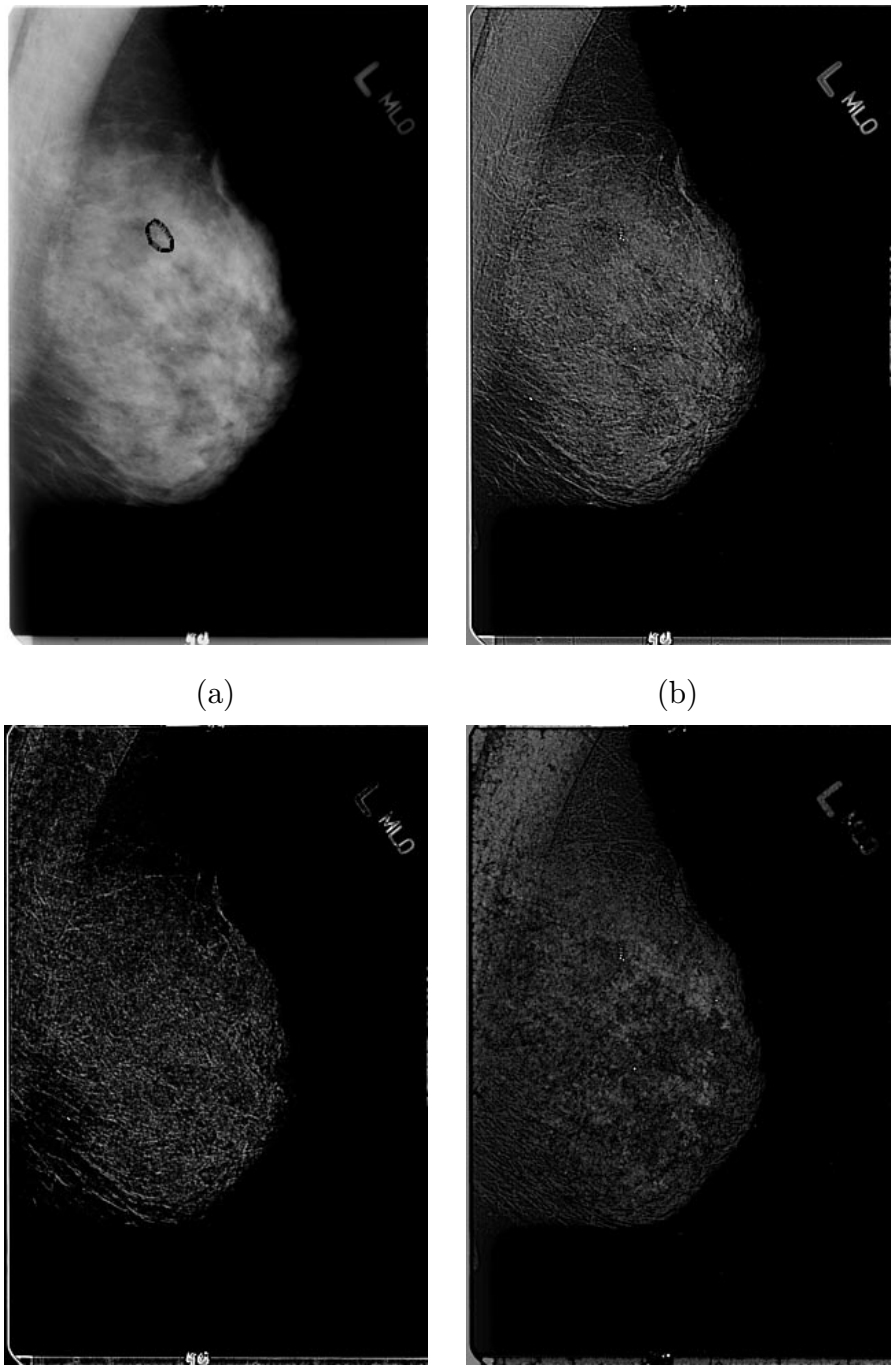

(a) (b)

(c) (d)

Fig. 5.63. (a) Original mammogram with the microcalcifications outlined. (b) Background subtracted image I_1. (c) Normal linear structure map I_m. (d) Residual image with more conspicuous microcalcifications.

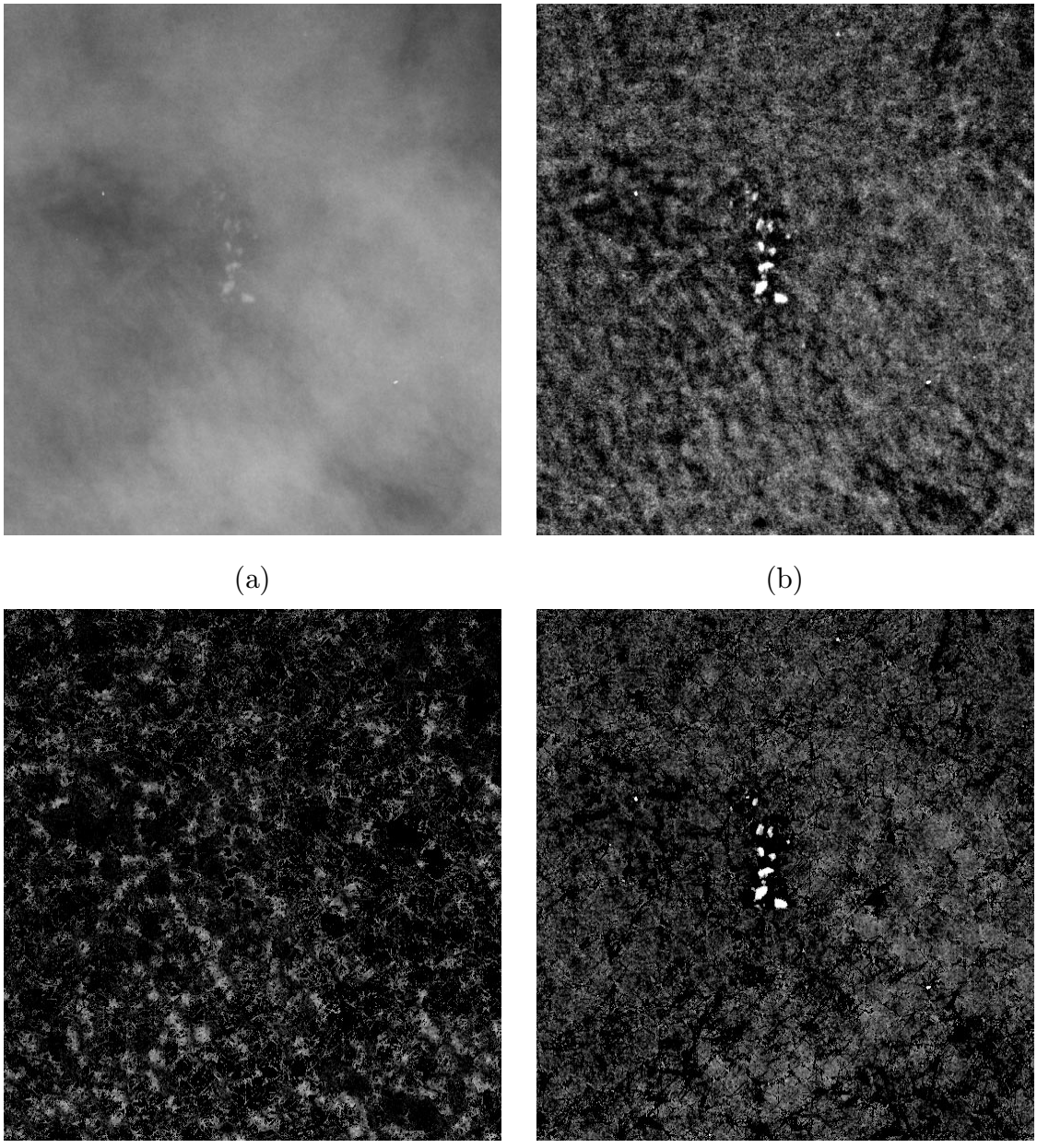

(a) (b)

(c) (d)

Fig. 5.64. Results in Figure 5.63 repeated for the region centered at the microcalcifications. (a) Original mammogram containing microcalcifications. (b) Background subtracted image I_1. (c) Normal linear structure map I_m. (d) Residual image with more conspicuous microcalcifications.

6. CONCLUSION

In this thesis, we have studied several aspects of computer aided diagnosis (CAD) in digital mammography. In particular, we proposed two CAD techniques — a multiresolution feature analysis and classification approach for the detection of spiculated lesions, and a normal mammogram characterization algorithm.

Spiculated lesions are strong indicators of malignant breast cancer, therefore it is very important to detect them as soon as possible. Computer aided detection of tumors generally consists of feature extraction followed by classification. However, it has proved difficult to determine the size of the neighborhood that should be used to extract local features of spiculated lesions. Our proposed multiresolution image analysis algorithm addressed this problem by extracting and classifying features at multiple resolutions. This is a fundamental difference in our method compared to other approaches. In addition, this multiresolution feature analysis scheme enables us to choose a fairly small neighborhood for feature extraction at each resolution, hence computationally more efficient than having to use a larger neighborhood for feature extraction to accommodate larger lesions. Furthermore, the top-down classification scheme we use requires less computation by starting with the coarsest resolution image (least amount of data) and propagating detection results to finer resolutions. Experimental results showed that our algorithm is capable of detecting spiculated lesions of very different sizes at low false positive rates.

We designed a new feature, known as the standard deviation of the folded gradient orientations, that responds strongly to stellate patterns in the image. We showed that this feature reflects the actual local gradient orientation variances, and is robust with regard to image rotation. However, some spiculated lesions lack of visible

spiculations in all directions, hence easily cause miss detection. On the other hand, some normal regions in a mammogram may have linear markings in several different directions and be mistakenly detected as abnormal spiculations. A thorough study of the contribution of each feature in detecting the spiculated lesions would improve the overall performance of this algorithm. This study would involve measuring performance of individual feature as well as performance of different feature combinations in detecting tumors. It can help further refine the features, and optimize the number of features that should be used in classification. This is one topic for future work.

Another possible improvement to this algorithm would be splitting the classification process into two stages: detection and confirmation. In the detection stage, only those features that are especially responsive to spiculated lesions, such as the standard deviation of the folded gradient orientations, are used to identify candidate spiculated regions. Sensitivity would be essential in this stage and higher false positive rate is allowed so that very subtle spiculated lesions can be detected. The confirmation stage is used to eliminate those false positives by using features that identify tumor centers, such as the local mean pixel brightness. This two-stage process is also expected to be faster, not only because fewer features are used for classification in each stage, but also because significantly less amount of data need to be considered in the second stage. This is one topic for future work.

Characterizing normal mammograms is an important issue that has been overlooked by most researchers. Since cancer treatment is most effective when the cancer is detected early, better methods for analyzing hard abnormal mammograms is required, which are hard because they are very similar to normal mammograms. Without good understanding of what is normal, cancer treatment decision maybe highly suboptimal. We presented a normal mammogram characterization algorithm that specifically identifies and removes normal tissue structures shown in mammograms. This is fundamentally different than other approaches that identify normal mammograms by screening out a specific type of tumor. On the contrary, our technique is independent of the types of abnormalities that may exist in the mammogram.

We proposed a new model for lines and presented a novel line detection algorithm based on this model for extracting normal linear structures from complex background in mammograms. This line detector is capable of extracting lines with very different width, lines with irregular width, as well as curves. It also responds to region boundaries that have a high curvature, because pixels there have properties similar to those of pixels at the end of a thick line. This may not be desirable in some applications. A length check along the direction of the detected lines would be able to distinguish these two situations, since only a few pixels on the boundary would be detected as belonging to a line.

The presented line model is for lines in grayscale images. It can be extended to lines in color images as follows: 1) there exists a string of pixels with similar colors along a certain direction; 2) the surrounding pixels have different colors; and 3) the length is greater than its width. The extension of the corresponding line detection algorithm to color images would require substitute scalar (graylevel) operations with vector (color components) operations. Note that it may be necessary to first convert images to a uniform color space, such as (L^*, u^*, v^*), where visual difference between two colors is proportional to their Euclidean distance. This is one topic for future work.

Experimental results have shown that suppressing normal background structures enhances the contrast and obviousness of microcalcifications and circumscribed masses. The microcalcification enhancement results of our residual images compared favorably to those of other technique reported in the literature. However, the normal linear structure removal algorithm presented in this thesis removed spiculations of spiculated lesions along with real normal structures. This problem can be dealt with by detecting stellate patterns in the "normal" mask before removal so that abnormal spiculations remain in the residual image. The line orientation information obtained during line detection can be used for this stellate pattern detection. This is one topic for future work.

Ideally, the residual image of a normal mammogram would be uniformly dark and featureless; whereas the residual image of an abnormal mammogram would show abnormalities against a featureless background. However, some much finer normal structures persist in the residual images after removal of the larger linear markings. These constitute fine reticulated patterns of normal background texture. In addition, the removal of the larger linear markings generates black regions that interrupt the finer texture, which makes the identification and removal of the remaining normal background texture more difficult. It may be helpful to fill in those black regions with textures similar to their neighboring normal regions to form a uniform normal background texture. This filling task has to be done with great care since it easily produces another texture in the black regions if the filled texture does not match well with that in the neighborhood. A possible way to do the filling would be modeling the normal texture as an autoregressive process, then estimating its parameters from the non-black regions, and finally generating textures for the black regions based on the estimated parameters. This is one topic for future work.

Another important topic for future work is to directly recognize normal mammograms, rather than mammograms with various possible abnormalities. It is essential to find features that characterize normal regions in the residual images. An analysis of some texture features, such as mean, variance, and skewness, based on a large number of normal residual images could help to make a decision as to what feature combination best characterize normal regions. Since abnormalities in mammograms are highly localized and occupy only a small portion of the whole image, normal detection should be done in small regions. A possible way to achieve this goal would be using a multiresolution image analysis framework similar to the one we presented for spiculated lesion detection. The normal detection shall start from the coarsest resolution. Any region that is classified as abnormal at coarser resolutions eliminate the need for further analysis at finer resolutions, while regions that are classified as normal should be evaluated in more detail at finer resolutions.

LIST OF REFERENCES

LIST OF REFERENCES

[1] D. B. Kopans, *Breast Imaging*. J. B. Lippincott Company, 1989.

[2] L. W. Bassett, V. P. Jackson, R. Jahan, Y. S. Fu, and R. H. Gold, *Diagnosis of Diseases of the Breast*. W. B. Saunders Company, 1997.

[3] G. Cardenosa, "Mammography: An overview," *Proceedings of the 3rd International Workshop on Digital Mammography*, June 9–12 1996, Chicago, Illinois, pp. 3–10.

[4] K. Woods and K. Bowyer, "A general view of detection algorithms," *Proceedings of the 3rd International Workshop on Digital Mammography*, June 9–12 1996, Chicago, U.S.A., pp. 385–390.

[5] M. L. Giger, F.-F. Yin, K. Doi, C. E. Metz, R. A. Schmidt, and C. J. Vyborny, "Investigation of methods for the computerized detection and analysis of mammographic masses," *Proceedings of SPIE*, February 6 - 8 1990, Bellingham, Washington, pp. 183–184.

[6] N. Karssemeijer, "A stochastic model for automated detection of calcifications in digital mammograms," *12th International Conference on Information Processing in Medical Imaging*, 1991, Wye, UK, pp. 227–238.

[7] C. J. Vyborny and M. L. Giger, "Computer vision and artificial intelligence in mammography," *American Journal of Roentgenology*, vol. 162, no. 3, pp. 699–708, March 1994.

[8] W. P. Kegelmeyer, Jr., J. M. Pruneda, P. D. Bourland, A. Hillis, M. W. Riggs, and M. L. Nipper, "Computer-aided mammographic screening for spiculated lesions," *Radiology*, vol. 191, no. 2, pp. 331–336, May 1994.

[9] M. L. Comer, S. Liu, and E. J. Delp, "Statistical segmentation of mammograms," *Proceedings of the 3rd International Workshop on Digital Mammography*, June 9–12 1996, Chicago, Illinois, pp. 475–478.

[10] S. Liu and E. J. Delp, "Multiresolution detection of stellate lesions in mammograms," *Proceedings of the IEEE International Conference on Image Processing*, October 26–29 1997, Santa Barbara, California, pp. 109–112.

[11] S. Liu, C. F. Babbs, and E. J. Delp, "Multiresolution detection of spiculated lesions in mammograms," *IEEE Transactions on Image Processing (in review)*, 1998.

[12] S. Liu, C. F. Babbs, and E. J. Delp, "Normal mammogram analysis and recognition," *Proceedings of the IEEE International Conference on Image Processing*, October 4–7 1998, Chicago, Illinois, pp. 727–731.

[13] L. Tabar and P. B. Dean, *Teaching Atlas of Mammography.* Georg Thieme Verlag, 2nd revised ed., 1985.

[14] D. Brzakovic and M. Neskovic, "Mammogram screening using multiresolution-based image segmentation," *International Journal of Pattern Recognition and Artificial Intelligence*, vol. 7, no. 6, pp. 1437–1460, 1993.

[15] J. G. Elmore, C. K. Wells, C. H. Lee, D. H. Howard, and A. R. Feinstein, "Variability in radiologists' interpretations of mammograms," *New England Journal of Medicine*, vol. 331, no. 22, pp. 1493–1499, December 1994.

[16] D. B. Spring and K. Kimbrell-Wilmot, "Evaluating the success of mammography at the local level: how to conduct an audit of your practice," *Radiologic Clinics of North America*, vol. 25, no. 5, pp. 983–992, September 1987.

[17] E. A. Sickles, "Quality assurance. how to audit your own mammography practice," *Radiologic Clinics of North America.*, vol. 30, no. 1, pp. 265–275, January 1992.

[18] P. Y. Poon, P. Cairns, A. C. Lata, D. W. Marcuzzi, and G. M. Cooke, "Medical audit of mammography: A simplified alternative," *Canadian Association of Radiologists Journal*, vol. 43, no. 3, pp. 191–194, June 1992.

[19] L. Berlin and R. W. Hendrix, "Perceptual errors and negligence," *American Journal of Roentgenology*, vol. 170, no. 4, pp. 863–867, April 1998.

[20] P. J. Robinson, "Radiology's achilles' heel: Error and variation in the interpretation of the roentgen image," *British Journal of Radiology*, vol. 70, no. 839, pp. 1085–1098, November 1997.

[21] D. B. Kopans, "The positive predictive value of mammography," *American Journal of Roentgenology*, vol. 158, no. 3, pp. 521–526, March 1993.

[22] A. M. Knutzen and J. J. Gisvold, "Likelihood of malignant disease for various categories of mammographically detected, nonpalpable breast lesions," *Mayo Clinic Proceedings*, vol. 68, no. 5, pp. 454–460, May 1993.

[23] R. N. Strickland and H. I. Hahn, "Wavelet transforms for detecting microcalcifications in mammograms," *IEEE Transactions on Medical Imaging*, vol. 15, no. 2, pp. 218–229, April 1996.

[24] R. M. Nishikawa, M. L. Giger, K. Doi, C. J. Vyborny, and R. A. Schmidt, "Computer-aided detection of clustered microcalcifications on digital mammograms," *Medical and Biological Engineering and Computing*, vol. 33, no. 2, pp. 174–178, March 1995.

[25] H.-D. Cheng, Y. M. Lui, and R. I. Freimanis, "A novel approach to microcalcification detection using fuzzy logic technique," *IEEE Transactions on Medical Imaging*, vol. 17, no. 3, pp. 442–450, June 1998.

[26] H.-P. Chan, S.-C. B. Lo, B. Sahiner, K. L. Lam, and M. A. Helvie, "Computer-aided detection of mammographic microcalcifications: Pattern recognition with an artificial neural network," *Medical Physics*, vol. 22, no. 10, pp. 1555–1567, October 1995.

[27] R. H. Nagel, R. M. Nishikawa, J. Papaioannou, and K. Doi, "Analysis of methods for reducing false positives in the automated detection of clustered microcalcifications in mammograms," *Medical Physics*, vol. 25, no. 8, pp. 1502–1506, August 1998.

[28] M. N. Gurcan, Y. Yardimci, A. E. Cetin, and R. Ansari, "Detection of microcalcifications in mammograms using higher order statistics," *IEEE Signal Processing Letters*, vol. 4, no. 8, pp. 213–216, August 1997.

[29] L. Shen, R. M. Rangayyan, and J. E. L. Desautels, "Applications of shape analysis to mammographic calcifications," *IEEE Transactions on Medical Imaging*, vol. 13, no. 2, pp. 263–274, June 1994.

[30] A. P. Dhawan, Y. Chitre, C. Kaiser-Bonasso, and M. Moskowitz, "Analysis of mammographic microcalcifications using gray-level image structure features," *IEEE Transactions on Medical Imaging*, vol. 15, no. 3, pp. 246–259, June 1996.

[31] S.-M. Lai, X. Li, and W. F. Bischof, "On techniques for detecting circumscribed masses in mammograms," *IEEE Transactions on Medical Imaging*, vol. 8, no. 4, pp. 377–386, December 1989.

[32] N. Petrick, H.-P. Chan, B. Sahiner, and D. Wei, "An adaptive density-weighted contrast enhancement filter for mammographic breast mass detection," *IEEE Transactions on Medical Imaging*, vol. 15, no. 1, pp. 59–67, February 1996.

[33] F.-F. Yin, M. L. Giger, K. Doi, C. J. Vyborny, and R. A. Schmidt, "Computerized detection of masses in digital mammograms: Automated alignment of breast images and its effect on bilateral-subtraction technique," *Medical Physics*, vol. 21, no. 3, pp. 445–452, March 1994.

[34] A. J. M'endez, P. G. Tahoces, M. J. Lado, M. Souto, and J. J. Vidal, "Computer-aided diagnosis: Automatic detection of malignant masses in digitized mammograms," *Medical Physics*, vol. 25, no. 6, pp. 957–964, June 1998.

[35] D. Wei, H.-P. Chan, N. Petrick, B. Sahiner, M. A. Helvie, D. D. Adler, and M. M. Goodsitt, "False-positive reduction technique for detection of masses on digital mammograms: Global and local multiresolution texture analysis," *Medical Physics*, vol. 24, no. 6, pp. 903–914, June 1997.

[36] M. A. Kupinski and M. L. Giger, "Automated seeded lesion segmentation on digital mammograms," *IEEE Transactions on Medical Imaging*, vol. 17, no. 4, pp. 510–517, August 1998.

[37] D. Brzakovic, X. M. Luo, and P. Brzakovic, "An approach to automated detection of tumors in mammograms," *IEEE Transactions on Medical Imaging*, vol. 9, no. 3, pp. 233–241, September 1990.

[38] H. D. Li, M. Kallergi, L. P. Clarke, V. K. Jain, and R. A. Clark, "Markov random field for tumor detection in digital mammography," *IEEE Transactions on Medical Imaging*, vol. 14, no. 3, pp. 565–576, September 1995.

[39] W. P. Kegelmeyer, Jr., "Computer detection of stellate lesions in mammograms," *Proceedings of the SPIE Conference on Biomedical Image Processing and Three-Dimensional Microscopy*, February 10-13 1992, San Jose, California, pp. 446–454.

[40] N. Karssemeijer and G. M. Brake, "Detection of stellate distortions in mammograms," *IEEE Transactions on Medical Imaging*, vol. 15, no. 5, pp. 611–619, October 1996.

[41] Z. Huo, M. L. Giger, C. J. Vyborny, U. Bick, P. Lu, D. E. Wolverton, and R. A. Schmidt, "Analysis of spiculation in the computerized classification of mammographic masses," *Medical Physics*, vol. 22, no. 10, pp. 1569–1579, October 1995.

[42] H. Kobatake and Y. Yoshinaga, "Detection of spicules on mammogram based on skeleton analysis," *IEEE Transactions on Medical Imaging*, vol. 15, no. 3, pp. 235–245, June 1996.

[43] B. Sahiner, H.-P. Chan, N. Petrick, M. A. Helvie, and M. M. Goodsitt, "Computerized characterization of masses on mammograms: The rubber band strightening transform and texture analysis," *Medical Physics*, vol. 25, no. 4, pp. 516–526, April 1998.

[44] R. M. Rangayyan, N. M. El-Faramawy, J. E. L. Desautels, and O. A. Alim, "Measures of acutance and shape for classification of breast tumors," *IEEE Transactions on Medical Imaging*, vol. 16, no. 6, pp. 799–810, December 1997.

[45] J. Kilday, F. Palmieri, and M. D. Fox, "Classifying mammographic lesions using computerized image analysis," *IEEE Transactions on Medical Imaging*, vol. 12, no. 4, pp. 664–669, December 1993.

[46] S. Pohlman, K. A. Powell, N. A. Obuchowski, W. A. Chilcote, and S. Grundfest-Broniatowski, "Quantitative classification of breast tumors in digitized mammogramsquantitative classification of breast tumors in digitized mammograms," *Medical Physics*, vol. 23, no. 8, pp. 1337–1345, August 1996.

[47] J. J. Heine, S. R. Deans, D. K. Cullers, R. Stauduhar, and L. P. Clarke, "Multiresolution statisitical analysis of high-resolution digital mammograms," *IEEE Transactions on Medical Imaging*, vol. 16, no. 5, pp. 503–515, October 1997.

[48] B. L. Kalman, W. R. Reinus, S. C. Kwasny, A. Laine, and L. Kotner, "Prescreening entire mammograms for masses with artificial neural networks: Preliminary results," *Academic Radiology*, vol. 4, no. 6, pp. 405–414, June 1997.

[49] E. L. Thurfjell, K. A. Lernevall, and A. A. Taube, "Benefit of independent double reading in a population-based mammography screening program," *Radiology*, vol. 191, no. 1, pp. 241–244, April 1994.

[50] S. G. Mallat, "A theory for multiresolution signal decomposition: The wavelet representation," *IEEE Transactions on Pattern Analysis and Machine Intelligence*, vol. 11, no. 7, pp. 674–693, July 1989.

[51] M. Unser and A. Aldroubi, "A review of wavelets in biomedical applications," *Proceedings of the IEEE*, vol. 84, no. 4, pp. 626–638, April 1996.

[52] J. G. Proakis and D. G. Manolakis, *Digital Signal Processing.* Macmillan Publishing Company, second ed., 1992.

[53] N. J. Fliege, *Multirate Digital Signal Processing.* John Wiley & Sons, 1994.

[54] A. Cohen, I. Daubechies, and J. C. Feauveau, "Biorthogonal bases of compactly supported wavelets," *Communications on Pure and Applied Mathematics*, vol. XLV, pp. 485–560, 1992.

[55] I. Daubechies, "The wavelet transform, time-frequency localization and signal analysis," *IEEE Transactions on Information Theory*, vol. 36, no. 5, pp. 961–1005, September 1990.

[56] O. Rioul and P. Duhamel, "Fast algorithms for discrete and continuous wavelet transforms," *IEEE Transactions on Information Theory*, vol. 38, no. 2, pp. 569–586, March 1992.

[57] I. Daubechies and J. C. Lagarias, "Two-scale difference equations i. existence and global regularity of solutions," *SIAM Journal of Mathematical Analysis*, vol. 22, no. 5, pp. 1388–1410, September 1991.

[58] P. P. Vaidyanathan, *Multirate Systems and Filter Banks.* P T R Prentice-Hall, Inc., 1993.

[59] J. Kovačević and M. Vetterli, "Nonseparable multidimensional perfect reconstruction filter banks and wavelet bases for R^n," *IEEE Transactions on Information Theory*, vol. 38, no. 2, pp. 533–555, March 1992.

[60] L. Prasad and S. S. Iyengar, *Wavelet Analysis with Applications to Image Processing*. CRC Press LLC, 1997.

[61] A. F. Laine, S. Schuler, J. Fan, and W. Huda, "Mammographic feature enhancement by multiscale analysis," *IEEE Transactions on Medical Imaging*, vol. 13, no. 4, pp. 725–752, December 1994.

[62] C. H. Chen and G. G. Lee, "Image segmentation using multiresolution wavelet analysis and expectation-maximization (EM) algorithm for digital mammography," *International Journal of Imaging Systems and Technology*, vol. 8, no. 5, pp. 491–504, 1997.

[63] L. Breiman, J. H. Friedman, R. A. Olshen, and C. J. Stone, *Classification and Regression Trees*. Wadsworth, Inc., 1984.

[64] S. B. Gelfand, C. S. Ravishankar, and E. J. Delp, "An iterative growing and pruning algorithm for classification tree design," *IEEE Transactions on Pattern Analysis and Machine Intelligence*, vol. 13, no. 2, pp. 163–174, February 1991.

[65] J. Suckling, J. Parker, D. R. Dance, S. Astley, J. Hutt, C. R. M. Doggis, I. Ricketts, E. Stamatakis, N. Cerneaz, S. L. Kok, P. Taylor, D. Betal, and J. Savage, "The mammographic image analysis society digital mammogram database," *Proceedings of the 2nd International Workshop on Digital Mammography*, July 10–12 1994, York, England, pp. 375–378.

[66] C. E. Metz, "Evaluation of digital mammography by ROC analysis," *Proceedings of the 3rd International Workshop on Digital Mammography*, June 9–12 1996, Chicago, Illinois, pp. 61–68.

[67] H. P. Chan, K. Doi, C. J. Vyborny, K. L. Lam, and R. A. Schmidt, "Computer-aided detection of microcalcifications in mammograms: methodology and preliminary clinical study," *Investigative Radiology*, vol. 23, no. 9, pp. 664–671, September 1988.

[68] F.-F. Yin, M. L. Giger, K. Doi, C. J. Vyborny, R. A. Schmidt, and C. E. Metz, "Computer-vision system for the detection and characterization of masses for use in mammographic screening programs," *Applications of Optical Engineering: Proceedings of OE/Midwest '90*, vol. 1396, September 27-28 1990, Rosemont, Illinois, pp. 2–4.

[69] R. M. Rangayyan, N. El-Faramawy, J. E. L. Desautels, and O. A. Alim, "Discrimination between benign and malignant breast tumors using a region-based measure of edge profile acutance," *Proceedings of the 3rd International Workshop on Digital Mammography*, June 9–12 1996, Chicago, Illinois, pp. 213–218.

[70] R. N. Strickland and G. J. Lukins, "Fuzzy system improves the performance of wavelet-based correlation detectors," *Proceedings of the IEEE International Conference on Image Processing*, October 26–29 1997, Santa Barbara, California, pp. 404–407.

[71] S. N. C. Cheng, H.-P. Chan, M. A. Helvie, M. M. Goodsitt, D. D. Adler, and D. C. St. Clair, "Classification of mass and nonmass regions on mammograms using artificial neural networks," *Journal of Imaging Science and Technology*, vol. 38, no. 6, pp. 598–603, November-December 1994.

[72] K. Bowyer, D. Kopans, J. W. P. Kegelmeyer, R. Moore, M. Sallam, K. Chang, and K. Woods, "The digital database for screening mammography," *Proceedings of the 3rd International Workshop on Digital Mammography*, June 9–12 1996, Chicago, Illinois, pp. 431–434.

[73] A. K. Jain, *Fundamentals of Digital Image Processing.* Prentice-Hall, 1989.

[74] R. O. Duda and P. E. Hart, *Pattern Recogntion and Scene Analysis.* New York: John Wiley, 1973.

[75] J. Illingworth and J. Kittler, "Survey of the Hough transform," *Computer Vision, Graphics, and Image Processing*, vol. 44, no. 1, pp. 87–116, October 1988.

[76] R. Lo and W. Tsai, "Gray-scale Hough transform for thick line detection in gray-scale images," *Pattern Recognition*, vol. 28, no. 5, pp. 647–661, 1995.

[77] C. Daul, P. Graebling, and E. Hirsch, "From the Hough transform to a new approach for the detection and approximation of elliptical arcs," *Computer Vision and Image Understanding*, vol. 72, no. 3, pp. 215–236, December 1998.

[78] R. A. McLaughlin, "Randomized Hough transform: improved ellipse detection with comparison," *Pattern Recognition Letters*, vol. 19, no. 3–4, pp. 299–305, March 1998.

[79] J. Y. Goulermas and P. Liatsis, "Genetically fine-tuning the Hough transform feature space, for the detection of circular objects," *Image and Vision Computing*, vol. 16, no. 9–10, pp. 615–625, July 1998.

[80] D. H. Ballard and C. M. Brown, *Computer Vision.* Englewood Cliffs, New Jersey: Prentice-Hall, 1982.

[81] R. C. Agrawal, R. K. Shevgaonkar, and S. C. Sahasrabudhe, "A fresh look at the Hough transform," *Pattern Recognition Letters*, vol. 17, pp. 1065–1068, 1996.

[82] Y. Zhang and R. Webber, "A windowing approach to detecting line segments using Hough transform," *Pattern Recognition*, vol. 29, no. 2, pp. 255–265, 1996.

[83] N. Guil, J. Villalba, and E. L. Zapata, "Fast Hough transform for segment detection," *IEEE Transactions of Image Processing*, vol. 4, no. 11, pp. 1541–1548, November 1995.

[84] P.-K. Ser and W.-C. Siu, "New generalized Hough transform for the detection of irregular objects," *Journal of Visual Communications and Image Representation*, vol. 6, no. 3, pp. 256–264, September 1995.

[85] H. Koshimizu and M. Numada, "On the extensive reconstruction of Hough-type transform for line pattern detection," *Journal of Information Processing*, vol. 15, no. 2, pp. 243–251, 1992.

[86] Y. Pan, "More efficient constant time algorithm for computing the Hough transform," *Parallel Processing Letters*, vol. 4, no. 1–2, pp. 45–52, June 1994.

[87] J. D. Bruguera, N. Guil, T. Lang, J. Villalba, and E. L. Zapata, "Cordic based parallel/pipelined architecture for the Hough transform," *Journal of VLSI Signal Processing*, vol. 12, no. 3, pp. 207–221, June 1996.

[88] V. Kamat-Sadekar and S. Ganesan, "Complete description of multiple line segments using the hough transform," *Image and Vision Computing*, vol. 16, no. 9–10, pp. 597–613, July 1998.

[89] R. Nevatia and K. Babu, "Linear feature extraction and description," *Computer Graphics and Image Processing*, vol. 13, pp. 257–269, 1980.

[90] J. Basak, B. Chanda, and D. D. Majumder, "On edge and line linking with connectionist," *IEEE Transactions on Systems, Man and Cybernetics*, vol. 24, no. 3, pp. 413–428, March 1994.

[91] J.-W. Lee and I.-S. Kweon, "Extraction of line features in a noisy image," *Pattern Recognition*, vol. 30, no. 10, pp. 1651–1660, October 1997.

[92] S. Zucker, R. Hummel, and A. Rosenfield, "An application of relaxation labelling to line and curve enhancement," *IEEE Transactions on Computers*, vol. C-26, no. 4, April 1977.

[93] Y. Kanazawa and K. Kanatani, "Optimal line fitting and reliability evaluation," *IEICE Transactions on Information and Systems*, no. 9, pp. 1317–1322, September 1996.

[94] R. C. Nelson, "Finding line segments by stick growing," *IEEE Transactions on Pattern Analysis and Machine Intelligence*, vol. 15, no. 5, pp. 519–523, May 1994.

[95] A.-R. Mansouri, A. S. Malowany, and M. D. Levine, "Line detection in digital pictures: a hypothesis prediction/verification paradigm," *Computer Vision, Graphics, and Image Processing*, vol. 40, no. 1, pp. 95–114, October 1987.

[96] J. B. Burns, A. R. Hanson, and E. M. Riseman, "Extracting straight lines," *IEEE Transactions on Pattern Analysis and Machine Intelligence*, vol. 8, no. 4, pp. 425–455, July 1986.

VITA

Sheng Liu was born in Wuhan, P.R.China. At the age of 15, she was admitted by the Juvenile Ace Undergraduate Program of Shanghai Jiao Tong University, where she received her BSEE (highest honors) and MSEE degrees, in July 1990 and October 1992, respectively.

In 1993, she was an assistant researcher in the Department of Electronic Engineering at Shanghai Jiao Tong University. Her research work included real time image processing and video source coding. From 1994 to 1995, she was awarded a research assistantship in the Department of Electrical Engineering at University of Hawaii at Manoa, where her research was on parallel image compression and content-addressable image database system.

Since Fall 1995, she has been pursuing a Ph.D. degree in the School of Electrical and Computer Engineering at Purdue University, West Lafayette, Indiana. She is a research assistant in the Video and Image Processing Laboratory (VIPER) under the supervision of Professor Edward J. Delp. Her current research interests include multiresolution signal analysis, medical imaging, image segmentation and compression.

During summer 1997 and winter 1998, she worked as a research intern at the Networked Image Technology Center (NITC) in Eastman Kodak Company, Rochester, New York. She created a digital photo database that is currently being used both inside and outside Kodak for the research of face recognition and image segmentation technologies. She also conducted research on using object distance information to improve image segmentation results.

Sheng Liu is a member of the Tau Beta Pi national engineering honor society, the Eta Kappa Nu national electrical engineering honor society, the Phi Kappa Phi national honor society, and a student member of the IEEE professional society.